CERN-THESIS-2012-197

Paramagnetism in ion-implanted oxides

Torben Esmann Mølholt

Faculty of Physical Sciences
University of Iceland
2012

Meðseglun í jónígræddum oxíðum

Torben Esmann Mølholt

Raunvísindadeild
Háskóli Íslands
2012

Paramagnetism in ion-implanted oxides

Torben Esmann Mølholt

Philosophiae Doctor degree in Physics

Doctoral Committee

Senior Sci. Haraldur Páll Gunnlaugsson
(principal supervisor)
Department of Physics and Astronomy, Aarhus University,
Aarhus Denmark

Dr. Sveinn Ólafsson (co-supervisor)
Prof. Hafliði Pétur Gíslason (co-supervisor)
Science Institute, University of Iceland,
Reykjavík Iceland

Opponents

Dr. Ulrich Wahl
Unidade de Física e Aceleradores
Instituto Superior Técnico/Instituto Tecnológico e Nuclear
Universidade Técnica de Lisboa, Portugal

Prof. Örn Helgason
Science Institute, University of Iceland,
Reykjavík Iceland

Science Institute
School of Engineering and Natural Sciences
University of Iceland
Reykjavík, November 2012

Paramagnetism in ion-implanted oxides
180 ECTS thesis submitted in partial fulfillment of PhD degree in Physics

Faculty of Physical Sciences
School of Engineering and Natural Sciences
University of Iceland
VR-III, Hjarðarhagi 2-6
107 Reykjavík
Iceland

Telephone: (+354) 525 4000

Bibliographic information:
Torben Esmann Mølholt, 2012, Paramagnetism in ion-implanted oxides,
PhD thesis, Faculty of Physical Sciences, University of Iceland.

ISBN: 978-9935-9069-5-3

Printing: Háskólaprent ehf., Fálkagata 2, 107 Reykjavík
Reykjavík, Iceland, November 2012

Abstract

This thesis describes the investigation on paramagnetism in dilute ion-implanted single-crystal oxide samples studied by on- and off-line ^{57}Fe emission Mössbauer spectroscopy. The ion-implantation of the radioactive isotopes (^{57}Mn and ^{57}Co) was performed at the ISOLDE facility at CERN in Geneva, Switzerland. The off-line measurements were performed at Aarhus University, Denmark.

Mössbauer spectroscopy is a unique method, giving simultaneously local information on valence/spin state of the ^{57}Fe probe atoms, site symmetry and magnetic properties on an atomic scale. The utilisation of emission Mössbauer spectroscopy opens up many new possibilities compared with traditional transmission Mössbauer spectroscopy. Among them is the possibility of working with a low concentration below 10^{-4}–10^{-3} at.%, where the implanted Mössbauer ^{57}Fe probes are truly dilute impurities exclusively interacting with their nearest neighbours and therefore the possibility of creating precipitations or clusters are avoided.

The main results were obtained on the wide-band gap semiconductor ZnO. Two other oxides, MgO and α-Al_2O_3, were studied as comparative model systems. The ZnO system is of great interest in terms of theoretically predicted dilute ordered magnetism at room temperature.

In all the three oxides Fe^{3+} was found to exhibit slow paramagnetic spin relaxation and there is no evidence of Fe atoms taking part in a dilute magnetic order. A model was developed to extract the temperature dependent relaxation rate of paramagnetic Fe^{3+}. The spin-lattice relaxation rates of Fe^{3+} in MgO and α-Al_2O_3 was found to be consistent with theory and available experimental data in the literature, but ZnO was found to exhibit a $\sim T^9$ temperature dependence above room temperature, which cannot be explained by the expected Raman processes.

In ZnO a fluence dependency ($<10^{12}$ cm^{-2}) of the charge state of Fe^{3+}/Fe^{2+} was found in the temperature range of 300–390 K. This behaviour was explained as caused by a change of the Fermi level upon ion-implantation.

In MgO and α-Al_2O_3 interstitial Fe was suggested to exhibit a novel type of cage motion. In addition it was proposed that the interstitial Fe in MgO exhibits long-range diffusion, with diffusivity orders of magnitude higher than that expected for vacancy assisted diffusion of Fe in MgO.

Útdráttur

Ritgerð þessi lýsir rannsóknum á meðseglun í oxíðkristöllum sem ígræddir voru með lágum styrk jóna. Rannsóknirnar fólust í Mössbauer geislunarmælingum frá járnsamsætunni ^{57}Fe. Jónígræðsla geislavirkra samsæta (^{57}Mn og ^{57}Co) fór fram á ISOLDE rannsóknastofunni við CERN rannsóknastofnunina í Genf. Þar voru mælingar einnig gerðar á meðan jónígræðslan fór fram. Aðrar Mössbauer mælingar voru gerðar við Árósaháskóla.

Mössbauer mælingar hafa þá sérstöðu að gefa samtímis staðbundnar upplýsingar um hleðslu- og/eða spunaástand ^{57}Fe frumeindanna, samhverfu grindarsæta þeirra og seguleiginleika umhverfisins. Mössbauer geislunarmælingar hafa ýmsa kosti umfram hefðbundnar Mössbauer gegnskinsmælingar. Þannig er mögulegt að mæla sýni með mjög lágan styrk af ígræddum Mössbauer ^{57}Fe járnjónum, eða 10^{-4} – 10^{-3} at.%. Þetta er nægilega lágur styrkur til að jónirnar víxlverka einungis við næstu granna sína en ekki hver við aðra og litlar sem engar líkur eru á járnútfellingum.

Meginniðurstöður rannsóknanna varða hálfleiðarann ZnO, sem hefur víða orkugeil. Til hliðsjónar og viðmiðunar voru mælingar gerðar á tveimur öðrum oxíðum, MgO og α-Al_2O_3. ZnO er mikilvægur og áhugaverður hálfleiðari þar sem fræðilegir útreikningar hafa spáð fyrir um uppröðun segulvægja gildisrafeinda við stofuhita þrátt fyrir lágan styrk þeirra.

Rannsóknirnar leiddu í ljós að járnjónin Fe^{3+} reyndist meðseglandi með langan slökunartíma í öllum þremur oxíðunum. Engin merki fundust um uppröðun segulvægja gildisrafeinda. Líkan var þróað til að finna hitastigsháðan slökunartíma hinnar meðseglandi Fe^{3+} jónar. Slökunartími vegna víxlverkunar spuna og brautar fyrir Fe^{3+} jónina í MgO og α-Al_2O_3 reyndist vera háður hitastigi sem T^2 í samræmi við fræði og birtar tilraunaniðurstöður. Hins vegar kom í ljós að slökunartíminn í ZnO sýnir T^9 hegðun sem ekki er hægt að skýra með Raman hrifum sem valda slökun segulvægjanna.

Mælingar sýndu að hlutfall jónanna Fe^{3+}/Fe^{2+} í ZnO er háð styrk ígræddra jóna á hitastigsbilinu 300 – 390 K. Þessar niðurstöður voru útskýrðar með færslu Fermiorkunnar vegna íbætingar frá jónaígræðslunnar.

Niðurstöður sýna nýja staðbundna sveimhegðun járns í milligrindasæti MgO og α-Al_2O_3 Ásamt því sýna niðurstöður langdræga, hraða sveimhegðun járns milli þessara grindarsæta í MgO, með sveimstuðul sem er mörgum stærðarþrepum hærri en búast má við frá sveimi járns með hjálp eyðuveilna í MgO.

Publications in this thesis

This thesis is based on the following **Papers I-VIII**.

Paper I

Temperature and dose dependence of defect complex formation with ion-implanted Mn/Fe in ZnO

Mølholt, T. E., Mantovan, R., Gunnlaugsson, H. P., Bharuth-Ram, K., Fanciulli, M., Gíslason, H. P., Johnston, K., Kobayashi, Y., Langouche, G., Masenda, G., Naidoo, D., Ólafsson, S., Sielemann, R., and Weyer, G.:
Physica B **404**, 4820-4822 (2009).

Paper II

Paramagnetism in Mn/Fe implanted ZnO

Gunnlaugsson, H. P., **Mølholt, T. E.**, Mantovan, R., Masenda, H., Naidoo, D., Dlamini, W. B., Sielemann, R., Bharuth-Ram, K., Weyer, G., Johnston, K., Langouche, G., Ólafsson, S., Gíslason, H. P., Kobayashi, Y., Yoshida, Y., Fanciulli, M., and the ISOLDE Collaboration:
Applied Physics Letters **97**, 142501(3pp) (2010).

Paper III

Observation of spin-lattice relaxations of dilute Fe^{3+} in MgO by Mössbauer spectroscopy

Mølholt, T. E., Mantovan, R., Gunnlaugsson, H. P., Naidoo, D., Ólafsson, S., Bharuth-Ram, K., Fanciulli, M., Johnston, K., Kobayashi, Y., Langouche, G., Masenda, H., Sielemann, R., Weyer, G., and Gíslason, H. P.:
Hyperfine Interactions **197**, 89–94 (2010).

Paper IV

*Mössbauer spectroscopy of ^{57}Fe in α-Al_2O_3 following implantation of ^{57}Mn**

Gunnlaugsson, H. P., Mantovan, R., **Mølholt, T. E.**, Naidoo, D., Johnston, K., Masenda, H., Bharuth-Ram, K., Langouche, G., Ólafsson, S., Sielemann, R., Weyer, G., Kobayashi, Y., and the ISOLDE collaboration:
Hyperfine Interactions **198**, 5–13 (2010).

Paper V
Magnetism in iron implanted oxides: a status report
Gunnlaugsson, H. P., Sielemann, R., **Mølholt, T. E.**, Dlamini, W. B., Johnston, K., Mantovan R., Masenda, H., Naidoo, D., Sibanda, W. N., Bharuth-Ram, K., Fanciulli, M., Gíslason, H. P., Langouche, G., Ólafsson, S., Weyer, G., and the ISOLDE collaboration:
Hyperfine Interactions **197**, 43–52 (2010).

Paper VI
Spin-lattice relaxations of paramagnetic Fe^{3+} in ZnO
Mølholt, T. E., Gunnlaugsson, H. P., Johnston, K. Mantovan, R., Masenda, H., Naidoo, D., Ólafsson, S., Bharuth-Ram, K., Gislason, H. P., Langouche, G., Sielemann, R., Weyer, G. and the ISOLDE Collaboration:
Physica Scripta **T148**, 014006(4pp) (2012).

Paper VII
Lattice locations and properties of Fe in Co/Fe co-implanted ZnO
Gunnlaugsson, H. P., Johnston, K., **Mølholt, T. E.**, Weyer, G., Mantovan, R., Masenda, H., Naidoo, D., Ólafsson, S., Bharuth-Ram, K., Gíslason, H. P., Langouche, G., Madsen, M. B., and the ISOLDE Collaboration:
Applied Physics Letters **100**, 042109(4pp) (2012).

Paper VIII
Lattice Location and Diffusion of Interstitial Fe in MgO
Mølholt, T. E., Mantovan, R., Gunnlaugsson, H. P., Svane, A., Bharuth-Ram, K., Fanciulli, M., Gíslason, H. P., Johnston, K., Kobayashi, Y., Langouche, G., Masenda, H., Naidoo, D., Ólafsson, S., Sielemann, R., and Weyer, G.:
Manuscript in preparation (Nov. 2012)

Reprints were made with the permission of the publishers, and are found in chapter 8.

Presentations at conferences:

Conference talks:

Fe/V superlattices studied using short lived isotopes at ISOLDE/CERN
T. E. Mølholt, S. Ólafsson, H. P. Gíslason and the ^{57}Mn Collaboration at ISOLDE/CERN:
Workshop on Magnetic Order 2011, 8-9 November, Reykjavik, Iceland.

Paramagnetism of Fe^{3+} in $^{57}Mn^{+}$ implanted ZnO
T. E. Mølholt, H. P. Gunnlaugsson, R. Mantovan, H. Masenda, D. Naidoo, W. B. Dlamini, R. Sielemann, K. Bharuth-Ram, G. Weyer, K. Johnston, G. Langouche, S. Ólafsson, H. P. Gíslason, and the ISOLDE Collaboration:
The 24th NSM 2011, 19-22 June, Aarhus, Denmark.

Mössbauer study of spin-lattice relaxations of dilute Fe^{3+} in MgO
T. E. Mølholt, R. Mantovan, H. P. Gunnlaugsson, D. Naidoo, S. Ólafsson, K. Bharuth-Ram, M. Fanciulli, K. Johnston, Y. Kobayashi, G. Langouche, H. Masenda, R. Sielemann, G. Weyer and H. P. Gíslason:
The 3rd HFI/NQI 2010, 12-17 September, CERN, Switzerland.

Mössbauer spectroscopy at ISOLDE/CERN using short-lived parent isotopes
T. E. Mølholt, S. Ólafsson, H. P. Gíslason and the ^{57}Mn Collaboration at ISOLDE/CERN
R-VoN 2010, 8-9 September, University of Iceland, Reykjavik, Iceland.

Mössbauer Spectroscopy of Substitutional and Interstitial Fe in MgO, following implantation of ^{57}Mn
T. E. Mølholt, R. Mantovan, H. P. Gunnlaugsson, K. Bharuth Ram, M. Fanciulli, K. Johnston, Y. Kobayashi, G. Langouche, H. Masenda, D. Naidoo, S. Ólafsson, R. Sielemann, A. Svane, and G. Weyer:
23rd NSM 2009, University of Iceland, 14-17 June, Reykjavik, Iceland.

Conference posters:

Lattice Location and Diffusion of Interstitial Fe in MgO
T. E. Mølholt, R. Mantovan, H. P. Gunnlaugsson, K. Bharuth-Ram, M. Fanciulli, K. Johnston, Y. Kobayashi, G. Langouche, H. Masenda, D. Naidoo, S. Ólafsson, R. Sielemann, A. Svane, G. Weyer, and H. P. Gíslason:
The 3rd HFI/NQI 2010, 12-17 September, CERN, Switzerland.

Paramagnetism in Mn/Fe implanted ZnO
H. P. Gunnlaugsson, **T. E. Mølholt**, R. Mantovan, H. Masenda, D. Naidoo, W. B. Dlamini, R. Sielemann, K. Bharuth-Ram, G. Weyer, K. Johnston, G. Langouche, S. Ólafsson, H. P. Gíslason, Y. Kobayashi, and M. Fanciulli:
The 3rd HFI/NQI 2010, 12-17 September, CERN, Switzerland.

Temperature and dose dependence of defect complex formation with ion-implanted Mn/Fe in ZnO
T. E. Mølholt, R. Mantovan, H. P. Gunnlaugsson, K. Bharuth-Ram, M. Fanciulli, H. P. Gíslason, K. Johnston, Y. Kobayashi, G. Langouche, H. Masenda, D. Naidoo, S. Ólafsson, R. Sielemann, and G. Weyer:
Presented by K. Bharuth-Ram at 25th ICDS 2009, 20-24 July, St. Petersburg, Russia.

Activities:

Participated at the ^{57}Mn beam-times at ISOLDE/CERN and the Mössbauer collaborating team meetings in connection: 2008, 2009, 2010 (also ^{119}In), and 2011 (also ^{119}In).

Participated at the team meetings of the Mössbauer collaborating team, 2009 (CERN, Switzerland), 2010 (Milano, Italy), 2011 (Cape Town and Johannesburg, South Africa and Copenhagen, Denmark).

The ISOLDE separator course, 24-25 November 2009.

Acknowledgments

I am for sure grateful to the people who both directly and indirectly have been involved during this work and who have supported me.

First and foremost I would like to thank my supervisor Haraldur Páll Gunnlaugsson, whom I have now had the pleasure of working with through two major projects. For his constant willingness to help me with skilled guidance and a patience that seems endless. It is and has always been a pleasure to collaborate with him, and I hope for more joint future research and investigations. Thanks for always taking good care of me in Aarhus as well as abroad.

I am grateful to my co-supervisor Sveinn Ólafsson for his guidance and sense for details. Helping and teaching me in the laboratory in the basement of VR-III. For receiving me when I first came to Iceland and making me feel like at home, showing me around Iceland the first weeks.

Thanks to my co-supervisor Hafliði Pétur Gíslason for giving me the opportunity to work with this project and for his skilled advice and patience with me.

I also want to thank the members of "The Mössbauer Collaboration at ISOLDE/CERN" for sharing knowledge and experiences and for making me feel a part of the group. The discussions of results and good times at the yearly team meetings and of course the big event coming together for beam time at ISOLDE. Also thanks for the "not-so-intelligent" and fun discussions in the late hours during night-shift of beam time and the good hours spent outside the CERN gates (Beam On!).

Living abroad is a great adventure and experience, but it has not always been as easy. Had it not been for the enriching company of fellow students and postdocs in VR-III, and friends, life as a PhD student would definitely not have been the same and unbearable. Thanks for the many good hours together at everything from waffle Monday to BBQ burger Friday. Especially I would like to address my thanks to: Gunnar (likewise thanks for all the coffee), Rikke (sharing the nice Danish tradition of a Friday beer after university), Mustafa

(arranging fun game evenings), Cosmin (for the ping pong games which I seldom won), Àrni and Fridirik (for taking the time to teach me in the VR-III laboratory), Tryggvi (for your lab.-assistance), Csaba, Mohammad, Björn, Pauline, Balthasar, Nzar, Tiberiu, Kristján, Bing, Nina, Gabriel, Anna, and Jen.

Thank you Cristina for coming into my life and for your support - happy that we met. It would not have been the same without you ♥.

Last but not least, I thank my parents and brother for their support and unconditional love. I really enjoyed your visit here in Iceland.

The research presented in this thesis was supported by the Icelandic Research Fund and the beam time at ISOLDE/CERN by the European Union Seventh Framework through ENSAR (contract no. 262010). This support is greatly acknowledged.

Often something fancy is written here on this page
but not in my thesis .

Contents

Chapter 1

Scientific background

Mankind has always exploited or altered nature to its own benefit by tailoring materials for beneficial usage. This is and has been an ongoing and continuing process.

A hot topic in the field of semiconductors is the possibility to tailor a dilute magnetic semiconductor, which exhibit properties of both semiconductors and ordered magnetism at room temperature. These are of current interest as potential semiconductor-compatible magnetic components for "spin-(elec)tronic" or magneto-optic applications.

One possibility of obtaining such magnetic semiconductors is through dilute doping (below 5 at.%) of wide-bandgap nonmagnetic semiconductors with 3d-transition metal atoms. The field of dilute magnetic semiconductors (semimagnetic semiconductors) was developed in the 1980s [Furdyna, 1988], as it was realised that introducing a dilute amount of magnetic impurities would not affect the optical or electrical properties of the host, and would introduce a magnetic moment. New interest aroused as a theoretical study by Dietl *et al.* [2000] predicted dilute ordered magnetic behaviour in wide-bandgap semiconductor materials such as GaN and ZnO, with magnetic ordering temperatures T_C well above room temperature. It is of importance for useful applications to possess the magnetic as well as the semiconducting properties at room temperature. This prompted extraordinary experimental and theoretical efforts to achieve, understand and exploit these materials to find evidence of room temperature ordered magnetism, in view of the obvious potential of such

materials for the fabrication of novel spin-(elec)tronic or magneto-optic devices [Pearton *et al.*, 2003]. This effort can be seen in Figure 1.1 by the number of publications in this field.

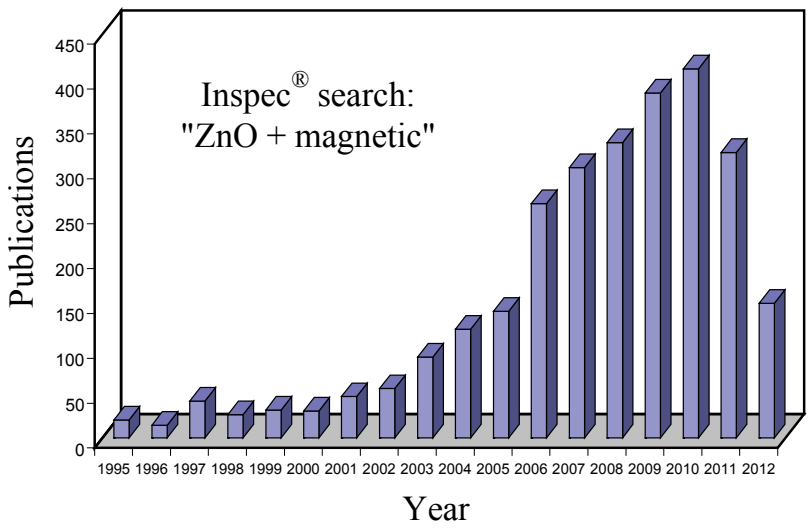

Figure 1.1: Graph illustrating the interest of magnetism in ZnO (1995 – Sep. 2012). The number of publications increases rapidly after it was theoretically suggested possible at room temperature in 2000 [Dietl *et al.*, 2000]. The number of publications was found with a search using Inspec® (Institution of Engineering and Technology).

A full working read-write device (disk) using the (Ga,Mn)As system has been demonstrated, where the information is written fully electrically and the information storage in the device is non-volatile. However, it is only useful below 61 K [Mark *et al.*, 2011], which renders it not suitable for larger applications, thus reducing it to a useful model system with limited if any practical applications at present.

Introducing magnetic behaviour into semiconductor materials and developing spintronic devices, offers the exciting prospect of having for example a single device with both non-volatile magnetic storage capability and conventional semiconductor device behaviour. The spintronic device could consist of a non-volatile spin transistor, using the transport of electrons with long coherence spin lifetime to deliver or store information, just like a flow of charge is used today. Such a device could be smaller (have denser integrated circuits), have less energy consumtion and be more efficient than current technology, which is based on only the electron charge. It would be possible to rapidly switch the device on

and off and would allow for example a long battery time of mobile gadgets, since the device would mostly be turned off [Pearton *et al.*, 2003].

Possible mechanisms resulting in DMS at room temperature were proposed by Dietl *et al.* [2000] and Coey *et al*. [2005]. Despite extensive experimental effort, evidence for observation of dilute magnetism at room temperature in the studied systems is often contradictory and not convincing since the theoretical description of this behaviour is still under discussion and the phenomenon is incompletely understood [Ando, 2006; Özgur *et al.*, 2005; Zunger *et al.*, 2010]. Some groups have suggested unintentional precipitation of 3d-metal impurities to be the source of at least some of the positive findings of dilute magnetism [Potzger and Zhou, 2009].

Few analytical techniques, which can give atomic scale information on electronic configurations and magnetic properties, have been applied to the studies of these systems. Among techniques used is on-line emission Mössbauer spectroscopy utilising the ^{57}Fe Mössbauer isotope ($T_{½} = 98.3$ ns) after the implantation of ^{57}Mn ($T_{½} = 85.4$ s), which allows a very low implantation fluence. This results in truly dilute samples with a concentration below 10^{-3} at.% and with this method a spectrum is recorded on-line after 5–10 minutes of implantation. For comparison in normal transmission Mössbauer measurement a concentration level above ~0.1 at.% is needed. Here precipitation is a possibility (risk) due to the longer measurement time (above 15 days).

Using ion-implantation of short-lived isotopes for studying the phenomenon of dilute magnetism with Mössbauer spectroscopy was initiated in 2005 by the "*Mössbauer collaboration at ISOLDE/CERN*" with tests that resulted in a formal proposal to the INTC (ISOLDE and Neutron Time-of-flight committee) committee in 2006, where beam time was granted for a full study (the IS443 experiment [Fanciulli *et al.*, 2006]). The experimental work of this thesis was carried out under the IS443 experiment and the follow-up IS501 experiment [Gunnlaugsson *et al.*, 2010].

The first experimental results obtained on single-crystal ZnO utilising ^{57}Mn ion-implantation for ^{57}Fe Mössbauer spectroscopy suggested that ordered magnetism due to the dilute (low concentration) ion-implanted 3d-metal (Mn/Fe) had indeed been observed at room temperature, and paramagnetism seemed excluded [Weyer *et al.*, 2007]. These interpretations led to initiation of this PhD project with the main objective to further study and understand the fundamental physics of dilute magnetism in wide band-gap semiconductors and oxides. The

systems studied and presented in this PhD thesis are single-crystalline ZnO, MgO, and α-Al_2O_3. During this work, as new experiments were made and more data were obtained and analysed, the project evolved and took a new direction. In particular, when the first ^{57}Fe emission Mössbauer measurements of Mn/Fe implanted ZnO in an external magnetic field disproved that the Fe atoms contribute to dilute ordered magnetism in ZnO, a new direction of interpreting the experimental data was taken. This evidently led to a change of the original title of the PhD project.

Although the study of magnetism in dilute implanted/doped semiconductors is still novel and in its early days it is a fascinating physical phenomenon which will contribute to understanding the fundamental physics of magnetism and the implanted atoms in the host as well as practical its applications of this phenomenon.

Chapter 2

Magnetism and semiconductors

For the purposes of this thesis magnetism in materials can be simply classified into paramagnetism or ordered magnetism. The difference between the two types of magnetism is that paramagnetism does not exhibit a long-range spontaneous magnetic order of the spin directions, except when exposed to extremely strong magnetic fields at very low temperature – and in this case the effect can certainly not be called spontaneous. In the case of a spontaneous magnetic order the spins are on the average aligned in a preferred direction which is counteracted by thermodynamic effects until at a critical temperature. In general for paramagnetism the spin directions show rapid fluctuations averaging to zero and therefore there is no preferred magnetic field direction.

2.1 Paramagnetism

The magnetic properties of paramagnetic materials originate from the spins of unpaired electrons which give rise to magnetic dipoles. The dipoles are randomly orientated and do not interact strongly. This implies that a time average of the fluctuations is observed, resulting in a measured zero net-magnetisation. The spin fluctuations lead to the relaxation phenomena which will be presented later (in section 3.7). With applied magnetic field, the dipoles begin to align somewhat on the average along the direction of the applied field, resulting in a net magnetic moment. This effect increases with decreasing temperature.

Usually the induced magnetic field increases linearly with the magnetic field strength, but when the field is removed the magnetisation disappears.

2.2 Magnetic order

The magnetic moments of atoms can be visualised as spin vectors. In a crystal exhibiting magnetic order (e.g. ferro-, antiferro-, ferri-magnetism) the spins of the atoms are on the average preferentially aligned in a specific direction by the exchange interaction, but this is counteracted by lattice vibrations and coupled spin waves at higher temperatures.

The exchange interaction originates from an overlap of the electron wave functions and therefore the range of this interaction is on the order of atomic distances. In a solid the exchange interaction between two metal atoms with electron spins $\mathbf{S}_1$ and $\mathbf{S}_2$ can be written as [Crangle, 1991];

$$E_{ex} = -2J_{1,2}\mathbf{S}_1 \cdot \mathbf{S}_2 \quad . \tag{2.1}$$

Where $J_{1,2}$ is the exchange-coupling constant. Its sign determines the magnetic order, $J_{1,2} > 0$ describes ferromagnetism and $J_{1,2} < 0$ describes antiferromagnetic order [Crangle, 1991].

Thermal fluctuations break down the alignment of the spins in the crystal. Thus the magnetic order can only be observed below a certain critical Curie temperature T_C (or Neel temperature for antiferromagnetic). Above T_C thermal fluctuations dominate, the alignment of the spins is random and the system behaves as a paramagnet (see Figure 2.1). Typical ferromagnetic elements are for example the 3d-transition metals Fe, Ni, and Co, all with a T_C far above room temperature [Crangle, 1991].

In non-metallic crystals like oxides and semiconductors the ground state configuration and thus the magnetic moment of an implanted Fe ion can be predicted using Hund's rules [Crangle, 1991]. Since electrons with parallel spins first fill the *d*-shell, the d^5 configuration of the ground state is expected to have five parallel spins which maximises the total spin to $S = 5/2$ (high-spin). As a contrast the low-spin case of $S = 1/2$ has two pairs of antiparallel spins and an unpaired one [Stöhr and Siegmann, 2006].

Normally both the spin and the angular moment contribute to the resultant magnetic moment of the ion and have to be combined to a total angular momentum J. However for 3d-metals like Fe one can assume a spin-only magnetic moment due to quenching of the orbital momentum ($L = 0$ and $S = J$) due to crystal field effects [Kittel, 1996].

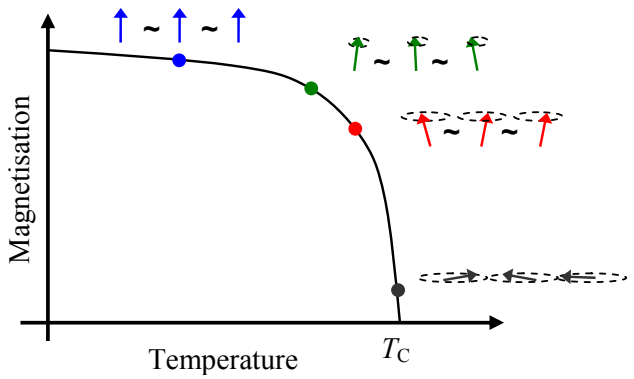

Figure 2.1: The magnetisation caused by magnetic order decreases with increasing temperature, and breaks down when the temperature approaches the Curie temperature T_C. With increasing temperature the spins become randomly aligned (fluctuate).

By means of ^{57}Fe Mössbauer spectroscopy, it is possible to measure the magnetic interactions through the hyperfine interactions (interaction of nuclear levels with the electronic configuration, see section 3.6), both in the case of the ^{57}Fe Mössbauer isotope being responsible for the magnetic behaviour and when the ^{57}Fe acts as a local probe in the crystal.

2.3 Dilute magnetism in semiconductors

One of the most important properties of semiconductors is the possibility of changing their basic conduction properties through doping, i.e. by introducing a small amount of extrinsic atoms (dopants) into the crystal. The doping provides majority charge carriers, either electrons or holes, depending on the valence of the extrinsic atoms relative to the host atoms replaced. Doping with acceptors results in p-type semiconductors with hole conductivity. Doping with donors gives n-type semiconductors with electron conductivity [Sze, 1969]. According to the type of doping the Fermi level (E_f) shifts in the band gap as illustrated in Figure 2.2.

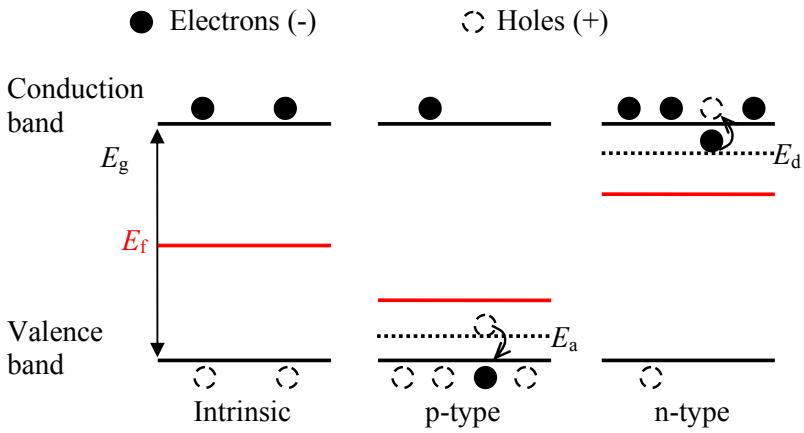

Figure 2.2: Energy band diagram of a doped semiconductor. p-type doping introduces extra holes shifting the Fermi level towards the valence band. n-type doping introduces extra electrons shifting the Fermi level towards the conduction band. E_d is typically located 20–30 meV below the conduction band. Adopted from [Sze, 1969].

Doping of semiconductors also controls other vital properties of these important materials, in addition to the electrical conductivity. These include thermal, optical and, as discussed in this thesis, magnetic properties. Even a point defect concentration of only 1 out of 10^9 atoms may greatly affect different properties of semiconductors [Deicher, 2002].

This approach of altering the properties of the crystal material can be followed by doping of magnetic elements. When low doping (dilute concentration) of magnetic 3d-element dopants (notably Mn, Fe, and Co) are introduced into a non-magnetic host material it can promote magnetism. Normally semiconductor electronics make use of only the charge of the electrons and in contrast to this the electron spins are used for (permanent) information storage in a magnetic material. In spintronics both the charge and the magnetic spin of the electron are involved. One way of achieving a spintronic device is using nonmagnetic semiconductors and/or oxides which during growth or by subsequent ion-implantation are doped with dilute 3d-transition metal ions or by intentionally created defects that promote dilute magnetism. A brief overview of the current status and the more frequently cited models behind the origin of dilute magnetism is given here. It should be noted that there are many explanations and models to be found in the literature.

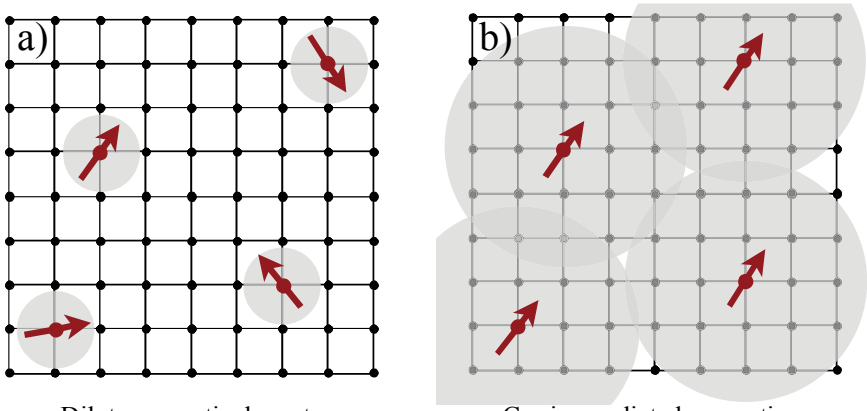

Figure 2.3: Dilute 3d-element dopants introduce magnetic spins (red arrows). Conventional exchange interaction is not long-range, hence no (spontaneous) magnetic order but instead paramagnetic states are randomly distributed in the material (a). Due to carrier (hole or electron) mediated magnetism the interaction can become long-range whereby spontaneous magnetic order could be introduced (b).

The magnetic 3d dopants introduce spins as illustrated in Figure 2.3 a) by the red arrows. Conventional exchange interactions (or superexchange in oxides) cannot produce a long-range magnetic order at dilute concentrations of magnetic dopant-ions of a few percent at room temperature [Coey *et al*., 2005].

The magnetic exchange interaction is limited by the extent of the polarised wave-functions decaying exponentially with distance and the dilute dopants do not interact with each other. Hence the 3d dopants are paramagnetic states in the material with fluctuating spin directions.

It is possible for this interaction range of the dopant to increase due to screening of the dopant atom's Coulomb potential. This screening occurs through the surrounding electrons or electrical permittivity of the host material and the electron wave-function range is extended. This increased interaction distance can give rise to a long-range carrier mediated magnetism as illustrated in Figure 2.3 b). Here holes [Dietl *et al.*, 2000] or electrons [Coey *et al.*, 2005] carry the magnetic interaction to larger extent creating an effective ferromagnetic coupling at dilute dopant concentration. This mechanism has been invoked to explain the dilute magnetism in Mn (5–8%) doped GaAs [Dietl *et al.*, 2000]. Here the Mn^{2+} substitutes Ga^{3+} creating an orbiting hole that aligns the spin of Mn^{2+}. An increased concentration will increase the interaction and T_C. However, T_C can not be enhanced indefinitely as a larger impurity concentration will lead

to occupying interstitial sites or the formation of clusters/precipitates thus resulting in a global ferromagnetic order [Coey *et al.*, 2005].

Structural point defects in doped and undoped materials have also been suggested to explain dilute magnetism in e.g. ZnO [Hong *et al.*, 2005 and 2007; Wang *et al.*, 2008 and 2009; Kapilashrami *et al.*, 2009] or in InN [Xie *et al.*, 2012]. Here, crystal defects (vacancies or grain boundaries) provide the carrier needed for the 3d-dopant to become long-range interacting as illustrated in Figure 2.4 a). In undoped materials the structural defects (vacancies or intrinsic structural defects) are suggested to cause a spin polarisation of the material leading to an ordered magnetism (Figure 2.4 b).

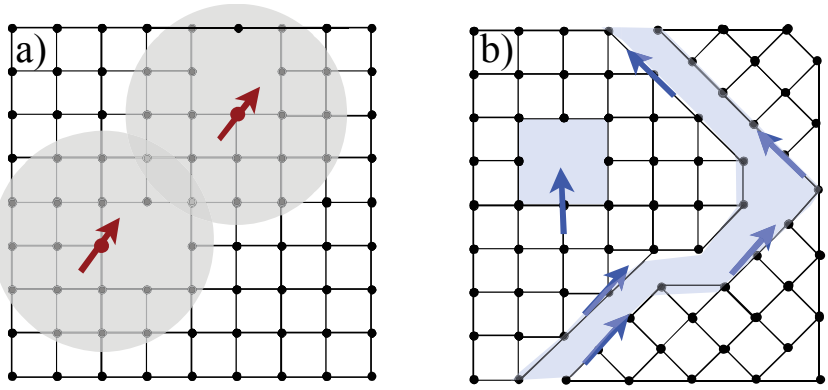

Figure 2.4: Structural defects like vacancies gives the dopants (red arrow) the carrier needed to become long-range magnetically interacting (a). Structural defects without dopants are also suggested to cause a spin polarisation of the material resulting in ordered magnetism (b).

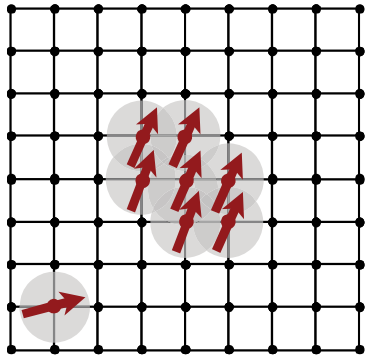

Figure 2.5: Clustering of the dilute dopants (red arrows) result formation of islands of localised spontaneous magnetic order.

The last model illustrated in Figure 2.5 is the formation of clusters or nanoparticles of the dilute dopants, resulting in a magnetic ordering of the closely interacting 3d-dopants. Clustering may be a result of unintentional precipitation [Potzger and Zhou 2009; Zhou et al., 2009].

If only the average concentration of dopants is known, it can be difficult to distinguish between the situations described in Figure 2.3 b) and Figure 2.5, showing that unintentional precipitation has a major impact on the conclusions.

To have a magnetic ordering temperature T_C (or T_N) requires a certain minimum spin density for the classical exchange interaction (Equation (2.1)). A plot of the Curie temperature (or Néel temperature) as a function of the spins/atoms (spin density) for selected metals and oxides is shown in Figure 2.6 (not all materials are labelled). The blue shaded area illustrates dilute magnetism above room temperature for useful applications. To enter this area would likely require a new mechanism behind magnetic ordering.

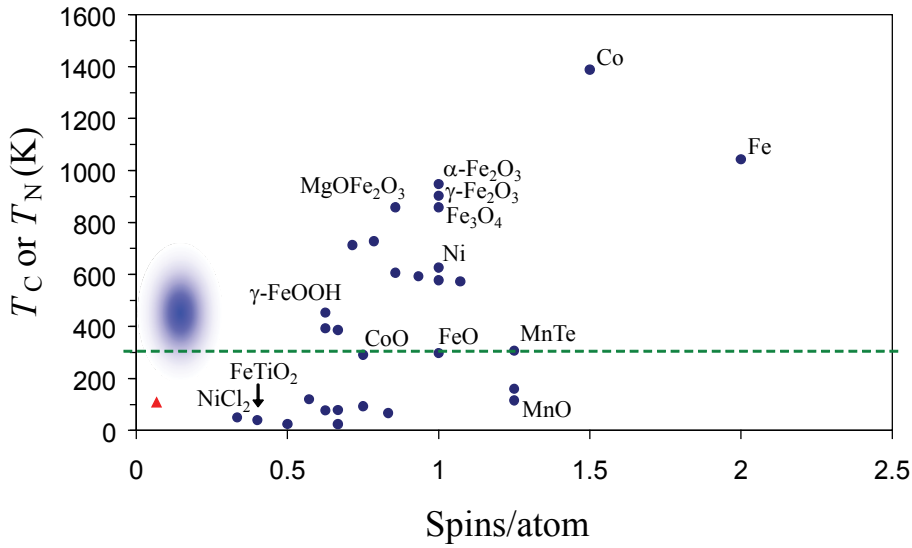

Figure 2.6: Plot of Curie temperature (or Néel temperature) as a function of their calculated spins/atom (spin density) for selected metals and oxides (not all are labelled). The red triangle indicates dilute magnetism in $(Ga_{0.947}, Mn_{0.053})As$ [Ohno, 1998]. The plot illustrates that a certain minimum of spins/atoms is required for a given T_C. The shaded blue area marks the region were useful dilute magnetic semiconductors above room temperature would be expected.

An obstacle for current dilute magnetic systems for usage is that they have a T_C far below room temperature. $(Ga_{1-x}, Mn_x)As$ has a T_C = 110 K for x = 0.053

[Ohno, 1998] (red triangle in Figure 2.6) and this material represent one of the better semiconductor systems for practical applications.

Dilute magnetism in semiconductors at room temperature would mean new applications that would be of significant interest. In order to further improve and develop semiconductor devices it is required to obtain a detailed understanding of the physical mechanisms and effects of the magnetic dilute extrinsic dopants (point defects) introduced into non-magnetic semiconductors and/or oxides.

Chapter 3

Mössbauer spectroscopy

The purpose of this chapter is to give the reader an outline of the basic principles of Mössbauer spectroscopy relevant to interpret the experimental results presented in this thesis. For more general information the reader is referred to text books on Mössbauer spectroscopy [Gütlich *et al.*, 2011; Mørup, 2011; Gonser, 1975].

The nucleus of a free atom which emits a γ-ray recoils due to the conservation of momentum. This lowers the energy of the γ-ray below the nuclear transition energy. Similarly, in the absorption process the absorbing nucleus recoils, and the energy of the resonantly absorbed photon has to be greater than that of the transition. Hence, for a free atom the recoil prevents resonant emission and absorption.

The German physicist Rudolf Ludwig Mössbauer (1929–2011) discovered the phenomenon of recoil-free nuclear resonance fluorescence as a PhD student in 1957. In 1961 he received the Nobel price in physics (together with Robert Hofstadter's research of electron scattering in atomic nuclei) for this discovery, which became commonly known and referred to as the Mössbauer effect resulting in the technique of Mössbauer spectroscopy [Kalvius and Kienle, 2012].

3.1 Recoil-free fraction of nuclear events (Mössbauer effect)

The recoil energy of a nucleus emitting a γ-quantum with transition energy E_0 is [Gütlich *et al.*, 2011 Ch. 2];

$$E_R \approx \frac{E_0^2}{2Mc^2} \quad . \tag{3.1}$$

When a nucleus is located in a solid crystal lattice, the mass M of the system is effectively the crystal, reducing the energy loss due to recoil to a negligible amount. For ^{57}Fe the emitted recoil-free γ-energy is $E_\gamma \approx E_0 = 14.4$ keV. It should be noted that not all nuclei undergo recoil-free γ-emission, but only a certain fraction.

The Mössbauer effect depends on the bond strength in a crystal lattice. Placing the Mössbauer atom in a solid sufficiently reduces the recoil. However, the bound nucleus still vibrates as the lattice does. At higher temperatures the vibrational energy and amplitude increase. The recoil energy can still be transferred to the lattice as quantised lattice vibrations, or phonons. A recoil-free event occurs if E_R is smaller than the lowest quantised vibrational mode. This probability is given by the *f*-factor, also called the Debye-Waller factor or Lamb-Mössbauer factor, and indicates the fraction of nuclear transitions that occur without recoil.

The recoil-free fraction of the γ-quanta, *f*, can be written as [Gütlich *et al.*, 2011 Ch. 2]:

$$f = \exp\left(-\frac{E_\gamma{}^2}{\hbar^2 c^2} \langle x^2 \rangle \right) \quad , \tag{3.2}$$

where $\langle x^2 \rangle$ is the mean square vibrational amplitude of the emitter (or absorber) in the radiation direction. The γ-energy (E_γ) is squared, which is why the Mössbauer effect is only detected in isotopes with a fairly low excited state (amongst the highest energy transitions observed is ^{117}Sn with a Mössbauer transition of 158.6 keV). The recoil-free fraction is temperature dependent and elevated temperatures result in a larger mean-square displacement $\langle x^2 \rangle$ and a lower value of the *f*-factor. To evaluate $\langle x^2 \rangle$ it is necessary to have a model of

the vibrational spectrum, which could be the Debye or Einstein model. Applying the Debye model, the *f*-factor can be calculated [Gütlich *et al.*, 2011 Ch. 2], and this is illustrated in Figure 3.1 for the case of ^{57}Fe.

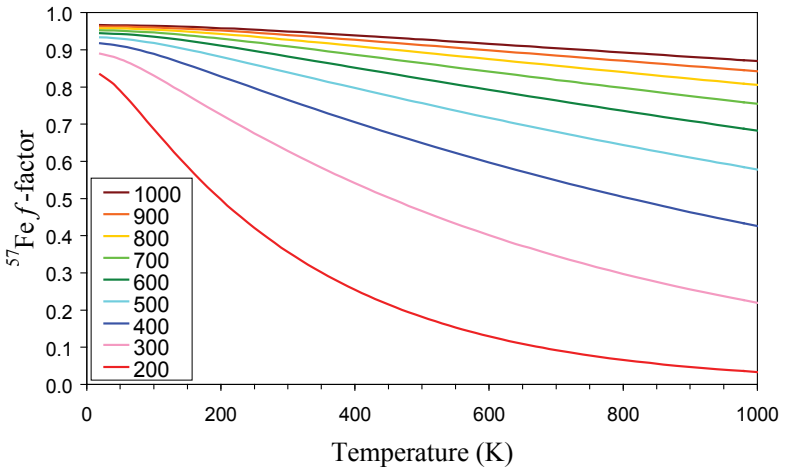

Figure 3.1: The temperature dependent *f*-factor of ^{57}Fe calculated for the indicated Debye temperatures (θ_D) ranging from 200–1000 K.

The largest recoil-free fraction is found for low γ-energy and small lattice vibrations. It is therefore necessary for the solid to have a high Einstein- and Debye vibrational frequencies (ω_E, ω_D) and temperatures (θ_E, θ_D) respectively. Typically the Debye temperature is slightly higher for Fe^{3+} than for Fe^{2+} if the sites are roughly identical, due to a stronger interaction of Fe^{3+} to the ligands. A substitutional ^{57}Fe probe atom has a higher Debye temperature than an interstitial one, since the former is more strongly bound to the lattice. Generally this property can be used to distinguish between implanted interstitial sites and substitutional ones.

3.2 Mössbauer measurements

Mössbauer spectra are recorded by measuring the count-rate (or total-counts during the experiment) as a function of the relative velocity between the source and absorber. The velocity is defined as positive if the source and absorber approach each other. If the source moves with the velocity v relative to the absorber, the emitted γ-quanta from the source have the energy $E(v)$ in the absorber rest frame due to the Doppler effect [Gütlich *et al.*, 2011 Ch. 2]:

$$E(v) = E_\gamma\left(1 + \frac{v}{c}\right) \quad , \tag{3.3}$$

where $E_\gamma \approx E_0$ is the source transition energy at rest. For most Mössbauer nuclei the necessary velocity is a few mm/s, thus the non-relativistic expression of the Doppler effect has been used. The emitted γ-quanta have therefore slightly different energies due to the Doppler effect. For ^{57}Fe Mössbauer spectroscopy a velocity change between $v = \pm 10$ mm/s equals $\Delta E = \pm 4.8 \times 10^{-7}$ eV and due to the high resolution the resonance profile is resolved.

The number of Mössbauer γ-counts registered above background (intensity) in the detector over a time span as a function of the relative Doppler velocity (negative to positive) defines the emission Mössbauer spectrum, as shown in Figure 3.2. For the transmission Mössbauer spectrum it is the γ-counts below background.

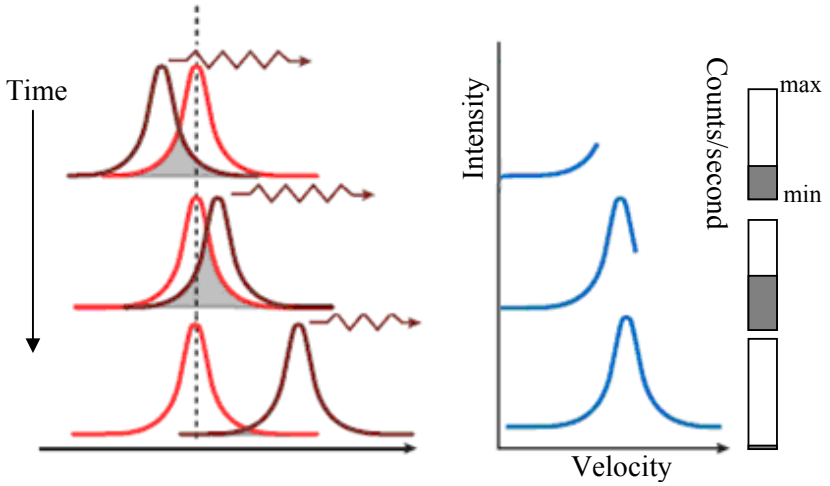

Figure 3.2: Temporal picture of the measurement of an emission Mössbauer spectrum. The absorber/detector spectrum moving from higher (+*v*) to lower (-*v*) energies (Doppler shifted), is shown with the brown line, relative to the fixed source/sample spectrum (red). At each velocity the intensities of the emission spectrum (blue) corresponds to how much the two lines overlap. Greater overlap (better resonance) results in an increased emission and more γ counts/second as indicated with the bars on the right side (minimum counts are the background). Adapted from [Dyar *et al.*, 2006].

The high spectral resolution arises from the half-life of the Mössbauer isotope. For ^{57}Fe one gets a theoretical resolution determined by the natural line-width $\Gamma_{NAT} = 4.69 \times 10^{-9}$ eV corresponding to a Doppler velocity of 0.097 mm/s.

This energy resolution is sufficient to probe the hyperfine interactions between the nucleus and its electronic configuration.

The intensity profile as a function of energy for the emitted gamma quanta can be described by a Lorentzian profile with the FWHM (full width at half maximum) line-width Γ_{NAT} centred at the most likely transition energy, not including the recoil effect (Lorentz profile) [Gütlich *et al.*, 2011 Ch. 2]:

$$I(E) \propto \frac{\Gamma_{NAT}/2\pi}{(E-E_0)^2 + (\Gamma_{NAT}/2)^2} \quad . \tag{3.4}$$

In the experimental Mössbauer spectrum the FWHM maximum is twice the natural line-width, $\Gamma_{exp} = 2\Gamma_{NAT} = 0.194$ mm/s, because an emission line of the same width overlaps the absorption line. Such narrow lines are never observed due to vibrations in the experimental setup and inhomogeneous Fe probe sites in the sample/absorber causing perturbations broadening the lines. The random perturbations result in a Gaussian broadening of the Lorentz profile. This is why a Voigt profile, which is a convolution of a Lorentzian with FWHM Γ and a Gaussian profile with standard deviation σ, is used for fitting the Mössbauer spectra.

Thickness effect can be neglected in this work, due to the low ^{57}Fe concentration used (below ~4×10^{12} ^{57}Fe/cm^2). The thickness effect is first observed above 3×10^{15} ^{57}Fe/cm^2.

3.3 Diffusional broadening

The diffusivity of the Mössbauer isotope can be determined by analysing the Lorentzian broadening of the Mössbauer line. Generally the broadening can be written as [Singwi and Sjölander, 1960];

$$\Delta E = 2\hbar f_j (1 - \sum_n p_n \exp(i\mathbf{k}\mathbf{r}_n)) \quad , \tag{3.5}$$

where f_j is the jump frequency, $\mathbf{k}$ is the wave-vector of the radiation, $\mathbf{r}_n$ is the jump vector and p_n the probability of finding the atom at $\mathbf{r}_n$ after a single jump.

Here the angular term can be neglected, as it does not contribute in the rather large solid angle in our experimental setup (~30º). To find a relationship between jump frequency f_j and the macroscopic diffusion coefficient D, the diffusion profile needs to be considered. With initial conditions of a delta-function at origo, the solution of Fick's second law is a Gaussian in 3-dimensions,

$$P(R,t) = \frac{1}{8(Dt\pi)^{3/2}} \exp\left(-R^2/(4Dt)\right) \quad , \tag{3.6}$$

where D is the macroscopic diffusion coefficient, t the time and R the distance from origo. Along a specific direction (e.g. x-direction), the profile will be Gaussian with a standard deviation of $\sigma = \sqrt{2Dt}$.

For a set of atoms taking random N number of jumps in a cubic symmetry along the x-direction the x-distribution is a Gaussian with $\sigma = \frac{l}{\sqrt{3}}\sqrt{N}$, where l is the elementary jump length. Combining the two standard deviations and the jump frequency can be written as $f_j = N/t = 6D/l^2$. This can be used in Equation (3.5) to give the line-broadening as,

$$\Delta E = \frac{12\hbar D}{l^2} \Rightarrow \Delta\Gamma = \frac{12c\hbar D}{E_0 l^2} \quad . \tag{3.7}$$

In the Mössbauer spectrum a Lorentzian broadening of $\Delta\Gamma$ = 0.06–0.6 mm/s equals a diffusion constant, $D = 2\times10^{-10}$–2×10^{-9} cm^2/s or 0.3–3 lattice jumps of the ^{57}Fe Mössbauer probe atom during its lifetime (τ_M = 141.8 ns).

3.4 Isomer shift, δ

The isomer shift is observed in the Mössbauer spectrum as a shift of the emission (absorption) line and is due to a difference in the s-electron density between the absorber and emitter nuclei (electric monopole interaction). This leads to a difference between the absorber and the source transition energies ($E_a - E_s$). With a known isomer shift reference of the source, the isomer shift becomes a linear function only depending on the s-electron wave function of the

absorber/detector, since the electron probability density $|\psi(0)|_s^2 = constant$ the isomer shift can be written as:

$$\delta = \alpha\{|\psi(0)|_a^2 - C\} \quad , \tag{3.8}$$

where α = -0.3666 mm s^{-1} a.u.^{3} is the isomer shift calibration constant [Gütlich *et al.*, 2011 Ch. 4]. The known reference is defined to have $\delta = 0.0$ mm/s and commonly for ^{57}Fe Mössbauer spectroscopy the reference is α-Fe at room temperature, which is also the case in this study. When the energy levels are shifted it results in an isomer shift and the resulting effect of the emission spectrum is illustrated in Figure 3.3.

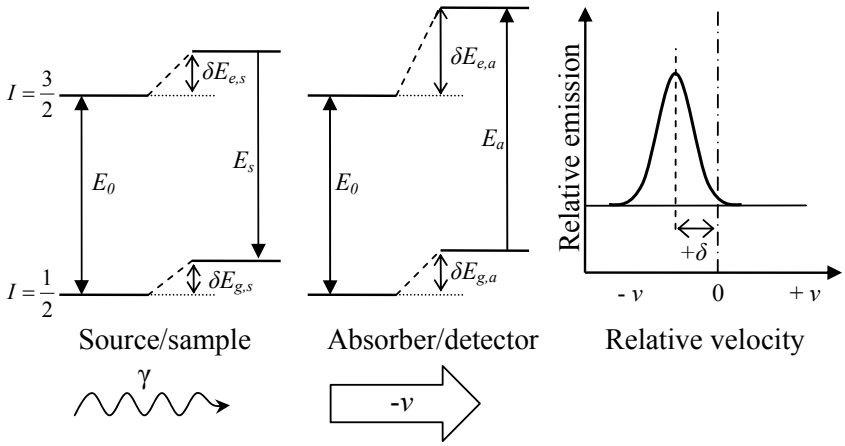

Figure 3.3: Illustration of the isomer shift ($E_a > E_s$ gives a $+\delta$) of ^{57}Fe and the resulting emission Mössbauer spectrum. For emission Mössbauer spectroscopy the velocity shift and the isomer shift are opposite. Here the sample/source is fixed (emitting a γ) and the absorber/detector moving away from the sample ($-v$). The energy levels are not drawn to scale.

In home laboratories (often transmission Mössbauer spectroscopy is used) normally the emitter nucleus is the source and the sample is the absorber (absorber experiment). Then the isomer shift of the absorption is at positive velocity if $E_a > E_s$ and the velocity shift and the isomer shift are equal. This is not the case for emission Mössbauer spectroscopy that is the experimental method used in this thesis. Here the sample is a fixed source and the detector is the moving absorber. Then if $E_a > E_s$ the absorber/detector has to move away ($-v$) from the source/sample to get resonance. Therefore, due to the standard definition of the Mössbauer velocity scale, the observed line position in emission

Mössbauer spectra is opposite compared with the line position in spectra obtained on fixed samples with stable isotopes (e. g. transmission Mössbauer spectroscopy).

The isomer shift is normally presented with the unit mm/s, and is the relative velocity the source needs to compensate for the difference in the s-electron density between the absorber and source nucleus. Reported isomer shifts (and other relevant component variables) are always given at room temperature (if nothing else is implied), and for emission Mössbauer spectroscopy note that the velocity shift and the isomer shift are opposite according to the standard definition.

Generally the contribution to $|\psi(0)|_a^2$ in Equation (3.8) originates from the s-electrons' ability to penetrate the nucleus (1s and 2s electrons with the far major contributions), and would not be expected to depend on the number of d-electrons in the case of Fe. However, the d-electrons shield (or screen) the nucleus from the s-electrons causing a dependence on the valence/spin state of the atom. Figure 3.4 illustrates a guideline of the approximate most common velocity ranges of the isomer shifts at different charge and spin states of Fe.

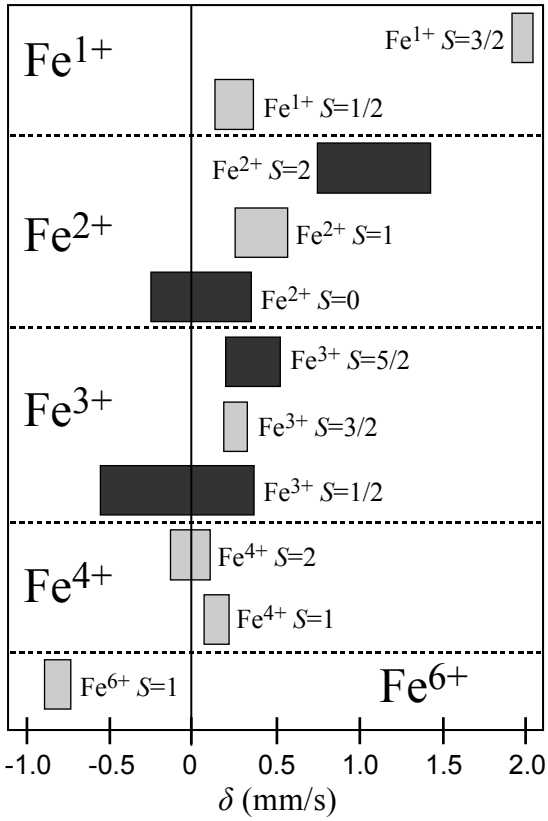

Figure 3.4: Isomer shift ranges observed for ^{57}Fe compounds relative to α-Fe at room temperature that can be used as a guideline. *S* indicates the spin state of the different oxidation levels of Fe. The darker marked ranges are the more often observed Fe states (adapted from [Gütlich *et al.*, 2011 Ch. 4]).

High-spin Fe^{2+} which have six 3d-electrons ($3d^6$), has more shielding than high-spin Fe^{3+}, having only five 3d-electrons ($3d^5$). The larger shielding effect, due to the more 3d-electrons, reduces the s-electron density at the nucleus and consequently results in a higher isomer shift since the value of α in Equation (3.8) is negative [Gütlich *et al.*, 2011 Ch. 4].

As seen in Figure 3.4 there are overlapping ranges of isomer shift for different Fe valence/spin states and therefore it is not possible to distinguish alone from the isomer shift the valence/spin state of Fe. E.g. if $\delta = 0.3$ mm/s is measured in the spectrum roughly seven Fe states are possible. To make a possible distinction it is also necessary to have further information on the natural valence state of the Fe in the material and determine the quadrupole splitting and also the magnetic hyperfine interaction that give additional restrictions on the possible valence/spin state of Fe. Typical observed ^{57}Fe isomer shifts are of the order of 0.0–1.0 mm/s equal to $\sim 3 \times 10^{-8}$ eV.

3.4.1 Second order Doppler shift (SOD)

As stated above, the movement of the source in a Mössbauer experiment is of the order of a few mm/s and relativistic effects negligible. However, due to lattice vibrations there is a temperature dependent shift, which is attributed to the average velocity of the nuclei $\langle v^2 \rangle$. This is called the second order Doppler shift (SOD). The SOD adds to the genuine isomer shift, so the experimentally observed isomer shift is [Gütlich *et al.*, 2011 Ch. 4];

$$\delta_{\text{exp.}} = \delta + \delta_{\text{SOD}} \quad , \tag{3.9}$$

$$\delta_{\text{SOD}} = \frac{-E_\gamma \langle v^2 \rangle}{2c^2} \quad . \tag{3.10}$$

Applying the Debye model to describe the lattice vibrations one obtains the second order shift represented in terms of Debye temperature θ_D [Gütlich *et al.*, 2011 Ch. 4]. Illustrated in Figure 3.5 is the SOD vs. temperature depends on the Debye temperature of the ^{57}Fe Mössbauer probe.

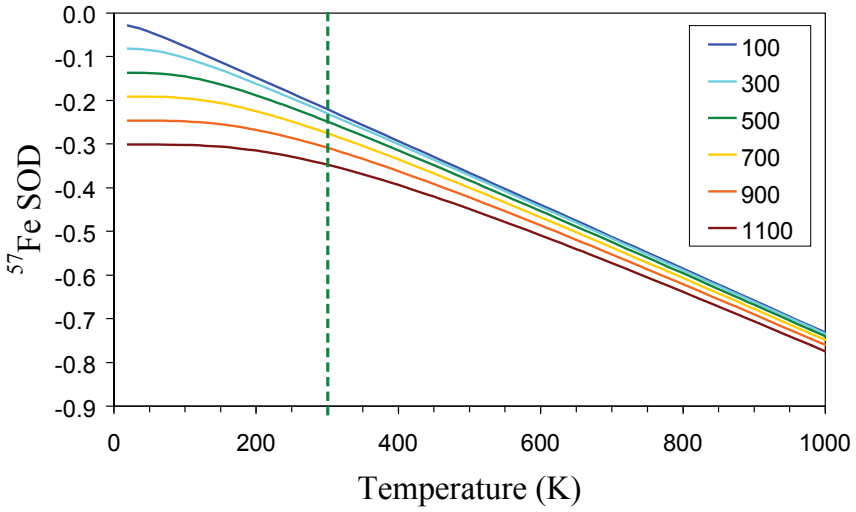

Figure 3.5: Temperature dependence of the isomer shift due to the second-order Doppler shift (SOD). Calculated curves for the indicated Debye temperatures. Above room temperature (300 K) their slopes or almost all equal.

As the slope above room temperature is more or less always equal, it is possible to follow the isomer shift of Mössbauer lines in temperature series, without knowing the Debye temperature exactly. In comparison with low temperature measurements this has the application for possible determination of Debye temperatures.

3.5 Quadrupole splitting, ΔE_Q.

The quadrupole splitting is due to the electrical quadrupole interaction and applies only for a nucleus with an angular quantum number $I > 1/2$ since they have an anisotrpic charge distribution and therefore a non-zero quadrupole moment, Q. Therefore, it can interact with an inhomogeneous electric field at the nucleus which is described by an *E*lectric *F*ield *G*radient 3×3 second-order tensor ($\vec{\nabla}\vec{E} = EFG$) in a Cartesian coordinate system [Gütlich *et al.*, 2011 Ch. 4]:

$$V_{ij} = \frac{\partial^2 V}{\partial x_i \partial x_j} \quad \text{where } (i, j = x, y, z) \ . \tag{3.11}$$

It is possible to find a coordinate system so that all non-diagonal elements in the tensor equal zero and since the Laplace equation requires the *EFG* tensor to be traceless,

$$V_{xx} + V_{yy} + V_{zz} = 0 \quad , \tag{3.12}$$

the end result is a tensor with only two independent elements that fully describes the EFG. We choose $|V_{zz}| \geq |V_{yy}| \geq |V_{xx}|$ and present the EFG in terms of V_{zz} and the asymmetry parameter, η;

$$\eta = (V_{xx} - V_{yy}) / V_{zz} \quad , \tag{3.13}$$

which is in the range $0 \leq \eta \leq 1$ with the above definition. In the case of axial symmetry $V_{xx} = V_{yy}$ then $\eta = 0$, but the total *EFG* tensor only becomes zero for a cubic lattice with an isotropic valence electron distribution.

If a ^{57}Fe probe is located in a non-cubic environment and no magnetic interaction is present, split lines (a doublet) will be observed in the ^{57}Fe Mössbauer spectrum with centre at the isomer shift. The energy difference between the doublet is the quadrupole splitting ΔE_{Q}. The displacement of the energy levels caused by the isomer shift and quadrupole splitting and its effects in the emission Mössbauer spectrum is illustrated in Figure 3.6.

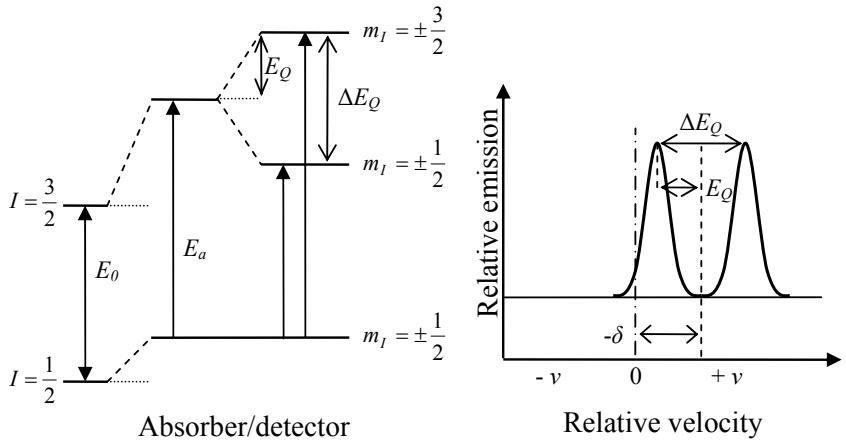

Figure 3.6: Illustration of the isomer shift ($E_s > E_a$ gives a $-\delta$) and quadrupole splitting of ^{57}Fe and the resulting emission Mössbauer spectrum. Energy levels are not drawn to scale.

For ^{57}Fe in its excited state $I_e = 3/2$ is $Q \neq 0$ the electric quadrupole interaction result in a splitting of the excited state into two twofold degenerate energy levels due to $\pm m_I$. The ground state $I_g = 1/2$ does not split, since $Q = 0$, but also becomes a twofold degenerate level. The degeneracy of the energy levels can only be lifted by an external magnetic field. The energy of the quadrupole interaction ΔE_Q for ^{57}Fe can be determined by the equation [Gütlich *et al.*, 2011 Ch. 4]:

$$\Delta E_Q = \frac{eQV_{zz}}{2}\left(1+\frac{1}{3}\eta^2\right)^{1/2} \quad . \tag{3.14}$$

As seen the quadrupole splitting is directly proportional to V_{zz}. In the event of axial symmetry ($\eta = 0$) of the *EFG* the quadrupole splitting can be written as $\Delta E_Q = (eQV_{zz})/2$. In the Mössbauer spectrum the splitting results in a quadrupole doublet component. With the quadrupole splitting it is possible to retrieve information about the chemical bindings and whether the surrounding crystal structure is cubic ($V_{zz} = 0$) or not ($V_{zz} \neq 0$). In Mössbauer spectroscopy, ΔE_Q is given in units of Doppler velocity (mm/s).

In principle the quadrupole interaction originates from two contributions to the total *EFG* [Gütlich *et al.*, 2011 Ch. 4]:

◊ Lattice contribution due to the charge of neighbouring ions in a non-cubic lattice symmetry.

◊ Valence electron contribution: Anisotropic (non-cubic) charge distribution of the atoms electronic structure.

The lattice contribution can be evaluated in a point-charge model and it is possible to calculate the magnitude of the quadrupole interaction to some level. The resulting *EFG* is then a sum over the lattice atoms *l*,

$$V_{ij} = (1-\gamma_\infty)\frac{\partial^2}{\partial x_i x_j}\left(\frac{1}{4\pi\varepsilon_0}\sum_l \frac{ep_l}{|\mathbf{r}-\mathbf{r}_l|}\right) \quad . \tag{3.15}$$

Where p_l is the charge of the lattice atom located at $\mathbf{r}_l$, ε_0 is the electric constant. Shielding effects of the outer shell electrons are taken into account by the Sternheimer antishielding factor ($1-\gamma_\infty$) which has the value of ~10 [Gütlich *et al.*, 2011 Ch. 4]. The lattice contribution is the only source of quadrupole splitting for high-spin Fe^{3+}, as it has a symmetric wave function resulting in $(V_{zz})_{val} = 0$ (see below), which is not expected to show any major temperature dependence, and usually gives a small splitting in the range of $|\Delta E_Q| \sim 0–1$ mm/s.

To evaluate the valence contribution from anisotropic electrons in the case of ^{57}Fe, it is necessary to have a closer look on the energy levels of the 3d orbitals. To illustrate this effect, it is appropriate to look specifically at high-spin Fe^{2+} as observed in wurtzite ZnO. The local environment is close to a tetrahedral symmetry elongated in the *z*-direction. Placing the ^{57}Fe probe in a crystal with tetrahedral symmetry there are four ligands attached to the central probe, three in the plane perpendicular to the symmetry axis, and one above. In tetrahedral symmetry the 3d orbital splits into two different energy levels, as it takes more energy to have an electron in the d_{xy}, d_{xz} and d_{yz} energy levels than in one of the other orbitals. The lowest energy levels are for the x^2-y^2 and z^2 orbitals, as these orbitals are least affected by the electron-electron repulsion and the ligands. This causes a splitting of the energy levels of the 3d orbitals, known as crystal field splitting as illustrated in Figure 3.7.

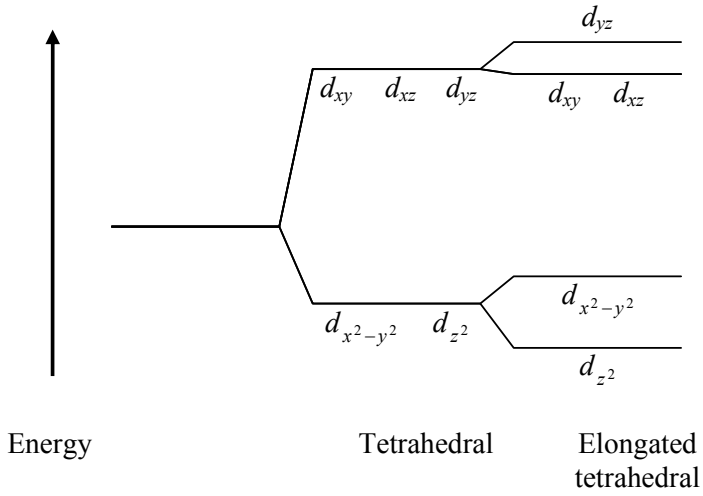

Figure 3.7: Crystal field splitting diagram of the tetrahedral site and for an elongated tetrahedral site [Zuckerman, 1965] as in the case of ZnO (see i.e. section 5.5.1).

The elongation in the *z*-direction in the case of ZnO, due to its wurtzite crystal structure (see i.e. section 5.5.1), result in an additional shift in energy of the orbitals, placing the z^2 orbital at the lowest energy [Zuckerman, 1965]. Each of the 3d valence electrons contribute to the *EFG* and the magnitude and η_{val} are given in Table 3.1. Neglecting covalent effects and lattice contribution an estimate of $(\Delta E_Q)_{val}$ for Fe can be obtained with the conversion factor 4.5 mm·s^{-1}/[(4/7)$e\langle r^{-3}\rangle$] [Gütlich *et al.*, 2011 Ch. 4].

Table 3.1: Expectation values of $(EFG)_{val}$ tensor elements and η_{val} for 3d-electrons relevant for the ^{57}Fe orbitals. *e* is the proton charge [Ingalls, 1964].

Orbital	$\frac{(V_{zz})_{val}}{e\langle r^{-3}\rangle}$	η_{val}
d_{xy}	+4/7	0
d_{xz}	-2/7	+3
d_{yz}	-2/7	-3
$d_{x^2-y^2}$	+4/7	0
d_{z^2}	-4/7	0

The total value of V_{zz} is the sum over the contributions from the individual electrons and their population of the orbitals. The population is determined by the Boltzmann factor, $e^{-\varepsilon/kT}$, where ε is the separation of levels. For $kT >> \varepsilon$ all the orbital levels are equally populated, but for $kT << \varepsilon$ only the lowest orbital is populated, resulting in a temperature dependent quadrupole splitting.

To evaluate the quadrupole splitting of high-spin Fe^{2+} both the lattice and the temperature dependent valence contribution have to be included, since it does not have a symmetric wave function.

In general the temperature dependence of the quadrupole splitting can be used to distinguish between the spin states of the Fe, although this also depends on the crystal symmetry of the probe site. If no temperature dependence is observed it is often the case that there is no valence contribution, as only this contribution has temperature dependence. Usually the lattice contribution is least significant for most iron compounds because it is superseded by a strong *EFG* from the valence electron contribution [Gütlich *et al.*, 2011 Ch. 5].

3.6 Magnetic hyperfine interaction, B_{hf}

An atomic nucleus has a nuclear magnetic dipole moment $\boldsymbol{\mu}$ when the nuclear spin $I > 0$, which interacts with a magnetic field $\mathbf{B}_{\mathrm{hf}}$ at the nucleus. The magnetic field can both arise from an external source and from the atom itself and its neighbouring unpaired electrons. The interaction is the nuclear Zeeman effect (or magnetic dipole interaction) and its energy E is [Gütlich et al., 2011 Ch. 4]:

$$E = -\boldsymbol{\mu} \cdot \mathbf{B}_{\mathrm{hf}} = -g_n \mu_{\mathrm{N}} \mathbf{I} \cdot \mathbf{B}_{\mathrm{hf}} \quad , \tag{3.16}$$

where g_n is the nuclear Landé-factor and μ_{N} is the nuclear magneton. The magnetic interaction splits levels with nuclear momentum I into $(2I+1)$ equally spaced energy states. The twofold degenerate energy levels split into two states with energies proportional to the size and sign of the nuclear spin state m_I:

$$E_m = -g_n \mu_{\mathrm{N}} B_{\mathrm{hf}} m_I \quad . \tag{3.17}$$

For ^{57}Fe the spectrum splits into six lines (a sextet) due to the nuclear Zeeman effect (see Figure 3.8 on the next page). B_{hf} has at least four contributions [Gütlich et al., 2011 Ch. 4].

$$\mathbf{B}_{\mathrm{hf}} = \mathbf{B}_{\mathrm{ext}} + \mathbf{B}_{\mathrm{C}} + \mathbf{B}_{\mathrm{L}} + \mathbf{B}_{\mathrm{D}} \quad . \tag{3.18}$$

$\mathbf{B}_{\mathrm{ext}}$ is the external magnetic field, $\mathbf{B}_{\mathrm{L}}$ arises from the orbital motion of the electrons and $\mathbf{B}_{\mathrm{D}}$ is the contribution from the magnetic moment of the spins of the electrons around the nucleus. In the systems studied here, the dominating term is the Fermi contact term $\mathbf{B}_{\mathrm{C}}$, originating from spin polarisation of s-electrons at the nucleus and can be expressed as [Goldanskii and Herber, 1968];

$$B_C = -\frac{16\pi\mu_B}{3} \left\langle \sum_{\mathrm{s-electrons}} \left(\left|\psi_{\mathrm{s}}^{\uparrow}\right|^2 - \left|\psi_{\mathrm{s}}^{\downarrow}\right|^2 \right) \right\rangle \quad . \tag{3.19}$$

A non-zero contribution comes from an uneven shielding of the 3d-electrons. Hence the contact term is a measure of the polarisation of 3d-electrons that is proportional to the magnetisation of the material. Typical the hyperfine field of

high-spin Fe^{3+} ($S = 5/2$) is $B_{hf} \sim 50$ T and results in a hyperfine splitting of ~16 mm/s. The splitting is much higher than both the quadrupole interaction and isomer shifts, and is usually easily observed in the Mössbauer spectra.

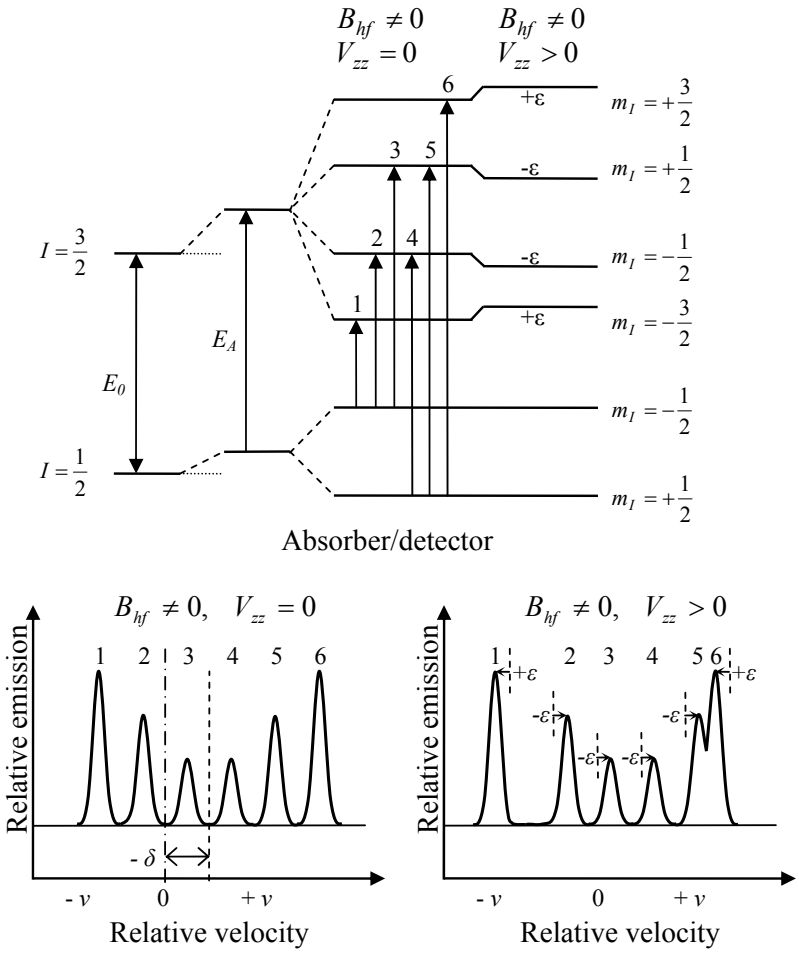

Figure 3.8: Top) Illustration of the energy shift and splitting of ^{57}Fe due to the isomer shift ($E_s > E_a$ gives a $-\delta$) and the magnetic hyperfine interaction. The energy levels are not to scale. Bottom) The resulting emission Mössbauer spectrum (left) and right the effect on the spectrum having combined magnetic and quadrupole interactions.

Increased temperature reduces the magnetic hyperfine field of the spectrum, due to thermal vibrations of the spins. This reduces the Zeeman splitting, as seen from Equation (3.17). The line-width is not affected at elevated temperatures.

A sextet component in the ^{57}Fe Mössbauer spectrum is not exclusively observed due to ordered magnetism, but can also originate from paramagnetism

due to dynamic effects under certain circumstances of slow relaxation. This paramagnetic Mössbauer component has different characteristics and behaviour in the Mössbauer spectrum and is not necessarily a simple sextet (see section 3.7).

3.6.1 Combined magnetic and quadrupole interactions

If both quadrupole and magnetic interactions are present the spectrum can be more complex, as they both have an angular dependence on the quantisation axis. The quantisation axes of the quadrupole interaction and the magnetic hyperfine field interaction are not necessarily the same, but often the quadrupole interaction is much smaller than the magnetic hyperfine field interaction, and can be treated as a perturbation. In the case of axial symmetry ($\eta = 0$) the perturbation can be described with the angle ω between the hyperfine field and the principal axis of the *EFG* tensor and the energy levels shift according to [Gütlich et al., 2011 Ch. 4];

$$E_{Q,m} = -g_n \mu_N B m_I + (-1)^{|m_I|+½} \frac{eQV_{zz}}{8}(3\cos^2\omega - 1) \quad . \qquad (3.20)$$

The last term is called the quadrupole shift ε. For $V_{zz} > 0$ the energy levels with $I = 3/2$ and $m_I = \pm 3/2$ (line 1 and 6) are shifted $+\varepsilon$ and the states with $m_I = \pm 1/2$ are shifted $-\varepsilon$ in energy, see Figure 3.8 bottom left. Note that a quadrupole doublet with line separation of ΔE_Q has its lines identical to a sextet calculated with $B_{hf} = 0$ and 2ε. Therefore, there is often the convention to give the value of the quadrupole split as 2ε.

3.7 Relaxation effects on the Mössbauer spectrum

Relaxation phenomena play an important role in the interpretation of the experimental results in this thesis. This section gives a review of how these effects influence the shape of the Mössbauer spectrum. The measured relaxation time can be varied with experimental conditions, in particular the temperature.

^{57}Fe Mössbauer spectroscopy gives information on the magnetic hyperfine field reflecting interactions of the ^{57}Fe nucleus with the local electron spin (see section 3.6). Assuming that the Fermi-contact term dominates, the magnetic

hyperfine field at the Mössbauer nucleus arises from unpaired electrons of the Mössbauer probe atom.

A paramagnetic environment arises from a fluctuating magnetic hyperfine field at the nucleus. The characteristic timescale of the paramagnetic fluctuations can range from fast lattice vibrations of 10^{-12} s to hours for certain spin glass materials. The average time period between changes of the magnetic hyperfine field is the relaxation time τ.

The relaxation time relative to the lifetime of the ^{57}Fe Mössbauer state which is $\tau_M = 141.8$ ns ($T_{½} = 98.3$ ns) determines how relaxations effects affect the ^{57}Fe Mössbauer spectrum as illustrated in Figure 3.9.

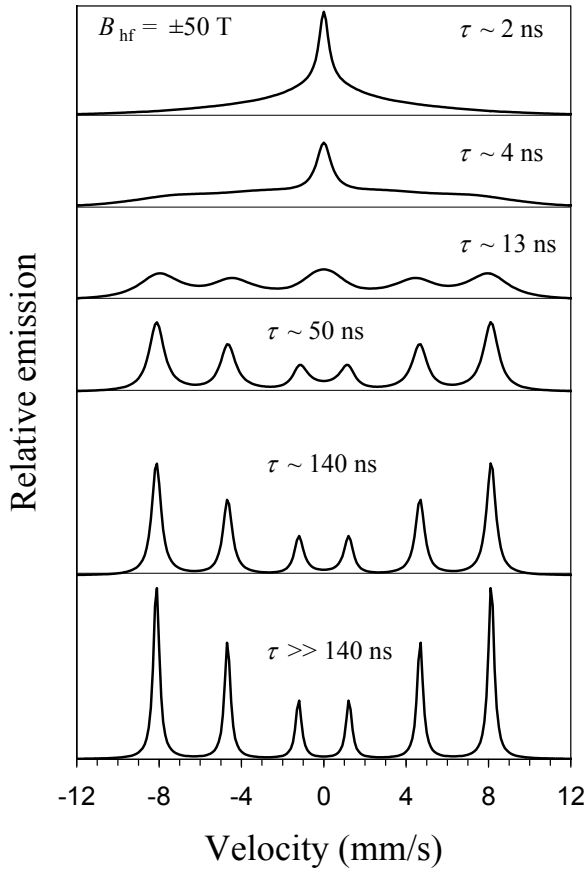

Figure 3.9: Simulations according to the Blume-Tjon model [Blume and Tjon, 1968] describing the ^{57}Fe emission Mössbauer relaxation spectra for the indicated relaxation times in a magnetic hyperfine field that can take the value $B_{hf} = \pm 50$ T and no quadrupole interaction. With decreasing relaxation time, the lines broaden and finally collapse in pairs.

In the case of a short relaxation time relative to the lifetime of the Mössbauer state ($\tau/\tau_M << 1$) the ^{57}Fe nucleus only experiences an average value of the fast fluctuating magnetic field resulting in a zero net-magnetic hyperfine field (see the calculated spectrum for $\tau = 2$ ns in Figure 3.9). In the case of a long relaxation time ($\tau/\tau_M >> 1$) a magnetic hyperfine splitting can be observed in the ^{57}Fe Mössbauer spectrum (see the calculated spectrum for $\tau > 140$ ns in Figure 3.9). For intermediate relaxation times ($\tau/\tau_M \sim 1$) the spectra broaden followed by collapse of the sextet splitting. Broadening of the lines is the first effect of relaxation observed when a long relaxation time decreases. The broadening ($\Delta\Gamma$) of the spectral line-width can be written as [Blume and Tjon, 1968];

$$\Delta\Gamma = \frac{2\hbar c}{E_0}\tau^{-1} \quad . \tag{3.21}$$

The broadening is evident for τ ~50 ns in Figure 3.9. A further decrease of the relaxation time results in a collapse of the sextet splitting. In the simple case of pure longitudinal relaxation with a magnetic hyperfine field taking the two values $+B_{hf}$ and $-B_{hf}$, the lines collapse at the critical relaxation time $\tau_{cri}(m_e, m_g)$ [Mørup, 2011];

$$\tau_{cri}(m_e, m_g) = \frac{\hbar}{\left|(g_e m_e - g_g m_g)\mu_N B_{hf}\right|} \quad , \tag{3.22}$$

where g and m are the nuclear g-factors and m_e and m_g the z-components of the nuclear spins in the exited (e) and the ground state (g), respectively. As seen from Equation (3.22) the lines of the sextet collapse in pairs. First the inner lines (3 and 4) collapse to a single line at relaxation time $\tau \approx 13$ ns, the central lines (2 and 5) collapse at $\tau \approx 4$ ns and finally the outermost lines (1 and 6) collapse at $\tau \approx 2$ ns (see Figure 3.9).

Two mechanisms of spin relaxation are important here, the spin-spin and spin-lattice relaxation which results in the collapse into a paramagnetic single line or a quadrupole doublet in case of non-cubic environment. In paramagnetic materials, the relaxation time is generally determined by contributions from both spin–lattice relaxation and spin-spin relaxation, as described below.

3.7.1 Spin-spin relaxation

The spin-spin relaxation process involves an energy transfer between interacting spins via magnetic dipole and/or exchange interactions. This mechanism depends heavily on the concentration since the relaxation is primarily induced by magnetic dipole interactions between paramagnetic ions in the sample, and the dipole interaction depends on the distance between the ions. Increased concentration decreases the relaxation time. The cross-relaxation process is usually a more important process for the spin-spin relaxation. Here the transition of the state of an ion i ($|M_a^i\rangle$ to $|M_{a+\alpha}^i\rangle$) is accompanied by a transition of another ion j ($|M_b^j\rangle$ to $|M_{b+\beta}^j\rangle$). This changes the energy of the ions by E_α^i and E_β^j, respectively. Assuming a Gaussian broadening of the transition lines, due to random dipolar fields from neighbouring ions, the expression for the transition probability may be written as [Bloembergen *et al*., 1959];

$$\Omega_{ss}^{ij} \cong \frac{(2\pi)^{-1/2}}{\hbar^2} \frac{\left|\left\langle M_{a+\alpha}^i, M_{b+\beta}^j \middle| \hat{H}_{dd}^{ij} \middle| M_a^i, M_b^j \right\rangle\right|^2}{\{(\Delta E_\alpha^i)^2 + (\Delta E_\beta^j)^2\}^{1/2}} \times \exp\left[-\frac{(E_\alpha^i - E_\beta^j)^2}{2\{(\Delta E_\alpha^i)^2 + (\Delta E_\beta^j)^2\}^2} \right] p_j(M_b^j) \quad . \tag{3.23}$$

The dipole interaction between ions i and j is described by the Hamiltonian $\hat{H}_{dd}^{ij}$, and $p_j(M_b^j)$ is the probability that ion j is in the initial state $|M_b^j\rangle$. The matrix element of Equation (3.23) contains the interaction between the ions i and j, and the exchange interaction may also contribute if it is not negligible (the exchange interaction is responsible for ferromagnetism). The transition probability increases with increasing concentration of magnetic ions and can be considered negligible in Mössbauer spectra of systems with impurities below ~10^{-2} at.% [Mørup, 2011]. The spin-spin relaxation is largely temperature independent compared to the spin-lattice relaxation which is strongly temperature dependent.

The exponential term of Equation (3.23) shows that the energy levels of the spin transitions (E_α^i and E_β^j) have to match. This means that an Fe ion

predominantly interacts with other Fe ions, and spin-spin relaxation between Fe and another species (i.e. structural vacancy) is limited. Level mismatch, can also be introduced by applying an external magnetic field. Since there is no guarantee that the dipole axes of ions *i* and *j* are identical, the energy levels (E_α^i and E_β^j) will be affected differently by the external magnetic field.

The concentration of implanted Mn/Fe into the samples here studied is below 10^{-3} at.%. Therefore spin-spin relaxation can be considered negligible [Mørup, 2011], although this may not be the case for the ^{57}Co implanted samples, as the fluence of this beam is much higher (< 0.17 at.%).

3.7.2 Spin-lattice relaxation

Spin-lattice relaxation processes can conveniently be studied in samples with a low concentration (<10^{-2} at.%) of paramagnetic ions because this results in a vanishing spin-spin relaxation [Mørup, 2011].

The spin-lattice mechanism involves energy transfer between the electron spin of the ion and lattice vibrations mainly through the spin-orbit interaction, but also through the weaker magnetic dipolar interaction. The spin-lattice relaxation is also referred to as the nuclear spin relaxation (T_1). It measurers how fast or slowly the spins return to their orientation in the longitudinal direction.

The spin-lattice relaxation is strongly temperature dependent because of the temperature dependence of the population of the phonon states which results in a decreased spin-lattice relaxation time with increasing temperature. The spin-lattice relaxation time also depends on the coupling strength to the lattice. For high-spin Fe^{3+} ($3d^5$) $^6S_{5/2}$, the coupling between the spin and the lattice is weak due to the spherical symmetry of the ^{6}S ground state. This leads to a small crystal field splitting and relatively long spin-lattice relaxation times which can be studied by Mössbauer spectroscopy at room temperature (see section 3.7.3).

In comparison, the non-spherical ions, such as Fe^{2+} ($3d^6$) $^5D_4$ have a stronger spin-lattice coupling and short spin-lattice relaxation times. Usually a single line or doublet is observed from Fe^{2+} in the resulting ^{57}Fe Mössbauer spectrum at room temperature.

Theoretical description of the temperature dependent spin-lattice relaxation involves different processes in different temperature ranges relative to the Debye temperature (θ_D) [Mørup 2011; Abragam and Bleaney, 1970; Srivastava and

Mishra, 1980]. Here only the most important spin-lattice relaxation processes are described.

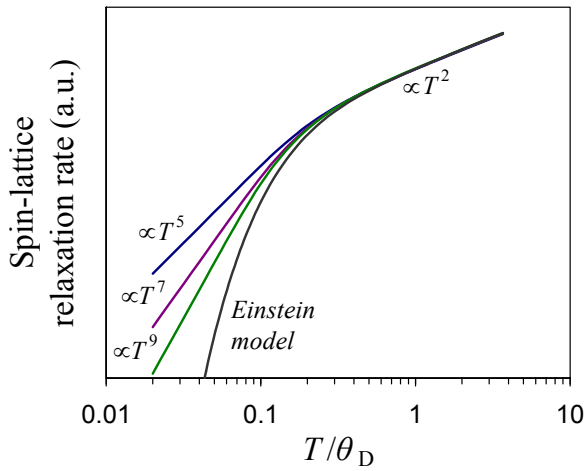

Figure 3.10: Graphical representation of Equations (3.24) and (3.25) showing the different temperature dependences related to the Raman process involved. All of the spin-lattice relaxation processes follow a $\tau^{-1} \propto T^2$ dependence when $T > \theta_D/3$.

At low temperatures only low energy phonons contribute and the direct process dominates. In this simple case the relaxation rate is linear, i.e. $\tau^{-1} \propto T$. At higher temperatures the two-phonon Raman process dominates, where a phonon is annihilated and created which results in an energy difference of $\hbar\omega_a$ - $\hbar\omega_b$, that is taken up in a transition of the electron spin. Using the Debye approximation, this relaxation rate can be written as;

$$\tau^{-1} \propto \left(\frac{T}{\theta_D}\right)^n \int_0^{\theta_D/T} \frac{x^{n-1}e^x}{\left(e^x-1\right)^2}\,dx \quad , \tag{3.24}$$

where n is an integer depending on the process. The first-order and second-order Raman processes result in $n = 7$ and $n = 9$, respectively. For multiple ground states as well as non-Kramers doublets usually $n = 5$ is found. In this temperature range several different relaxation processes can take place. But for temperatures $T > \theta_D/3$ all Raman processes are expected to follow a $\tau^{-1} \propto T^2$ temperature dependence. If optical phonons are responsible for the Raman process, the Einstein model for the phonon spectrum is usually more appropriate,

$$\tau^{-1} \propto \frac{e^{-\theta_E / T}}{\left(1 - e^{-\theta_E / T}\right)^2} \quad . \tag{3.25}$$

A graphical representation of the above-described processes of the temperature dependent spin-lattice relaxation process is shown in Figure 3.10.

3.7.3 Mössbauer spectrum of slow relaxing Fe^{3+}

^{57}Fe Mössbauer spectra exhibiting slow relaxing paramagnetism are more complex than magnetically ordered spectra, since they consist of a superposition of more than one sextet as well as additional lines [Mørup, 2011]. High-spin Fe^{3+} ($3d^5$) has the electronic ground-state configuration $^6S_{5/2}$. The crystal field splits the ground state into three degenerate Kramers doublets $M_S = \pm 5/2, \pm 3/2, \pm 1/2$. An external magnetic field splits the Kramers doublets into six magnetic substates with energies $E_s = g\mu_B B_{hf} S_Z$, where μ_B is the Bohr magneton, as shown in Figure 3.11.

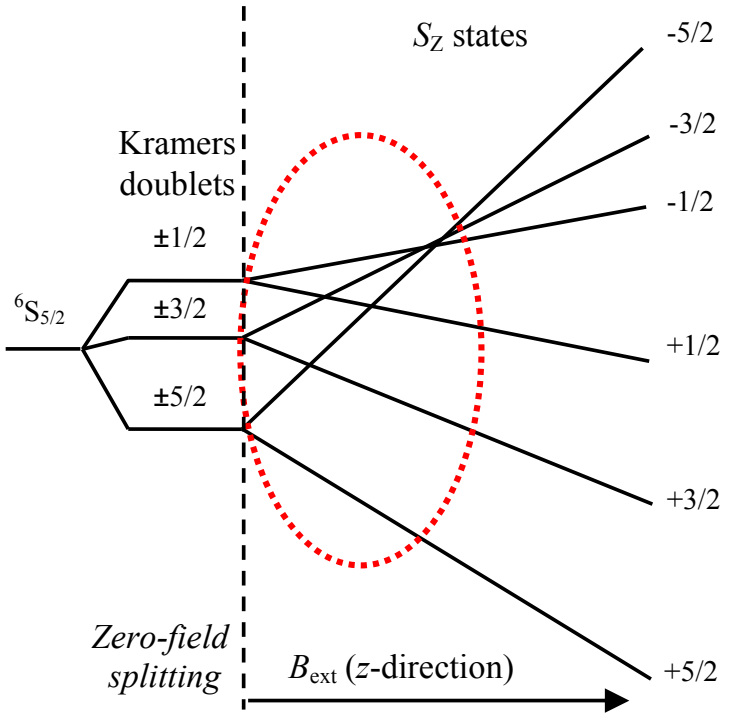

Figure 3.11: Illustration of the electronic Zeeman splitting of the $^6S_{5/2}$ term of the ground state of high-spin Fe^{3+} ($3d^5$). Applying an external magnetic field (*z*-direction) results in a Zeeman splitting of the Kramers doublets into six S_Z states. Red circle indicates $B_{ext} < 0.3$ T where the lines overlap. Above $B_{ext} = 0.3$ T the Zeeman energy dominates over the crystal field interaction.

A weak external magnetic field in the *z*-direction is sufficient in order to lift the Kramers degeneracy into the six S_Z states. This is illustrated in Figure 3.11. Without an external "polarisation" field the magnetic hyperfine field may fluctuate in different directions due to local effects [Lang, 1968] which results in more complex Mössbauer spectra. The spacing of the S_Z states is about 5 K [Wickman *et al.*, 1965]. Above this temperature the Kramers doublets give rise to six sextets from the evenly populated $S_Z = \pm 5/2, \pm 3/2, \pm 1/2$ states which are observed as three sextets as the positive and negative states give rise to identical sextets.

In the Mössbauer spectrum of paramagnetic high-spin Fe^{3+} with slow relaxation there are three ranges of the external magnetic field that can be distinguished (see Figure 3.12).

In the absence of a sufficiently large external magnetic field ($B_{ext} < 20$ mT) the spectral component originating from the S_Z states may be rather complex, since the eigenstates of the system are combined nuclear and electronic states. The complex components consist of a superposition of more or less than six lines of uneven splitting and likewise unfamiliar line intensities.

For $B_{ext} > 30$–50 mT the spectrum begins to exhibit the behaviour of a normal sextet from the S_Z states originating from the Kramers doublets, since they begin to align with the magnetisation axis of the external field.

Above $B_{ext} \sim 0.3$ T the Zeeman split S_Z states no longer overlap (see i.e. Figure 3.11), since the Zeeman energy dominates over the crystal field interaction. The magnetic hyperfine field fluctuates between the six different energy states with $|S_Z| \propto B_{hf}$ resulting in normal sextet behaviour of the $S_Z = \pm 5/2, \pm 3/2, \pm 1/2$ states. When $|S_Z| \propto B_{hf}$ the resulting sextets exhibit the same angular dependence as expected for a "normal" ordered magnetic sextet (see Table 3.3).

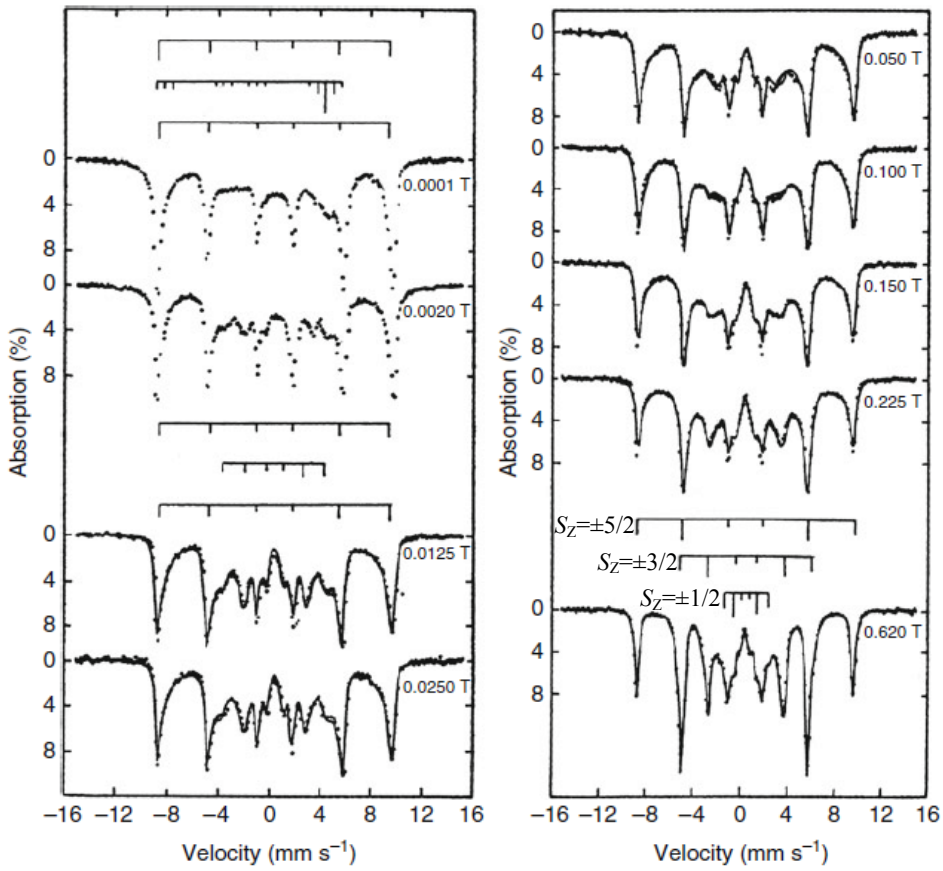

Figure 3.12: ^{57}Fe Mössbauer spectra of amorphous frozen aqueous solution of 0.03 M $Fe(NO_3)_3$, obtained at 4.5 K with various applied transverse magnetic fields demonstrates the effect of an increased external magnetic field on slow paramagnetic relaxation. Above ~0.3 T the S_Z states are proportional to B_{hf}. In the absence of a sufficiently large field (below ~20 mT) the spectra are rather complex due to combined nuclear and electronic states. Figure from [Mørup, 2011].

3.8 Angular dependence of relative line intensities

Lines that exhibit splitting (doublet or sextet component) in the Mössbauer spectrum can show an angular dependence changing the relative line intensities of the split lines. The absolute area of the split component does not change.

For a quadrupole split doublet originating from a polycrystalline material the two lines will have equal intensities in the Mössbauer spectrum. However, a measured quadrupole split doublet in single-crystalline material may exhibit an angular dependence of the relative line intensities. The two transitions (lines), labelled π and σ depend on the angle between the principal axis of the *EFG*

tensor (i.e. see section 3.5) and the γ-direction. The angular dependence of the doublet (θ) is listed in Table 3.2.

Table 3.2: Transition probabilities for the quadrupole split doublet in the Mössbauer emission spectrum.

Transitions ($m_g \rightarrow m_e$)	Line position for $\Delta E_Q > 0$	Relative intensity	Poly-crystalline
π: ±1/2 → ±3/2	$-\delta - \Delta E_Q/2$ (left peak)	$3+3\cos^2\theta$	4
σ: ±1/2 → ±1/2	$\delta + \Delta E_Q/2$ (right peak)	$5-3\cos^2\theta$	4

For the sextets originating from single-crystal materials the internal line ratio depends on the angle θ between the magnetic hyperfine field direction and the observed γ-direction. For the ^{57}Fe transition the relative intensity ratios of the sextet lines are listed in Table 3.3.

Table 3.3: Transition probabilities for $I = 1/2 \rightarrow 3/2$ (^{57}Fe). θ is the angle between the γ-direction and the magnetic hyperfine field.

Transition ($m_g \rightarrow m_e$)	Lines	Relative intensity	Poly-crystalline	$B_{hf} \parallel \gamma$	$B_{hf} \perp \gamma$
-1/2 → -3/2, 1/2 → 3/2	1, 6	3	3	3	3
-1/2 → -1/2, 1/2 → 1/2	2, 5	$\frac{4\sin^2\theta}{1+\cos^2\theta}$	2	0	4
-1/2 → 1/2, 1/2 → -1/2	3, 4	1	1	1	1

From Table 3.3 it is seen that only the intensity of the lines 2 and 5 of the sextet ($\Delta m_I = 0$ transition) varies from 0 to 4 in relative intensity depending on the angle. In the case of a polycrystalline sample there is no angular dependence, since the random orientation will cancel out the angular dependence, resulting in a sextet of line ratio 3:2:1:1:2:3. Due to an often symmetry of the sextet only the 3 lines are usually noted. Pure bulk α-Fe used for calibration breaks up into randomly orientated magnetic domains resulting in the polycrystalline case. The 3:2:1 sextet line ratio can be obtained in single-crystalline samples by measuring at the so called magic angle $\theta = 54.74°$.

3.9 Spectral analysis

The measured Mössbauer spectra were analysed with the spreadsheet based tool Vinda [Gunnlaugsson, 2012b] which runs under Microsoft Excel. The package allows for simultaneous analysis of Mössbauer spectra. Each spectrum is analysed in a specific spreadsheet with components (models) that minimise the χ^2-value;

$$\chi^2 = \sum_{i=1}^{N} \left(\frac{d_i - m_i}{\sigma_i} \right)^2 \quad , \tag{3.26}$$

where N is the number of data points (channels) in the spectrum and $\sigma_i = \sqrt{d_i}$ is the standard variation. d_i and m_i are the experimental value and the model value in data point i, respectively.

When spectra are analysed individually, the χ^2 value is minimised by varying the hyperfine parameters, spectral area of each component and the background count value. In a simultaneous analysis of more than one spectrum some of these parameters depend on global fitting variables that apply for the whole series. Global variables are set to fit all spectra, such as a temperature independent line-widths or a component following the second order Doppler shift (SOD) in a temperature series (Equation (3.9) and (3.10)). Other examples are hyperfine parameters in angular dependent measurements, where only line intensities (see section 3.8) are allowed to vary between the spectra. Free variables fit the individual spectrum, like the area of components and background.

The simultaneous analysis has the advantage to control and guide the fitting of smaller and/or overlapping components and capture details that else would drift to physically meaningless values.

Chapter 4

Ion-implantation

The investigated single-crystal oxide samples (MgO, ZnO, and α-Al_2O_3) in this thesis are studied using on-line ^{57}Fe emission Mössbauer spectroscopy by ~50 keV ion-implantation of ^{57}Mn into the samples. Additionally a single-crystal ZnO was implanted at 60 keV with long-lived ^{57}Co also for ^{57}Fe emission Mössbauer spectroscopy and measured off-line at Aarhus University, Denmark. In this section relevant details of the ion-beams used and an overview of the resulting implantation sites (point defect) onto the crystal lattice are described.

When a fast ion passes through matter, it loses energy principally by scattering with electrons within the matter it passes through and, more importantly at low energies, by scattering from the nuclei of the atoms. It may take many atomic layers, before there is a collision with a target atom which is hard enough to stop the incoming ion, by displacing the lattice. The energy required to push the host atom just far enough from its lattice site so that it cannot move back into the created empty site, is the displacement energy. Typical threshold displacement energies in solids are of the order of 10–100 eV.

The energy of the incoming ion-beam at ISOLDE/CERN ranges from 40–60 keV resulting in a maximum penetration depth of ~500–1000 Å into the samples studied here as demonstrated in Figure 4.1 by SRIM simulations (The Stopping and Range of Ions in Matter) [Ziegler, 2012].

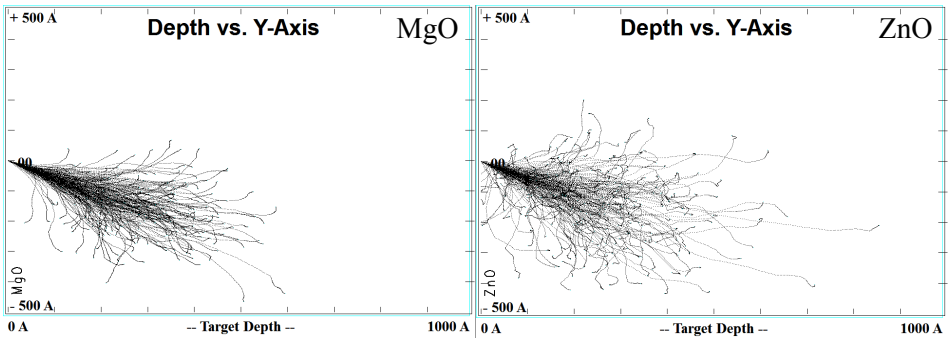

Figure 4.1: SRIM simulation of ion-implantation of 250 ^{57}Mn ions at 60 keV into MgO (3.6 g/cm^3) and ZnO (5.6 g/cm^3) at an incident angle of 30° showing the penetration depth [Ziegler, 2012]. Less penetration depth in ZnO due to the higher density.

The SRIM Monte Carlo simulation uses a point-like input beam and not actual real-beam optics, but still gives a good picture of the implantation. The ion-implantation beam spot at ISOLDE hitting the sample is about 0.33 cm^2. The implanted ions end up as point defects in the crystal and the penetration depth of the beam is related to the density of the crystal material. The point defects observed in the studied ^{57}Fe emission Mössbauer spectra are explained below in section 4.3.

4.1 Mössbauer isotopes (ISOLDE/CERN)

The ISOLDE (Isotope Separator On-Line DEvice) facility delivering the radioactive beam used for the ^{57}Fe emission Mössbauer spectroscopy method is located at CERN (European Organization for Nuclear Research. The name is abbreviated from the original French name, Conseil Européen pour la Recherche Nucléaire) on the border between Swiss and French close to Geneva, Switzerland. As seen from Figure 4.2 the ISOLDE facility at CERN is one experimental facility among other experimental endeavours utilising the CERN accelerator complex. The accelerator complex used for ISOLDE is marked within the dashed box.

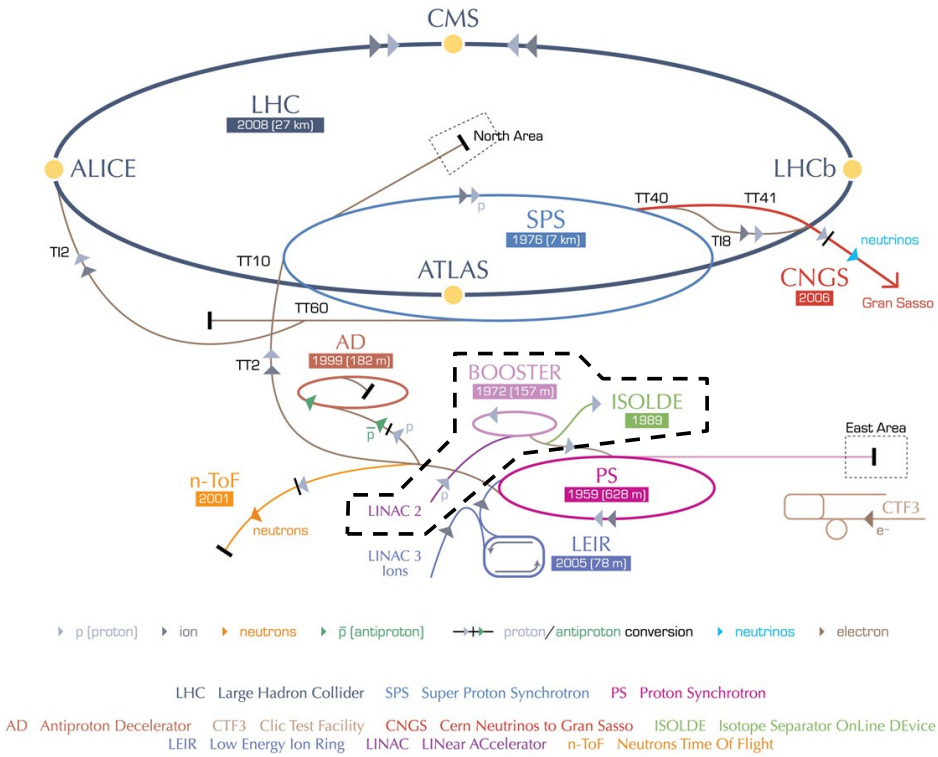

Figure 4.2: The CERN accelerator complex at Geneva, Switzerland. Marked with the dashed box is the accelerators used for ISOLDE to receive the 1.4 GeV protons. The coloured text explains the various endeavours at CERN (adapted from [CERN, 2012]).

At the ISOLDE facility the radioactive beam of ions are produced by a high energy proton beam (1.4 GeV) irradiating a fixed target material. The volatile nuclear reaction products are released from the target and extracted. The proton beam is received from the Proton Synchrotron Booster that contains four superimposed rings with a radius of 25 meters. It receives the protons from the linear accelerator Linac2 with energy of 50 MeV and accelerates them to 1.4 GeV. More details about the used radioactive beams are described in the following section.

4.1.1 ^{57}Mn

The $^{57}Mn^{+}$ ($T_{½}$ = 85.4 s) radioactive ion beam is produced by 1.4 GeV proton-induced Uranium fission in a heated UC_2 target. The fission fragment atoms diffuse to the surface were they are desorbed and are ionised with elemental selective multi-photon laser ionisation [Fedoseyev et al., 1997]. The laser

settings can be used to increase the amount of extracted and accelerated Mn^+ relative to other isotopes released from the target in the violent fission. The laser desorbed Mn^+ ions are accelerated to 40–60 keV and a magnetic field is used to mass separate the $^{57}Mn^+$ isotopes and produce a pure beam of ~2×10^8 $^{57}Mn^+$/s.

At the beam-time in 2010 it was only possible to perform the implantation at 40 keV, due to problems with the high voltage at the ISOLDE facility. 40 keV is at the lower edge of acceptable implantation energy, as a larger fraction of the implanted ions will end up too close to the sample surface resulting in surface effects.

The ^{57}Mn isotope is not a Mössbauer isotope, but it decays via β^- to ^{57}Fe. This daughter nucleus is the Mössbauer probe atom detected by the ^{57}Fe emission Mössbauer spectroscopy method. The ^{57}Mn nucleus decay has a half-life of $T_{½}$ = 85.4 s favourable for on-line measurements, as the implanted probes will not have enough time to out-diffuse and high statistics ^{57}Fe Mössbauer spectra can be collected within 5–10 min. This on-line method of populating the 14.4 keV ^{57}Fe Mössbauer state ($T_{½}$ = 98.3 ns) via β^- decay of ^{57}Mn allows the study of truly dilute samples with local concentration of the implanted species below ~10^{-3} at.% (see calculation in section 4.2). After-effects (i.e. metastable electronic states formed in the nuclear reaction) following the ^{57}Mn β^- decay are considered negligible and this is supported by no observed evidence in the measured implanted samples.

For implanted ^{57}Mn for ^{57}Fe emission Mössbauer measurements, there are two time-scales that are of importance. The stopping of the Mn atom takes of the order of 10^{-12} seconds. Hereafter, the ^{57}Mn resides in the sample during its half-life of 85.4 s, where possible annealing can take place. In the β^- decay, on the average 40 eV recoil is imparted on the daughter Fe atom and can result in a relocation of the Fe atom in the crystal. The Mössbauer spectrum (the results obtained) is recorded on the average 98.3 ns after this event.

4.1.2 ^{57}Co

In 2010, a beam of ^{57}Co ($T_{½}$ = 272 days) was developed at ISOLDE. The radioactive beam of $^{57}Co^+$ ions were produced by proton-induced spallation in a YO target and accelerated to 60 keV before implantation at a fluence of (5-6)$\times10^{12}$ ^{57}Co/cm^2. The beam production is made without selective laser multi-photon ionisation, resulting in a significant beam contamination of stable ^{57}Fe

implanted impurities, that has been estimated to (5-6)×10^{14} ^{57}Fe/cm^2 with 99% as stable ^{57}Fe (K. Johnston, private communication 2010). This gives a maximum concentration of 0.17 at.% ^{57}Co/^{57}Fe(stable). However, this side-effect turned out as beneficial for the current study, bridging the gap between ISOLDE experiments with ^{57}Mn and home laboratory measurements utilising stable ^{57}Fe (~10^{16} cm^{-2}) (see description in **Paper VII**). After the implantation, the samples are transported and measured in home-laboratories (Aarhus University, Denmark). The long half-life of ^{57}Co ($T_{½} = 272$ days) makes this isotope unsuitable for on-line measurements.

The ^{57}Co isotope decays via electron capture (EC) to the 14.4 keV Mössbauer state of ^{57}Fe ($T_{½} = 98.3$ ns). In comparison to the β^- decay of ^{57}Mn EC has negligible recoil of 4.6 eV imparted on the daughter ^{57}Fe nucleus which is not enough to break the chemical bond, but is instead transferred to the lattice. In this work no evidence of after-effects due to the EC decay has been observed of the ^{57}Co implanted samples.

For the long lived Mössbauer isotopes (i.e. ^{57}Co and ^{119}Sn) experience (G. Weyer, private communication 2010) is that a source strength of ~0.1 MBq (~3 μCi) is the minimum required for having a useful source to use in home-laboratories for off-line Mössbauer measurement (10–20 measurements of sufficient quality during 1 year).

The much higher fluence of the not pure ^{57}Co beam compared to the ^{57}Mn beam makes it far more likely that clusters or precipitates are created in the process and has to be considered when analysing the Mössbauer spectra.

ISOLDE is actually not the place for ion-implantation of long-lived isotopes for off-line measurements, but the number of facilities performing such an implantation is decreasing (H. P. Gunnlaugsson, private communication 2010). The reason for this, is that implantation of long lived isotopes require special attention due to possible long term contamination effects.

4.2 ^{57}Mn fluence calculation

The fluence of the ^{57}Mn$^+$ beam used at ISOLDE varies from year to year of measurements, due to the performance of the targets used at the ISOLDE facility. It is difficult to get an accurate yield of the fluence or beam intensity, and in recent years, this has been estimated using the signal of the Mössbauer

spectrum. There were reasonable beam yield measurements performed in 2006 (H. P. Gunnlaugsson, private communication).

The fluence (in units of number of $^{57}Mn/cm^2$) to record a specific Mössbauer spectrum, is given as the product of the signal (S) and a calibration constant which depends on the geometry, amount of Be in the window and on the detector. The signal is defined as;

$$S = Bck \cdot \sum_i A_i / f_i \quad , \tag{4.1}$$

where the spectral components area (A_i) is given in units of %·mm/s (standard unit in Vinda), and the background (*Bck*) in units of counts per 256 channels (counts/channel).

From the signal calculated fluence the maximum concentration of implanted ^{57}Mn can be estimated. For the calculation the upper fluence limit of 3.6×10^{12} $^{57}Mn/cm^2$ is used which equals 100 minutes of implantation into the sample (beam intensity of 2×10^8 $^{57}Mn/s$ and beam spot of 0.33 cm^2). To convert the fluence in units of $^{57}Mn/cm^2$ to concentration ($^{57}Mn/cm^3$), SRIM simulations [Ziegler, 2012] are used in order to calculate the ion-range profile. The ion-range profile is found to give a maximum ion-concentration of $\sim3.0\times10^5$ ($^{57}Mn/cm^3$)/($^{57}Mn/cm^2$) in ZnO and $\sim3.5\times10^5$ ($^{57}Mn/cm^3$)/($^{57}Mn/cm^2$) in MgO (see Figure 4.3). This gives a maximum concentration of 1×10^{18} $^{57}Mn/cm^3$ equal to $\sim10^{-3}$ at.% in the samples here studied (the total atoms per cm^3 is 8.3×10^{22} and 1.1×10^{23} for [Zn + O] and [Mg + O], respectively).

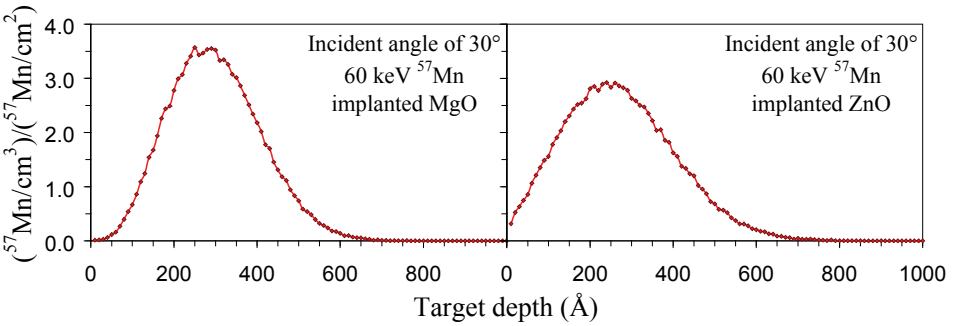

Figure 4.3: Ion-range SRIM simulations [Ziegler, 2012] of 60 keV ^{57}Mn implanted samples at 30º angle. Left) A maximum ion-concentration of $\sim3.5\times10^5$ ($^{57}Mn/cm^3$)/($^{57}Mn/cm^2$) is reached in MgO. Right) A maximum ion-concentration of $\sim3.0\times10^5$ ($^{57}Mn/cm^3$)/($^{57}Mn/cm^2$) is reached in ZnO.

4.3 Point defects

Here will be given a brief description of possible point defects created by ion-implantation that may be identified in the ^{57}Fe emission Mössbauer spectrum. After the 40–60 keV implanted ^{57}Mn or ^{57}Co ions have come to rest in the sample they can end up in different types of environment depending on the properties of the crystal and the experimental conditions.

There are different types of sites where Fe can be observed, and below is a discussion on how they can be identified in the Mössbauer spectra.

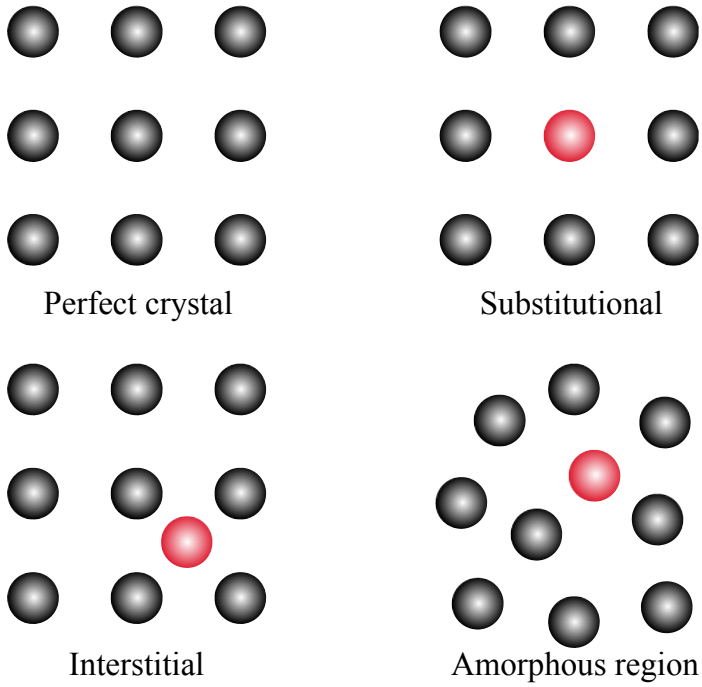

Figure 4.4: Schematic illustration of the different point defects that can be observed in the emission Mössbauer spectrum after ion-implantation. Gray atoms represent the host crystal and red the implanted Mössbauer ^{57}Fe probe.

4.3.1 Implantation damage

If the ^{57}Mn ion-implantation is performed at low enough temperatures (depending on the material), the probes can be observed in amorphous regions, as the lattice has not enough time or energy to recover/recrystallise from the damage imparted on the lattice.

The Mössbauer spectra of Fe in damage regions have been studied in details in Si [Gunnlaugsson *et al.*, 2002; Weyer *et al.*, 2003] and diamond studies [Weyer *et al.*, 2004].

The ^{57}Fe emission Mössbauer spectrum of Fe in amorphous regions is an asymmetric doublet due to an average probing of different amorphous regions with somewhat different isomer shifts and quadrupole splittings. This asymmetric doublet therefore exhibits no angular dependence, as the local affected amorphous regions have no preferred symmetry or any information on the host lattice orientation.

Characteristics for amorphous regions are that they anneal and recrystallise at a lower temperature then amorphous layers. In the case of implanted Si the amorphous regions anneal (recrystallise) at ~500 K, while amorphous layers recrystallise at ~1000 K [Mayer *et al.*, 1968]. Since this study uses low fluence below 10^{13} ions/cm^2 there will be formed amorphous regions and not amorphous layers. This results in a damage component that exhibits a strong temperature dependent annealing and is strongly reduced in spectra obtained at higher temperatures (above 400–500 K). This decrease of the damage component at elevated temperatures is often linked to an increase of a component resulting from substitutional Fe sites (see 4.3.2), indicating a lower probability of ending up in a damaged region or it anneals within the ^{57}Mn ($T_{½}$ = 85.4 s) and ^{57}Fe ($T_{½}$ = 98.3 ns) half-life.

4.3.2 Substitutional

In the case of a substitutional site the ion-implanted Fe/Mn impurity replace a host atom in the crystal lattice. This happens either by direct implantation onto this site or after the phase of recrystallisation of the amorphous region.

In the Mössbauer measurements the substitutional site can be identified using the theory of mass defect approximation, that assumes an unchanged force constant and use the Debye model to approximate the lattice vibrations. This describes the change in the Debye temperature when replacing the mass of the host atom m_{host}, with the implanted probe atom m_{probe}.

$$\theta_{D,\text{probe}} = \theta_{D,\text{host}} \sqrt{\frac{m_{\text{host}}}{m_{\text{probe}}}} \quad . \tag{4.2}$$

If the implantation is performed at high temperatures (fastest re-crystallisation) the largest fraction of the ion-implanted probe atoms ends up in the crystal on substitutional sites and can therefore be the dominating feature in the emission Mössbauer spectrum.

4.3.3 Interstitial

The interstitial site in the host crystal fills the void or interstice among the host atoms. Interstitial ^{57}Fe in the crystal after the ^{57}Mn ion-implantation can be created as directly implanted onto the interstitial site or more likely as a result of the following β^- decay of ^{57}Mn. In the β^- decay of the implanted ^{57}Mn the daughter ^{57}Fe nucleus is given an average recoil of $\langle E_R \rangle = 40$ eV. Depending on the binding energy this can cause a sizeable fraction of the Fe-atoms to be expelled into interstitial sites. In the resulting ^{57}Fe emission Mössbauer spectra an indication of an interstitial component is a temperature independent constant site population (spectral area fraction). Normally the interstitial site has a lower Debye temperature than compared to the substitutional site, since it has a weaker binding to the lattice [Werer *et al.*, 1999]. Presumably interstitial Fe in oxides is uncharged, and the isomer shift does not have to be characteristic for the charge state for interstitial defects, which are more characterised by strain at the voids from neighbouring host atoms [Weyer *et al.*, 2004].

4.4 Application to emission Mössbauer spectroscopy

Mössbauer spectroscopy differs from many other physics experiments performed at ISOLDE. In nuclear physics, the interest is to study the characteristics of the nucleus (radioactive beam) with different methods, evaluating fundamental parameters such as shape, size, mass, magnetic moments etc. In our case the characteristics of the radioactive beam is not of the primary interest, it is applied as a tool used to investigate the material/crystal into which the radioactive Mössbauer probes are implanted and measured using emission Mössbauer spectroscopy. Among the advantages compared to the traditional (absorption) Mössbauer spectroscopy is the possibility to work with a very low concentration below 10^{-3} at.%, where the probe atoms are true dilute impurities in the studied sample of interest. These dilute implanted probe atoms do not interact with each other, but are only predominantly hyperfine perturbed by their

local atomic environment within the host crystal they are located. The method allows to measure magnetism on an atomic scale.

Additional some parent nuclei, like ^{57}Mn (see 4.1.1), have recoil in their decay which can be used to create interstitial type of impurities that can be difficult to study with conventional Mössbauer methods.

Chapter 5

Experimental setup at ISOLDE/CERN

In this chapter a short description of the experiments performed at the ISOLDE facility (building 170) at CERN is given and the method of measuring the ^{57}Fe emission Mössbauer spectrum. Specifications on the studied samples are also included.

At ISOLDE the users are given the radioactive ion-beam just before it enters the experimental hall and the experiment is installed on the General Purpose Separator (GPS) beam line as shown in Figure 5.1. The users have to align and direct the beam to their experiment themselves and are usually allowed to setup their equipment a few days in advance.

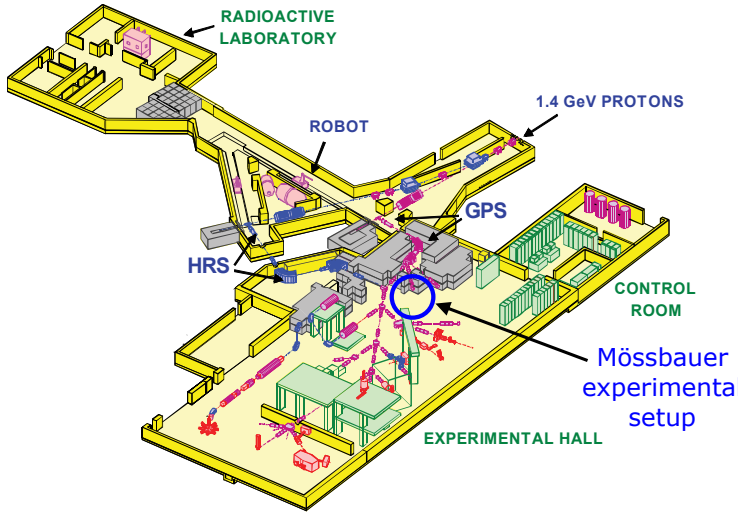

Figure 5.1: Layout of the ISOLDE facility (building 170) at CERN. The circle marks the location of the experimental Mössbauer setup on the GPS beam line.

5.1 Emission Mössbauer spectroscopy

The experimental equipment for the ^{57}Fe emission Mössbauer measurements is stored at ISOLDE and the setup is installed by the collaboration for each beam time. This requires a precise alignment of the chamber position relative to the beam-line, to make sure the samples are in line with the beam, setting up the vacuum system and the Mössbauer electronics. A Faraday cup is mounted behind the sample position on the implantation chamber for beam alignment. Figure 5.2 shows a picture of the installed implantation chamber and the Mössbauer setup at ISOLDE.

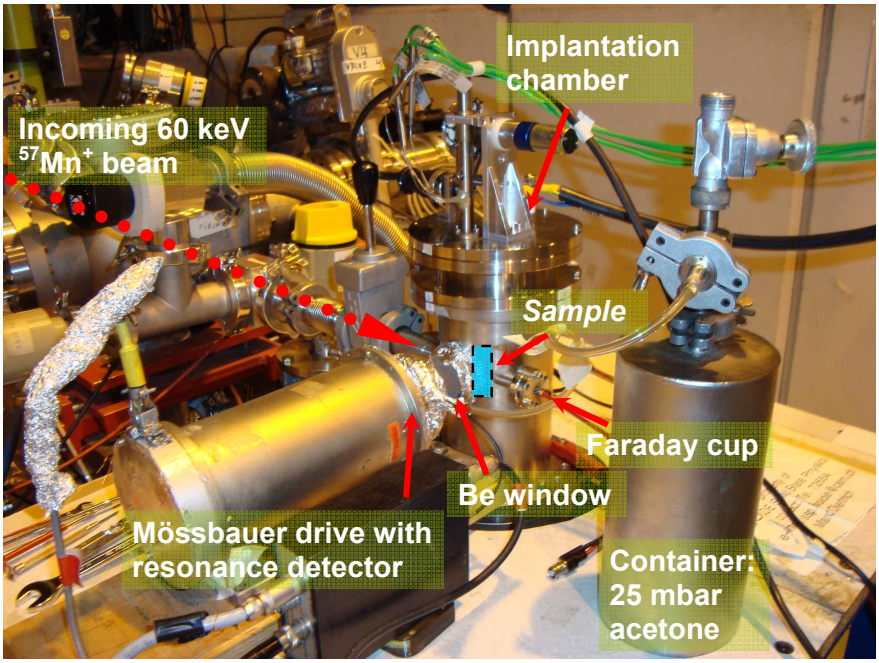

Figure 5.2: Picture of the implantation chamber and the experimental Mössbauer setup at ISOLDE/CERN. The samples are mounted on different chamber top flanges depending on the experimental conditions required. The chamber is evacuated with a turbo pump, and high vacuum conditions are achieved by an ion-pump below the chamber (for more details see Figure 5.4).

In Figure 5.2 is shown the implantation chamber mounted on the beam-line that is held in constant vacuum. Various valves ensure the beam-line vacuum when the chamber is opened. The single line resonance detector (PPAD) [Weyer, 1976] is placed outside the implantation chamber at 90º relative to the beam direction on a conventional constant-acceleration Mössbauer drive. The

container holding the counter-gas used in the detector is also seen. The ion-implanted sample inside the chamber is located behind a 6 mm window of Beryllium, to block high-energy electrons (2.677(3) MeV max energy [NNDC, 2012]) emitted in the β^- decay from entering the detector, but only absorbs ~10% of the 14.4 keV Mössbauer γ-rays. Ion-implantation is performed at an incident angle of 30° relative to the sample surface normal.

To investigate samples under different experimental conditions a multi-purpose implantation chamber is applied, in which it is possible to perform measurements with different sample orientations, in an external magnetic field, and at high and low temperatures. This is done by changing between three different top flanges for the chamber, which is the best suitable setup for the investigation.

5.1.1 Resonance detector (PPAD)

For the ^{57}Fe emission Mössbauer spectroscopy performed at ISOLDE/CERN a resonance detector is used for detecting conversion electrons from the 14.4 keV decay of the ^{57}Fe Mössbauer transition ($T_{½} = 98.3$ ns). For Mössbauer transitions in ^{57}Fe the internal conversion coefficient is $\alpha = 8.2$, meaning that in only 9.9% of instances there is emission of a 14.4 keV γ-quantum. Otherwise, electrons and X-rays are emitted in the nuclear decay, but the conversion electrons are of interest here. They are called so because the absorbed γ-energy in the nucleus is converted to an electron. The kinetic energy of a conversion electron equals the difference between the nuclear transition energy and the binding energy of the electron. Mostly the conversion electrons are emitted from the K-shell (79% intensity) at 7.3 keV as they are closest to the nuclei. The penetration depth of the 7.3 keV conversion electrons in Fe is on the average of ~100 nm [Drouin *et al.*, 2007]. Figure 5.3 illustrates the decay of excited ^{57}Fe.

It is not feasible to detect a single low-energy conversion electron, so the resonance detector is equipped with a parallel plate avalanche detector (PPAD) [Weyer, 1976] to amplify the signal. Across a ~2 mm gap of the parallel absorber and collector there is a potential of ~1 keV and a suitable counter gas (here ~25 mbar of acetone gas). When an electron enters the gap it is accelerated by the potential, causing an ionisation of the gas molecules, and an avalanche is detected.

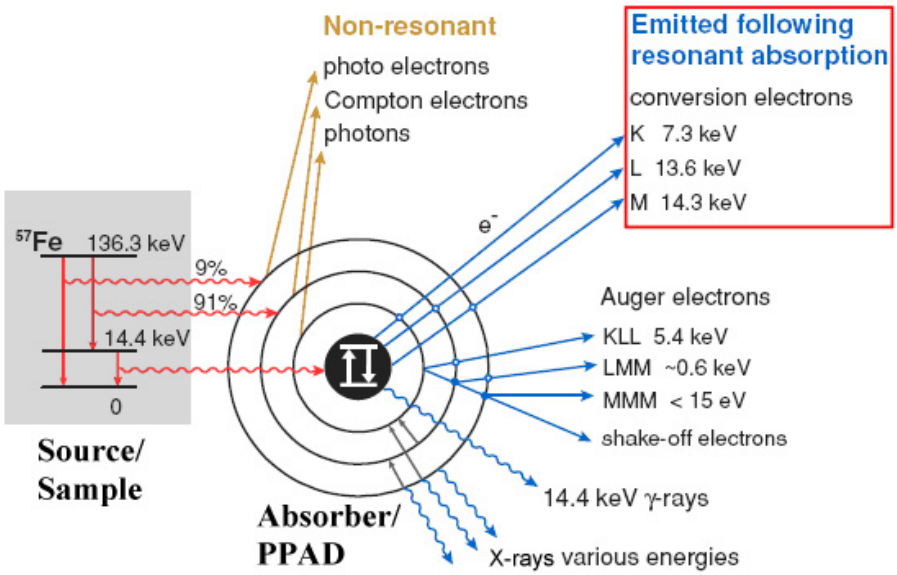

Figure 5.3: Decay of exited ^{57}Fe showing the possible radiation. Of interest are the conversion electrons which are detected. Adapted from Dyar *et al.* [2006]. The energy of the conversion electrons is the difference between the nucleus transition energy and the binding energy of the electrons.

The same principle is also used for conversion electron Mössbauer spectroscopy (CEMS). Resonance detectors are CEMS detectors with a single line absorber material. A more detailed picture of the setup in Figure 5.2 is shown in Figure 5.4.

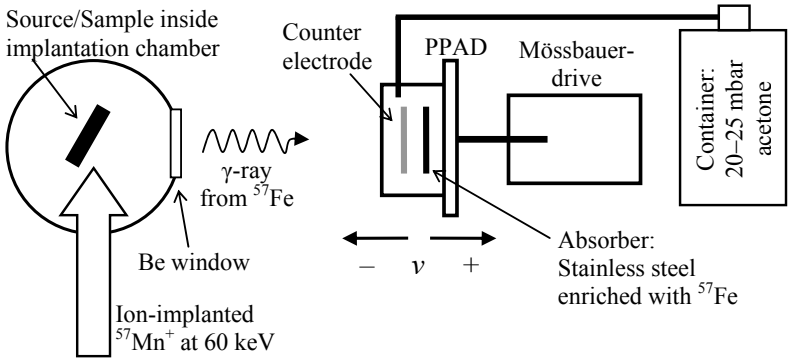

Figure 5.4: Schematic of the ^{57}Fe emission Mössbauer spectroscopy setup at ISODLE/CERN for ^{57}Mn ion-implantation. The sample is implanted inside a vacuum chamber. The γ-rays pass through a 6 mm Beryllium window and are detected in the moving resonance detector. Ion-implantation is performed at an incident angle of 30° relative to the sample surface normal.

5.1.2 ^{57}Fe resonance detector

The resonance detector used for ^{57}Fe emission Mössbauer spectroscopy is a PPAD where the absorber electrode is a single line stainless steel absorber enriched with ^{57}Fe. The diameter of the detector electrode is Ø = 31 mm. They are enclosed in a housing made of Plexiglas, with a 1.85 mm gap between the counter electrode and the stainless steel absorber which can be filled with 25 mbar acetone gas. The window of the Plexiglas detector is 1 mm thick. A potential of around 1 keV is applied over the gap. Calibration is usually performed by implantation into α-Fe.

The PPAD has a high signal to background ratio, a high time resolution on the scale of 10^{-9} s, and can be used within a very high dynamic range. It can detect signals from samples with low activity (~0.1 μCi) count rates of 0.1 c/s, in a setup where the source is close to the detector (geometrical broadening), to highly radioactive samples ~50 mCi (in the setup used at ISOLDE it should begin to reach saturation at ~500 mCi). Such a broad range a common gas proportional detector used in the single line experimental setup would have difficulties dealing with. The ^{57}Fe resonance detector (PPAD) is shown in Figure 5.4 and Figure 5.5

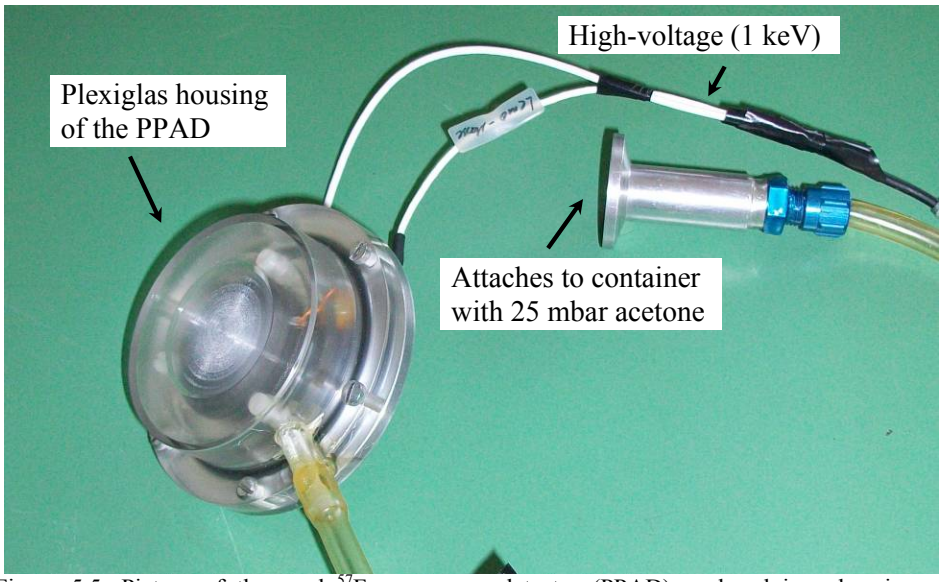

Figure 5.5: Picture of the used ^{57}Fe resonance detector (PPAD) enclosed in a housing of Plexiglas (1 mm thick window). The single line absorber (not visible inside the housing) is a stainless steel absorber (Ø = 31 mm) enriched with ^{57}Fe.

5.2 Temperature series measurements

In the experimental setups applied here, the sample can be held at temperatures ranging from 90 K to about 800 K. The low temperature measurements were performed with the sample mounted on a cold finger as shown in Figure 5.6. The temperature is controlled by the flow of N_2 gas from a liquid nitrogen container. The temperature readout is done by a type K thermocouple. An updated temperature calibration is used in this thesis, affecting the lowest temperatures (<300 K) by ±20 K. This minor temperature update neither affects findings nor conclusions.

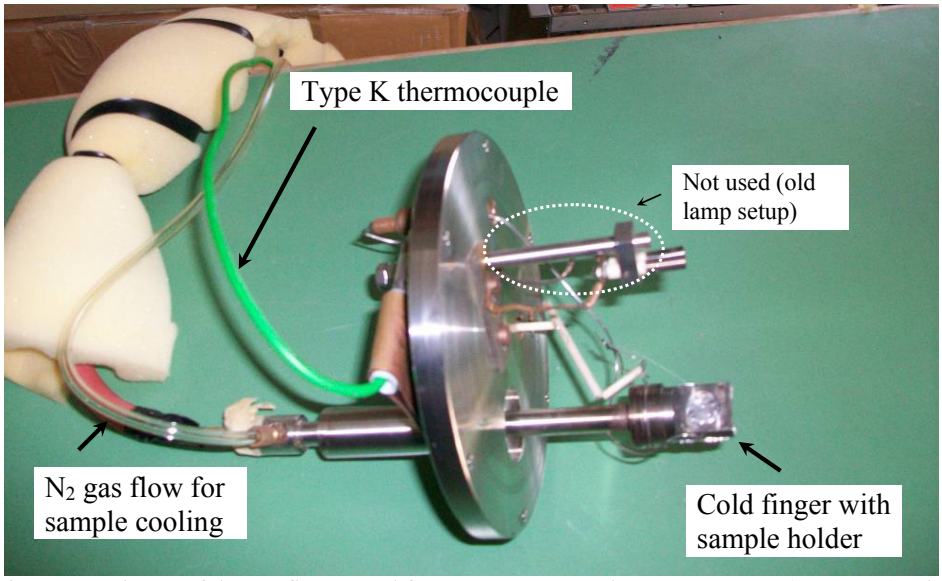

Figure 5.6: Picture of the top flange used for measurements at low temperatures (90–300 K). The sample is mounted on a cold finger cooled by controlled flow of N_2 gas from LN_2.

High temperature measurements up to 800 K were performed with the top flange shown in Figure 5.7 where heating of the sample is performed by a halogen lamp (can go up to 1000 K). The lamp is also used to bake out the chamber before measurement in order to obtain better vacuum and to anneal samples under vacuum. The flange used for high temperatures has a moveable four position sample holder. This reduces the time spent on breaking the vacuum for sample change. The sample is lowered or raised into the beam spot and the heating of the lamp. To ensure correct sample temperature each position has its own type K thermocouple readout.

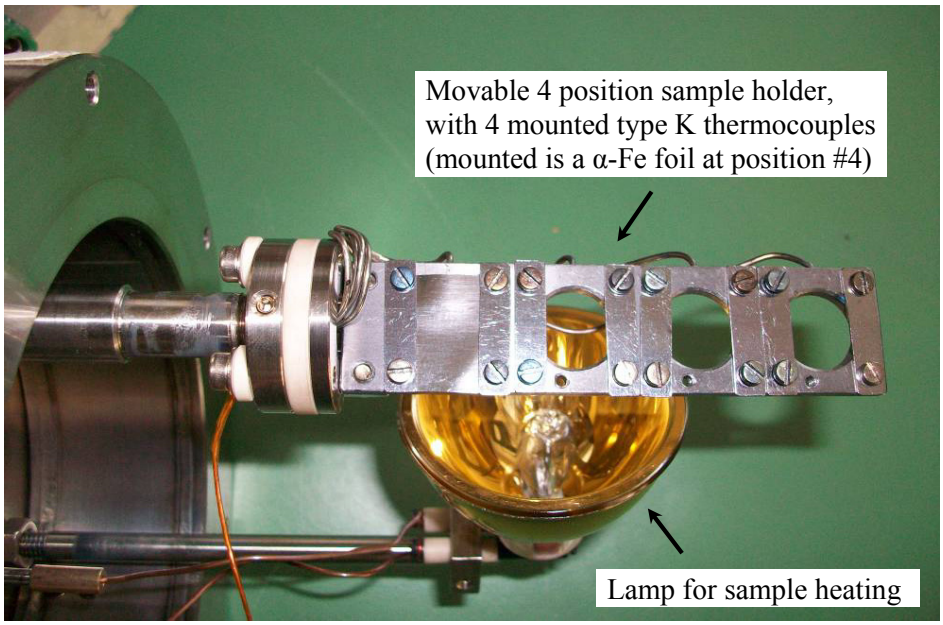

Figure 5.7: Picture of the top flange used for samples measured at high temperatures (300–800 K). It has four sample positions that are lowered or raised into the beam spot and the heating from the lamp. A foil of α-Fe used for calibration of the isomer shift and the Mössbauer velocity scale is mounted at position #4.

In home laboratories for off-line emission Mössbauer spectroscopy of the ^{57}Co sample it was possible to measure the sample down to ~17 K by mounting the sample in a closed-cycle He cryostat.

Mössbauer measurements of a sample after ion-implantation at different temperatures are referred to as a temperature series.

5.3 Angular dependence measurements

A top flange that allows the sample to be rotated is used to investigate angular dependence by changing the angle between the sample surface normal and the detector (see section 3.8). First a 4 minute implantation and measurement is performed at an incident angle of 30° relative to the sample surface normal (60° to the detector). The beam was then turned off and the sample rotated facing the detector at 90° relative to the beam direction and a 4 minute measurement of the decaying probe atoms is carried out. This method needs to be repeated at least three times to collect enough statistics in the summed spectra. The flange for angular dependence measurements was modified due to the developed holder for

measurement in an external magnetic field. The top flange and new holder is shown in Figure 5.8, but the magnet is then replaced by a nylon cylinder for angular measurements without an external field. The sample is also mounted using vacuum tape.

5.4 Measurements in an external magnetic field

The top flange used for angular dependent measurements is the simplest to modify for new experimental developments. For measurements in an external field the existing sample holder was replaced by a new developed nylon holder containing a cylindrical permanent NbFeB-magnet (B_{ext} = 1.0 T). The sample is mounted directly on the magnet using double sided vacuum tape to get the minimum distance from the magnet and hereby the maximum field strength (see Figure 5.8). The field direction is parallel to the sample surface normal and the field strength is B_{ext} = 0.6 T at the sample, measured using a Hall probe. The rotation is still functional so that angular dependent measurements within an external magnetic field can be performed or without by removing the permanent magnet. The holder is made of nylon not to interfere with the magnetic field.

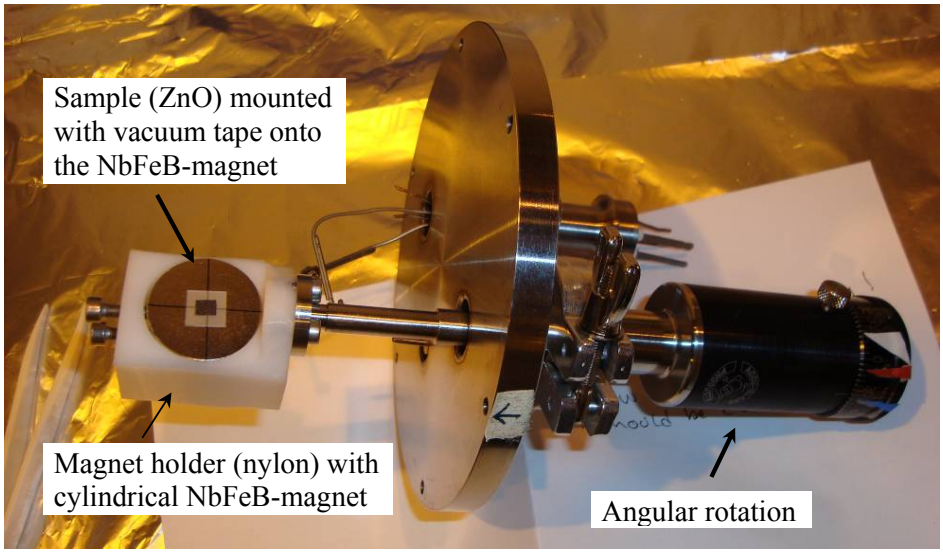

Figure 5.8: Picture of the top flange used for measurements of samples in an external applied magnetic field and angular dependence measurements. The cylindrical permanent NbFeB magnet applies a field of B_{ext} = 0.6 T parallel to the sample surface normal. Mounted is a ZnO sample (semitransparent) that reveals the vacuum tape used for attaching the sample at minimum distance from the magnet. The sample holder can be rotated.

Another sample holder was developed to be mounted on the same top flange in order to measure samples in a magnetic field at maximum 450 K. The permanent magnet used to tolerate the increased temperatures is made of a Sm-Co alloy. The heating is made by an electric heated wire of Constantan placed between the sample and the magnet. The wire is placed inside ceramic tubes to avoid it from shorting. This places the sample on top of the heater at a distance of only 3 mm from the field of the Sm-Co magnet (see Figure 5.9). The field direction is parallel to the sample surface normal and the field strength is $B_{ext} = 0.3$ T at the sample, measured using a Hall probe. Everything is held in place by the magnet, as it pulls the two screws and nuts attached in the Mylar sheets. Not to interfere with the magnetic field the holder for the magnet is made of aluminium and also in order to resist the elevated temperatures.

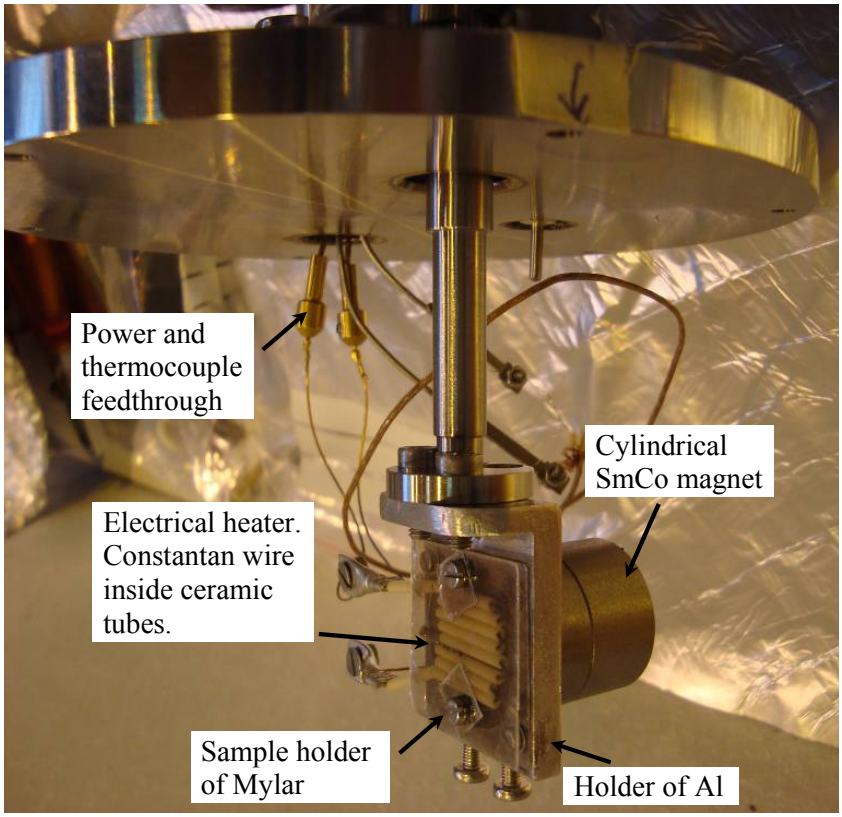

Figure 5.9: Picture of the sample holder used for measurements of samples in an external applied magnetic field for high temperatures (300–450 K). $B_{ext} = 0.3$ T at the sample location parallel to the sample surface normal.

5.5 Sample descriptions

The three oxides; ZnO, MgO, and α-Al_2O_3 were ion-implanted for the ^{57}Fe emission Mössbauer studies in this work. Here, relevant specifications of the used samples are found.

5.5.1 ZnO

The ZnO samples here studied are commercial [0001] single-crystals hydrothermally grown (wurtzite structure) by CrysTec GmbH. The wurtzite crystal structure of ZnO has the lattice constants $a = 0.34$ nm and $c = 0.52$ nm, and is a nonmagnetic wide-band gap semiconductor (II-VI) with a band gap of 3.4 eV. The samples have typical contaminations below 20 ppm of 3d elements (or ~4×10^{16} atoms/cm^3) and show n-type conductivity of 10^2–10^3 Ωcm. As received the ZnO samples are one or both side polished with surface roughness of 0.5 nm. There are some controversies in the reported Debye temperature for ZnO ranging from θ_D = 300–700 K [Wang and Giles, 2003]. The crystal structure of ZnO in Figure 5.10 shows 3×3×3 unit cells [111] in order to better visualise the near-tetrahedral symmetry of each Zn^{2+} atom (gray).

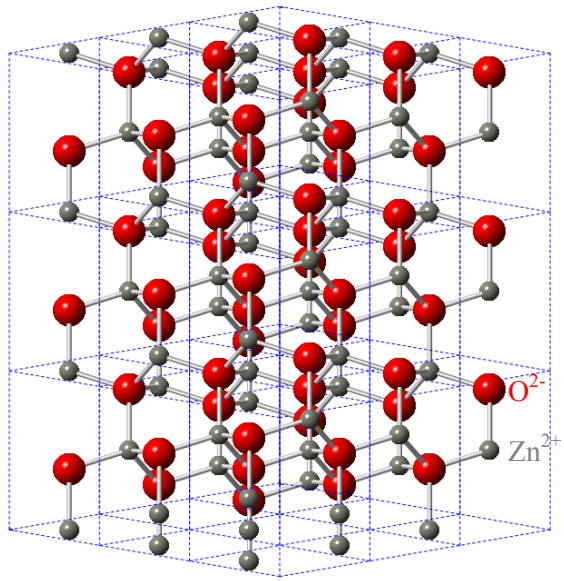

Figure 5.10: Illustration of the wurtzite structure of ZnO [Gražulis *et al.*, 2012] showing 3×3×3 unit cells with [111] orientation.

Each Zn^{2+} atom (gray) is in a near-tetrahedral symmetry, surrounded by three O^{2-} atoms at a distance of 0.197 nm roughly in plane and an O^{2-} atom at 0.199 nm distance along the c-axis.

5.5.2 MgO

MgO has a rock-salt crystal structure (face-centered cubic) with a lattice constant of a = 0.421 nm, and is a nonmagnetic insulator with a bandgap of 7.8 eV. The samples are grown with the flux melt method by CrysTec GmbH. As received the MgO samples are one side polished with surface roughness of 0.5 nm. MgO has a Debye temperature of θ_D ~750 K at 300 K [Sangster et al 1970]. The crystal structure of MgO in Figure 5.11 shows one unit cell.

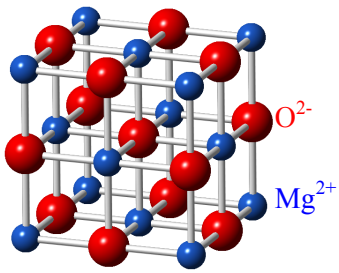

Figure 5.11: Illustration of the rock salt unit cell crystal structure of MgO [Gražulis *et al.*, 2012].

Each Mg^{2+} atom (blue) has 6 O^{2-} atoms along the principle axes. Each atom has six nearest neighbours.

5.5.3 α-Al_2O_3

α-Al_2O_3 has the hexagonal crystal structure with a lattice constant of a = 0.477 nm and c = 1.299 nm, and is a nonmagnetic insulator with a band gap of 9.5 eV. The samples are produced with the Edge-Defined Film-Fed Growth by CrysTec GmbH. As received the α-Al_2O_3 (0001) samples are one side polished with surface roughness of 0.5 nm. The Debye temperature for α-Al_2O_3 is θ_D ~1050 K [Wachtman *et al.*, 1961]. The crystal structure of α-Al_2O_3 in Figure 5.12 shows the unit cell expanded by 10% along each axis to better visualise the near-octahedral symmetry of each Al^{3+} atom (orange).

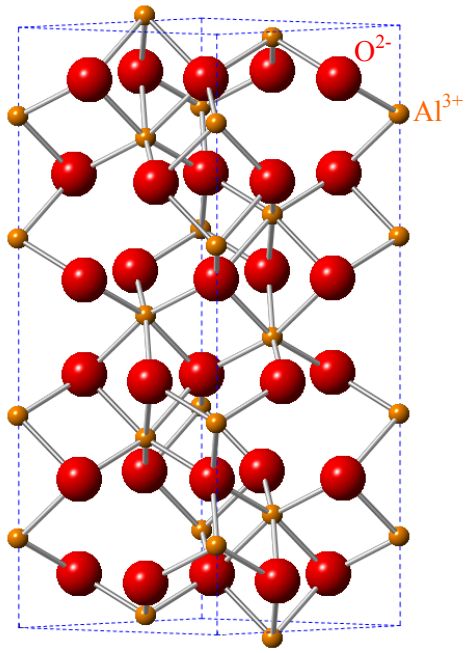

Figure 5.12: Illustration of the hexagonal crystal structure of α-Al_2O_3 [Gražulis *et al.*, 2012]. The unit cell is expanded by 10% along each axis and the orientation is slightly tilted from [111] in order to better see the near-octahedral Al^{3+} sites.

Each Al^{3+} atom is in a near-octahedral symmetry surrounded by 6 O^{2-} atoms. From the crystal structure it is seen that there is only one type of Al^{3+} site.

Chapter 6

Summary of papers

In this chapter the results of this work are summarised in five sections. Each section summarises related results with an introductory motivation and background where appropriate. The sections are not necessarily in the same chronological order as the papers. The list of included papers in this thesis is found on page **vii** and the papers are included in chapter 8.

The sections 6.1 and 6.2 deal with the magnetic spectral structure observed and are based on ^{57}Fe emission Mössbauer investigations of ^{57}Mn ion-implanted ZnO, MgO, and α-Al_2O_3 samples. Section 6.1 summarises the results on measured slow relaxing paramagnetism and no evidence of ordered magnetism observed in the spectra. The summary is based on the results found in **Papers II** and **V**.

The results in section 6.1 promoted a new interpretation of the temperature dependence of the magnetic spectral structure in terms of a semi-empirical model extracting spin-lattice relaxation rates described in section 6.2. Results in section 6.2 are found in **Papers III**, **IV**, **V** and **VI**.

Sections 6.3–6.5 describe in more details the measured ^{57}Fe emission Mössbauer spectra of each oxide together with new results where relevant. For ZnO the results are based on the **Papers I**, **II**, **V**, **VI** and **VII** and for MgO **Papers III, V** and **VIII**. For α-Al_2O_3 results are found in **Papers IV** and **V**.

6.1 Paramagnetism of dilute Fe in oxides

This section presents results on slow paramagnetic relaxations in the oxides studied (ZnO, MgO, and α-Al_2O_3). The relevant part of the spectra is the sextet-like structure in the wings of the ^{57}Fe emission Mössbauer spectra ranging from velocities, $v \sim \pm 9$ mm/s. In ZnO this structure has a relative area fraction of ~70% at 300 K (see e.g. Figure 6.2).

It is of great importance for the further Mössbauer analysis and physical modelling of the spectra to understand the mechanism involved in the origin of the observed magnetism. This is why the results obtained in an external magnetic field, which changed the direction of the project as discussed in chapter 1, are presented first.

In an earlier paper on ^{57}Fe emission Mössbauer results obtained after ion-implantation of ^{57}Mn into single-crystal ZnO [Weyer *et al.*, 2007] ferro-magnetism was favoured as an explanation for the sextet line components. The spectra [Weyer *et al.*, 2007] were analysed with a ordered (ferro)-magnetic hyperfine field sextet and two magnetic hyperfine field distributions as shown in Figure 6.1. The origin of the simple (normal) sextet was suggested to be Fe^{3+} coupled to a Zn vacancy (V_{Zn}) and the distribution III also attributed to pairs, but with more complicated V_{Zn} complexes.

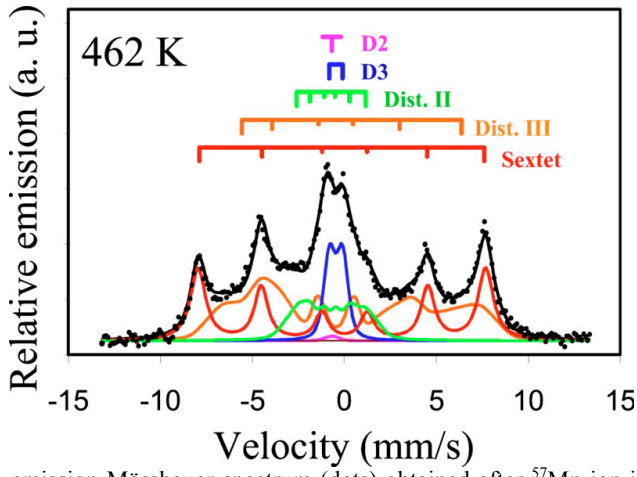

Figure 6.1: ^{57}Fe emission Mössbauer spectrum (dots) obtained after ^{57}Mn ion-implantation into ZnO at the temperature indicated, and analysed in terms of five components (from Weyer *et al.* [2007]).

There were at least three reasons for the interpretation in terms of ferromagnetism [Weyer *et al.*, 2007]:

◊ Lack of spectral features that could be assigned to the paramagnetic $S_Z = \pm 3/2$ state.

◊ Distribution II was assigned to interstitial high-spin Fe^{2+} and analysed as a sextet distribution. In the case of paramagnetism, high-spin Fe^{2+} would be expected to exhibit fast spin-lattice relaxation and observed as a doublet.

◊ Wealth of literature data, that at the time suggested dilute ferromagnetism at room temperature, both supported by experimental observations and theoretical studies (see e.g. Figure 1.1).

The status of ferro- and paramagnetism in ZnO is reviewed in the introduction of **Paper II**. Since then the number of reports claiming unintentional precipitation as an explanation for the observed magnetism has increased, a summary of some of these is given at the end of this section.

In order to further test the conclusion of Weyer *et al.* [2007] it was decided to perform measurements in an applied external magnetic field of $B_{ext} > 0.3$ T at room temperature. In the case of paramagnetism, one would be able to separate lines into sextets originating from the three Kramers doublets as described in section 3.7. However, in the case of ordered (ferro) magnetism, one would not expect major changes in the magnetic hyperfine field distributions, but at most a polarisation with the external field (see section 3.6).

For this purpose a sample holder was developed on which a sample could be placed in an external magnetic field at room temperature. The new sample holder was mounted on the already available rotation top flange after modifications (see section 5.4). This also gives the additional information on the angular dependence of the relative line ratio of the sextet in the field (see section 3.8).

A magnetic field of $B_{ext} = 0.6$ T was applied to the ZnO sample parallel to the sample *c*-axis (surface normal), and measurements performed at different emission angles θ relative to the external field direction and the detector. For more details on the setup, see section 5.4.

In order to obtain comparable measurements, a 30 minute $^{57}Mn^{+}$ pre-implantation of the ZnO sample was first performed at $\theta \sim 60°$ to record and avoid the fluence dependence of ZnO [**Paper I**] (described in section 6.3.1). Then a spectrum at emission angle $\theta \sim 60°$ was recorded during implantation for 4 minutes (Figure 6.2 (b)). Thereafter the implantation was halted, and a spectrum at $\theta \sim 0°$ was recorded for 4 minutes during the decay of ^{57}Mn (Figure 6.2 (c)). This process (not including the pre-implantation) was repeated at least three times to improve the spectral statistics.

Figure 6.2 shows ^{57}Fe emission Mössbauer spectra of ZnO at 300 K without (a) and with an applied external magnetic field of $B_{ext} = 0.6$ T at two different emission angles (b and c). Note that the zero external field is not absolutely zero, as the sample is neither shielded from the stray field from the ion-pump nor the Earth magnetic field (negligible).

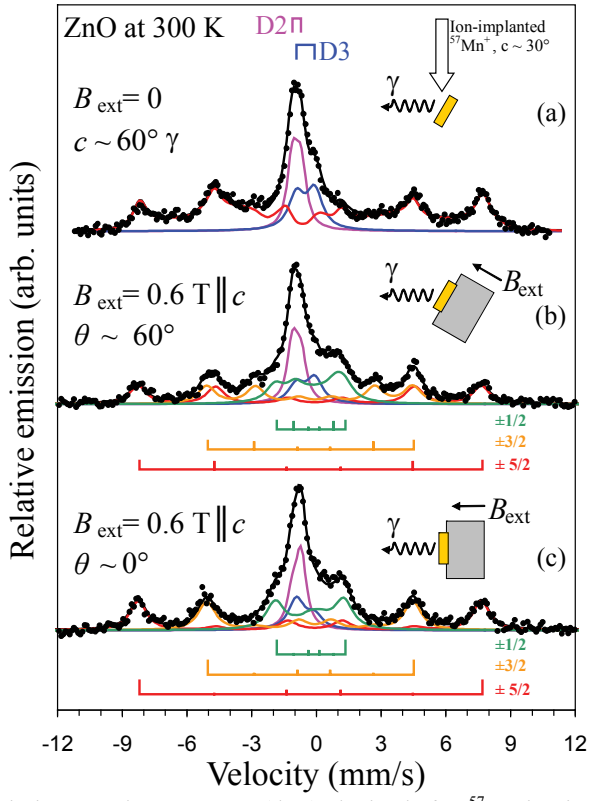

Figure 6.2: ^{57}Fe emission Mössbauer spectra (dots) obtained after ^{57}Mn ion-implantation at room temperature of ZnO without (a) and with an applied external magnetic field of $B_{ext} = 0.6$ T. The field is parallel to the samples *c*-axis at the γ-angles relative to the detector as illustrated (b and c). The bars indicate the fitted components. For spectrum (a) without field a magnetic distribution is used to fit the magnetic structure. Yellow and gray boxes represent the sample and magnet, respectively. Result presented in **Papers II** and **V**.

The magnetic hyperfine splitting (B_{hf} ~50 T for Δv ~16 mm/s) already identifies the component as originating from high-spin Fe^{3+}. High-spin Fe^{3+} is the only Fe state that can exhibit $B_{hf} > 40$ T as described in section 3.6, with the natural assumption that the Fermi contact term dominates. The magnetic hyperfine field at the ^{57}Fe nucleus must be stable (in classical terms pointing in the same direction) for more than $\tau_M = 141.8$ ns ($T_{½} = 98.3$ ns), or else a collapsed single line (or doublet) would be measured (see section 3.7).

In the spectrum measured at $\theta \sim 60°$ (Figure 6.2 (b)), small features (peaks) are observed at $v \sim$ -3 mm/s and $v \sim 2.5$ mm/s that are clearly absent in the spectrum measured in the magnetic field at $\theta \sim 0°$ angle in Figure 6.2 (c). This is characteristic for the disappearance of the pair of lines belonging to the $\Delta m_I = 0$ transition (lines 2 and 5) for the $S_Z = \pm 3/2$ electronic state as described in section 3.8. Such a state can only exist as a consequence of paramagnetism, since an ordered magnetic state (ferromagnetism) only shows a Mössbauer spectrum resembling the sextet spectrum from the Zeeman splitting ($S_Z = \pm 5/2$). The $\theta \sim 0°$ spectrum (Figure 6.2 (c)) can be analysed with a single Zeeman split sextet, however, with unphysical relative line intensities, since for ferromagnetism the intensities of the middle sextet lines (2 and 5, at $v \sim 5$ mm/s and $v \sim$ -5 mm/s) from a single $S_Z = \pm 5/2$ sextet are expected to be zero. The same implies for the spectrum at $\theta \sim 60°$, with a single ferromagnetic sextet. The line intensities should be close to 3:2:1, which is clearly not the case. More than one sextet must therefore be present to account for the observed intensity of the magnetic sextet structure.

A paramagnetic model of a superposition of three sextets originating from the three Kramers doublets belonging to the high-spin Fe^{3+} paramagnetic $S_Z = \pm 5/2$, $\pm 3/2$, $\pm 1/2$ spin states (see section 3.7.3) was therefore critically tested in the simulation of the spectra in Figure 6.2.

It is evident that this simple paramagnetic model ($S_Z = \pm 5/2$, $\pm 3/2$, $\pm 1/2$) describes adequately the observed ZnO spectra and their angular dependence in Figure 6.2 (b) and (c), thus demonstrating that the magnetically split components in the Mössbauer spectra can be attributed to Fe^{3+} paramagnetic states in ZnO. It should be noted that in order to fit the paramagnetic model it was necessary to add an angular dependence to the D2 (substitutional Fe^{2+}_{Zn}) and D3 (interstitial Fe_I) spectral components. This angular dependence is described in details in section 6.3.

Note that the line intensity ratio of the sextets originating from the three Kramers doublets in the $\theta \sim 0^{o}$ spectrum (Figure 6.2 (c)) is not exactly 3:0:1. This can be due to small misalignments in the experimental setup or due to the rather large solid angle in the emission. This does not affect the conclusion regarding the observed paramagnetism.

The measurements of ZnO within external magnetic field strongly suggest that the magnetic structure is not due to an ordered magnetic state, but Fe^{3+} exhibiting slowly relaxing paramagnetism. A residual broadening of the sextet lines is observed, implying a lower limit for the relaxation time of $\tau > 20$ ns at room temperature.

The angular dependence of the ZnO spectra makes it possible to determine the sign and magnitude of the quadrupole interaction of Fe^{3+} (see section 3.8). The quadrupole shift of the paramagnetic high-spin Fe^{3+} sextets (assuming the same isomer shift and same quadrupole shift for each Kramers doublet) was found to be $2\varepsilon = +0.12(1)$ mm/s. This gives an *EFG* consistent with results for isolated Zn^{2+} on substitutional sites determined from ^{67}Zn Mössbauer spectroscopy [Schäfer *et al.* 1988]. This indicates a similar type of crystal configuration as observed in this study. The paramagnetic Fe^{3+} ions are therefore concluded to be located on substitutional sites after implantation, which is also in accordance with results from emission channelling experiments [Rita *et al.*, 2004].

The two other oxides MgO and α-Al_2O_3 were also measured without and with an external magnetic field at different emission angles as performed on ZnO [**Paper V**].

Figure 6.3 shows a zoom of the wings and the magnetic structure of MgO, without (a) and with an external applied magnetic field (b and c).

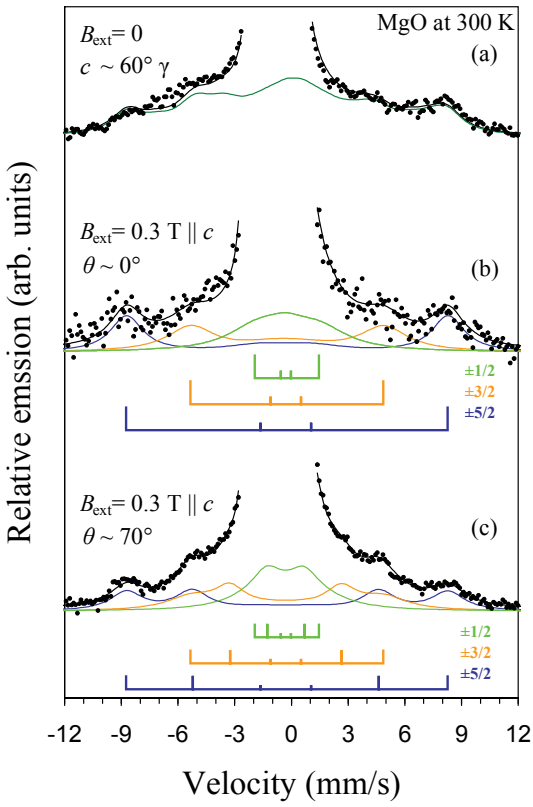

Figure 6.3: The wings of the ^{57}Fe emission Mössbauer spectra (dots) obtained after ^{57}Mn ion-implantation into MgO at room temperature. The topmost spectrum (a) was measured without an external applied magnetic field, and the two bottom spectra (b, c) were measured with B_{ext} = 0.3 T magnetic field parallel to the surface normal of the sample.

Although the external magnetic field is not as strong as for the measured ZnO, but only $B_{ext} = 0.3$ T (because a different sample holder was used as described in section 5.4), it is sufficient to express the similar angular characteristics of a magnetic sextet structure originating from paramagnetism (see section 3.7). The magnetic structure of the spectrum obtained without external magnetic field (Figure 6.3 (a)) was simulated using the method as described in section 6.2.

Figure 6.4 shows ^{57}Fe Mössbauer spectra obtained after implantation into α-Al_2O_3 at room temperature. A spectrum in an external magnetic field at $\theta = 0°$ was not measured. The spectrum measured without external magnetic field (Figure 6.4 (a)) was simulated using Blume-Tjon sextets (section 6.2).

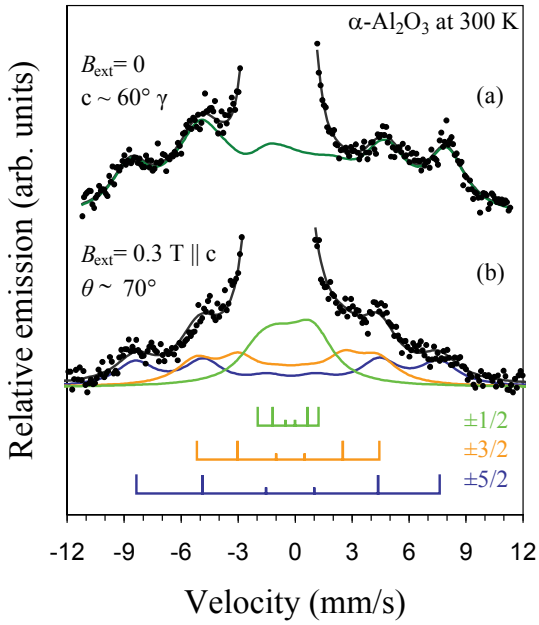

Figure 6.4: The wings of the ^{57}Fe emission Mössbauer spectra (dots) obtained after ^{57}Mn ion-implantation into α-Al_2O_3 at room temperature. The topmost spectrum (a) shows the spectrum measured without an external applied magnetic field, and the lower spectrum (b) was measured in a B_{ext} = 0.3 T magnetic field parallel to the surface normal of the sample.

The ^{57}Fe emission Mössbauer spectra of MgO and α-Al_2O_3 measured in an external magnetic field were also fitted using the three Kramers doublets and attributed to high-spin Fe^{3+} paramagnetism [**Paper V**].

The benefit of first measuring and analysing ZnO compared to MgO and α-Al_2O_3 is that ZnO exhibits the largest area fraction of the magnetic structure (~70% at room temperature), and the sharpest lines. Hence more detailed structural features can be identified with higher confidence. At room temperature the relative area fraction of the magnetic structure of α-Al_2O_3 and MgO are ~55% and ~25%, respectively.

Details on the paramagnetic behaviour concluded from ^{57}Fe emission Mössbauer measurements of the ^{57}Mn implanted oxides can be found in **Papers II**, and **V**.

The measured paramagnetism fitted with three Kramers doublets shows that the electronic spin of the Fe^{3+} atom is neither coupled to lattice defects from the implantation nor to the lattice, which would be expected to result in fast paramagnetic spin-spin relaxations which would show a singlet or a doublet component. The absence of such types of coupling shows that the Fe^{3+} atoms are

unlikely to act as the seed needed for the proposed (long-range) ferromagnetism (see e.g. discussion in Coey *et al.* [2005]). From the work presented here, it is not possible to claim that structural defects cannot have long-range magnetic moment, as suggested by Wang *et al.* [2009] and in principle long-range magnetism could have nothing do with the interacting spins of Fe atoms. Since the publication of **Paper II** an increased number of reports claiming misinterpretation of data, including unintentional precipitation, can be found in the literature. It is beyond the scope of this thesis to summarise all papers in the literature, but I put forward a statement from Scott Chambers that summarises this elegantly.

"*Because of the allure of discovering the first room-temperature diluted magnetic semiconductor, a sort of scientific gold-rush mentality set in. People grew films and did magnetometry. If they found evidence of room-temperature ferromagnetism, they often went straight to their word processors, rather than to their materials characterization facility. Many papers were written, and continue to be written, which claim successful synthesis of new high-T_C diluted magnetic semiconductors, but the ferromagnetism is often due either to magnetic contamination or magnetic secondary-phase formation*." Quote from Chambers [2010].

6.2 Spin-lattice relaxations of Fe^{3+} in oxides

This section concentrates on extracted spin-lattice relaxation rates of paramagnetic Fe^{3+} from the ^{57}Fe emission Mössbauer spectra obtained after ^{57}Mn ion-implantation of the oxide samples.

The confirmation of paramagnetism of dilute ^{57}Fe in the oxides ZnO, MgO, and α-Al_2O_3 (see section 6.1) [**Papers II** and **V**], allows for further analysis regarding the magnetic structure in the Mössbauer spectra, even without an applied external magnetic field. The broadening of the sextet structure with increased temperature is of interest here.

Figure 6.5 shows a temperature series measured between 304–770 K of ^{57}Fe emission Mössbauer spectra after ^{57}Mn ion-implantation of ZnO from Weyer *et al.* [2007].

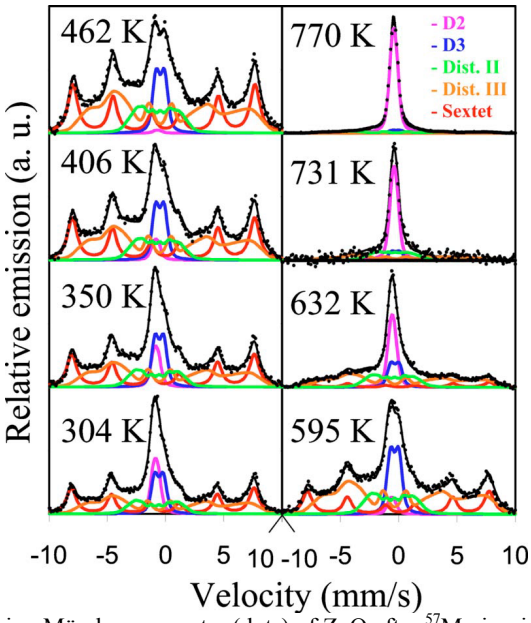

Figure 6.5: ^{57}Fe emission Mössbauer spectra (dots) of ZnO after ^{57}Mn ion-implantation measured at the temperatures indicated [Weyer *et al.*, 2007]. It was originally attributed to ordered magnetism. The broadening of the sextet structure is of interest here.

The overall broadening of spectral features of the sextet, as described by Weyer *et al.* [2007], was attributed to different populations of defect structures. The disappearing (broadening) magnetic structure with increased temperature was described in terms of breaking of the Fe^{3+}-V_{Zn} pairs (exhibiting ordered magnetism), as the mobility of the vacancy increases.

The suggestion of high-spin Fe^{3+} exhibiting slow paramagnetic relaxations (see section 6.1) led to a revision of the physics behind the broadening mechanism discussed in Weyer *et al.* [2007]. The obvious candidate is temperature dependent spin-lattice relaxation (see section 3.7). Here the important question arises: Can the observed spectral changes of the paramagnetic sextet structure for $B_{ext} = 0$ be used to extract temperature dependent paramagnetic spin relaxation rates?

It should be noted that the central components in the measured spectra (see e.g. Figure 6.5) do not affect the conclusions here. The results are extracted from the paramagnetic structure mainly observed in the wings and therefore not greatly affected by the central components. The central components of the oxides ZnO, MgO, and α-Al_2O_3 are described in sections 6.3, 6.4, and 6.5, respectively.

A thorough treatment of the Mössbauer spectra would analyse them in terms of a suitable relaxation model, taking into account the paramagnetic properties of

the system. This could for example be the relaxation model of Clauser [1971]. However, this requires solving the spin-Hamiltonian of the system and hereby retrieve the line positions or the overall shape of the non-relaxing spectrum, and then in addition include spin relaxations.

The spin-Hamiltonian includes many parameters [Gütlich *et al.*, 2011 Ch. 4], such as the zero-field splitting parameters, and parameters describing the interactions between the spin system, external magnetic field and the nuclear spin. Commonly, these parameters are obtained in experiments that would be either difficult (variation of external field) or not suitable (very low temperatures) in our measurements performed at ISOLDE/CERN.

Many of the spin-Hamiltonian parameters are better determined by e.g. electron paramagnetic resonance (EPR) techniques, but it would be of interest to verify that the spectra obtained without external magnetic field are compatible with a description based on the spin-Hamiltonian.

According to S. Mørup at the Technical University of Denmark, who has decades of experience in paramagnetic systems (see e.g. Mørup [2011]) this would require a substantial programming effort which would not necessarily benefit in the interpretation of the measured data. Spectra obtained in "zero" external magnetic field are difficult to simulate in the spin-Hamiltonian formalism (S. Mørup, private communication 2010).

Instead, a simulation method of more empirical character was used applying the relaxation line-shape by Blume and Tjon [1968] (see section 3.7) to extract the observed temperature dependent broadening of the paramagnetic Fe^{3+} structure. Blume and Tjon [1968] calculated the Mössbauer spectra for a paramagnetic sextet with random fluctuations of the magnetic hyperfine field ($\pm B_{hf}$) at a relaxation rate $1/\tau$ as described in section 3.7. This calculated sextet will be referred to as the **BT-sextet** (Figure 3.9).

The developed empirical relaxation model for describing the Mössbauer spectra of paramagnetic Fe^{3+} in oxides [**Paper III**] based on the Blume-Tjon line-shape is modelled with the following steps:

1) First, one considers the spectrum at the lowest temperature in a temperature series (where spin-lattice relaxation is assumed negligible). A BT-sextet that fits the outermost features of the spectrum (B_{hf} ~ 52 T) is inserted. One assumes $1/\tau = 0$ and the intrinsic line-width (Γ_i) is adjusted by visual inspection. This BT-sextet naturally interprets the sextet originating from electronic Zeeman splitting of the $M_S = \pm 5/2$ Kramers doublet, with a possible admixture of the $M_S = \pm 1/2$ split Kramers doublet (see spectrum in Figure 3.12 at ~0 T).

2) Thereafter additional BT-sextets with the same intrinsic line-widths (found in step 1) and $1/\tau = 0$ are added to fill-up the area of the paramagnetic Fe^{3+} structure, creating a magnetic distribution. Magnetic hyperfine splittings, quadrupole shifts, and isomer shifts are selected by visual inspection, such that the BT-sextets reasonably simulate the experimental data. This can result in the addition of 2–5 BT-sextets (depending on the intrinsic line-width and "sharpness" of the magnetic structure).

3) The same model of BT-sextet components from step 2 is applied to the spectra obtained at increased temperatures, and set to follow the second order Doppler shift. The magnetic hyperfine splitting is allowed to reduce for increased temperatures. This may be a simple linear reduction with temperature or a mean-field magnetisation curve for $J = 5/2$ [Crangle, 1991]. The relaxation rate is allowed to vary only for $1/\tau > 0$ at elevated temperatures. All added BT-sextets have the same relative area fraction.

4) Finally, the whole temperature series is fitted simultaneously, determining the best values of global variables. The only temperature dependent variable is the relaxation rate $1/\tau$ and the total spectral area of the BT-sextets of the model.

The above described empirical relaxation model based on the Blume-Tjon line-shape is for readability referred to as the **EmpBT** model. The EmpBT model is sensitive to a relaxation rate in the range of $1/\tau = 4\times10^6 – 1\times10^8$ s^{-1}. Above this range the spectral broadening becomes too large for the simulation, as spectral details have collapsed and disappeared (see Figure 3.9). Below no broadening is observed. Within this range, this method is mostly sensitive to the lifetime broadening of the BT-sextets, which is the same as that for the more general relaxation model based on the Clauser model [Clauser, 1971].

To test this semi-empirical approach of the EmpBT model the MgO temperature series was used, since there already exist EPR results of the relaxation of Fe^{3+} impurities in MgO [Biasi and Portella, 1980] in an overlapping

temperature range, where broadening was observed in the ^{57}Fe emission Mössbauer spectra. The relaxation results from Biasi and Portella [1980] were obtained with the continuous saturation method [Poole, 1983 Ch. 13] on the relaxation rate between the $S_Z = +1/2$ and $S_Z = -1/2$ states. The method is certainly not the best procedure to retrieve relaxation rates (M. Fanciulli, private communication 2010). However, their high temperature data (100–340 K) is compatible with the low temperature data (4.2–27 K) from Ammar and Thorp [1977] based on a more reliable pulsed EPR technique (M. Fanciulli, private communication 2010), giving us the confidence of making use of their data to test the overall feasibility of the EmpBT model presented here.

Figure 6.6 shows the wings of the magnetic structure in the ^{57}Fe emission Mössbauer temperature series of ^{57}Mn ion-implanted MgO. Slightly different temperatures than presented in **Paper III** are used here due to an updated temperature calibration as described in section 5.2. The updated temperatures affect the temperatures below 300 K by ±20 K which does not change any conclusions.

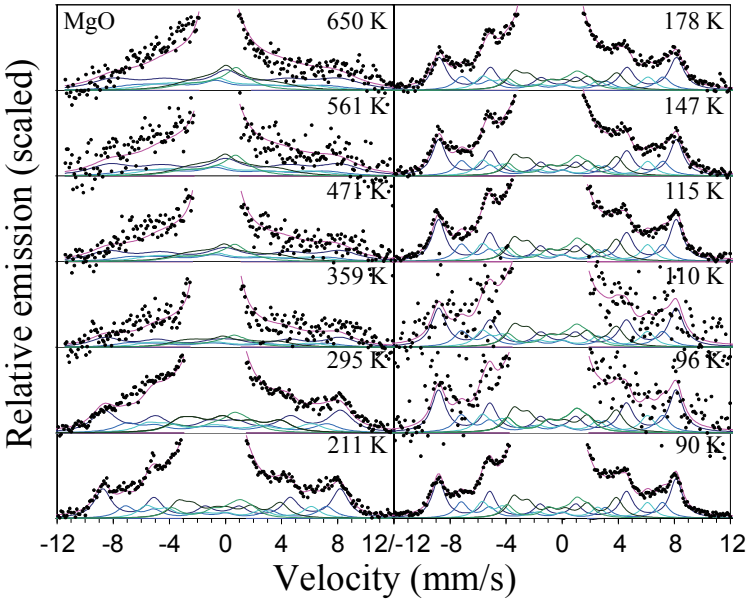

Figure 6.6: Wings of the ^{57}Fe emission Mössbauer spectra (dots) measured after ^{57}Mn ion-implantation ($\theta = 60°$) of MgO at the temperatures indicated (updated temperature calibration). Fitting components are indicated with solid lines. A clear broadening is observed with increased temperature; especially visual for the outermost lines (1 and 6) at 178–359 K

The EmpBT model was applied to the MgO spectral analysis [**Paper III**] as seen in Figure 6.6. In total, five BT-sextets were required, all with different

lower magnetic hyperfine fields, where the internal line ratio was restricted to 3:2:1 (random orientations). The hyperfine magnetic field $B_{hf,i}(T)$ of each sextet, was restricted to follow a linear decrease with increasing temperatures. If simulated with a ferro-magnetisation curve for $J = 5/2$ an unrealistic Curie temperature of $T_C \sim 2650$ K is obtained. The small observed reduction in the magnetic hyperfine field (1.3% within the measured range) is probably related to a temperature dependent expansion of the lattice. This supports the observed magnetic hyperfine pattern is due to slow relaxing paramagnetic Fe^{3+}, since in the case of ferromagnetism a higher hyperfine field reduction is expected.

In Figure 6.6 broadened features are observed at increasing temperatures; particularly clearly for the outermost lines at 178–359 K. The observed broadening at increased temperature can be taken as yet another support for the paramagnetic origin of the Fe^{3+}. In case of ordered magnetism an increased temperature would result in a decrease of the magnetic hyperfine field, reducing the nuclear Zeeman splitting in the spectrum and not affecting the line-shape.

In the wings of the Mössbauer spectra the feature with the largest splitting originates from the $M_S = \pm 5/2$ Kramers doublet of Fe^{3+}. It is well observable, since the resulting sextet from the $S_Z = \pm 5/2$ states is least affected by the lack of an external magnetic field (see section 3.7) and is often observed as a "normal" sextet, while the $M_S = \pm 3/2, \pm 1/2$ split Kramers doublets give rise to a more complicated spectral shape without external magnetic field (i.e. Figure 3.12).

Around 198 K, an increased broadening of the magnetic structure becomes visible and continues to broaden at elevated temperatures. Above ~471 K, the magnetic structure has completely collapsed and features in the wings of the spectrum have disappeared, leaving a dominating central structure and a flat magnetic structure. This is the limit for extracting the relaxation rate using the EmpBT model, since it relies on the line-width broadening of the structure – not the collapse of the lines.

The extracted relaxation rates from the EmpBT model mainly reflect the broadening of the $M_S = \pm 5/2$ split Kramers doublet, as the resulting sextet has the clearest observed features in the Mössbauer spectra. It is also as seen from Equation (3.22) that lines 1 and 6 with the largest B_{hf} are the last to collapse. Letting the inner BT-sextets in the EmpBT model follow either a faster or a slower relaxation rate than the outermost BT-sextet did not significantly change either the quality (χ^2) of the simultaneous fit or the relaxation rate. We hence conclude that the relaxation rate is reasonably estimated for the $S_Z = \pm 5/2$ states,

while the remaining sextets mostly account for the asymmetry in the spectra (more intensity in the left wing). Figure 6.7 shows the extracted relaxation rates of dilute Fe^{3+} in MgO compared with the EPR measurements from Biasi and Portella [1980].

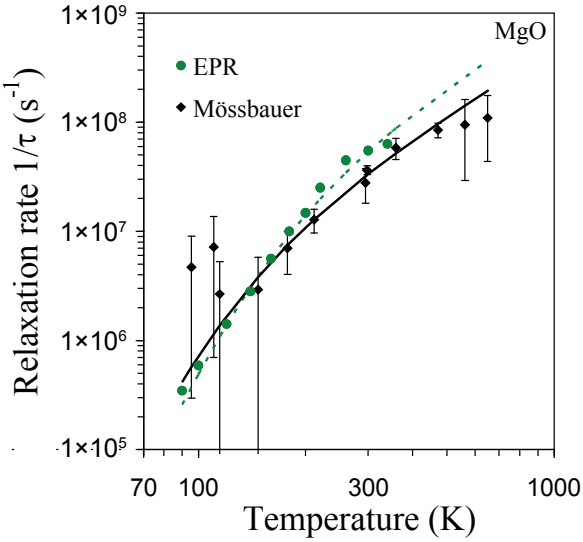

Figure 6.7: Relaxation rates obtained using the EmpBT model (diamonds) in comparison with results from EPR measurements (dots) on relaxation rates of dilute Fe^{3+} impurities in MgO [Biasi and Portella, 1980]. Above $T \sim 300$ K the relaxation rates roughly follow a T^2 temperature dependence [**Paper III**]. The lines are to guide the eye. Error bars indicate a variance of 1σ.

Despite the empirical nature of the EmpBT model the semi-empirical model for the temperature dependent paramagnetic relaxation in the Mössbauer spectra of Fe^{3+} in MgO, was found to give relaxation rates of the same order of magnitude [**Paper III**] as those observed with EPR measurements [Biasi and Portella, 1980].

In the temperature range where there are overlapping EPR and Mössbauer data (Figure 6.7), the spin-lattice relaxation rates obtained by Mössbauer spectroscopy seem to be underestimated by a factor of ~1.8 compared to the rates obtained using EPR. A possible explanation is that the EPR method measures the relaxation rate between the $S_Z = +1/2$ and $S_Z = -1/2$ states [Biasi and Portella, 1980], while Mössbauer spectroscopy measures the "lifetime" of the $S_Z = +5/2$ and $S_Z = -5/2$ states, since the Zeeman split sextet originating from the $M_S = \pm 5/2$ Kramers doublets is best expressed in the Mössbauer spectra. The two Kramers doublets do not have the same transition probability [Bhargava *et al.*, 1979], which could explain the factor of 1.8.

It is important to note that the overall reasonable quality of the fitting procedure is not a consequence of increasing the number of variables [**Paper III**]. The simultaneous analysis of the 12 MgO Mössbauer spectra in Figure 6.6 of the paramagnetic Fe^{3+} component uses 41 fitting variables (average of 3.4 variables per spectrum) which is considerably less than the analysis in terms of a sextet and distributions, as described by Weyer *et al.* [2007]. It required at least 55 variables (4–5 per spectrum).

The empirical relaxation model described above for the emission Mössbauer spectra of paramagnetic Fe^{3+} in oxides based on the Blume-Tjon line-shape (EmpBT) has also been used on the other two oxides α-Al_2O_3 [**Paper IV**] and ZnO [**Paper VI**], but unfortunately no data on the relaxation rates has been found in the literature for the temperature range of this study. The conclusion that the EmpBT model can be applied to extract relaxations rates from the Mössbauer spectrum, without the application of an external magnetic field, relies on the comparable rates obtained by the EPR method on MgO [**Paper III**].

Comparison of the extracted temperature dependent spin-lattice relation rates, using the EmpBT model on all three oxides (MgO, ZnO, and α-Al_2O_3) is shown in Figure 6.8 and presented in **Paper VI**.

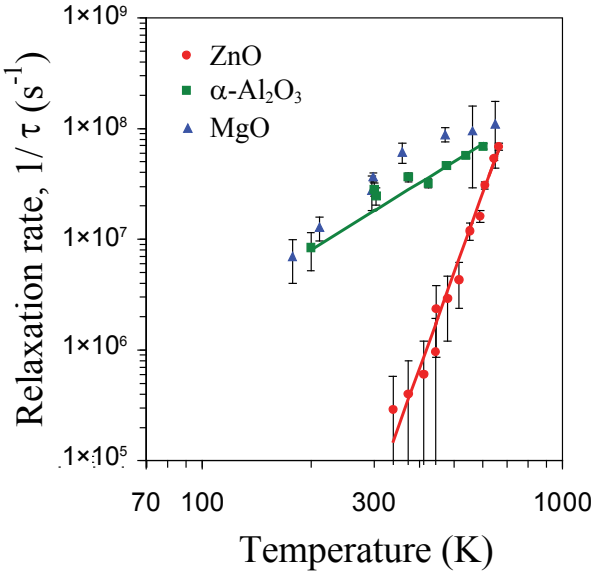

Figure 6.8: Comparison of the relaxation rates ($1/\tau$) of the studied oxides using the described EmpBT model [**Paper III**] for MgO (blue triangles, updated temperatures) and α-Al_2O_3 (green squares). The solid green line indicates a T^2 dependence that both MgO [**Paper III**] and α-Al_2O_3 [**Paper IV**] follow above ~300 K. Clearly, the relaxation rate in ZnO (red circles) follows a different slope. It fits a T^9 dependence as shown by the solid red line. Error bars indicate a variance of 1σ. Result presented in **Paper VI**.

The MgO data points in Figure 6.7 at the lower temperatures (below 150 K) are not included, since they have a large uncertainty and do not contribute to the conclusion. Comparing the extracted relaxation rates of paramagnetic Fe^{3+} in MgO [**Paper III**] and α-Al_2O_3 [**Paper IV**] using the EmpBT model both follow a T^2 temperature dependence above ~300 K as indicated by the solid green line. This is as theoretically expected for all Raman processes for temperatures $T > \theta_D/3$, as graphically illustrated in Figure 3.10. As seen from Figure 3.10, the relaxation rate can be divided into two regimes. At $T < \theta_D/3$ the relaxation rate follows $1/\tau \propto T^n$ with n = 5, 7, 9 and for $T > \theta_D/3$ it follows $1/\tau \propto T^2$ regardless of the model. Clearly, the spin-lattice relaxation rate of Fe^{3+} in ZnO (red circles) does not follow the T^2 dependence as expected from theory. This is in contrast with the relaxation rates obtained using the same method and analysis of the MgO and α-Al_2O_3 Mössbauer spectra. Instead the extracted spin-lattice relaxation rates of dilute Fe^{3+} in ZnO appear to follow a T^9 dependence as indicated by the solid red line in Figure 6.8. This is unexpected since ZnO has a reported lower Debye temperature than both MgO and α-Al_2O_3 (see section 5.5). Despite the fact that a wide range of very different values for the Debye temperature of ZnO has been reported, none of them fulfils the criterion for the observed T^9 dependence, since this would require a $\theta_D > 1900$ K according to the theory behind Figure 3.10.

The reason for the observed T^9 behaviour instead of a T^2 relaxation rate behaviour of paramagnetic Fe^{3+} in ZnO is unknown at present. Similarly, a deviation from a T^2 relaxation rate behaviour is observed at $T > \theta_D/3$ for Fe^{3+} in rutile TiO_2 (H. P. Gunnlaugsson, private communication 2012).

It should be emphasised that the study of spin-lattice relaxation effects is only possible when the local concentration of Fe is below 10^{-2} at.%. [Mørup, 2011]. At higher concentrations, spin-spin relaxations with other Fe/Mn ions begin to play a role, and severely hamper the interpretation of the Mössbauer spectrum. Therefore ISOLDE/CERN offers unique experimental facilities for ion-implanting Mössbauer probes into samples at low concentrations ($<10^{-4}$–10^{-3} at.%). This gives the opportunity to measure effects not explained by current theories on spin-lattice relaxation rates at dilution levels and temperatures outside the reach of other experimental methods. Slow paramagnetic relaxations in oxide systems were studied intensively by Mössbauer spectroscopy in the late 1960's using dilute systems with stable ^{57}Fe to avoid spin-spin relaxations (see e.g. [Wickman *et al*., 1966a; Wickman and Wertheim, 1966b; Wertheim and

Remeika, 1964] and e. g. [Schünemann and Winkler, 2000] for a recent overview). However, the details that could be derived from the studies were hampered by the high dilution required.

6.3 Properties of Fe in Mn/Fe implanted ZnO

After analysing and discussing the paramagnetic Fe^{3+} sextet structure, the attention is now turned to the complete picture of the emission Mössbauer spectra including the central components ($v \sim \pm 4$ mm/s).

Figure 6.9 shows the ^{57}Fe emission Mössbauer spectrum at room temperature after implantation of ^{57}Mn into ZnO [**Paper VI**].

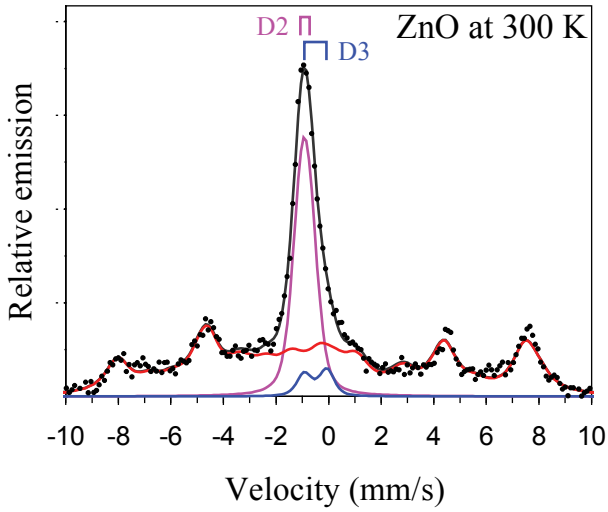

Figure 6.9: ^{57}Fe emission Mössbauer spectrum (dots) at room temperature after ^{57}Mn ion-implantation into ZnO. The two central components D2 and D3 indicated with bars have been identified as originating from substitutional and interstitial Fe sites, respectively. The paramagnetic structure has been fitted using the EmpBT model described in section 6.2. Spectrum is measured at a lower fluence (see section 6.3.1) than the ZnO spectrum in Figure 6.2 (a).

The central part of the spectrum that exhibits no magnetic hyperfine splitting has been analysed with two angular dependent (see section 3.8) quadrupole doublet components (D2 and D3). The paramagnetic Fe^{3+} structure is simulated using the EmpBT model described in section 6.2.

Figure 6.10 shows the ^{57}Fe emission Mössbauer spectra obtained after implantation of ^{57}Mn into ZnO in the temperature range 300–664 K. See **Paper VI** for details on the measurements and analysis.

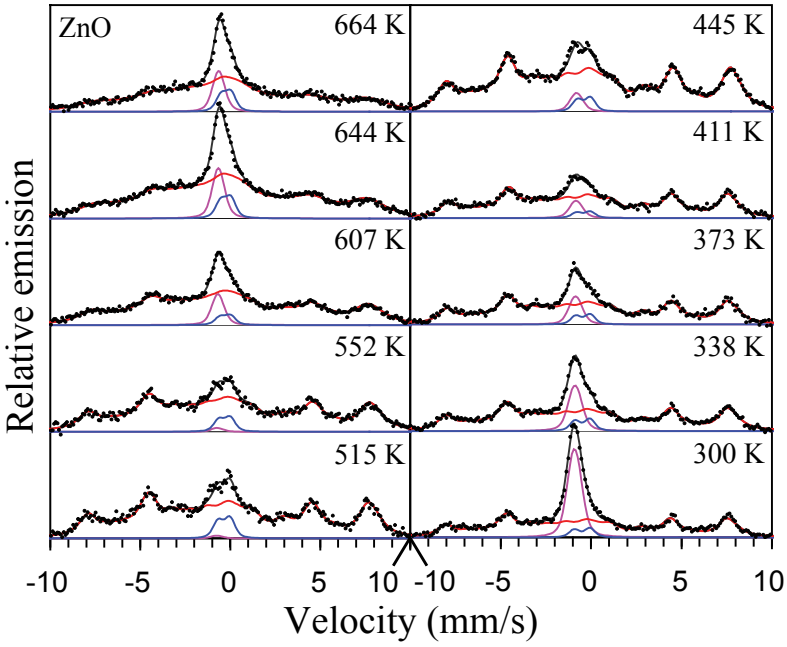

Figure 6.10: Representative ^{57}Fe emission Mössbauer spectra (dots) of the temperature series of ZnO after ^{57}Mn implantation at the indicated temperatures. The fitted components and their sum are shown by solid lines. The components are labelled in Figure 6.9.

The D2 component has an isomer shift of $\delta = 0.91(1)$ mm/s [**Paper II**] characteristic for high-spin Fe^{2+} (see Figure 3.4). It dominates the spectra at the highest temperature, where annealing of implantation related damage is considered complete, assigning the D2 as originating from Fe^{2+} on substitutional Zn, Fe_{Zn}^{2+} (see section 4.3.2).

The D3 component with $\delta = 0.50(3)$ mm/s [**Paper II**] exhibits more or less a constant area fraction of around 10% [**Paper VI**] over the whole temperature series. This suggests a recoil produced component, due to the β^- decay which assigns this component to interstitial Fe sites, Fe_I (see section 4.3.3).

Compared to the other oxides at room temperature, ZnO does not exhibit a spectral component originating from damage to the crystal caused by the ^{57}Mn ion-implantation. ZnO is known to be a radiation hard material supporting the absence of damage component at room temperature [Look *et al.*, 1999; Auret *et*

al., 2001]. For ^{57}Mn ion-implantation performed at temperatures <200 K a spectral component attributed to ^{57}Fe in damaged environment has been identified [H. P. Gunnlaugsson, private communication 2011].

The isomer shifts of the high-spin Fe^{2+}_{Zn} and Fe_I doublets were found to follow closely the second-order Doppler shift and were restricted in the final simultaneous analysis to follow that dependence.

The room temperature values of the hyperfine parameters of Fe^{2+}_{Zn} and Fe_I are in a good agreement with those previously obtained by Weyer *et al.* [2007]. In addition, the sign of the quadrupole interaction of the doublets was determined from the angular measurements at room temperature as presented in section 6.1.

The temperature dependence of the quadrupole splitting of Fe^{2+}_{Zn} in ZnO was analysed in terms of the model of Ingalls [1964] as presented in section 3.5. Calculation of the Boltzmann statistics of the orbital populations gives the following equation of the temperature dependent quadrupole splitting;

$$\Delta E_{\mathrm{Q}}(T) = \Delta E_{\mathrm{Q,L}} + \Delta E_{\mathrm{Q,V}} \times \tanh\left(\frac{E_0}{2kT}\right) \quad . \tag{6.1}$$

where $\Delta E_{\mathrm{Q,L}}$ is the lattice contribution from the non-cubic arrangement of lattice atoms and $\Delta E_{\mathrm{Q,V}}$ the valence contribution from the lowest d_{z^2} orbital in ZnO (see Figure 3.7). E_0 is the splitting between the $d_{x^2-y^2}$ and d_{z^2} orbitals. For $\Delta E_{\mathrm{Q,L}}$ the value $\Delta E_{\mathrm{Q,L}}$ = +0.12(1) mm/s was obtained from the quadrupole shift of paramagnetic high-spin Fe^{3+} originating from substitutional sites in ZnO measured in an external field [**Paper II**] (see section 6.1).

In **Paper VI** the used value of $\Delta E_{\mathrm{Q,V}}$ = -2.5 mm/s for Fe^{2+}_{Zn} was determined from ^{57}Co implanted ZnO [**Paper VII**], described in section 6.3.2. The value was not based on the final spectral analysis and in **Paper VII** the final analysis gave $\Delta E_{\mathrm{Q,V}}$ = -2.3(1) mm/s, but the difference does not change the conclusions.

6.3.1 Fluence dependence of Fe^{3+}/Fe^{2+} in ZnO

Although many types of samples have been measured during the ISOLDE experiments, ZnO is the only material for which fluence dependence was observed in the range 10^{10}–10^{12} #/cm^{-2} (H. P. Gunnlaugsson, private

communication 2009). It is found that the ratio of Fe^{3+}/Fe^{2+} observed in the ^{57}Fe emission Mössbauer spectra depends on the ion-implantation fluence of ^{57}Mn (i.e. Figure 6.11) in the temperature range from 300–390 K. Upon ion-implantation the Fe^{3+} sextet with long relaxation time builds up on the expense of the substitutional Fe^{2+} component D2 with short relaxation time. The Fe^{3+} continues to build-up until it reaches a saturation value of 70–85% relative area fraction above ~3.0×10^{11} $^{57}Mn/cm^2$ and further ^{57}Mn implantation only improves the statistics of the spectra shown in Figure 6.12 and Figure 6.13. The area fraction of the interstitial Fe (D3) component is roughly constant around 10% as shown in Figure 6.13.

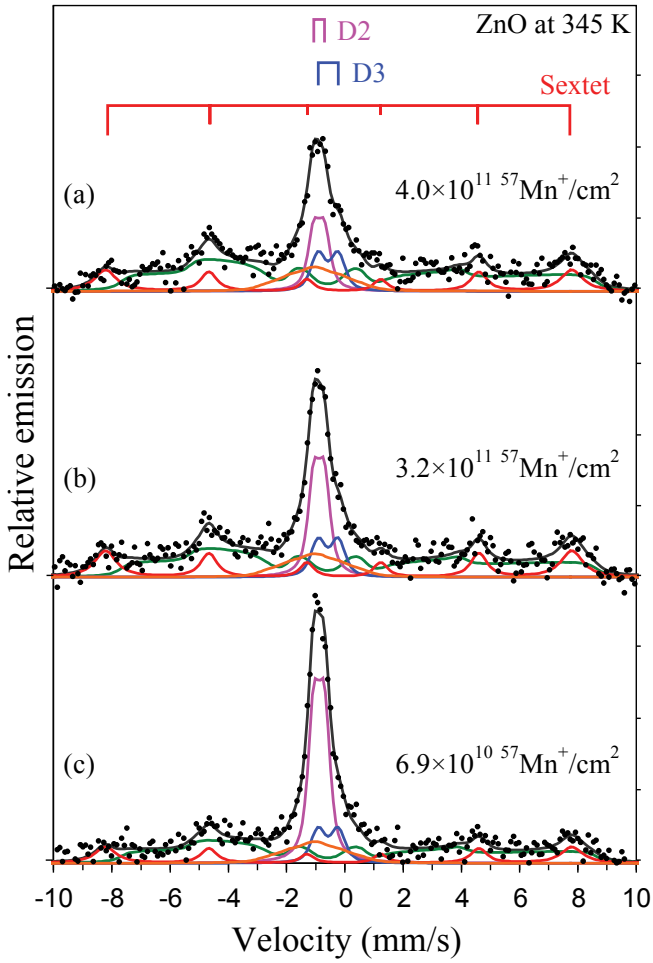

Figure 6.11: ^{57}Fe emission Mössbauer spectra (dots) of ZnO at 345 K at the ion-implanted $^{57}Mn^+/cm^2$ fluences indicated. The fitted components correspond to Figure 6.9. Although the magnetic structure has been analysed [**Paper I**] according to Weyer *et al.* [2007], this does not change the extracted area fractions of Fe^{3+}/Fe^{2+} significant.

At least two explanations for such a fluence dependence are possible. The simplest interpretation of the faster transformation of Fe^{2+} to Fe^{3+} at elevated temperatures (Figure 6.12) is a temperature dependent increase of the mobility of Zn vacancy (V_{Zn}), together with a trapping of the vacancy at the substitutional Mn/Fe site. It was assumed that substitutional Fe^{2+} transforms into a Fe^{3+}-V_{Zn} pair where the vacancy partially charge compensates the Fe^{3+} state [**Paper I**]. In **Paper I** an implantation induced change of the Fermi level was discussed, but the simpler pair creation mechanism was favoured.

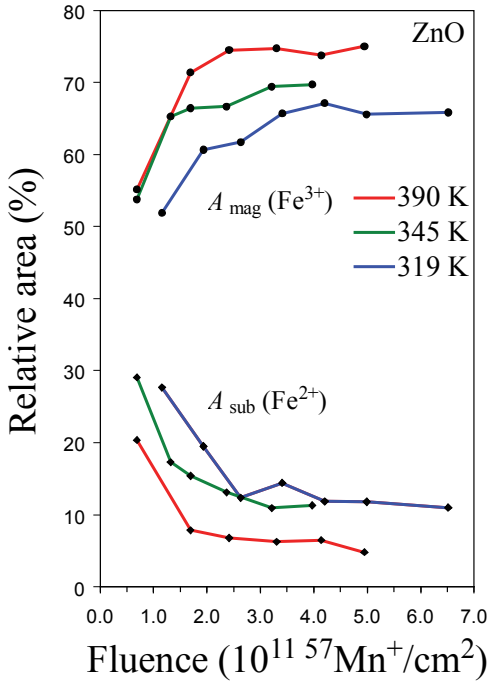

Figure 6.12: Relative area fractions of Fe^{3+} and Fe^{2+} in ZnO as a function of fluence at the three different temperatures indicated. A faster build-up of Fe^{3+} is observed at elevated temperatures [**Paper I**]. The variance is within ±2% of the relative area (not shown).

Measurements in an external magnetic field show that the paramagnetic substitutional Fe^{3+} component has a quadrupole interaction indistinguishable from the substitutional Fe^{2+} site (see section 6.1 and **Paper II**). In the case of Fe^{3+}-V_{Zn} pairing a different quadrupole interaction would be expected. The findings in **Paper II** resulted in a reinterpretation of the observed fluence dependence and turned back the attention on a Fermi level shift as the possible cause.

A more detailed measurement at room temperature of the relative areas of the ^{57}Fe Mössbauer components observed during ^{57}Mn ion-implantation is shown in Figure 6.13 supporting the fluence dependence in ZnO.

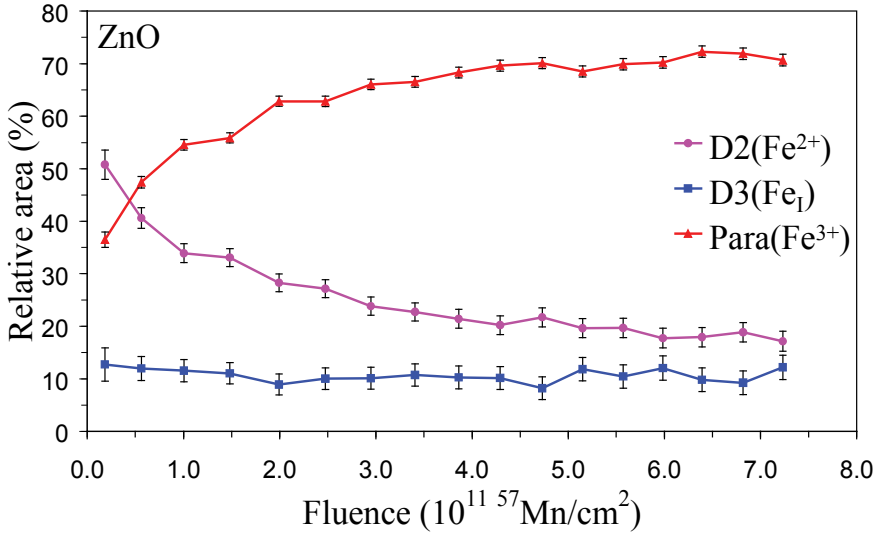

Figure 6.13: Detailed measurement of the Fe^{3+}/Fe^{2+} fluence dependence of ^{57}Mn ion-implanted ZnO at room temperature. Cleary an increased fluence results in a build-up of Fe^{3+} (Para component) on the expense of Fe^{2+} (D2 component). For Fe^{3+} a saturation level of ~70% is reached above ~3.0×10^{11} ^{57}Mn/cm^2 (see also Figure 6.12). Error bars shows a variance of 1σ.

A further study by Mantovan *et al.* [2012] gives more information and a better idea of the physical mechanism behind the fluence dependence. Figure 6.14 shows ^{57}Fe emission Mössbauer spectra of two single-crystal ZnO samples at room temperature under different fluence conditions (^{57}Mn and/or ^{23}Na implanted). The spectral areas of the components are shown in Figure 6.15 as a function of total ^{57}Mn/cm^2 fluence (for more details see Mantovan *et al.*, [2012]).

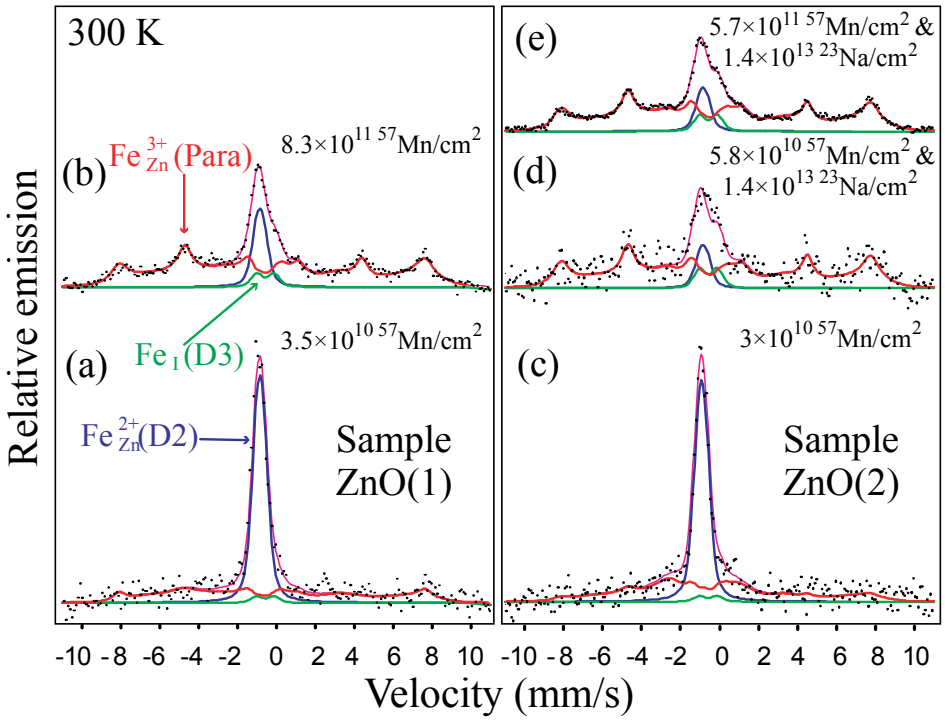

Figure 6.14: ^{57}Fe emission Mössbauer spectra (dots) obtained at room temperature in the two samples ZnO(1) [(a), (b)] and in ZnO(2) [(c), (d), (e)] after the ion-implantation of ^{57}Mn and ^{57}Mn & ^{23}Na respectively, to the indicated total fluences. See also Figure 6.15. [Mantovan *et al.*, 2012].

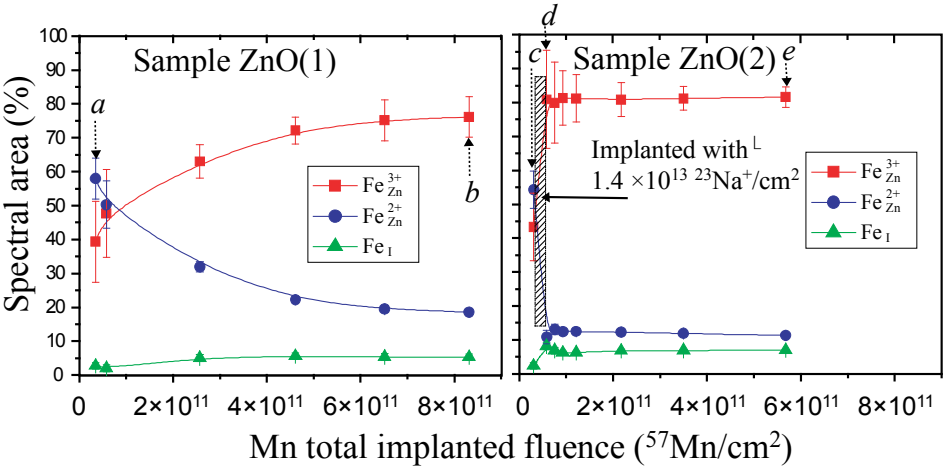

Figure 6.15: Fluence dependence of the components detected by ^{57}Fe emission Mössbauer spectroscopy in the two samples ZnO(1) and ZnO(2). Letters "*a*", "*b*", "*c*", "*d*", and "*e*" indicate the corresponding Mössbauer spectra presented in Figure 6.14 [Mantovan *et al.*, 2012]. The shaded area indicates implanted ^{23}Na. Error bars shows a variance of 1σ.

In the sample pre-implanted with a fluence of ~1.4×10^{13} ^{23}Na/cm^2 (ZnO(2)) followed by a low-fluence ^{57}Mn implantation, the paramagnetic Fe^{3+}_{Zn} fraction reaches a near saturation value of ~80%, as also observed for high ^{57}Mn fluences in sample ZnO(1) (see Figure 6.15 point (d) and (b)). Further ^{57}Mn implantation only improves the statistics in the spectrum in both samples.

The saturation level in ZnO(2) is achieved with about one order of magnitude lower ^{57}Mn fluence (point d) compared to the total ^{57}Mn fluence in ZnO(1) at point b, demonstrating that the combined fluence of both ^{57}Mn and ^{23}Na contribute to the build-up of the Fe^{3+} fraction in ZnO on the expense of Fe^{2+}. In light of the findings in [Mantovan *et al.*, 2012] the dependency of the fluence rate was further investigated.

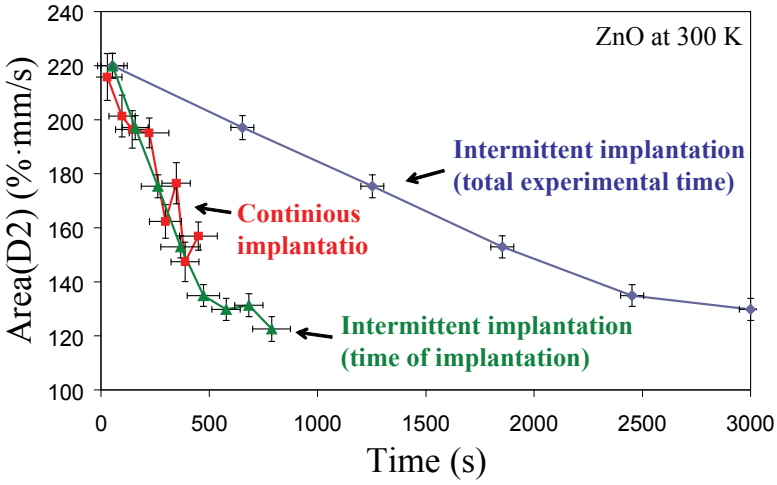

Figure 6.16: Relative area of the ZnO D2 component (Fe^{2+}) during continuous implantation and intermittent implantation (TDM) at room temperature. For comparison the D2 component area for the intermittent implantation is also plotted as would it have been a continuous implantation, skipping the periods of halted ion-implantation. Error bars shows a variance of 1σ of the relative area and the temporal error of the spectral average recording time.

Figure 6.16 show the absolute area of the spectral ^{57}Fe Mössbauer D2 (Fe^{2+}) component in ^{57}Mn ion-implanted ZnO under different fluence rate conditions. The D2 component is chosen as it is easier to model at low fluence (statistics) spectra, than the paramagnetic Fe^{3+} component. The intermittent implantation data used in Figure 6.16 are from time-delayed measurements (TDM) on ZnO. TDM spectra are obtained in three time intervals under and after implantation. The first interval was a 104.8 s of ^{57}Mn implantation and measurement of the

spectrum. Then the implantation was halted and two new spectra were recorded, the last after 538.1 s where only negligible ^{57}Mn decay was left in the sample (see Gunnlaugsson et al., [2009] for details). The data used here is the sum of all three spectra obtained after only 104.8 s of implantation resulting in a low fluence build-up as the TMD method is repeated eight times (blue points, not all points shown). By plotting the results from the TDM measurements as a function of only the implantation time (green points) they fall on top of the results obtained by a continues implantation (red points). This demonstrates that only the fluence determines the Fe^{2+} ratio, and not the time of the experiment. A time dependence would be expected if the 2+ to 3+ charge state conversion were due to the capture (pair creation) of a mobile charge compensating defect (e.g. V_{Zn}) diffusing between implantation cascades (~10's of nm) on the minute time-scale of the experiments. The absence of time dependence of the Fe^{3+}/Fe^{2+} ratio is in contradiction to pair formation due to mobile defects (within the time-scale of the experiment).

This means that the explanation for the faster transition from Fe^{2+} to Fe^{3+} at increasing temperatures (Figure 6.12) due to a temperature dependent diffusion of charge compensating defects [**Paper I**] must be too simple, and explanations in terms of a Fermi level shift have been adapted to the results of **Paper I**.

With the new measurements it seems that the Fermi level being affected by introduced defects through the implantation process is a more feasible explanation for the observed fluence dependence in ZnO. In the light of a similar fluence dependence observed in ^{23}Na pre-implanted ZnO [Mantovan *et al.*, 2012] the possible implantation-induced Fermi level change is not due to the specific chemical nature of the implanted species. Instead the decisive factor determining the Fe^{3+} fraction is the amount of implantation-induced defects. The implantation-induced change of the Fermi level could mainly be due to deep acceptor states created in the ZnO band-gap within the implantation-affected sample volume [Mantovan *et al.*, 2012]. Most likely the deep acceptor states are introduced by V_{Zn}, since they are stable at room temperature [Janotti and Walle, 2007], which shifts the Fermi level towards midgap. The single-crystal ZnO samples are n-type and the donor level of $Fe^{2+/3+}$ is located in the upper part of the bandgap [Dietl, 2002]. By lowering the Fermi level below the $Fe^{2+/3+}$ level an increased Fe^{3+}/Fe^{2+} ratio is observed. A possible model of the scenario is illustrated in Figure 6.17.

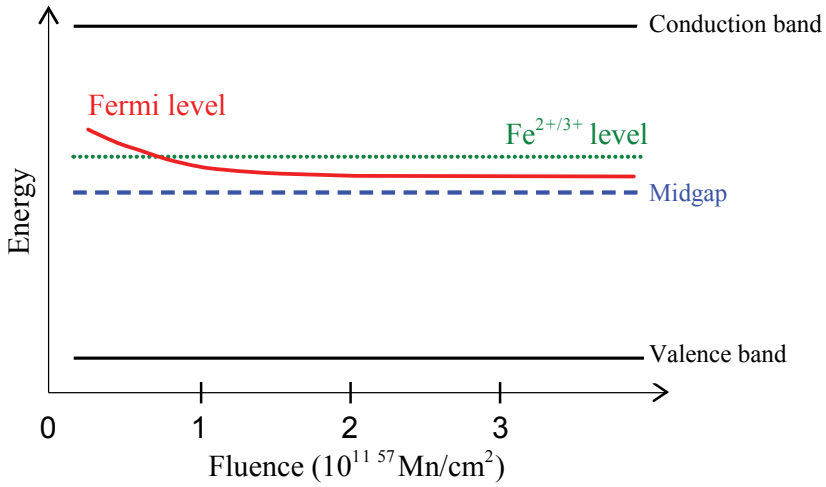

Figure 6.17: A possible model of the implantation-induced change of the Fermi level in the bandgap of ZnO upon increased fluence. A shift in the Fermi level towards midgap and below the $Fe^{2+/3+}$ level could be responsible for the increased Fe^{3+}/ Fe^{2+} ratio.

Also a shift of the Fermi level towards the $Fe^{2+/3+}$ level with elevated temperatures could explain the temperature dependent transition from Fe^{2+} to Fe^{3+} described in **Paper I**. This is schematically illustrated in Figure 6.18. With the Fermi level closer to the $Fe^{2+/3+}$ level at elevated temperatures the Fermi level shifts below the $Fe^{2+/3+}$ level at a lower fluence as observed in Figure 6.12.

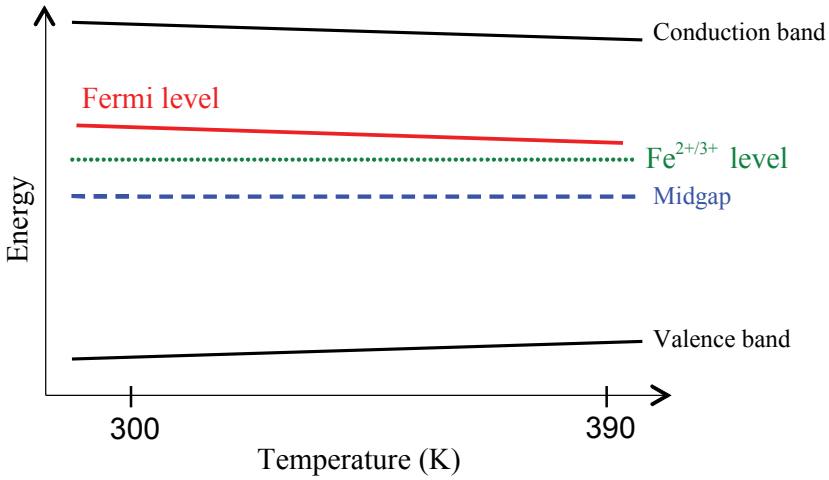

Figure 6.18: A possible model of the Fermi level in the band gap of ZnO shifting toward the $Fe^{2+/3+}$ level with increased temperature below a fluence of 2×10^{10} ^{57}Mn/cm^2. This could explain the faster transition from Fe^{2+} to Fe^{3+} at a lower fluence at elevated temperatures as observed in Figure 6.12.

It should be emphasised that the models proposed in Figure 6.17 and Figure 6.18 are not proven by our experimental data, but form a hypotheses to be tested in future experiments.

6.3.2 Damage in ^{57}Co ion-implanted ZnO

From the above results it seems that the ^{57}Fe Mössbauer spectra measured after implantation of ^{57}Mn into ZnO single-crystals, are well explained in terms of spectral lines originating from Fe_{Zn}^{2+}, Fe_{Zn}^{3+} showing slow paramagnetic relaxations, and interstitial Fe (see i.e. Figure 6.2 (a)). However, these spectra look different from spectra obtained by ^{57}Fe implanted ZnO [Potzger *et al.*, 2006 and 2007; Zhou *et al.*, 2007 and 2008] (see Figure 6.19).

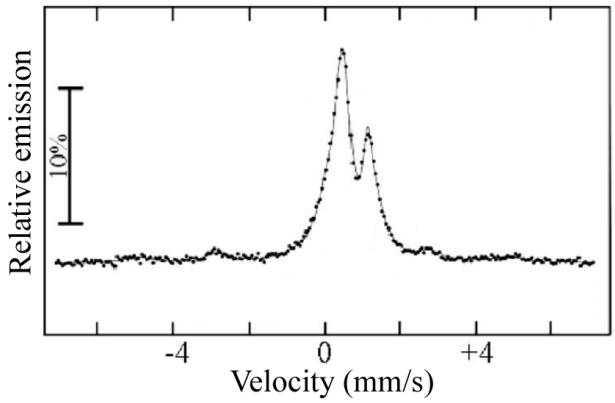

Figure 6.19: ^{57}Fe CEMS spectrum (dots) obtained at room temperature of single-crystal ZnO implanted at 623 K with 180 keV 4×10^{16} stable ^{57}Fe/cm^2 [Potzger *et al.,* 2006]. The spectrum has to be compared with e.g. Figure 6.2 (a). Note that the CEMS spectrum is on an inverse velocity scale compared with the emission ^{57}Fe Mössbauer spectra, that also have more broad lines.

This dissimilarity could indicate different lattice locations and/or electronic configurations of Fe after high fluence (>10^{14} cm^2) Fe implantations and low fluence (<10^{12} cm^2) Mn implantations into ZnO. See full discussion in **Paper VII**.

To further study and understand the properties of Fe in ZnO, off-line ^{57}Fe emission Mössbauer spectroscopy measurements of ^{57}Co/^{57}Fe ion-implanted ZnO were performed at different emission angles θ and temperatures [**Paper VII**]. Single-crystal ZnO was implanted with $(5–6)\times10^{12}$ ^{57}Co/cm^2 which is a higher fluence than that of the ^{57}Mn implanted samples (below 10^{12} ^{57}Mn/cm^2).

The beam also contained a significant contribution of stable ^{57}Fe impurities that had been estimated to (5–6)×10^{14} ^{57}Fe/cm^2 and gave a maximum concentration of ~0.04 at.%.

Mössbauer results obtained by ion-implantation of ^{57}Co/^{57}Fe(stable) into single crystalline ZnO are given in **Paper VII**. The off-line ^{57}Fe emission Mössbauer spectra obtained (from the decay of ^{57}Co) at room temperature under different emission angles θ are shown in Figure 6.20.

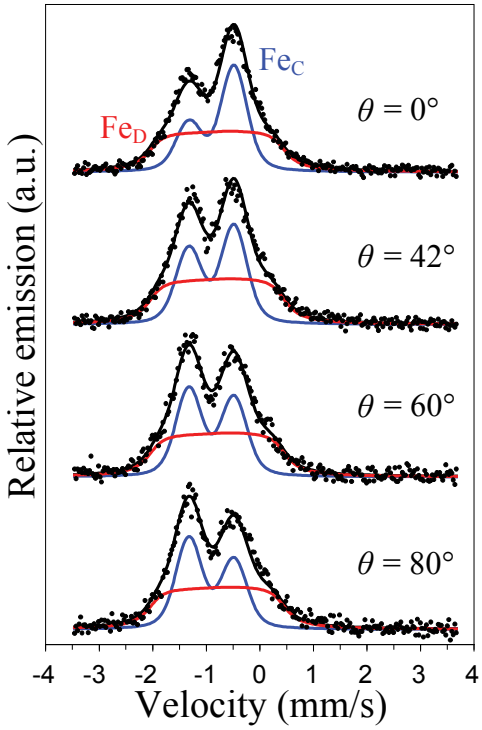

Figure 6.20: Room temperature off-line ^{57}Fe emission Mössbauer spectra (dots) of ^{57}Co/^{57}Fe(stable) ion-implanted ZnO (dots), measured at the indicated emission angles θ relative to the sample normal. The fitted components and their sum are shown. Fe_D is a damage and Fe_C a crystalline fraction.

The ^{57}Fe emission Mössbauer spectrum in Figure 6.20 at $\theta = 0°$ is consistent with the ^{57}Fe implanted CEMS spectra of Potzger *et al.* [2006] (Figure 6.19), but their approach of fitting components deviates from the angular dependence measured in this study. This shows the importance of measuring at different emission angles for identifying quadrupole split components in materials, especially in single-crystals.

The angular dependence of the spectra in Figure 6.20 can be analysed in terms of two contributions: (1) a crystalline fraction (Fe_C) assigned to Fe^{2+} on substitutional Zn sites showing angular dependence and has an isomer shift consistent with Fe^{2+}_{Zn} in ^{57}Mn implanted ZnO [**Paper II**] (2) a damage fraction (Fe_D) showing no angular dependence. Both of these fractions display a pronounced quadrupole splitting (see **Paper VII**). Due to the detailed angular measurements this study allowed the determination of the sign and value of $\Delta E_{Q,V}$ = -2.3(1) mm/s of Fe^{2+}_{Zn} used in Equation (6.1) [**Paper VI**], getting a complete picture of the substitutional site in ZnO.

The Fe_D component exhibiting no angular dependence is likely to originate from Co/Fe in a heavily damaged/amorphous environment due to the implantation process. Hence the local environment of the probe does no longer contain any information on the lattice orientation through the quadrupole interaction. In comparison, the ZnO spectra from implanted ^{57}Mn have much lower fluence which is likely why a component originating from damaged sites is not observed.

6.4 Properties of Fe in Mn/Fe implanted MgO

In this thesis MgO was applied as a model system for studying paramagnetism in oxides (see sections 6.1 and 6.2).

The physics of 3d-metal impurities in MgO is of interest in view of recent discoveries of dilute magnetism [Narayan *et al.*, 2008; Li *et al.*, 2009] and anomalous behaviour of impurities in this material [Lu et al., 2002; Weeks *et al.*, 1980]. Fe/MgO systems are also used for magnetic tunnel junctions in spintronic devices which are why diffusion studies are of interest. These motivations are described in **Paper VIII**. In MgO, anomalous diffusion of metal impurities has been reported by several authors. If a fast diffusion mechanism of Fe in MgO exists, this could evidently lead to the (unexpected) formation of Fe precipitates. This mechanism has to be taken into account, when interpreting data suggesting dilute magnetism in MgO or other systems. Figure 6.21 shows the ^{57}Fe emission spectra of the temperature series of ^{57}Mn ion-implanted MgO.

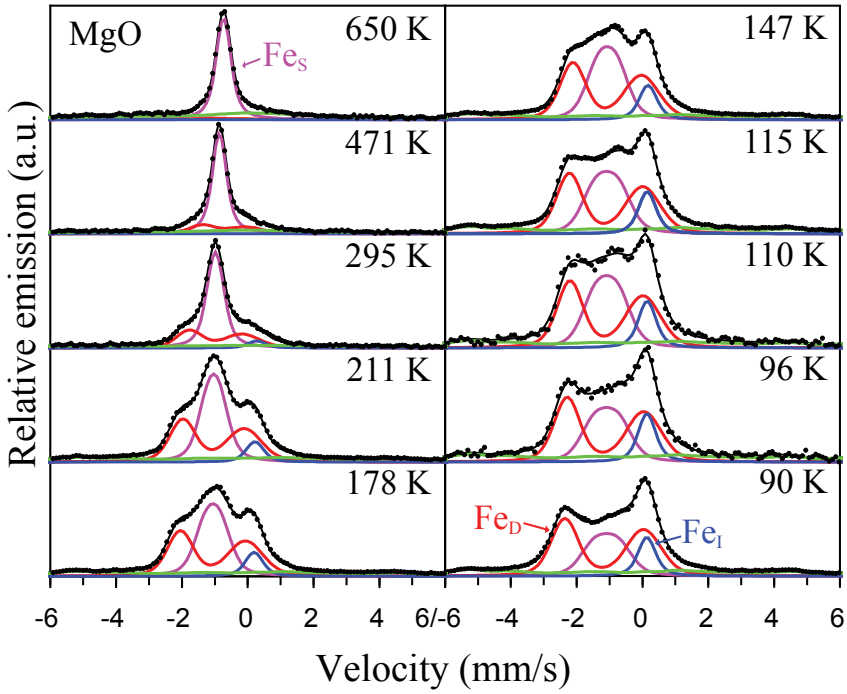

Figure 6.21: Central part of ^{57}Fe emission Mössbauer spectra (dots) of ^{57}Mn ion-implanted MgO at the indicated temperatures. The component assignments are described in the text. Wings of MgO are shown in details in Figure 6.6.

The spectrum obtained at the highest temperature is dominated by a single line with isomer shift $\delta \sim 1$ mm/s, assigned to substitutional high-spin Fe^{2+} substituting Mg. The vanishing broadening or quadrupole splitting at high temperatures is consistent with substitutional Fe on the cubic Mg site (Fe_S). At lower temperatures the line broadens, presumably due to interactions with implantation defects in the neighbourhood of the Fe probe atoms. At lower temperatures the crystal lattice is less flexible and needs a longer time to recrystallize after the disturbance caused by the implantation, and the substitutional site is found to deviate from cubic symmetry.

At the lowest temperature a peak appears at $v \sim -2.5$ mm/s and is still visible at 295 K, where it is the left shoulder of the dominating central peak. Such a high isomer shift ($\delta \sim 2.5$ mm/s) for a ^{57}Fe line is not possible (see Figure 3.4), indicating that this must be the left leg of a quadrupole split doublet component. Another peak with a higher intensity at $v \sim 0$ mm/s is observed. If it is the right leg of the quadrupole split component with the following values; $\Delta E_Q \sim 2.5$ mm/s and $\delta = 1.25$ mm/s (at 90 K). The considerable annealing of this

quadrupole split component at increased temperatures suggests that it is high-spin Fe^{2+} in implantation-related heavily damaged regions (Fe_D). The relative area of the Fe_D component reduces when the Fe_S begins to dominate as expected for a metastable damage component (see section 4.3).

This model could not fully describe the spectra. A single line at $v \sim 0.1$ mm/s at 90 K had to be introduced corresponding to an isomer shift of $\delta = -0.28(2)$ mm/s. The obvious interpretation of such a line would be to assign it to recoil produced (see section 4.3.3) interstitial Fe (Fe_I). This interpretation turned out to be more challenging as the analysis progressed.

To support this assignment A. Svane (Aarhus University, Denmark) performed quantum mechanical *ab initio* calculations of the isomer shifts for different lattice locations of an Fe atom in MgO. Details on these calculations are given in **Paper VIII**.

The isomer shift of Fe_I at the high-symmetry site with four Mg^{2+} and four O^{2-} neighbours with $\delta = +0.66$ mm/s was found. Although the absolute error in *ab initio* calculations can be as high as $\Delta\delta \sim 0.1$ mm/s (A. Svane and H. P. Gunnlaugsson, private communication 2009), the theoretical value did not agree with experimental findings. Calculations show that this site is not an energetically favourable position, and an energetically more favourable position was found close to the face of the MgO cube as illustrated in Figure 6.22.

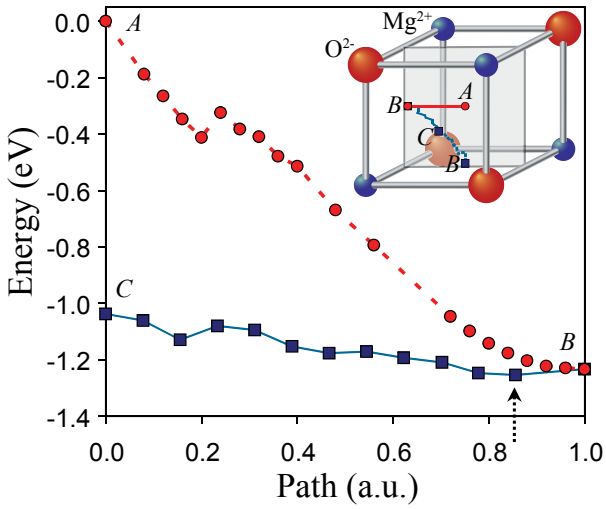

Figure 6.22: Energy of the interstitial Fe atom calculated along the paths indicated in the insert figure showing the (004) plane within the unit cell. *A* indicates the interstitial site at the cube centre, *B* the interstitial site at the centre of the cube face. *C* is halfway on the path from one face side to the next. Arrow indicates a possible energy minimum on the *C* to *B* path.

The interstitial site on the face (site *B*) has a calculated isomer shift of δ = -0.33 mm/s which is in a better agreement with the experimental value and more energetically favourable [**Paper VIII**]. An Fe probe located at this interstitial site would be expected to give rise to a sizeable quadrupole splitting of the Fe_I line due to a non-zero electrical field gradient (*EFG*) at this location which is not cubic. However, this is not observed in the simultaneous analysis of the experimental measurements. Replacing the Fe_I single line with a quadrupole doublet component in the simultaneous analysis does not give a convincing simulation of the temperature series Figure 6.21.

A possible explanation of the missing quadrupole splitting might arise from a careful study of the energy landscape around point *B* (~ ±0.2 Å) in Figure 6.22. The energy minimum is found to be very flat, with a possible minimum at ~0.17 of the distance from the ideal face site (point *B*) towards *C* (~0.25 Å from *B*) as indicated by the arrow in Figure 6.22. This interpretation of the theoretical calculations could suggest jumps of the interstitial Fe in a cage around site *B* at specific equivalent locations, a process often called "localised diffusion in an interstitial cage" [Petry and Vogl, 1982]. The barrier for such a cage motion seems to be low ~0.05 eV (presumably less than the accuracy of the calculations) which would result in fast jumps between different cage positions at $T > 50$ K. The interstitial Fe would be expected to jump through the face to another favourable position without long-range diffusion. A fast cage motion compared to the lifetime of the Mössbauer state can result in a vanishing quadrupole splitting [Tjon and Blume, 1968], and reduce the intensity of the Fe_I line [Petry and Vogl, 1982].

Another interesting result of the calculations is that the barrier for long-range diffusion (jumps from site *B* through *C* to a similar site *B*) is only ~0.2 eV. Such a low barrier could give rise to a long-range jump mechanism which would expect to result in a Lorentzian broadening of the interstitial Fe single line in the Mössbauer spectra, as described in section 3.3. In order to address a possible long-range diffusion of Fe_I a new analysis of the MgO spectra in Figure 6.21 was made.

The Lorentzian broadening of the interstitial line Fe_I for the re-analysed temperature series is shown in Figure 6.23. This analysis gives lower χ^2 values of the simulation (see section 3.9), and also allows the isomer shift of Fe_D to follow the second order Doppler shift throughout the temperature series. Above 260 K the interstitial line is too broad for the simulation to fit the broadening, but

the re-analysis is consistent with increased broadening throughout the whole temperature series.

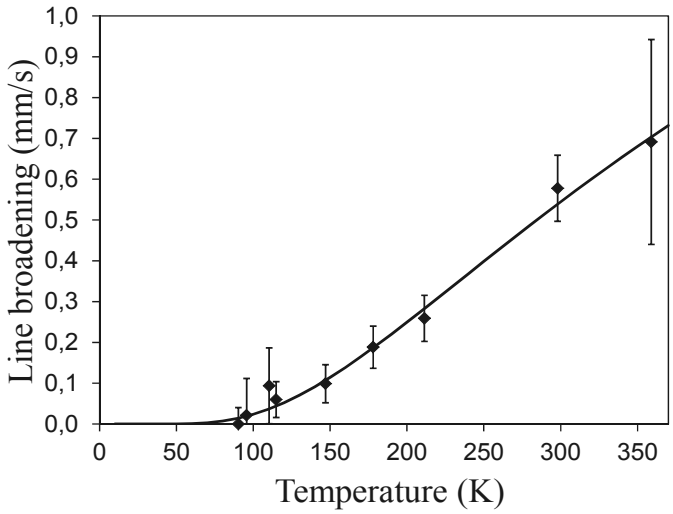

Figure 6.23: A Lorentzian broadening of the interstitial single line (Fe_I) as a function of temperature. The solid line is to guide the eye. Higher temperatures are not shown, see text. Presented in [**Paper VIII**]. Error bars shows a variance of 1σ.

The suggested long-range diffusion resulting in a Lorentzian broadening at room temperature of $\Delta\Gamma \sim 0.5$ mm/s, is consistent with a few jumps (0.5–2 jumps) of the Fe_I probe atoms during the lifetime of the Mössbauer state. Using Equation (3.7) for jumps to adjunct sides of the rock salt MgO structure gives a diffusion coefficient of $D \sim 7(2)\times10^{-10}$ cm^2/s at $T = 300$ K. This broadening is orders of magnitude higher than suggested for vacancy-assisted Fe diffusion in MgO [**Paper VIII**]. Such a fast diffusion could lead to unintentional precipitation of Fe impurities.

6.5 Properties of Fe in Mn/Fe implanted α-Al_2O_3

α-Al_2O_3 has been applied as a model system for studying paramagnetism in oxides (see sections 6.1 and 6.2). Mössbauer spectroscopy of Fe impurities in α-Al_2O_3 has been of interest for the last four decades with some of the pioneering Mössbauer work on slow paramagnetic relaxations of Fe^{3+} impurities being performed in this material (see discussion in **Paper IV**).

Our first Mössbauer results obtained by ion-implantation of ^{57}Mn into single-crystal α-Al_2O_3 are given in **Paper IV**. The ^{57}Fe emission Mössbauer spectrum

from the temperatures series (110–666 K) measured at 403 K is shown in Figure 6.24.

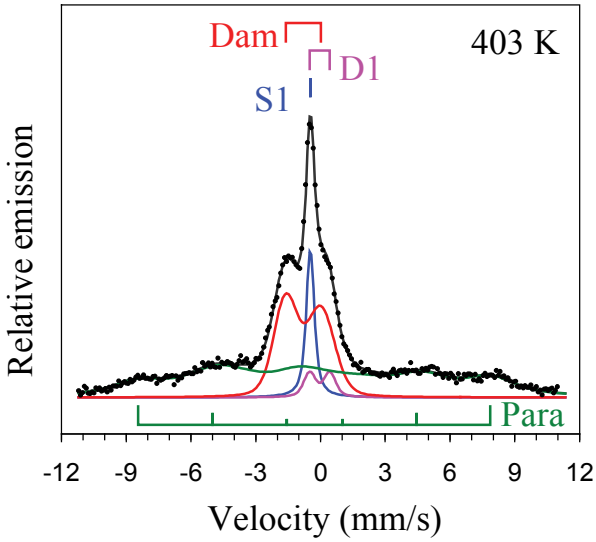

Figure 6.24: ^{57}Fe emission Mössbauer spectrum (dots) of α-Al_2O_3 after ^{57}Mn ion-implantation at 403 K. The spectrum has been analysed with the four components indicated by bars.

The spectra are analysed in terms of four components as indicated in Figure 6.24. Para, assigned to Fe^{3+} showing slow paramagnetic relaxation analysed with the EmpBT (see section 6.2). Dam, assigned to high-spin Fe^{2+} in amorphous environments. S1 tentatively assigned to Fe in cubic η-Al_2O_3 precipitates, and D1 tentatively assigned to Fe^{4+} (only observed in the spectra >300 K). The arguments behind these assignments are given in **Paper IV** together with temperature series and spectral areas. Relaxation rates extracted in this study of Fe^{3+} by applying the EmpBT were used in Figure 6.8 and **Paper VI**. Three BT-sextets were used for the EmpBT model of paramagnetic Fe^{3+}, and the intrinsic line-width was determined to be $\Gamma = 1.8(1)$ mm/s (at room temperature), suggesting that the Fe^{3+} sites are not perfect substitutional sites, but associated with implantation damage causing broadening.

α-Al_2O_3 spectra measured in an applied external magnetic field are presented in **Paper V** and in section 6.1. There it was demonstrated that performing the analysis in terms of three BT-sextets with $B_{hf} \propto S_Z$ support paramagnetic origin.

Since the publication of **Paper IV** the nature of the S1 line has been revisited, due to an additional angular dependent ^{57}Fe emission Mössbauer measurements

of both ^{57}Mn and ^{57}Co/^{57}Fe(stable) ion-implanted α-Al_2O_3 samples. Figure 6.25 shows the angular dependence of the ^{57}Co/^{57}Fe(stable) implanted α-Al_2O_3.

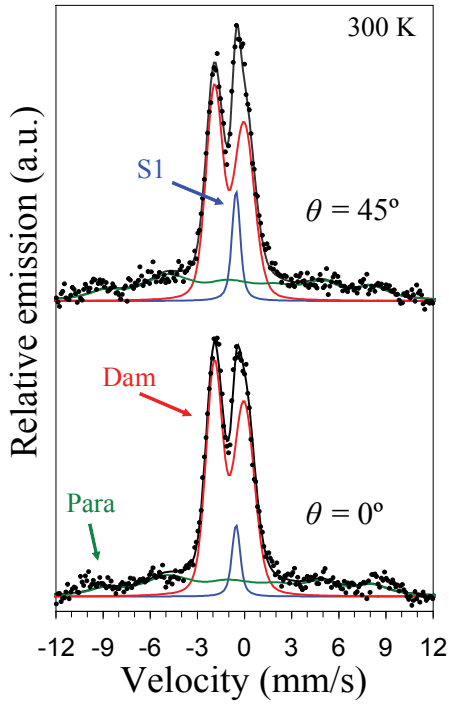

Figure 6.26: ^{57}Fe emission Mössbauer spectra (dots) of α-Al_2O_3 after ^{57}Co/^{57}Fe(stable) ion-implantation at 300 K [Gunnlaugsson *et al.*, 2012a].

The additional measurements in Figure 6.26 shows that the intensity of S1 exhibits an angular dependence [Gunnlaugsson *et al.*, 2012a] which is incompatible with a component originating from Fe in cubic η-Al_2O_3 nano-precipitates as is suggested in **Paper IV**.

With the new angular dependence measurements other explanations have to be sought for the tentatively assigned components. Angular dependence can be caused both by cage jumping of interstitial Fe and an angular dependent Debye-Waller factor [Gunnlaugsson *et al.*, 2012a]. The latter suggestion does not explain the missing quadrupole interaction which is expected for interstitial Fe in the α-Al_2O_3 lattice. Therefore the idea in terms of cage jumping was favoured [Gunnlaugsson *et al.*, 2012a]. This supports the conclusions given in **Paper VIII** suggesting that cage jumping of interstitial Fe created by ^{57}Mn ion-implantation of oxides might be common.

6.6 Contribution of the author

The experimental findings presented in this thesis have been obtained in collaboration with the "Mössbauer collaboration at ISOLDE/CERN" making use of the radioactive beams produced at the ISOLDE facility at CERN for solid state physics research by Mössbauer spectroscopy (the collaboration name was updated from "The ^{57}Mn collaboration at ISOLDE/CERN" after the successful usage of both ^{57}Co and ^{119}In beams). During this PhD work, 14 members have been involved in the collaboration, each with their own areas of expertise and interests. Usually several different systems are investigated during each beam time, and it is impossible to be involved in all sub-projects, but the spectral analyses often have common features. Hence, the collaboration benefits from exchanging ideas and expertise.

I was assigned and responsible to the tasks of recording Mössbauer data relevant for this thesis. I also developed two new sample holders for not previously performed on-line ^{57}Fe emission Mössbauer measurements.

6.6.1 Contribution to the included papers

Paper I
I was responsible for analysing the spectra and performed a part of the interpretations. Responsible for writing the manuscript of the paper.

Paper II
I was responsible for the experimental development, analysed the spectra and performed a part of the interpretations. Contributed to writing the manuscript.

Paper III
I was responsible for developing a method of analysing the spectra and performed a part of the interpretations. Responsible for writing the manuscript.

Paper IV
I assisted the analysis and interpretations of the spectra. Contributed to writing the manuscript.

Paper V

I contributed with previous findings and results together with a new spectral analysis and interpretation. Contributed to writing the manuscript.

Paper VI

I was responsible for analysing the spectra and performed a part of the interpretations. Responsible for the manuscript and writing of the paper.

Paper VII

I assisted in the analysis and interpretation of the spectra. Contributed to the manuscript.

Paper VIII

I was responsible for analysing the spectra and performed a part of the interpretation. Responsible for the manuscript. The submission has been delayed until after the delivery of this thesis.

Chapter 7

Conclusions

^{57}Fe emission Mössbauer spectroscopy was performed on ^{57}Mn ion-implanted (<10^{-3} at.%) into single-crystal ZnO, MgO, and α-Al_2O_3 samples, with special emphasis in ZnO. The two other oxides were studied for comparison, and also these gave rise to interesting physics. Additional ^{57}Co/^{57}Fe(stable) ion-implantation (<0.17 at.%) for off-line measurements were performed for further investigation of the oxides.

Paramagnetism

In all three Fe/Mn implanted oxides the dilute Fe^{3+} impurities were found in a paramagnetic state exhibiting slow spin relaxation rates of $1/\tau < 1\times10^{8}\,s^{-1}$ at room temperature. This result shows that Fe^{3+} is unlikely to act as the seed needed for the proposed long-range ordered (ferro-)magnetism. From the work presented here, it is not possible to claim that Fe^{3+} couples to structural defects to give static spins.

An empirical model based on the Blume-Tjon line-shape for relaxing Fe^{3+} (EmpBT) was developed for the extraction of information on the spin-lattice relaxation rates of Fe^{3+} in Mössbauer spectra obtained without external magnetic field. This model was applied for the three oxides with the interesting result that ZnO showed an unexpected behaviour by not following the expected T^2 temperature dependence like the other two oxides, but instead exhibited a T^9 temperature dependence at $T > \theta_D/3$.

ZnO

The charge state of Fe in ZnO was found to depend on the implantation ^{57}Mn fluence ($<10^{12}$ cm^{-2}), and this was interpreted as due to an Fe state in the band-gap and a fluence dependent Fermi level.

Higher doses ($>10^{14}$ cm^{-2}) reveal a portion of the Fe being located in an implantation damaged amorphous environment and a possible clustering of Fe with annealing at increased temperature. Identification of this spectral component as originating from damaged sites was used to explain the apparent discrepancy between emission Mössbauer spectroscopy results and existing literature Mössbauer data.

MgO

The EmpBT model was found to give spin relaxation rates of Fe^{3+} consistent with literature data. A single line was suggested to originate from interstitial Fe located close to the face centred site in MgO, exhibiting a possible cage motion. Long-range diffusion of interstitial Fe was proposed, with diffusivity orders of magnitude higher than expected for vacancy assisted diffusion of Fe in MgO.

α-Al_2O_3

Spin-lattice relaxations of Fe^{3+} in single-crystal α-Al_2O_3 samples was found to follow the expected T^2 temperature dependence at $T > \theta_D/3$. Additional angular dependence measurements indicated that a single line observed in the spectra originates from interstitial Fe exhibiting fast cage motion.

7.1 Outlook

Although not directly a part of this thesis, some of the consequences of this work should be mentioned for completeness. The EmpBT model has now become a standard tool for analysing spectral features due to Fe^{3+} in dilute samples showing slow spin-lattice relaxations and measured without external magnetic field. Future applications of this model include TiO_2 [Gunnlaugsson *et al.*, manuscript in preparation], and GaN [Masenda *et al.*, Manuscript in preparation]. Other applications are being considered for existing datasets (SiO_2, $SrTiO_3$, ALD ZnO, and Fe pre-implanted ZnO (H. P. Gunnlaugsson, private communication 2012). I will be involved in the analysis of the Mössbauer data on ALD ZnO and $SrTiO_3$.

The identification of the Mössbauer spectrum of Fe on implantation created damaged sites in ZnO, has allowed for a meaningful analysis of spectra obtained from ZnO pre-implanted with ^{56}Fe. Much of the measurements were recorded in 2006 and 2007, but have never been fully understood (H. P. Gunnlaugsson, private communication 2012). With the EmpBT model and the line-shape due to Fe in amorphous regions it is possible to analyse these spectra in a consistent way [Mantovan *et al.*, manuscript in preparation].

In at least two oxides (single-crystal MgO and α-Al_2O_3), evidence of interstitial cage motion has been presented. This suggests that it might be a more common effect than previously believed and possibly has to be taken into account in future analysis.

Utilising the ^{57}Mn beam gives a unique method of creating interstitial Fe due to the recoil of the β^- decay. As more measurements on different oxides are collected it could be of interest for future work to study the possible correlation between the displacement energy of the host metal site and the interstitial Fe fraction (Fe_I) in the oxide created by the recoil. First look of this work in progress is provided in Figure 7.1 (based on unpublished and presented data (displacement energies from literature)).

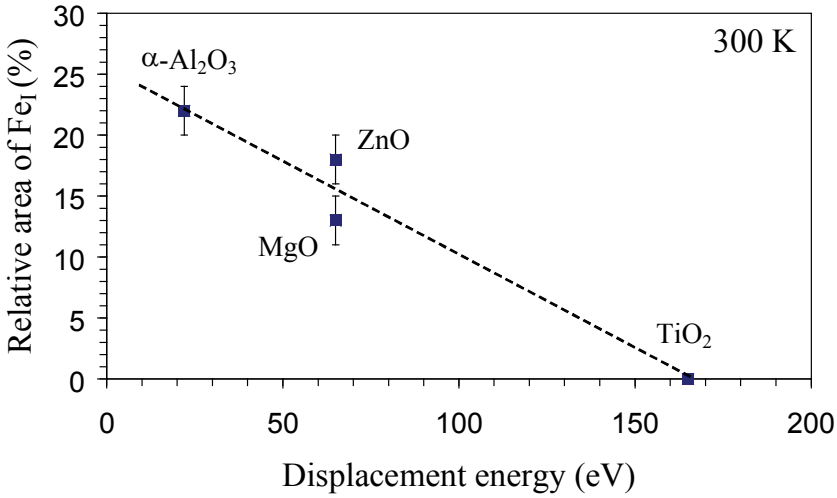

Figure 7.1: Plot of the relative area of the fraction of interstitial Fe at room temperature versus the displacement energy of the metal host site in the indicated oxides. Line is provided to guide the eye.

The latest reports on observed dilute magnetism due to structural defects now turns our focus to study samples which are not single-crystalline, but contain a relatively large amount of grain boundaries. This will ensure that a larger fraction of the dilute implanted ^{57}Fe probes end up at the crystal defects after ^{57}Mn implantation. With the analysis and findings of the single-crystalline sample, it will simplify the analysis of the corresponding poly-crystalline sample.

8 Included papers

Paper I: *Temperature and dose dependence of defect complex formation with ion-implanted Mn/Fe in ZnO*
Physica B **404**, 4820-4822 (2009).

Paper II: *Paramagnetism in Mn/Fe implanted ZnO*
Applied Physics Letters **97**, 142501(3pp) (2010).

Paper III: *Observation of spin-lattice relaxations of dilute Fe^{3+} in MgO by Mössbauer spectroscopy*
Hyperfine Interactions **197**, 89–94 (2010).

Paper IV: *Mössbauer spectroscopy of ^{57}Fe in α-Al_2O_3 following implantation of ^{57}Mn**
Hyperfine Interactions **198**, 5–13 (2010).

Paper V: *Magnetism in iron implanted oxides: a status report*
Hyperfine Interactions **197**, 43–52 (2010).

Paper VI: *Spin-lattice relaxations of paramagnetic Fe^{3+} in ZnO*
Physica Scripta **T148**, 014006(4pp) (2012).

Paper VII: *Lattice locations and properties of Fe in Co/Fe co-implanted ZnO*
Applied Physics Letters **100**, 042109(4pp) (2012).

Paper VIII: *Lattice Location and Diffusion of Interstitial Fe in MgO*
Manuscript in preparation (Nov. 2012)

Paper I

Temperature and dose dependence of defect complex formation with ion-implanted Mn/Fe in ZnO

Mølholt, T. E., Mantovan, R., Gunnlaugsson, H. P., Bharuth-Ram, K., Fanciulli, M., Gíslason, H. P., Johnston, K., Kobayashi, Y., Langouche, G., Masenda, G., Naidoo, D., Ólafsson, S., Sielemann, R., and Weyer, G.:

*Physica B: Physics of Condensed Matter, Volume **404**,*
Issue 23-24, p. 4820-4822 (2009).

DOI: 10.1016/j.physb.2009.08.187

Physica B 404 (2009) 4820–4822

Contents lists available at ScienceDirect

Physica B

journal homepage: www.elsevier.com/locate/physb

Temperature and dose dependence of defect complex formation with ion implanted Mn/Fe in ZnO

T.E. Mølholt [a], R. Mantovan [b], H.P. Gunnlaugsson [c], K. Bharuth-Ram [d,*], M. Fanciulli [b,e], H.P. Gíslason [a], K. Johnston [f], Y. Kobayashi [g], G. Langouche [h], H. Masenda [i], D. Naidoo [i], S. Ólafsson [a], R. Sielemann [j], G. Weyer [c]

[a] Science Institute, University of Iceland, Dunhaga 3, IS-107 Reykjavík, Iceland
[b] Laboratorio Nazionale MDM CNR-INFM, 20041 Agrate Brianza (MI), Italy
[c] Department of Physics and Astronomy, Aarhus University, Ny Munkegade 120, DK-8000 Åarhus C, Denmark
[d] iThemba LABS, P.O. Box 722, Somerset West 7129, South Africa
[e] Dipartimento di Scienza dei Materiali, Università di Milano Bicocca, Milano, Italy
[f] EP Division, CERN, CH-1211 Geneva 23, Switzerland
[g] The Institute of Physical and Chemical Research (RIKEN), Wako, Saitama 351-0198, Japan
[h] Instituut voor Kern-en Stralingsfysika, University of Leuven, B-3001 Leuven, Belgium
[i] School of Physics, University of the Witwatersrand, WITS 2050, South Africa
[j] Helmholtz Forschungszentrum, D-14109 Berlin, Germany

ARTICLE INFO

Keywords:
ZnO
Mössbauer spectroscopy
Mn and Fe ion implantation
Defect complexes

ABSTRACT

^{57}Fe Mössbauer spectroscopy following ion implantation of radioactive ^{57}Mn^{+} ($T_{1/2} = 85.4$ s) has been applied to study the formation of Fe/Mn implantation-induced defects in ZnO at temperatures between 319 and 390 K. The formation of ferric iron–vacancy complexes is found to depend strongly on the implanted dose and to be faster and more efficient at higher temperatures. The results at these temperatures suggest the mobility of the Zn vacancy, together with vacancy trapping at the substitutional Mn/Fe impurities are responsible for the formation of Fe–V_{Zn} complexes.

1. Introduction

Diluted magnetic semiconductors are important for their possible use in spintronics. Room-temperature ferromagnetism has been predicted for transition-metal doped ZnO [1,2] and observed experimentally (see e.g. [3]). There is, however, not a general consensus on the microscopic origin of the magnetism in ZnO. Recent papers have suggested that zinc vacancies play an important role in the occurrence of magnetism in different (in principle nonmagnetic) oxides [2,4–7].

In this contribution we present results of temperature- and dose dependent ^{57}Fe Mössbauer spectroscopy on ZnO following the implantation of radioactive ^{57}Mn^{+} ions. Mössbauer spectroscopy is a powerful experimental method for investigating iron impurities in solids, giving information on the local electronic structure of the probe Mössbauer atoms.

Weyer et al. [7] reported Mössbauer spectra obtained after implantation of ^{57}Mn^{+} into ZnO. They concluded that a magnetically split sextet seen in the spectra originated from Fe_{Zn}-V_{Zn} defect complexes. Mantovan et al. [8] showed that the area fraction of the formed sextet increased during implantation, illustrating that the lattice defects created in the implantation process played a key role. Here we report on the dose dependence of the formation of magnetically split components at different temperatures.

2. Experimental

Radioactive beam of ^{57}Mn^{+} ($T_{1/2} = 85.4$ s) is produced at the ISOLDE facility at CERN by 1.4 GeV proton-induced fission in a heated UC_2 target. After elemental selective laser ionization, acceleration to 60 keV and magnetic mass separation, a pure beam of $\sim 1.9 \times 10^8$ ^{57}Mn^{+}/s is produced. Using a beam spot area equal to 0.3 cm^2 this corresponds to $\sim 6.2 \times 10^8$ ^{57}Mn^{+}/(cm^2 s). The ^{57}Mn^{+} was implanted into single-crystal samples of ZnO (Crystec GmbH) held at temperatures of 319–390 K up to a maximum dose of 10^{12} ions/cm^2. The implantation of the sample was performed at an incident angle of 30° relative to the sample surface normal.

The ^{57}Mn ions decay to the 14.41 keV Mössbauer state of ^{57*}Fe ($T_{1/2} = 98$ ns). Mössbauer spectra were measured on-line with an acetone gas-filled resonance detector equipped with ^{57}Fe enriched stainless steel electrodes. The detector was mounted outside the

* Corresponding author.
E-mail address: kbr@tlabs.ac.za (K. Bharuth-Ram).

0921-4526/$ - see front matter © 2009 Elsevier B.V. All rights reserved.
doi:10.1016/j.physb.2009.08.187

implantation chamber on a conventional constant-acceleration drive system at 90° to the beam direction, which is 60° relative to the crystal surface normal. Velocities are given relative to the centre of the spectrum of α-Fe at room temperature.

The experimental data presented here were measured in a so-called time-delay-mode [9]. The samples were implanted for 114 s, and the spectrum was recorded from the start of the implantation continuously up to ~10 min, when most of the implanted ^{57}Mn had decayed. This process was repeated several times right after the spectrum was stored, in order to collect data at different doses and investigate the dose dependence.

In this type of experiment it is difficult to obtain a good measure of the implanted $^{57}Mn^{+}$ dose, due to the fluctuating beam intensity. Instead of making use of rather inaccurate yield estimates, we made use of the resonance area obtained in the Mössbauer spectra. This may result in an uncertainty up to 30% in the absolute dose, but relative doses between the different measurements are more accurate.

3. Results

Fig. 1 shows representative Mössbauer spectra obtained at 345 K. The spectra were analysed with the same set of spectral components as well as their isomer shifts and line widths determined in our earlier work [7–9] where each spectrum was collected for longer times and had much better statistics than in the time-dependent measurements presented here. The components include a single line (D2) dominating the spectrum obtained at the lowest dose, assigned to substitutional iron on zinc site (Fe_{Zn}), a six line (sextet) component that increases in intensity with increased dose assigned to Fe_{Zn}–V_{Zn} defect complexes, and a doublet (D3) that has a roughly constant area fraction. In addition, the spectra contain two magnetic hyperfine distributions (Dist. III and Dist. II), respectively, assigned to ferric iron associated with more than one Zn-vacancy and interstitial Fe [7].

The dose dependence was tracked by monitoring the sum of the fitted Mössbauer spectral component areas, which can be sorted into the following fractions: magnetic ($A_{Mag} = A_{Sextet} + A_{Dist.\ III}$), substitutional ($A_{Sub} = A_{D2}$) and interstitial ($A_{Int.} = A_{Dist.II} + A_{D3}$). The dose dependence of these three fractions is shown as an example in Fig. 2 for the data obtained at 345 K. The interstitial fraction is roughly constant as expected for a recoil-produced fraction; an average recoil energy of $\langle E_R \rangle = 40$ eV expels only a fraction of about 20% of the daughter ^{57}Fe atom from substitutional sites.

To further analyse the dose dependence, we assume the following behaviour of spectral fractions with dose, d:

$$A_{Int} = \text{constant}$$

$$A_{Mag} = A_0 + (A_{sat} - A_0)[1 - \exp(-d/d_0)]$$

$$A_{sub} = 100 - A_{Int} - A_{Mag}$$

where d is the dose measured in units of $^{57}Mn^{+}/cm^2$ and d_0 is a fitting parameter describing how quickly a saturation level is reached. A_0 describes the amount of vacancy-related defects formed directly in the implantation ($A_0 = A_{Mag}(d = 0)$), and A_{Sat} describes the saturation level of the A_{Mag} fraction, where $A_{Sat} = A_{Mag}$ when $d \to \infty$. The proposed model fits well with the experimental data (Fig. 2), and the results obtained are listed in Table 1 for the conditions described above.

The d_0 and the saturation level A_{Sat} show a clear temperature dependence, indicating that the kinetics is temperature dependent. A_0 is not well determined in these experiments; partly due to the fact that a 114 s implantation has already resulted in the A_{Mag} fraction curves approaching saturation level at these temperatures. In similar experiments with implantation performed at room-temperature Mantovan et al. [8] find A_0 ~25% in accordance with the A_0 values obtained here at higher temperatures.

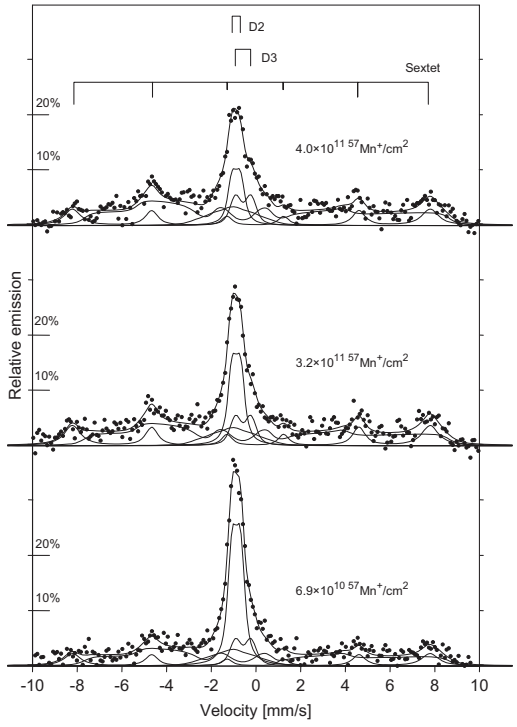

Fig. 1. Mössbauer spectra obtained at 345 K at the implanted $^{57}Mn^{+}/cm^2$ doses indicated. The bar diagram shows the individual fitting components (Distributions II and III are not indicated).

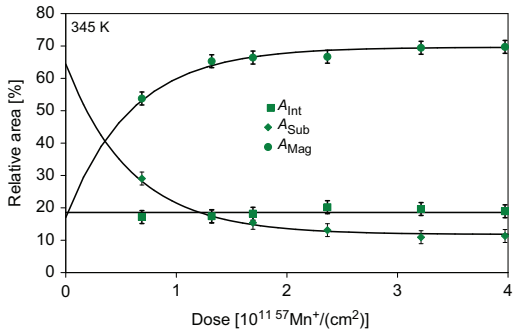

Fig. 2. Area fractions as a function of dose at 345 K. The solid lines represent a fit to the model described in the text.

Table 1
Summary of the fitted data obtained in this study.

T (K)	d_0 (10^{11} $^{57}Mn^+/cm^2$)	A_{Int} (%)	A_{Sat} (%)	A_0 (%)
319	0.94(17)	21.8(5)	66.6(8)	14(12)
345	0.59(8)	18.6(4)	69.6(6)	17(9)
390	0.53(12)	20.5(5)	74.2(7)	12(18)

4. Discussion

Results from emission channelling experiments from Rita et al. [10], in which ^{59}Mn ($T_{1/2} = 4.6$ s) were implanted into ZnO at 60 keV, are relevant to this discussion. The ^{59}Mn decays to ^{59}Fe ($T_{1/2} = 44.6$d) giving the Fe atom an average recoil energy of about 200 eV, which is sufficient to re-implant the ^{59}Fe atoms away from their initial lattice location. The β^- emission from ^{59}Fe is monitored relative to a specific crystal axis to deduce the lattice position of the ^{59}Fe atoms. Rita et al. found 95% of the Fe atoms to occupy the ideal substitutional Zn sites (Fe_{Zn}).

As Fe and Mn are both 3d-metals and expected to behave similarly in ZnO we propose that ^{57}Mn is also implanted into substitutional sites. This is also evident from the spectrum obtained at the lowest dose, which is dominated by the D2 fraction. This furthermore means that the Mn atom has only a minor chance of capturing a vacancy created in its own implantation cascade. This is illustrated by the A_0 parameter, which represents the fraction formed at the (extrapolated) lowest implantation dose. As already mentioned this parameter is not well determined in our experiments and no correlation with temperature is observed.

The increased vacancy related fraction (A_{Mag}) must therefore occur as a consequence of the increased defect concentration in the sample with implantation. In the implantation event an order of ~1000 vacancies are created for each implanted ^{57}Mn atom, but most of these recombine with interstitials well within the ^{57}Mn lifetime. Any model of the kinetics has to assume that only <10 vacancies survive uncompensated at temperatures where the created interstitials are highly mobile.

The A_{Mag} fraction approaches saturation in our measurements at an implanted dose of $\sim(1–2)\times10^{11}$ $^{57}Mn^+/cm^2$. Taking into consideration the implantation profile (TRIM calculations), this should correspond to vacancy concentration of the order of $\sim(2–20)\times10^{16}\,cm^{-3}$. For an Fe atom randomly placed after implantation, it would mean that the average distance to a nearest vacancy is of the order of ~25 nm. This is still far from being close enough to form a Fe_{Zn}–V_{Zn} pair, and we must therefore propose that the diffusivity of the vacancy during the lifetime of the ^{57}Mn atom is sufficient to cover this distance. This would require the vacancy diffusion coefficient to be larger than $\sim10^{-13}\,cm^2/s$ at these temperatures, which would hardly be regarded as macroscopic diffusion, since in 30 min annealing, the diffusion length would still be too small.

An alternative explanation could be that the implantation leads to changes in the Fermi level because of creation of defects, and that the area fractions of the ferric sites (A_{Mag}) simply reflect the position of the Fermi level. However, in this case strong temperature dependence seems unlikely in the relative small temperature range of these experiments, while it would be expected if mobile vacancies played a role, as increased mobility of the vacancy at elevated temperatures, increase the probability of forming Mn_{Zn}–V_{Zn} complexes.

Mössbauer experiments do not observe directly the V_{Zn} behaviour in ZnO. However, the comparison of our data with other experimental evidence reported in literature suggests that the V_{Zn} is the most likely candidate for being responsible for the magnetic fraction observed with Mössbauer spectroscopy in Mn/Fe-implanted ZnO. In particular Tuomisto et al. [11] used positron annihilation spectroscopy to study the introduction and recovery of point defects in electron-irradiated n-type ZnO. They found V_O to be stable up to 600 K and V_{Zn} to anneal in two steps, partially at 420 K and fully at 600 K. We suggest that the V_{Zn} is mobile at 420 K and the reason for an incomplete annealing is a trap limited diffusion of V_{Zn}, especially caused by strong binding to 3d-metal impurities [9,12]. Taking our value of the diffusion coefficient, this would be consistent with a migration energy of diffusion for the vacancy of the order of ~1.0(5) eV. This is in agreement with the migration energy of 1.19 eV calculated for the neutral zinc vacancy [13].

5. Conclusions

We have investigated the dose dependence of magnetic fractions at different temperatures in Mn/Fe-implanted ZnO single crystals by means of Mössbauer spectroscopy. The results suggest that mobile defects (mainly V_{Zn}) are responsible for the observation of a magnetic signal in the Mössbauer spectra, in agreement with earlier experiments [7–9].

Acknowledgements

This work was supported by the European Union Sixth Framework through RII3-EURONS. K. Bharuth-Ram, H. Masenda and D. Naidoo acknowledge support from the South African National Research Foundations. T.E. Mølholt acknowledges support from the Icelandic Research Fund.

References

[1] T. Dietl, H. Ohno, F. Matsukura, J. Cibert, D. Ferrant, Science 287 (2000) 1019.
[2] K. Sato, H. Katayama-Yoshida, Japan. J. Appl. Phys. 39 (2000) 555.
[3] M. Venkatesan, C.B. Fitzgerald, J.G. Lunney, J.M.D. Coey, Phys. Rev. Lett. 93 (2004) 177206.
[4] N.A. Spaldin, Phys. Rev. B 69 (2004) 125201.
[5] W. Yan, Z. Sun, Q. Liu, Z. Li, Z. Pan, J. Wang, S. Wei, D. Wang, Y. Zhou, X. Zhang, Appl. Phys. Lett. 91 (2007) 062113.
[6] D. Karmakar, S.K. Mandal, R.M. Kadam, P.L. Paulose, A.K. Rajarajan, T.K. Nath, A.K. Das, I. Dasgupta, G.P. Das, Phys. Rev. B 75 (2007) 144404.
[7] G. Weyer, H.P. Gunnlaugsson, R. Mantovan, D. Naidoo, K. Bharuth-Ram, M. Fanciulli, T. Agne, J. Appl. Phys. 102 (2007) 113915.
[8] R. Mantovan, et al., Manuscript under preparation, 2009.
[9] H.P. Gunnlaugsson, G. Weyer, R. Mantovan, D. Naidoo, R. Sielemann, K. Bharuth-Ram, M. Fanciulli, K. Johnston, S. Olafsson, G. Langouche, Hyperfine Interact 188 (2009) 85–89.
[10] E. Rita, U. Wahl, J.G. Correia, E. Alves, J.C. Soares, Appl. Phys. Lett. 85 (2004) 4899.
[11] F. Tuomisto, K. Saarinen, D.C. Look, G.C. Farlow, Phys. Rev. B 72 (2005) 085206.
[12] A. Debernardi, M. Fanciulli, Appl. Phys. Lett. 90 (2007) 212510.
[13] P. Erhart, N. Juslin, O. Goy, K. Nordlund, R. Muller, K. Albe, J. Phys. Cond. Matt. 18 (2006) 6585.

Paper II

Paramagnetism in Mn/Fe implanted ZnO

Gunnlaugsson, H. P., **Mølholt, T. E.**, Mantovan, R., Masenda, H., Naidoo, D., Dlamini, W. B., Sielemann, R., Bharuth-Ram, K., Weyer, G., Johnston, K., Langouche, G., Ólafsson, S., Gíslason, H. P., Kobayashi, Y., Yoshida, Y., Fanciulli, M., and the ISOLDE Collaboration:

*Applied Physics Letters, Volume **97**,*
Issue 14, id. 142501 (3 pages) (2010).

DOI: 10.1063/1.3490708

Paramagnetism in Mn/Fe implanted ZnO

H. P. Gunnlaugsson,[1,a] T. E. Mølholt,[2] R. Mantovan,[3] H. Masenda,[4] D. Naidoo,[4] W. B. Dlamini,[5] R. Sielemann,[6] K. Bharuth-Ram,[5,7] G. Weyer,[1] K. Johnston,[8] G. Langouche,[9] S. Ólafsson,[2] H. P. Gíslason,[2] Y. Kobayashi,[10] Y. Yoshida,[11] M. Fanciulli,[3,12] and ISOLDE Collaboration[8]

[1]*Department of Physics and Astronomy, Aarhus University, DK-8000 Århus C, Denmark*
[2]*Science Institute, University of Iceland, Dunhaga 3, IS-107 Reykjavík, Iceland*
[3]*CNR-IMM MDM Laboratory, Via C. Olivetti 2, 20041 Agrate Brianza (MB), Italy*
[4]*School of Physics, University of the Witwatersrand, Private Bag 3, Wits 2050, South Africa*
[5]*School of Physics, University of KwaZulu-Natal, Durban 4001, South Africa*
[6]*Helmholtz-Zentrum Berlin für Materialien und Energie, D-14109 Berlin, Germany*
[7]*iThemba Laboratories, P.O. Box 722, Somerset West 7129, South Africa*
[8]*PH Department, ISOLDE/CERN, 1211 Geneva 23, Switzerland*
[9]*Instituut voor Kern-en Stralings fysika, University of Leuven, B-3001 Leuven, Belgium*
[10]*The Institute of Physical and Chemical Research (RIKEN), Wako, Saitama 351-0198, Japan*
[11]*Shizuoka Institute of Science and Technology, Shizuoka 437-8555, Japan*
[12]*Department of Material Science, Università degli Studi di Milano Bicocca, Via R. Cozzi 53, 20125 Milano, Italy*

(Received 14 July 2010; accepted 28 August 2010; published online 4 October 2010)

Prompted by the generally poor understanding of the nature of magnetic phenomena in 3*d*-metal doped ZnO, we have undertaken on-line ^{57}Fe Mössbauer spectroscopy on ZnO single crystals in an external magnetic field of 0.6 T, following the implantation of radioactive ^{57}Mn ions at room temperature. The Mössbauer spectra of the dilute Fe impurities are dominated by sextets whose angular dependence rules out an ordered magnetic state (which had been previously proposed) but are well accounted for on the basis of Fe^{3+} paramagnetic centers on substitutional Zn sites with unusually long relaxation times (>20 ns). © *2010 American Institute of Physics*.
[doi:10.1063/1.3490708]

Dilute magnetic semiconductors, obtained in compound semiconductors by partial replacement of cations by magnetic transition-metal ions, are of current interest as potential semiconductor-compatible magnetic components for spintronic applications. For ZnO, room temperature dilute magnetism has been predicted by theory[1] and observed experimentally.[2] However, the origin of magnetism in transition-metal doped ZnO is poorly understood[3,4] and there are inconsistent reports in the literature. Recently, a possible role of defects has been discussed by several authors[5–8] while others have suggested unintentional precipitation.[9,10]

In continuation of our previous study,[11] we have applied ^{57}Fe Mössbauer spectroscopy in an external magnetic field to study the nature of the magnetism in ion implanted ZnO single crystals. Radioactive ion beams of $^{57}Mn^{+}$ ($T_{1/2}$ = 1.5 min) ions are produced at the ISOLDE facility, CERN, following proton induced fission in a UC_2 target and element-selective laser ionization.[12] After acceleration to 60 keV, high purity beams of up to $(1-3)\times10^{8}$ ions/s are obtained. These have been implanted to fluences $<10^{12}/cm^2$ into ZnO single crystals held in an external magnetic field. Commercial [0001] single crystals (CrysTec), hydrothermally grown, with typical contaminations <20 ppm for 3*d* elements ($\sim4\times10^{16}$ $3d/cm^3$) and n-type conductivity (10^2-10^3 Ω cm) were used.

This on-line method of populating the ^{57}Fe Mössbauer state via β-decay of ^{57}Mn allows for the study of truly dilute samples with local concentration of the implanted species below 2×10^{16} cm^{-3} ($\sim5\times10^{-5}$ at. %). The probe nucleus is sensitive predominantly to its local atomic environment (up to second next nearest neighbors) and to electric and magnetic hyperfine interactions[13] and the resultant Mössbauer spectrum gives information on the magnetic and valence state of the Fe ions and their electronic configurations.

In previous publications based on similar measurements in ZnO (Refs. 11 and 14) the spectra were analyzed differently. Although the nature of the magnetism could not be deduced, ferromagnetism was favored.[11] This interpretation is revised here in the light of the Mössbauer measurements performed with the ZnO sample held in an external magnetic field, which prove paramagnetism.

In the case of ordered magnetism, e.g., ferromagnetism, the relative line intensities of the resulting sextet are expected to show a well-known dependence on the angle θ between the γ-detection direction and the magnetic field direction thus enabling one to substantiate or discard such an interpretation. Spectra of paramagnetic states, on the other hand, may be more complex, consisting of the superposition of more than one sextet,[15] as is shown to be the case here.

Two samples were employed in this study, one for measurements in an external magnetic field B_{ext}=0.6 T, and another in zero field. For the magnetic field measurements the sample was placed directly on a permanent magnet mounted on a rotation stage with the sample *c*-axis collinear with the external field. Mössbauer emission spectra were recorded using a resonance detector equipped with a stainless steel absorber enriched in ^{57}Fe. The detector was mounted on a conventional velocity drive unit outside the implantation chamber at 90° relative to the beam direction. First, Möss-

[a]Electronic mail: hpg@phys.au.dk.

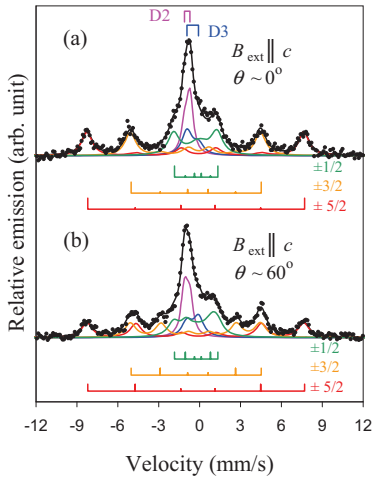

FIG. 1. (Color online) Room temperature Mössbauer spectra obtained in B_{ext}=0.6 T applied parallel to the c-axis and at two different emission angles (θ) relative to the c-axis as indicated.

bauer spectra were recorded during an implantation period of 4 min with the crystal mounted in such a way that the angle between the (0001) direction and the detected γ-rays was $\theta \sim 60°$ [Fig. 1(b)]. The implantation was then halted, the sample rotated toward the detector and a Mössbauer spectrum recorded with $\theta \sim 0°$ [Fig. 1(a)] for four minutes. The sample measured in zero external magnetic field was mounted with the (0001) direction at $\theta \sim 60°$ toward the detector (Fig. 2). Both samples were preimplanted with $>10^{11}$ $^{57}Mn/cm^2$ to avoid dose dependence effects.[14] Velocities and isomer shifts are given relative to the spectrum of α-Fe at room temperature.

Mössbauer spectra obtained in the external magnetic field are shown in Fig. 1. Compared to previously reported spectra,[11,14] the sextet parts of the spectra, as visibly best represented by the four outermost lines, show much sharper spectral lines. Hence the consideration of a magnetic hyperfine field distribution in the analysis is not required. The relative intensities of the lines change with the angle θ, but do not follow the behavior expected for the case of an ordered magnetic state. A notable difference between the two spectra is that spectral line intensities at $v \sim -2.5$ mm/s and $v \sim 3$ mm/s observed in the $\theta \sim 60°$ spectrum [Fig. 1(b)] seem to have disappeared in the $\theta \sim 0°$ spectrum [Fig. 1(a)]. This strongly suggests the disappearance of the $\Delta m_I = 0$ nuclear transition for a $S_Z = \pm 3/2$ electronic state, related to the splitting of the middle member of the crystal field Kramers doublets expected for Fe^{3+} in a paramagnetic state.[15] Paramagnetic $^6S_{5/2}$ states have been reported earlier by electron paramagnetic resonance spectroscopy[16] and photoluminescence[17] in nonimplanted $ZnO:Fe^{3+}$.

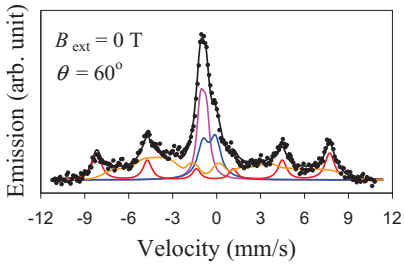

FIG. 2. (Color online) Room temperature Mössbauer spectrum obtained after implantation into ZnO single crystal in zero external magnetic field.

TABLE I. Hyperfine parameters obtained from simultaneous analysis of the spectra in Fig. 1. The table lists the magnetic hyperfine field (B_{hf}) for the $S_Z = \pm 5/2$ subsextet, isomer-shift (δ), quadrupole splitting/shift ($\Delta E_Q = 2\varepsilon$ for the sextet), full width at half maximum line-width (Γ) with the detector line-width subtracted, and the area fractions.

Component	D2	D3	Parameter sextet
Assignment	Fe_{Zn}^{2+}	Fe_I	Fe_{Zn}^{3+}
B_{hf}(T)			49.3(1)
δ(mm/s)	0.91(1)	0.50(3)	0.19(1)
ΔE_Q(mm/s)	−0.39(2)	+0.85(4)	+0.12(1)
Γ(mm/s)	0.17(3)	0.5(1)	0.63(5)
Area (%)	17(1)	12(1)	71(1)

To test this hypothesis, the spectra in Fig. 1 have been analyzed in terms of a superposition of three sextets originating from the three Kramers doublets belonging to the $S_Z = \pm 5/2$, $\pm 3/2$, and $\pm 1/2$ crystal field states. Such an ansatz was shown to be applicable for the case of dilute Fe^{3+} in α-Al_2O_3.[18] In sufficiently high external magnetic field, where level crossings are avoided ($B_{ext} > 0.3$ T according to the data from Ref. 17) the magnetic hyperfine splitting of the three Kramer doublets is proportional to $|S_Z|$ (Ref. 15) and the relative intensities of each six-line spectrum behave as in an effective magnetic field. At room temperature all three Kramers doublets are equally populated and the final spectrum is the sum of those. We make the reasonable assumptions that each sextet has the same isomer and quadrupole shifts. In addition, doublets assigned to substitutional Fe^{2+} (D2) and interstitial Fe (D3) have been included in the simultaneous analysis of the two spectra. As is evident, from the fit presented in Fig. 1, this simple model describes adequately the observed spectra and their angular dependence, thus demonstrating that the magnetically split components in the Mössbauer spectra are attributable to Fe^{3+} paramagnetic states in ZnO.

The hyperfine parameters obtained from the analysis of the spectra in Fig. 1 are collected in Table I. The parameters obtained for D2 and D3 are in good agreement with those obtained in Ref. 11. In addition, in the present work the sign of the quadrupole interaction of the doublets can be deduced from their angular dependence. The line-widths of the paramagnetic sextets are considerably larger than that of D2. The value of the principal component of the electrical field gradient (EFG) deduced from the quadrupole shift in the paramagnetic sextet, $V_{ZZ} = +5.5(5) \times 10^{20}$ V/m^2, is very similar to the value $V_{ZZ} = +6.6 \times 10^{20}$ V/m^2 at 4.2 K for isolated Zn^{2+} on substitutional sites determined from ^{67}Zn-Mössbauer spectroscopy,[19] (in both cases only a lattice contribution to the EFG) suggesting a similar type of configuration and allowing us to conclude that the Fe^{3+} ions observed after implantation are on substitutional sites in a paramagnetic state. The assignment of lattice site is in accordance with finding from emission channeling experiments.[20]

Figure 2 shows the Mössbauer spectrum without external magnetic field. The spectral shape is considerably different as compared with the spectra in Fig. 1. The spectrum has been analyzed in the same way as in Ref. 11 with a sextet and two magnetic hyperfine field distributions in addition to components D2 and D3. These distributions are not observed in the spectra presented in Fig. 1.

It is not possible to analyze the zero-field spectrum with the same ansatz as used for the spectra in Fig. 1. A variety of effects may contribute to the rather "diffuse" or "smeared" shape, most likely distributions of local perturbing fields (static) and/or relaxation effects, due to fluctuating hyperfine fields. Additional temperature dependent measurements between 300 K and about 600 K (Ref. 11) showed that the line-width of the sextet is largely temperature independent up to 400 K and increases above 400 K. From this, further information on the nature of the spectrum-perturbing interaction may be inferred. Since the Fe probes in the sample have been implanted, they all find themselves at the end of an implantation cascade in a local defect concentration of several percentages. Since many of the defects produced are paramagnetic, one has a situation similar to the case of a concentrated paramagnetic solution (alloy) with a paramagnetic neighbor in at least every second or third neighbor shell. This can lead to strong broadening and distortion ("smearing") due to dipolar (electronic-) spin–spin interaction well known from experiments in chemical solutions and well described as function of spin dilution.[21] These (mostly) static dipolar interactions may result in magnetic fields reaching 10 mT or more, large enough to strongly perturb the paramagnetic Mössbauer spectrum. These static fields can be decoupled by the external magnetic field of 0.6 T, resulting in an effective quantization of all interactions along the external field direction (and z-direction of the crystal) resulting in the much sharper lines given in Fig. 1. There is, however, a residual line broadening as mentioned above even when the magnetic field is applied. This may indicate either an incompletely decoupled interaction which could be removed by applying a larger magnetic field or a perturbation caused by time fluctuating spin–spin interaction (a T_2 type relaxation if described in terms of magnetic resonance spectroscopy). Since the latter is essentially temperature independent it cannot easily be distinguished from a static perturbation. If the line-broadening at room temperature is interpreted as due to relaxation effects it implies relaxation times $\tau > 20$ ns.[15,22]

At temperatures above 400 K the increasing line-broadening shows that temperature dependent relaxation is active. This is most likely the expected spin–lattice relaxation which describes the coupling of the Fe ion to the lattice and in resonance spectroscopy is denoted T_1. Since the sextet spectrum is observable up to 600 K,[11] it is found that the isolated Fe in ZnO in its 3+ state is a system with one of the longest relaxation time found so far.

Our results show that substitutional Fe assumes both 2+ and 3+ charge states after implantation into ZnO. The natural charge state for Fe substituting a metal ion in ZnO is 2+. However, even for Fe contaminations occurring unintentionally in ZnO, isolated substitutional Fe^{3+} has been detected.[16,17] After implantation Fe^{3+} might easily occur and might be stabilized by defects occurring from the implantation induced nearby defects (electrically active and charge compensating). Implantation may also lead to local changes in the Fermi level favoring the 3+ state. The spectra presented here do not provide direct evidence that the Fe^{3+} state is due to charge compensating defects nor for a complex formation with the Zn vacancy as proposed previously.[11] However, it has been observed that the 2+/3+ ratio depends on implantation dose and temperature, and this has been attributed to charge compensation due to mobile zinc vacancies.[14]

In conclusion, the Mössbauer measurements in an external magnetic field provide unequivocal evidence that the magnetic structure observed in the Mössbauer spectra of Mn/Fe implanted ZnO is attributed to substitutional paramagnetic Fe^{3+} impurities with unusually long spin-lattice relaxation times, an effect attributable to the weak coupling of Fe^{3+} to the lattice. The results also provide direct insight in the charge states of the Fe ions as well as their lattice sites.

This work was supported by the European Union Sixth Framework through RII3-EURONS. K. Bharuth-Ram, W. Dlamini, H. Masenda, and D. Naidoo acknowledge support from the South African National Research Foundation. T. E. Mølholt acknowledges support from the Icelandic Research Fund. Financial support of the German BMBF (Contract No. 05KK4TS1/9) is also gratefully acknowledged.

[1] T. Dietl, H. Ohno, F. Matsukura, J. Cibert, and D. Ferrand, Science **287**, 1019 (2000).
[2] R. Janisch, P. Gopal, and N. A. Spaldin, J. Phys.: Condens. Matter **17**, R657 (2005).
[3] K. Ando, Science **312**, 1883 (2006).
[4] Ü. Özgür, Y. I. Alivov, C. Liu, A. Teke, M. A. Reshchikov, S. Doğan, V. Avrutin, S.-J. Cho, and H. Morkoç, J. Appl. Phys. **98**, 041301 (2005).
[5] M. Kapilashrami, J. Xu, V. Ström, K. V. Rao, and L. Belova, Appl. Phys. Lett. **95**, 033104 (2009).
[6] M. Khalid, M. Ziese, A. Setzer, P. Esquinazi, M. Lorenz, H. Hochmuth, M. Grundmann, D. Spemann, T. Butz, G. Brauer, W. Anwand, G. Fischer, W. A. Adeagbo, W. Hergert, and A. Ernst, Phys. Rev. B **80**, 035331 (2009).
[7] Q. Wang, Q. Sun, G. Chen, Y. Kawazoe, and P. Jena, Phys. Rev. B **77**, 205411 (2008).
[8] Q. Wang, Q. Sun, P. Jena, and Y. Kawazoe, Phys. Rev. B **79**, 115407 (2009).
[9] K. Potzger and S. Zhou, Phys. Status Solidi B **246**, 1147 (2009).
[10] S. Zhou, K. Potzger, Q. Xu, G. Talut, M. Lorenz, W. Skorupa, M. Helm, J. Fassbender, M. Grundmann, and H. Schmidt, Vacuum **83**, S13 (2009).
[11] G. Weyer, H. P. Gunnlaugsson, R. Mantovan, M. Fanciulli, D. Naidoo, K. Bharuth-Ram, and T. Agne, J. Appl. Phys. **102**, 113915 (2007).
[12] V. N. Fedoseyev, K. Bätzner, R. Catherall, A. H. M. Evens, D. Forkel-Wirth, O. C. Jonsson, E. Kugler, J. Lettry, V. I. Mishin, H. L. Ravn, G. Weyer, and ISOLDE Collaboration, Nucl. Instrum. Methods Phys. Res. B **126**, 88 (1997).
[13] *Chemical Applications of Mössbauer Spectroscopy*, edited by V. I. Goldanskii and R. H. Herber (Academic, New York, 1968).
[14] T. E. Mølholt, R. Mantovan, H. P. Gunnlaugsson, K. Bharuth-Ram, M. Fanciulli, H. P. Gíslason, K. Johnston, Y. Kobayashi, G. Langouche, H. Masenda, D. Naidoo, S. Ólafsson, R. Sielemann, and G. Weyer, Physica B **404**, 4820 (2009).
[15] S. Mørup, in *Mössbauer Spectroscopy and Transition Metal Chemistry: Fundamentals and Application*, edited by P. Gütlich, E. Bill, and A. X. Trautwein (Springer, Berlin, 2010).
[16] W. M. Walsh, Jr. and L. W. Rupp, Jr., Phys. Rev. **126**, 952 (1962).
[17] R. Heitz, A. Hoffmann, and I. Broser, Phys. Rev. B **45**, 8977 (1992).
[18] G. K. Wertheim and J. P. Remeika, Phys. Lett. **10**, 14 (1964).
[19] C. Schäfer, W. Potzel, W. Adlassnig, P. Pöttig, E. Ikonen, and G. M. Kalvius, Phys. Rev. B **37**, 7247 (1988).
[20] E. Rita, U. Wahl, J. G. Correia, E. Alves, and J. C. Soares, and ISOLDE Collaboration, Appl. Phys. Lett. **85**, 4899 (2004).
[21] G. Lang, R. Aasa, K. Garbett, and J. P. Williams, J. Chem. Phys. **55**, 4539 (1971).
[22] M. Blume and J. A. Tjon, Phys. Rev. **165**, 446 (1968).

Paper III

Observation of spin-lattice relaxations of dilute Fe^{3+} in MgO by Mössbauer spectroscopy

Mølholt, T. E., Mantovan, R., Gunnlaugsson, H. P., Naidoo, D., Ólafsson, S., Bharuth-Ram, K., Fanciulli, M., Johnston, K., Kobayashi, Y., Langouche, G., Masenda, H., Sielemann, R., Weyer, G., and Gíslason, H. P.:

*Hyperfine Interactions, Volume **197**,*
Issue 1-3, pp. 89-94 (2010)

DOI: 10.1007/s10751-010-0214-3

Hyperfine Interact
DOI 10.1007/s10751-010-0214-3

Observation of spin-lattice relaxations of dilute Fe^{3+} in MgO by Mössbauer spectroscopy

T. E. Mølholt · R. Mantovan · H. P. Gunnlaugsson · D. Naidoo · S. Ólafsson · K. Bharuth-Ram · M. Fanciulli · K. Johnston · Y. Kobayashi · G. Langouche · H. Masenda · R. Sielemann · G. Weyer · H. P. Gíslason

Abstract We present a method to describe the temperature dependence of emission Mössbauer spectra showing slow spin-lattice relaxations of Fe^{3+} in MgO single crystals, obtained after implantation of ^{57}Mn at ISOLDE/CERN. The analysis is based on the Blume-Tjon model for the line-shape of relaxing paramagnetic sextets with the spin relaxation rate, τ^{-1} as a parameter. The temperature dependent spin

T. E. Mølholt (✉) · S. Ólafsson · H. P. Gíslason
Science Institute, University of Iceland, Dunhaga 3, 107 Reykjavík, Iceland
e-mail: tem4@hi.is

R. Mantovan · M. Fanciulli
Laboratorio MDM-IMM-CNR, Agrate Brianza (MB), Italy

H. P. Gunnlaugsson · G. Weyer
Department of Physics and Astronomy, Aarhus University, Århus, Denmark

D. Naidoo · H. Masenda
School of Physics, University of the Witwatersrand, Johannesburg, South Africa

K. Bharuth-Ram
School of Physics, University of KwaZulu-Natal, Durban, South Africa

M. Fanciulli
Dipartimento di Scienza dei Materiali, Università di Milano Bicocca, Milano, Italy

K. Johnston
PH Dept, ISOLDE/CERN, 1211 Geneva 23, Switzerland

Y. Kobayashi
The Institute of Physical and Chemical Research, Wako, Japan

G. Langouche
Instituut voor Kern- en Stralingsfysika, University of Leuven, Leuven, Belgium

R. Sielemann
Helmholtz Zentrum, Berlin, Germany

Published online: 18 November 2010

relaxation rate of Fe^{3+} in MgO is found to increase to $\sim 10^8$ s^{-1} at 647 K by assuming a relaxation rate of $\tau^{-1} < 10^6$ s^{-1} at 77 K. The results are in accordance with those obtained by electron paramagnetic resonance spectroscopy demonstrating the possibility of retrieving spin-lattice relaxation rates of dilute Fe^{3+} from emission Mössbauer spectroscopy of Mn/Fe-implanted oxides.

Keywords Spin-lattice relaxations · Dilute Fe^{3+} · MgO · Emission Mössbauer spectroscopy

1 Introduction

The ^{57}Fe Mössbauer spectra obtained after implantation of $^{57}Mn^{+}(T_{1/2} = 85.4\ s)$ into oxides, can show spectral components due to Fe^{3+} electronic states showing slow paramagnetic relaxations. These spectral components are easily distinguishable in the Mössbauer spectra as they have intensity in the wings of the spectra for $|v| >$ 4 mm/s. Such components have been reported in ZnO [1, 2], MgO [3] and α-Al_2O_3 [4]. The reasons for such a slow relaxation process are presumably a negligible spin-spin relaxation caused by the low concentration ($<10^{-4}$ at. %) of implanted probe atoms and a low Fe^{3+} spin-lattice relaxation rate [5]. As the temperature is increased, a broadening of the Fe^{3+} spectral features is observed, which we attribute to temperature dependent spin-lattice relaxations [1].

It is of interest to model the broadening of the Fe^{3+} spectrum to see whether the temperature dependence of the broadening is consistent with spin-lattice relaxations at elevated temperatures. The part of the spectrum arising from the Fe^{3+} electronic states consists of spectral components originating from three Kramers doublets $S_Z = \pm 1/2$, $S_Z = \pm 3/2$ and $S_Z = \pm 5/2$. In a sufficiently large external magnetic field ($B_{\text{ext}} > \sim 0.3$ T) the three Kramers doublets are observed in Mössbauer spectroscopy as a collection of three sextets, each with a magnetic hyperfine splitting proportional to $|S_Z|$. In the absence of a sufficiently large applied external magnetic field the spectral shape is rather complicated as the eigenstates of the system are combined nuclear and electronic states [5–8]. The $S_Z = \pm 5/2$ state is least affected by this effect and is often observed as a "normal" sextet, while the $S_Z = \pm 1/2$ and $S_Z = \pm 3/2$ states give rise to more complicated spectral shapes [5].

Each paramagnetic sextet is calculated according to the line-shape described by Blume and Tjon [9] for random fluctuations of the magnetic hyperfine field, $\pm B_{\text{hf}}$. The line-shape depends on the nuclear spin relaxation rate τ^{-1}. For relaxation rates, $\tau^{-1} < 5 \times 10^6$ s^{-1}, the line-shape resembles that of a normal sextet showing broadening of all resonance lines according to $\Delta\Gamma = 2\hbar c\tau^{-1}/E_0$, where c is the speed of light and $E_0 = 14.4$ keV the energy of the Mössbauer transition. For a relaxation-broadened sextet with $B_{\text{hf}} = 50$ T, the inner lines (3 and 4) collapse to a single line for relaxation times (inverse relaxation rate) $\tau \approx 13$ ns, the central lines (2 and 5) collapse for $\tau \approx 4$ ns and the outer lines (1 and 6) collapse for $\tau \approx 2$ ns.

While the $S_Z = \pm 5/2$ state is well observable in the Mössbauer spectra as the features with the largest splitting, the central part is analysed in an empirical way. We show that such a semi-empirical approach can be successfully used to fit the broadening of Mössbauer spectra and hereby estimate the spin relaxation rates of Fe^{3+} in MgO.

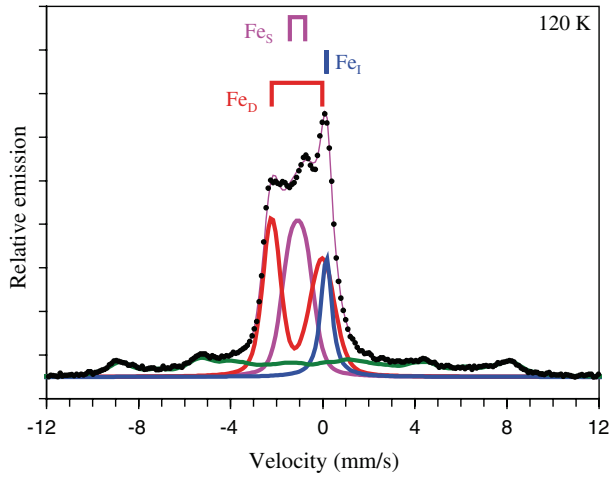

Fig. 1 ^{57}Fe Mössbauer spectrum obtained after implantation of $^{57}Mn^{+}$ into single crystal MgO at 120 K (*dots*). The *solid lines* show the fitting components and their sum

Our results corroborate electron paramagnetic resonance (EPR) spectroscopy data on spin-lattice relaxation rates that exist in the same temperature range as we observe [10], allowing us to compare results and to test our approach.

2 Experimental

Radioactive beam of $^{57}Mn^{+}(T_{1/2} = 85.4\,s)$ was produced at the ISOLDE facility at CERN by 1.4 GeV proton-induced fission in a heated UC_2 target and elemental selective laser multi-photon ionization [11]. After acceleration to 50 – 60 keV and magnetic mass separation, a beam of $\sim 1.9 \times 10^8$ $^{57}Mn^{+}$/s was obtained. This method allows us to study Fe impurities in concentrations $<10^{-4}$ at. % which means there are more than 100 atomic lattice constants between the positions of implanted atoms. $^{57}Mn^{+}$ was implanted into MgO single crystals that were mounted in an implantation chamber and held at temperatures ranging from 77 – 647 K.

The implantation was performed at an incident angle of 30° relative to the sample surface normal. Mössbauer emission spectra were measured on-line on the Mössbauer state of the daughter $^{57*}Fe(T_{1/2} = 98\,ns)$ with an acetone gas-filled resonance detector, equipped with ^{57}Fe enriched stainless steel electrodes, mounted outside the implantation chamber on a conventional constant-acceleration drive system at 90° to the beam direction (60° relative to the crystal surface normal). Velocities are given relative to the centre of the α-Fe spectrum at room temperature.

3 Results and discussion

Figure 1 shows in detail the ^{57}Fe Mössbauer spectrum of the Mn/Fe-implanted MgO at 120 K.

Fe_D assigned to Fe^{2+} in damaged/amorphous surroundings due to the implantation showing considerable annealing (i.e. less intensity) at increased temperatures.

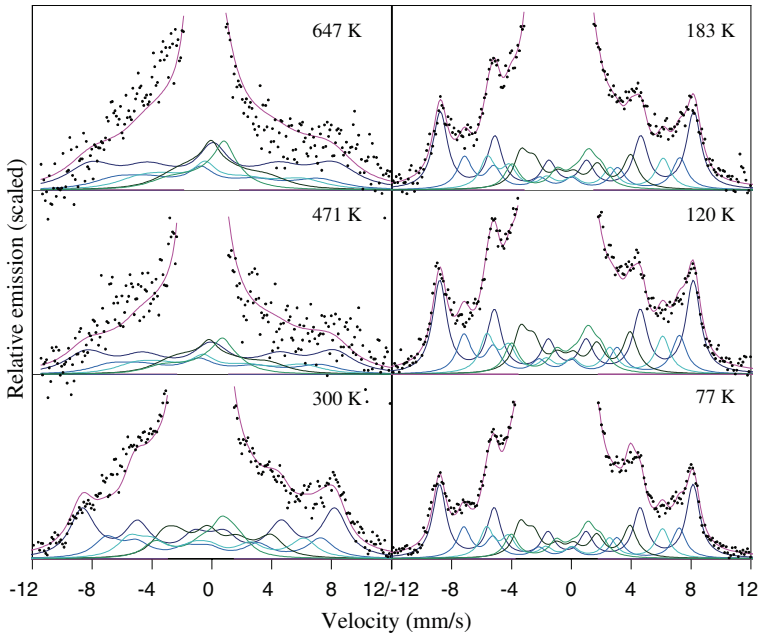

Fig. 2 Wings of representative Mössbauer spectra (*dots*) obtained in this study at the temperatures indicated. Fitting components are indicated with *solid lines*

Fe_S is assigned to substitutional Fe^{2+} on Mg sites due to the vanishing quadrupole splitting at high temperatures which is consistent with substitutional Fe on the cubic Mg site. Fe_I due to recoil produced interstitial Fe [3]. Above room temperature, the Mössbauer spectra are dominated by the Fe_S line and below the spectra are dominated by the asymmetric Fe_D quadrupole doublet, and a broadening of Fe_S is observed related to lattice distortions, due to defects in vicinity of the Fe atom annealing at increased temperatures. The central part of the spectrum will be described in more details in a forthcoming publication [T. E. Mølholt et al., manuscript in preperation]. At all temperatures the wings of the spectra show a magnetic sextet structure assigned to paramagnetic sextets showing temperature dependence as seen in Fig. 2.

The magnetic sextet structure show more broadened features at increasing temperatures. Importantly, we note that the description of the central part of the spectrum does not affect the conclusions that can be derived from the analysis of the wings of the spectra. To describe the wings in the spectra, we applied a model consisting of a number of relaxation sextets. Initially, in the spectrum obtained at 77 K where paramagnetic sextets are distinguishable, the outermost relaxation sextet with a magnetic hyperfine field of ∼52 T was added, and the internal line-width adjusted by visual inspection and the relaxation rate set to $\tau^{-1} = 0$. Thereafter, another relaxing sextet with the same relaxation rate, but with a slightly lower magnetic hyperfine field was included in order to describe the experimental part of the spectral structure reasonably. This was repeated until the magnetic distribution of the spectral structure was sufficiently fitted. In total, five relaxation sextets were

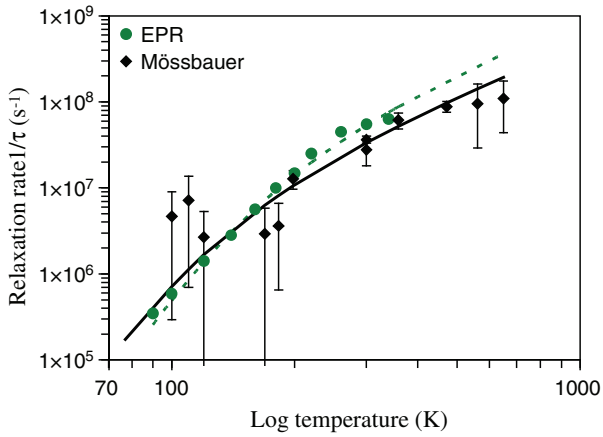

Fig. 3 Relaxation rates obtained in this work in comparison with results from EPR measurements on relaxation rates (T_1) of dilute Fe^{3+} impurities in MgO [10]. Above ~300 K the obtained relaxation rates roughly follows a T^2 temperature dependence

required with different magnetic hyperfine fields, where the internal line ratio was restricted to 3:2:1. For each of them, the relative area ratio, quadrupole shift and linewidths were treated as temperature independent constants. The isomer shift of each relaxation sextet was set to follow the second order Doppler shift leaving only the total area of all sextets and the relaxation rate to be temperature dependent variables in each spectrum. In the analysis where the magnetic hyperfine field was set as a free variable it showed unphysical variations at the highest temperatures. Therefore the internal magnetic field, $B_{\mathrm{hf},i}(T)$, was restricted to follow a linear decrease with increasing temperatures.

With this ansatz for the simultaneous analysis of the 12 Mössbauer spectra in the temperature series, the Fe^{3+} spectral part can be described in terms of 41 fitting variables (average of 3.4 variables per spectrum) which is considerably lower than performing analysis in terms of a sextet and distributions (as described by Weyer et al. [2]), which requires at least 55 variables (4.6 per spectrum).

In the analysis, τ was found to decrease down to ~10 ns with increasing temperature, assuming $\tau > 1$ μs at 77 K. Essentially the relaxation time is determined by the broadening of the sharpest outermost features in the spectra (outer peaks at ±9 mm/s), only moderately by the collapse of the inner lines 3 and 4 of the sextet, and negligibly by annealing reactions observed in the central part of the spectrum. We hence conclude that the relaxation time is reasonably estimated for the $S_Z = \pm 5/2$ state, while the remaining sextets mostly account for the asymmetry in the spectra. Letting the inner sextets in our description follow either a slower or a faster relaxation time than the outermost sextet did not significantly change either the quality of the fit or the relaxation time.

Figure 3 shows the spin-lattice relaxation rate obtained here in comparison to the spin-lattice relaxation rate (T_1) from EPR results [10]. A reasonably good correlation between the two sets of data is obtained, demonstrating the possibility of using Mössbauer spectroscopy for retrieving spin-lattice relaxation rates.

The extracted spin-lattice relaxation rate of Fe^{3+} impurities in MgO can not be directly compared to the T_1 obtained by EPR, but the rather similar values in Fig. 3, obtained by the two different methods, support our interpretation of the data. Above ~300 K the relaxation rates roughly follows a T^2 temperature dependence,

indicating that the Raman process dominates at temperatures higher than the Debye temperature of [5].

Spin relaxations take place either due to spin-spin interactions or spin-lattice interactions. In our experiments, the low concentration of implanted Mn/Fe atoms (>100 atomic lattice constants between Mn/Fe atoms) results in negligible spin-spin relaxations. The spherical ^{6}S ground state of Fe^{3+} causes weak interaction with the lattice, resulting in long spin-lattice relaxation times.

4 Conclusion

We have employed a semi-empirical model to describe the temperature dependent paramagnetic relaxation in the Mössbauer spectra of Fe^{3+} in MgO. Despite the nature of the analysis method, it has been found to give relaxation rates comparable to those observed with EPR measurements. We conclude that our approach can be used to obtain relaxation rates without the application of an external magnetic field.

Acknowledgements The European Union Sixth Framework through RII3-EURONS is acknowledged for supporting this work. K. Bharuth-Ram, H. Masenda and D. Naidoo acknowledge support from the South African National Research Foundation. Financial support of the German BMBF (contract no. 05KK4TS1/9) is also gratefully acknowledged. R. Mantovan acknowledges support from the Cariplo Foundation (SPAM^3 project, code no 2008.2363). T. E. Mølholt acknowledges support from the Icelandic Research Fund.

References

1. Gunnlaugsson, H.P., Mølholt, T.E., Mantovan, R., Masenda, H., Naidoo, D., Dlamini, W.B., Sielemann, R., Bharuth-Ram, K., Weyer, G., Johnston, K., Langouche, G., Ólafsson, S., Gíslason, H.P., Kobayashi, Y., Yoshida, Y., Fanciulli, M., and the ISOLDE Collaboration: Paramagnetism in Mn/Fe implanted ZnO. Appl. Phys. Lett. **97**, 142501 (2010)
2. Weyer, G., Gunnlaugsson, H.P., Mantovan, R., Fanciulli, M., Naidoo, D., Bharuth-Ram, K., Agne, T.: Defect-related local magnetism at dilute Fe atoms in ion-implanted ZnO. J. Appl. Phys. **102**, 113915 (2007)
3. Mølholt, T.E. et al.: In prep
4. Gunnlaugsson, H.P., Mantovan, R., Mølholt, T. E., Naidoo, D., Johnston, K., Masenda, H., Bharuth-Ram, K., Langouche, G., Ólafsson, S., Sielemann, R., Weyer, G., Kobayashi, Y., the ISOLDE collaboration: Mössbauer spectroscopy of ^{57}Fe in α-Al_2O_3 following implantation of ^{57}Mn*. Hyp. Int. (2010). doi:10.1007/s10751-010-0184-5
5. Mørup, S.: In: Gütlich, P., Bill, E., Trautwein, A.X. (eds.) Mössbauer spectroscopy and transition metal chemistry: fundamentals and application. Springer-Verlag, Berlin (2010)
6. Wickmann, H.H., Wertheim, G.K.: Chemical applications of Mössbauer spectroscopy. In: Goldanskii, V.I., Herber, R.H. (eds.) p. 548. Academic Press (1968)
7. Wickmann, H.H., Klein, M.P., Shirley, D.A.: Paramagnetic hyperfine structure and relaxation effects in Mössbauer spectra: Fe^{57} in ferrichrome. A. Phys. Rev. **152**, 354 (1966)
8. Knudsen, J.E.: Mössbauer spectroscopic studies of the magnetic hyperfine interaction in the ferric hexaquo complex in frozen aqueous solution. J. Phys. Chem. **38**, 883 (1977)
9. Blume, M., Tjon, J.A.: Mössbauer spectra in a fluctuating environment. Phys. Rev. **165**, 446–456 (1968)
10. de Biasi, R.S., Portella, P.D.J.: Spin-lattice relaxation of Fe^{3+} and Mn^{2+} in magnesium oxide. J. Magn. Magn. Mater. **15**, 737 (1980)
11. Fedoseyev, V.N., Baetzner, K., Catherall, R., Evensen, A.H.M., Forkel-Wirth, D., Jonsson, O.C.: Chemically selective laser ion source of manganese. Nucl. Instrum. Methods B **126**, 88 (1997)

Paper IV

Mössbauer spectroscopy of ^{57}Fe in α-Al_2O_3 following implantation of ^{57}Mn*

Gunnlaugsson, H. P., Mantovan, R., **Mølholt, T. E.**, Naidoo, D., Johnston, K., Masenda, H., Bharuth-Ram, K., Langouche, G., Ólafsson, S., Sielemann, R., Weyer, G., Kobayashi, Y., and the ISOLDE collaboration:

*Hyperfine Interactions, Volume **198**,*
Issue 1-3, pp. 5-13 (2010).

DOI: 10.1007/s10751-010-0184-5

Hyperfine Interact
DOI 10.1007/s10751-010-0184-5

Mössbauer spectroscopy of ^{57}Fe in α-Al_2O_3 following implantation of ^{57}Mn*

H. P. Gunnlaugsson · R. Mantovan · T. E. Mølholt · D. Naidoo · K. Johnston · H. Masenda · K. Bharuth-Ram · G. Langouche · S. Ólafsson · R. Sielemann · G. Weyer · Y. Kobayashi · the ISOLDE collaboration

Abstract The valence state and annealing reactions of Mn/Fe in single crystalline α-Al_2O_3 have been determined following low fluence ($<10^{12}$ cm^{-2}) 60 keV implantations of $^{57}Mn^+$ ($T_{1/2} = 1.5$ min) and emission Mössbauer spectroscopy on the ^{57m}Fe daughter nuclei in the temperature range from 110–700 K. At 110 K, most probe atoms are found in the Fe^{2+} state in amorphous surroundings due to the implantation damage. A fraction of the Fe is found in cubic environment, possibly nano-precipitates of η-Al_2O_3. This site is found to disappear from the

H. P. Gunnlaugsson (✉) · G. Weyer
Department of Physics and Astronomy, Aarhus University, 8000 Århus C, Denmark
e-mail: hpg@phys.au.dk

R. Mantovan
Laboratorio MDM, IMM-CNR, Via Olivetti 2, 20041 Agrate Brianza (MB), Italy

T. E. Mølholt · S. Ólafsson
Science Institute, University of Iceland, Dunhaga 3, 107 Reykjavík, Iceland

D. Naidoo · H. Masenda
School of Physics, University of the Witwatersrand, Private Bag 3, WITS 2050, South Africa

K. Johnston · the ISOLDE collaboration
PH Dept, ISOLDE/CERN, 1211 Geneva 23, Switzerland

K. Bharuth-Ram
School of Physics, University of KwaZulu-Natal, Durban 4001, South Africa

G. Langouche
Instituut voor Kern- en Stralingsfysica, University of Leuven, 3001 Leuven, Belgium

R. Sielemann
Helmholtz-Zentrum Berlin für Materialien und Energie, 14109 Berlin, Germany

Y. Kobayashi
The Institute of Physical and Chemical Research (RIKEN), Wako, Saitama 351-0198, Japan

Published online: 22 October 2010

spectra above 500 K. Annealing of the damage sites at increasing temperatures leads first to increased incorporation of the probe atoms as Fe^{3+} on Al sites, and, above room temperature, also as Fe^{4+}. The Fe^{3+} sub-spectrum is masked by slow paramagnetic relaxations following a T^2 dependence, as expected for a two-phonon Raman process. Our data is consistent with data from ^{57}Co and ^{57}Fe implantations, suggesting a general increase in the average Fe valence state with lower implantation dose and negligible annealing reactions at room temperature.

Keywords Emission Mössbauer spectroscopy · Al_2O_3 · ^{57}Fe · ^{57}Mn

1 Introduction

Mössbauer spectroscopy of Fe impurities in α-Al_2O_3 has been of interest for the last four decades with some of the pioneering Mössbauer work on slow paramagnetic relaxations of Fe^{3+} impurities being performed in this material [1–3]. Several authors [4–6] claimed that upon high fluence implantation ($\sim 10^{17}$ ^{57}Fe/cm^2) Fe was observed in the 4+ valence state. This claim was disproved by low temperature measurements of Kobayashi et al. [7] where it was shown that the spectral features assigned to Fe^{4+} were due to fine particles of metallic iron.

The fluence dependence of the ^{57}Fe Mössbauer spectrum upon implantation has been described by several authors. McHargue et al. [8] reported the fluence dependence in the range 10^{16}–10^{17} ^{57}Fe/cm^2, after implantation of 100–160 keV ^{57}Fe at room temperature. They observed a gradual change from an Fe^{2+} dominated spectrum to a spectrum dominated by uncharged iron. Dézsi et al. [9] performed 80 keV ^{57}Co implantations to fluences of (1–3) $\times$ 10^{14} ^{57}Co/cm^2 and observed Fe in the 3+ and 2+ charge states, together with a single line of unknown origin.

Here we present results obtained after 60 keV implantation of $^{57}Mn^+$ ($T_{1/2}$ = 1.5 min) performed at ISOLDE/CERN and emission ^{57}Fe Mössbauer spectroscopy on the daughter nuclei. The outstanding feature of this method, in the context of previous work, is the low total fluence needed to obtain a useful spectrum. The total fluence the sample received is of the order of $\sim 10^{12}$ ^{57}Mn/cm^2.

2 Experimental

Beam of radioactive $^{57}Mn^+$ ($T_{1/2} = 1.5$ min) ions is produced at the ISOLDE facility at CERN following proton induced fission in UC_2 target and element selective laser ionization [10]. The ions have been implanted into single crystals of α-Al_2O_3 with an intensity of (1–3) $\times$ 10^8 s^{-1} of $^{57}Mn^+$ to a total fluence of $\leq 10^{12}$ ^{57}Mn/cm^2. In the β^- decay of ^{57}Mn, the daughter nuclei are given a recoil of average energy $\langle E_R \rangle$ = 40 eV. The samples were mounted in an implantation chamber with the *c*-axes tilted 30° relative to the beam direction and the detector mounted at 60° relative to the *c*-axis of the orthorhombic Al_2O_3 lattice. For measurements above room temperature, the samples were heated with a Halogen lamp from behind. For measurements below RT the samples were mounted on a cold finger cooled with N_2 gas.

^{57}Fe Mössbauer spectra were measured with resonance detectors equipped with stainless steel electrodes enriched in ^{57}Fe. The detector is mounted on a conventional

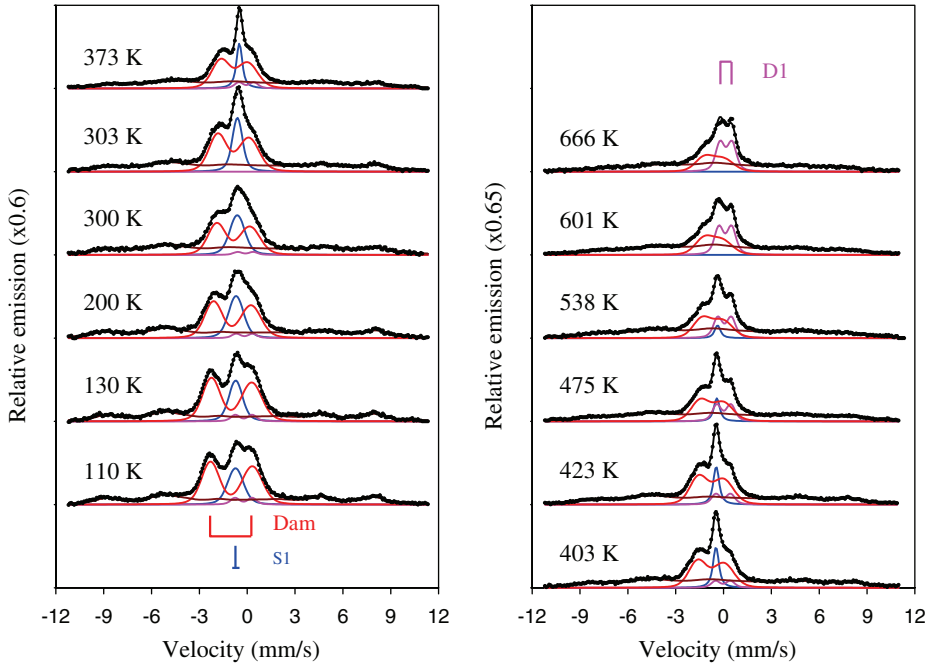

Fig. 1 ^{57}Fe Mössbauer spectra obtained after implantation of $^{57}Mn^{+}$ at the temperatures indicated. The *lines* indicate the fitting components explained in the text

drive system outside the implantation chamber. The intrinsic line-shape of the detector is best analyzed in terms of Voigt profiles with a Lorentzian width of 0.34 mm/s and Gaussian broadening of 0.08 mm/s. Isomer-shifts and velocities are given at room temperature relative to α-Fe.

3 Results and analysis

The spectra obtained at different temperatures are shown in Fig. 1. Measurements after implantation fluencies ranging from 10^{10} to 10^{11} ^{57}Mn/cm^2 at room temperature did not reveal any fluence dependence of the spectral components as has been reported in similar experiments in ZnO [11] and attributed to the mobility of intrinsic defects at room temperature.

In these on-line measurements, the total implantation increases with successive measurements. The spectrum observed at 403 K was measured after the series of high temperature measurements in the range 303–666 K. Its spectral features follow the systematic trend of the other temperature dependent spectra and verify the lack of any dependence on implantation fluence.

Below and at room temperature, the central part of the spectra is dominated by an asymmetric quadrupole doublet (Dam). The rather broad lines of this component suggest it is due to Fe in damage sites due to the implantation. Similar asymmetrically broadened quadrupole doublets due to implantation damage have been observed after implantation of ^{57}Mn into group IV semiconductors [12–15]. Additionally,

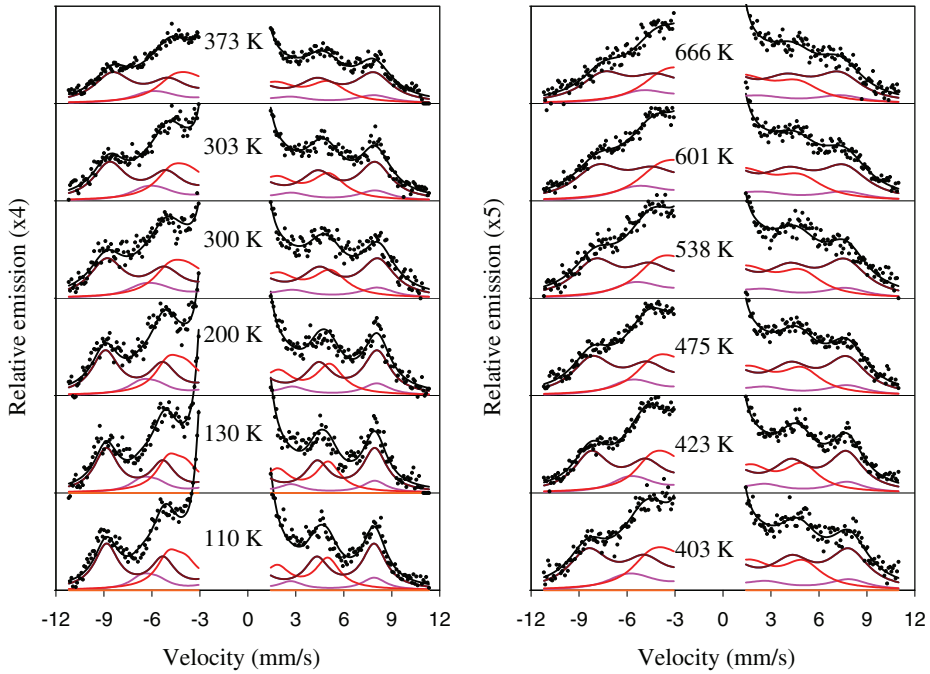

Fig. 2 The same spectra as in Fig. 1, but with the central part removed and the vertical scale expanded to reveal the structure in the outer flanks

the central part of the spectra contains a single line (S1) with room temperature parameters similar to those observed by Dézsi et al. [9]. Below room temperature, this line shows broadening and disappears from the spectra at $T > 500$ K. At $T > 600$ K, the central part of the spectra is dominated by a quadrupole doublet (D1). Due to the fact that this component only dominates the spectra in a relatively small temperature interval, its quadrupole splitting was restricted to follow a $T^{3/2}$ temperature dependence in the analysis. Spectra obtained at different emission angles at room temperature did not reveal any angular dependence of the doublet components.

In Fig. 2, we focus on the outer flanks of the spectra. The wings of the spectra show an asymmetric pattern (higher intensity on the left hand side), similar to that noted in ZnO [16, 17] and MgO [18]. The high maximum magnetic hyperfine field splitting (∼50 T) unambiguously determines the origin of this component being due to Fe^{3+}.

The spectral changes at elevated temperatures of the wings of the spectra are most likely due to increasing relaxation rates and were analyzed with the semi-empirical relaxation model described by Mølholt et al. [18]. In the case of Al_2O_3, it is assumed that the temperature dependent relaxation rate is negligible at 110 K and three relaxation sextets proved adequate to explain the spectral shape.

The final analysis was performed simultaneously where the line-widths were set to temperature independent constants and line positions set to follow the second order Doppler shift (except for S1 at T < 300 K). The Mössbauer fit parameters,

Table 1 Hyperfine parameters obtained from the simultaneous analysis of the spectra in Fig. 1

	δ (mm/s)	ΔE_Q (mm/s)	σ (mm/s)	
S1	0.546 (4)	0	0.087 (5)[c]	
D1	0.107 (5)	0.99 (3)[b]	0.195 (4)	
Dam[a]	0.869 (6)	2.0 (1)	0.484 (4)	0.563 (9)
Para. Fe^{3+}	0.35 (1)	n/a	n/s	

The table lists isomer shift (δ) and quadrupole splitting (ΔE_Q) at room temperature and Gaussian broadening (σ). All lines were analyzed using the Voigt profile with a Lorentzian broadening of 0.34 mm/s

[a]σ given for left and right legs, respectively

[b]At room temperature

[c]Observed broader ($\Delta\sigma \sim 0.30(5)$ mm/s) below room temperature, the value given here obtained at $T \geq 300$ K

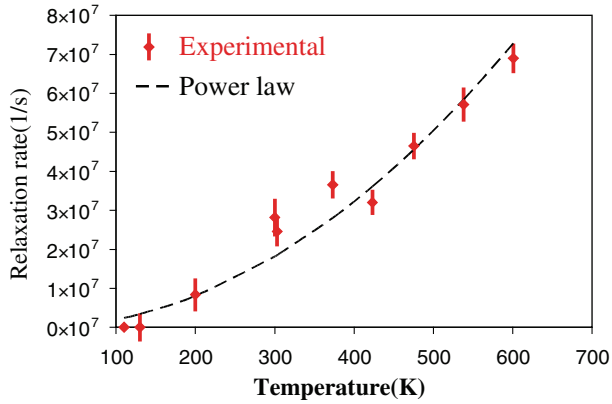

Fig. 3 Spin-relaxation rate obtained by fit to the semi-empirical relaxation model described in [18] compared to a T^2 law

isomer shift (δ), quadrupole splitting (ΔE_Q) at room temperature and Gaussian broadening (σ), are listed in Table 1. All lines were analyzed using a Voigt profile with a Lorentzian broadening of 0.34 mm/s. The quadrupole splitting of D1 was set to follow $\Delta E_Q = \Delta E_{Q,0}(1 - (T/T_k)^{3/2})$ and the values $\Delta E_{Q,0} = 1.09(4)$ mm/s and $T_k = 1{,}400(100)$ K were determined. The maximum hyperfine splitting of the paramagnetic Fe^{3+} component was found to decrease by 10(2) % between 110 K and 600 K.

The relaxation rates obtained for the paramagnetic Fe^{3+} at the different temperatures are shown in Fig. 3. The temperature dependence can easily be compared with a T^2 dependence suggesting a Raman process for the spin lattice relaxation as expected at $T > \theta_D/4$, where θ_D is the Debye temperature.

The area fractions obtained from the analysis are shown in Fig. 4. The total spectral area reduces in almost a linear way from 110 K to 666 K by a factor of 0.66, suggesting an average Debye temperature of ~450 K. There are no features in the total area that can be related to strong differences in the Debye temperatures of the appearing/disappearing fractions (S1 and D1).

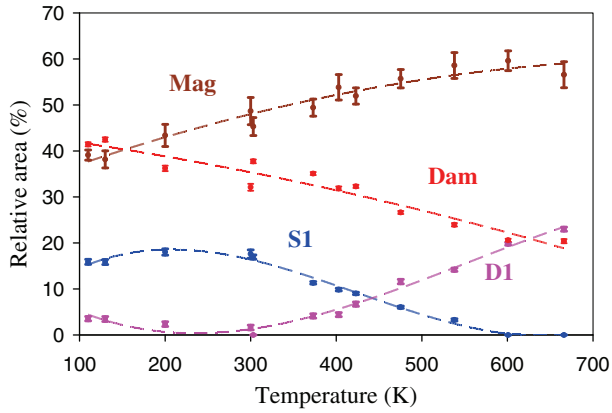

Fig. 4 Area fractions of the spectral components determined from the simultaneous analysis. *Dashed lines* are to guide the eye

4 Discussion

At low temperatures the spectra are dominated by a broad-lined component (Dam). Its isomer shift indicates that it is due to Fe^{2+}. The broad line width and asymmetry of this component is due to a correlated distribution of isomer shifts and quadrupole splittings at the Fe sites and is most probably a consequence of the probe atoms being incorporated in amorphous pockets, similar to observations in silicon [13]. Damaged sites with similar properties have been observed in other types of materials upon implantation of ^{57}Mn [12–15]. The area fraction of the damage decreases from ~42% at 110 K to 20% at ~650 K showing that the probability of ending up in such a site is lower at elevated temperatures or it anneals within the Mn lifetime.

The straight-forward interpretation of the single line (S1) would be to assign it to interstitial Fe owing to the average 40 eV recoil imparted on the Fe daughter nuclei in the β^- decay of ^{57}Mn. However, there are several inconsistencies in such an interpretation. The disappearance of this component above 500 K, would suggest that the interstitial site is not stable over the lifetime of the Mössbauer state (τ = 140 ns), and the interstitial atom is incorporated onto a regular lattice site at times shorter than 100 ns above 500 K. Such transformation should lead to broadening of the interstitial line due to the effective shortening of the lifetime of the atom in the interstitial site relative to the lifetime of the Mössbauer state [19]. This, however, is not supported by the experimental data at $T \leq 475$ K.

A similar (if not identical) single line component (δ = 0.54–0.55 mm/s) was observed in the ^{57}Co data of Dézsi et al. [9]. In the electron capture of ^{57}Co, only a minor (<1 eV) recoil is imparted on the ^{57}Fe daughter nuclei, so it seems unlikely that S1 originates from a recoil produced ^{57}Fe. These authors suggested that this component originates from a mixed valence state. ^{57}Co decays dominantly by electron capture, which leaves the daughter atom in a highly excited electronic state, often giving rise to after-effects and unusual charge states (see e.g. discussion in Ref. [20]). The β^- decay of ^{57}Mn on the other hand does not alter the electronic structure significantly and the creation of unusual charge states is unlikely.

The S1 component shows broadening and a possible small change in isomer-shift below room temperature. Such behaviour could be explained as due to lattice imperfections at low temperatures, where no, or only limited, annealing of damage

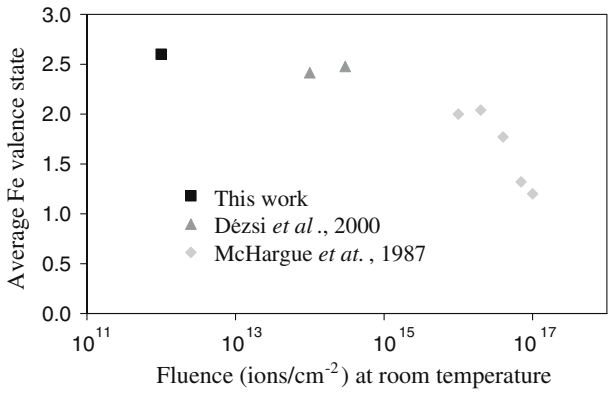

Fig. 5 Average valence state of Fe as a function of implantation fluence in α-Al_2O_3

due to the implantation takes place around the probe atom. Due to less binding of interstitial Fe to the lattice, less pronounced low temperature broadening would be expected.

The S1 component shows no significant broadening above 500 K and has negligible quadrupole interaction ($|\Delta E_Q| < 0.02$ mm/s, determined from lack of angular dependence). Interstitial sites in α-Al_2O_3 would be expected to give rise to detectable quadrupole splitting due to the rhombohedral lattice.

An alternative possibility for the origin of this line is that the Mn atom leads to a formation of another crystal structure upon re-crystallisation of the amorphous pockets. One possibility is the cubic η-Al_2O_3, but the data presented here is not able to distinguish one structure from another. XRD measurements on implanted material could test for the presence of precipitates of η-Al_2O_3 if it can be formed under low fluence ($<10^{15}$ cm^{-2}) implantations.

At temperatures above room temperature, a new component D1 is observed, with an isomer-shift consistent with both Fe^{3+} and Fe^{4+}. It would, however, seem to be a contradiction to have both a fast relaxation Fe^{3+} species (relaxation rates $> 10^{11}$ s^{-1}) and a slow relaxation Fe^{3+} (relaxation rates $< 10^8$ s^{-1}, cf. Fig. 3) species in the same temperature range. Furthermore, the parameters of D1 are not consistent with parameters of fast relaxing paramagnetic Fe^{3+} either in α-$(Al,Fe)_2O_3$ solid solutions [21] or from implanted material [8]. Hence the interpretation of D1 as due to Fe^{4+} is favoured. It should be noted that this component has no relationship to the proposed Fe^{4+} components claimed by other authors [4–6] upon high fluence implantation.

One could suspect that this component was due to interstitial Fe. However, recoil produced interstitial Fe is more likely to have decreasing spectral area due to lower average Debye temperatures, or disappear due to instability at elevated temperatures. If D1 were due to interstitial Fe, one would expect drastic changes in the total area at elevated temperatures, which is not observed. We therefore favour the origin of this component as due to Fe^{4+}, even though interstitial Fe formed upon annealing of the cubic site (S1) can not be excluded.

Together with the data from [8] and [9], we can extend the range in implantation fluence, where the average valence state of Fe is determined. The results are shown in Fig. 5.

Generally, lower fluence implantations result in higher average valence state of Fe. At higher temperatures, the average valence state of Fe increases up to ~3

(assuming D1 originates from Fe^{4+}), mostly due to annealing of Fe^{2+} damaged sites and incorporation of the probe atoms onto sites with higher valence state. For fluences above $\sim 10^{14}$ cm^{-2}, the material becomes completely amorphous, and this state is apparently characterized with Fe^{2+}. For fluences above $\sim 10^{16}$ cm^{-2} spontaneous formation of metallic precipitates takes place, and average valence state below 2+ are observed.

These findings are generally similar to those of Perez et al. [22] upon implantation into MgO. They found Fe^{3+} as the dominating species following 3×10^{15} $^{57}Fe/cm^2$ implanted at 100 keV. Fe^{2+} became the dominating species at $\sim 2 \times 10^{16}$ $^{57}Fe/cm^2$, and metallic iron started to dominate the spectra at $\sim 7 \times 10^{16}$ $^{57}Fe/cm^2$.

The general tendency seen in this data, spanning roughly five decades in implantation fluence suggests no or very limited annealing reactions in α-Al_2O_3. In our ^{57}Mn experiments, the Mössbauer data is obtained few minutes after implantation, while in ^{57}Co and ^{57}Fe experiments, the data is obtained ~days/weeks after the implantation, and there is no evidence of major changes in lattice fractions on this timescale.

5 Conclusions

The Mössbauer spectrum of ^{57}Fe following implantation of ^{57}Mn into single crystalline α-Al_2O_3 has been measured in low fluence implantations ($\leq 10^{12}$ $^{57}Mn/cm^2$) in the temperature range from 110–700 K.

At 110 K roughly 40% of the spectral area is assigned to probe atoms found in the Fe^{2+} state in amorphous surroundings owing to the implantation damage. A fraction of the Fe is found in cubic environment, possibly due to nano-precipitates of η-Al_2O_3which disappear from the spectra above 500 K.

Incomplete annealing of the damaged sites at increasing temperatures leads first to incorporation of the probe atoms in Fe^{3+} valence state, and above room temperature most likely as Fe^{4+}. The Fe^{3+} sub-spectrum is masked by slow paramagnetic relaxations, following T^2 dependence, characteristic for a two-phonon Raman process.

Our data is consistent with data from ^{57}Co and ^{57}Fe implantations, suggesting a general increase in valence state with lower implantation fluence.

Acknowledgements The European Union Sixth Framework through RII3-EURONS is acknowledged for supporting this work. K. Bharuth-Ram, H. Masenda and D. Naidoo acknowledge support from the South African National Research Foundation. Financial support of the German BMBF (contract no. 05KK4TS1/9) is also gratefully acknowledged. T. E. Mølholt acknowledges support from the Icelandic Research Fund.

References

1. Wertheim, G.K., Remeika, J.P.: Mössbauer effect hyperfine structure of trivalent Fe^{57} in corundum. Phys. Lett. **10**, 14–15 (1964)
2. Wickman, H.H., Wertheim, G.K.: Mössbauer hyperfine spectra of Fe^{3+} in corundum: magnetic- and crystal-field effects. Phys. Rev. B **148**, 211–217 (1966)
3. Hess, J., Levy, A.: Response of the Mössbauer spectrum of paramagnetic Fe^{3+} in Al_2O_3 to nuclear dipole fields. Phys. Rev. B **22**, 5068–5078 (1980)
4. Donnet, C., Jaffrezic, H., Marest, G., Moncoffre, N., Tousset, J.: Iron-implantation sintered alumina studied by RBS, CEMS and SEM techniques. Nucl. Instrum. Methods B **50**, 410–415 (1990)

5. McHargue, C.J., Sklad, P.S., McCallum, J.C., White, C.W., Ferez, A., Marest, G.: The structure of Al_2O_3 implanted with iron at 77 K. Nucl. Instrum. Methods B **46**, 144–148 (1990)
6. Guomei, W., Shipu, L., Ning, X., Donghui, F.: Structure and surface properties of polycrystalline ^{57}Fe implanted aluminas. Nucl. Instrum. Methods B **72**, 64–68 (1992)
7. Kobayashi, T., Nakanishi, A., Fukumura, K., Langouche, G.: Fine iron particles formed in a sapphire crystal by the ion implantation technique. J. Appl. Phys. **83**, 4631–4641 (1998)
8. McHargue, C.J., Farlow, G.C., Sklad, P.S., White, C.W., Perez, A., Kornilios, N., Marest, G.: Iron ion implantation effects in sapphire. Nucl. Instrum. Methods B **19/20**, 813–821 (1987)
9. Dézsi, I., Szũcs, I., Fetzer, Cs., Pattyn, H., Langouche, G., Pfannes, H.D., Magalhães-Paniago, R.: Local interactions of ^{57}Fe after electron capture of ^{57}Co implanted in α-Al_2O_3 and in α-Fe_2O_3. J. Phys., Condens. Matter **12**, 2291–2296 (2000)
10. Fedoseyev, V.N., Bätzner, K., Catherall, R., Evensen, A.H.M., Forkel-Wirth, D., Jonsson, O.C., Kugler, E., Lettry, J., Mishin, V.I., Ravn, H.L., Weyer, G., the ISOLDE Collaboration: Chemically selective laser ion source of manganese. Nucl. Instrum. Methods B **126**, 88–91 (1997)
11. Mølholt, T.E., Mantovan, R., Gunnlaugsson, H.P., Bharuth-Ram, K., Fanciulli, M., Gíslason, H.P., Johnston, K., Kobayashi, Y., Langouche, G., Masenda, H., Naidoo, D., Ólafsson, S., Sielemann, R., Weyer, G.: Temperature and dose dependence of defect complex formation with ion-implanted Mn/Fe in ZnO. Physica B **404**, 4820–4822 (2009)
12. Gunnlaugsson, H.P., Fanciulli, M., Dietrich, M., Baruth-Ram, K., Sielemann, R., Weyer, G., the ISOLDE collaboration: ^{57}Fe Mössbauer study of radiation damage in ion implanted Si, SiGe and SiSn. Nucl. Instum. Methods B. **168**, 55–60 (2002)
13. Weyer, G., Gunnlaugsson, H.P., Dietrich, M., Fanciulli, M., Baruth-Ram, K., Sielemann, R., the ISOLDE collaboration: Creation and annealing of defect structures in silicon-based semiconductors during and after implantation at 77–500 K. Nucl. Instrum. Methods B **206**, 90–94 (2003)
14. Weyer, G., Gunnlaugsson, H.P., Dietrich, M., Fynbo, H., Bharuth-Ram, K., the ISOLDE Collaboration: Mössbauer spectroscopy on Fe impurities in diamond. Eur. Phys. J. Appl. Phys. **27**, 317–320 (2004)
15. Gunnlaugsson, H.P., Bharuth-Ram, K., Dietrich, M., Fanciulli, M., Fynbo, H.O.U., Weyer, G.: Identification of substitutional and interstitial Fe in 6H-SiC. Hyp. Int. **169**, 1318–1323 (2006)
16. Weyer, G., Gunnlaugsson, H.P., Mantovan, R., Naidoo, D., Bharuth-Ram, K., Fanciulli, M., Agne, T.: Defect-related local magnetism at dilute Fe atoms in ion-implanted ZnO. J. Appl. Phys. **102**, 113915 (2007)
17. Gunnlaugsson, H.P., Mølholt, T.E., Mantovan, R., Masenda, H., Naidoo, D., Dlamini, W.B., Sielemann, R., Bharuth-Ram, K., Weyer, G., Johnston, K., Langouche, G., Ólafsson, S., Gíslason, H.P., Kobayashi, Y., Yoshida, Y., Fanciulli, M., the ISOLDE Collaboration: Paramagnetism in Mn/Fe implanted ZnO. Appl. Phys. Lett. **97**, 142501 (2010)
18. Mølholt, T.E., Mantovan, R., Gunnlaugsson, H.P., Bharuth-Ram, K., Fanciulli, M., Johnston, K., Kobayashi, Y., Langouche, G., Masenda, H., Naidoo, D., Ólafsson, S., Sielemann, R., Weyer, G., Gíslason, H.P.: Mössbauer study of spin-lattice relaxations of dilute Fe^{3+} in MgO. Hyp. Int. (2010, this conference)
19. Kankeleit, E.: The effect of decaying atomic states on integral and time differential Mössbauer spectra. Zeit. Physik. A. **275**, 119–121 (1975)
20. Gerard, A., Lerho, M.: Fe^{1+} and charge transfer in ZnS. Analysis of source experiments results. Hyp. Int. **29**, 1373–1376 (1986)
21. de Resende, V.G., Cordier, A., De Grave, E., Laurent, C., Eeckhout, S.G., Giuli, G., Peigney, A.M., da Costa, G., Vandenberghe, R.E.: Presence of metallic Fe nanoclusters in α-$(Al,Fe)_2O_3$ solid solutions. J. Phys. Chem. C. **112**, 16256–16263 (2008)
22. Perez, A., Marest, G., Sawicka, B.D., Sawicki, J.A., Tyliszczak, T.: Iron-ion-implantation effects in MgO crystals. Phys. Rev. B. **28**, 1227–1238 (1983)

Paper V

Magnetism in iron implanted oxides: a status report

Gunnlaugsson, H. P., Sielemann, R., **Mølholt, T. E.**, Dlamini, W. B., Johnston, K., Mantovan, R., Masenda, H., Naidoo, D., Sibanda, W. N., Bharuth-Ram, K., Fanciulli, M., Gíslason, H. P., Langouche, G., Ólafsson, S., Weyer, G., and the ISOLDE collaboration:

*Hyperfine Interactions, Volume **197**,*
Issue 1-3, pp. 43-52 (2010).

DOI: 10.1007/s10751-010-0195-2

Hyperfine Interact
DOI 10.1007/s10751-010-0195-2

Magnetism in iron implanted oxides: a status report

H. P. Gunnlaugsson · R. Sielemann · T. E. Mølholt · W. B. Dlamini · K. Johnston · R. Mantovan · H. Masenda · D. Naidoo · W. N. Sibanda · K. Bharuth-Ram · M. Fanciulli · H. P. Gíslason · G. Langouche · S. Ólafsson · G. Weyer · the ISOLDE collaboration

Abstract Emission Mössbauer spectroscopy on ^{57}Fe fed by ^{57}Mn ions implanted in the metal oxides ZnO, MgO and Al_2O_3 has been performed. The implanted ions occupy different lattice sites and charge states. A magnetic part of the spectra in each oxide can be assigned to Fe^{3+} ions in a paramagnetic state with unusually long relaxation time observable to temperatures up to several hundreds Kelvin. Earlier expectations that the magnetic spectra could correspond to an ordered magnetic state could not be confirmed. A clear decision for paramagnetism and against an ordered magnetic state was achieved by applying a strong magnetic field of 0.6 Tesla.

H. P. Gunnlaugsson · G. Weyer
Department of Physics and Astronomy, Aarhus University, 8000 Århus C, Denmark

R. Sielemann (✉)
Helmholtz-Zentrum Berlin für Materialien und Energie, 14109 Berlin, Germany
e-mail: sielemann@helmholtz-berlin.de

T. E. Mølholt · H. P. Gíslason · S. Ólafsson
Science Institute, University of Iceland, Dunhaga 3, 107 Reykjavík, Iceland

W. B. Dlamini · K. Bharuth-Ram
School of Physics, University of KwaZulu-Natal, Durban 4001, South Africa

K. Johnston · the ISOLDE collaboration
PH Department, ISOLDE/CERN, 1211 Geneva 23, Switzerland

R. Mantovan · M. Fanciulli
Laboratorio MDM, IMM-CNR, Via Olivetti 2, 20041 Agrate Brianza (MB), Italy

H. Masenda · D. Naidoo · W. N. Sibanda
School of Physics, University of the Witwatersrand, Private Bag 3, WITS 2050, South Africa

G. Langouche
Instituut voor Kern-en Stralingsfysica, University of Leuven, 3001 Leuven, Belgium

Published online: 25 November 2010

The relaxation times deduced were compared to spin–lattice relaxation times from electron paramagnetic resonance (EPR).

Keywords Magnetism · Iron implanted oxides · Magnetic ion · Mössbauer spectroscopy

1 Introduction

Magnetism in solids generally requires the presence of magnetic ions which by exchange coupling may form an ordered magnetic phase. Usually all or many of the material's constituent ions are magnetic (e.g., iron, magnetite). However, there have been strong efforts to develop materials in which the magnetic ions constitute only a minor fraction with the aim to produce materials with new functionalities. An example is the field of 'spintronics' where the spin of the electron, in addition to its charge, is used in novel electronic devices [1]. Semiconductors and oxides are utilized that can be doped with magnetic transition-metal ions (TM) in the percent range leading to magnetism ("dilute magnets" in contrast to the more usual "concentrated magnets" mentioned before). Originally, the main focus was on III–V semiconductors like GaAs or InAs doped with Mn. Later, II–VI materials doped with Mn and other TMs from the 3d series were considered, too. The indirect coupling of the magnetic TM ions by charge carriers (holes) were said to be the source of the observed magnetism [2].

Even more unusual results appeared stating that not only dilute TMs but also simple defects like vacancies might lead to magnetism in wide gap semiconductors, e.g., metal oxides like HfO_2 or ZnO. The interaction of partially occupied defect levels were assumed to lead to ordered spin arrangements (magnetism) when enough such centers were present [3].

The latter prospect triggered our project to use Mössbauer spectroscopy (MS) on ^{57}Fe in diverse metal oxides in which a large amount of defects are introduced. Defect introduction is achieved by implanting the Mössbauer source activity ^{57}Mn into the oxides which produces defect concentrations in the percent range around the Mössbauer probe in its own implantation cascade. It is known that the probe will end up in a region with individual vacancies and interstitials. In addition, depending on the material, strongly damaged zones or even amorphous pockets may develop around or close to the probe. The ^{57}Mn ions are provided by the ISOLDE facility at CERN.

2 Experimental aspects

Beams of radioactive ^{57}Mn ($T_{1/2} = 1.5$ min) are produced at the ISOLDE facility at CERN by 1.4 GeV proton induced fission in a heated UC_2 target. Mn ions are singled out by an elemental selective laser ionization process [4]. After acceleration and magnetic mass separation a beam of 1–2 $\times$ 10^8/s Mn^{1+} is obtained at an energy of 50–60 keV and directed to the experimental chamber. Single ion implantation is achieved by keeping the total fluence for each sample $\leq 10^{12}$ cm^{-2} corresponding to 10^{16} cm^{-3}, creating a truly dilute sample. Mössbauer emission spectra were measured

on the daughter ^{57m}Fe ($T_{1/2} = 98$ s) with a gas filled resonance detector equipped with an ^{57}Fe enriched stainless steel electrode. Isomer shifts are given relative to an α-Fe spectrum at room temperature. Due to the short Mn halflife implantation and measuring temperatures are identical. A special feature is that in the Mn/Fe decay an average recoil energy of 40 eV is imparted to the ^{57}Fe probe. This can create single defects even when implantation induced defects have found some annealing during the 98 s halflife of Mn at elevated temperatures. In some cases samples have been mounted in a way that Mössbauer measurements in an external field of 0.6 T could be made.

3 Magnetism in Mössbauer spectroscopy

When magnetism is discussed in Mössbauer spectroscopy usually a six line spectrum is meant where the probe ^{57}Fe sits in a magnetic field $\mathbf{B}$ which is either an external field $\mathbf{B}_{ext}$ or stems from magnetically ordered systems leading to an effective magnetic field $\mathbf{B}_{eff}$. The interaction is expressed by $\mathbf{H} = -\boldsymbol{\mu}\cdot\mathbf{B} = -g_N\beta_N\mathbf{I}\cdot\mathbf{B}$ involving the nuclear spin operator $\mathbf{I}$ and a classical field $\mathbf{B}$. $\mathbf{B}_{eff}$ is temperature dependent showing that the seemingly static $\mathbf{B}_{eff}$ as given, e.g., by a Weiss molecular field, is the net result of an ensemble of individual spins fluctuating between different allowed spin quantum states. Due to the presence of the Weiss field the spin will have on the average a preferred direction counteracted by thermodynamic properties.

Paramagnetism is another magnetic phenomenon observable by MS which under certain conditions also leads to magnetically split spectra. An ion with unfilled electron shells and not bound in a magnetic exchange field experiences a magnetic hyperfine field $\mathbf{B}_{Hf}$ at its nucleus resulting from electron spin and orbital angular momentum. Usually, paramagnetic materials show a single line spectrum (or doublet due to quadrupole interaction) which results from the fact that $\mathbf{B}_{Hf}$ shows rapid fluctuations averaging to zero because there is no preferred field direction [5]. Only in the particular case of a static $\mathbf{B}_{Hf}$ magnetic field splitting will arise. The explicit conditions to observe such a static field are given by: (1) $\tau_C \geq \tau_L$ and (2) $\tau_C \geq \tau_N$, where τ_C is the fluctuation time of the field, τ_L is the time for a full Larmor precession of the nucleus and τ_N the lifetime of the excited Mössbauer state. If τ_C is neither small enough for a complete field averaging nor long enough to provide a static field situation one observes relaxation effects affecting the spectra (line broadening and line distortion).

To express $\mathbf{B}_{Hf}$ in such a case electron spin operators have to be involved. Here, we present Mössbauer spectroscopy investigations of Fe atoms in ionic compounds like ZnO and other metal oxides. 3d transition metals (TM) like Fe substitute for Zn when incorporated in these materials and display charge states 2+ and 3+ (1+ and 4+ is also suspected sometimes). In a weak crystal field (CF), as in ZnO, compared to the electron coupling energy, high spin configurations are formed (maximum number of unpaired spins) according to Hund's rules. For the 5 d-electrons of Fe^{3+} a $^6S_{5/2}$configuration ($L = 0$, $S = 5/2$, $J = 5/2$) and the 6 for Fe^{2+} a $^5D_4$ ($L = 2$, $S = 2$, $J = 4$) configuration results. The Fe^{3+} state has vanishing orbital momentum $L = 0$ which means that it is only weakly coupled to the lattice. With its spin $S = 5/2$ it can it interact mainly with other spins. When coupling to the lattice is expressed by spin lattice relaxation time T_1 and coupling to other spins by T_2 (spin–spin relaxation)

one expects for L = 0 (Fe^{3+}) long T_1 which is favorable for observing static $\mathbf{B}_{Hf}$ if a shorter T_2 does not prevent this. For Fe^{2+} however, L = 2 speaks for short T_1 averaging the magnetic hyperfine interaction (-to zero-).

How the magnetic HFI of the Fe^{3+} term becomes observable by MS is demonstrated by the following observations: the $^6S_{5/2}$ state is split in an axially symmetric crystal field (CF) into three Kramers doublets $S_Z = \pm 1/2$, $\pm 3/2$ and $\pm 5/2$ (lowest), split only by a few K so that at temperatures higher than a few K all doublets are populated. Each doublet creates its own $\mathbf{B}_{Hf}$ at the nucleus (+ and − yields the same field but with different sign). As result the final magnetic structure is a superposition of the individual Kramers states. The interaction for an individual doublet involves both nuclear and electron spin operators: $\mathbf{H} = \mathbf{H}_{CF} + \mathbf{H}_{HFI} = \mathbf{H}_{CF} + A\mathbf{I}\cdot\mathbf{S}$. $\mathbf{H}_{CF}$ is the CF operator containing electron spin operators **S**, A is the hyperfineinteraction constant. Since for this expression eigenstates are a combination of nuclear $|I,m_I\rangle$ and electron spin wave functions $|S,S_Z\rangle$, rather complicated spectra may result with more or less than six lines of uneven splitting and likewise unfamiliar line intensities. 'Normal' six line spectra ('effective magnetic field' spectra) can be obtained by applying a strong external field $\mathbf{B}_{ext}$ in the z-direction which decouples nuclear and electron spins and lets the nuclei (and electron spins) precess around the z-direction. S_Z and m_I become good quantum numbers and the three doublets are observed as sum of three 'normal' sextets with $\mathbf{B}_{Hf}$ proportional to S_Z, $\mathbf{B}_{Hf} = A\cdot S_Z/g_N\cdot\beta_N$. To obtain the total field at the nucleus one needs to add $\mathbf{B}_{ext}$. A is an effective hyperfine constant which for the L = 0 term is the free ion hyperfine constant 'a' perturbed by size and symmetry of the CF. $\mathbf{B}_{ext}$ splits (broadens) the Mössbauer spectral lines because it adds to $\mathbf{B}_{Hf}$ consisting of + and - components but is a rather small effect at 0.6 T (see below) compared to $\mathbf{B}_{Hf}$. Finally, the nuclear quadrupole interactions have to be added, also small against $\mathbf{B}_{Hf}$.

4 Experimental results and discussion

4.1 ZnO

Single crystals of hydrothermally grown ZnO (Wurtzit structure) were implanted with ^{57}Mn at an incident angle of 30° relative to the sample surface normal. The temperature for implantation and Mössbauer measurements ranged from 77 to 837 K. Figure 1 shows a spectrum taken at 300 K in zero external field and the γ radiation taken at an angle $\theta = 60°$ to the sample.

The spectrum shows broad lines with four discernible peaks at velocities out to about 8 mm/s and a rather complicated structure forming the central part around zero. Also, a broad background lingers below the peaks. This spectrum was originally fit [6] with five components, a magnetic sextet, two quadrupole doublets D2 and D3 and two magnetic field distributions accounting for the broad lines and high background. An ordered magnetism leading to this complex spectrum was tentatively assumed. To gain more information spectra were measured over a large temperature range, Fig. 2.

It is seen that the spectral fraction of the sextet is increasing with increasing temperature and that above about 400 K the spectra show line broadening of the sextet lines, which increase with rising temperature T, but the lines are still visible

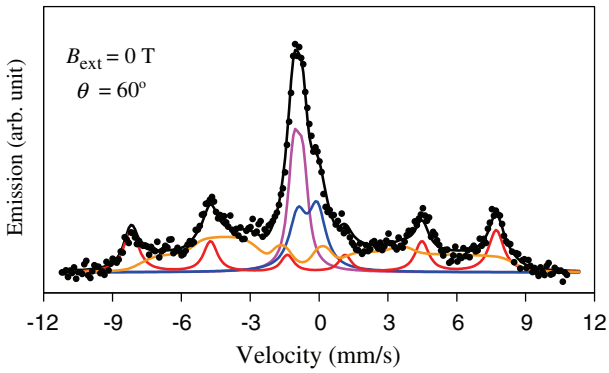

Fig. 1 Room-temperature Mössbauer spectrum obtained after implantation into ZnO single crystal in zero external magnetic field (from [7])

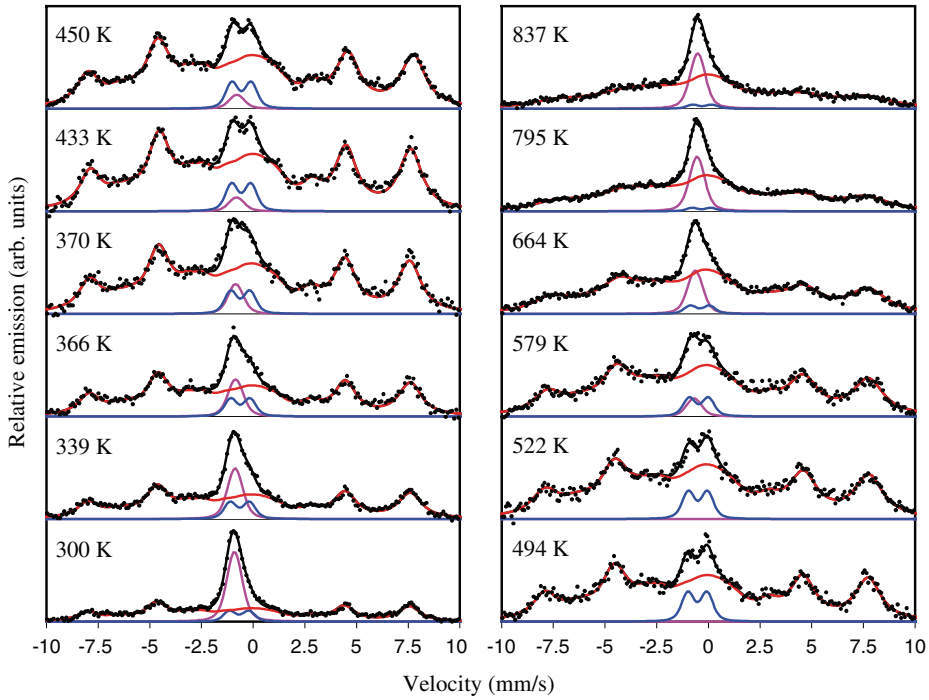

Fig. 2 Mössbauer spectra obtained in zero external magnetic field at the temperatures indicated. *Solid lines* show the fitting components and their sum

at 837 K. In addition spectra in an external magnetic field of 0.6 T were measured. Figure 3 shows spectra measured at RT with the field parallel to the crystal's c-axis and the γ's observed under 0° (top) and 60°(bottom) to the c-axis.

It is evident that the spectra have sharpened up and the broad background has disappeared. This spectrum allows a clear-cut decision that the sextet is not due to an ordered magnetic state which would require for the top spectrum (γ's at 0°) the intensities of the middle sextet (lines 2 and 5) to be zero and in the lower spectrum (60°) the intensities of outer (lines 1 and 6) and middle sextet to be the same. On the

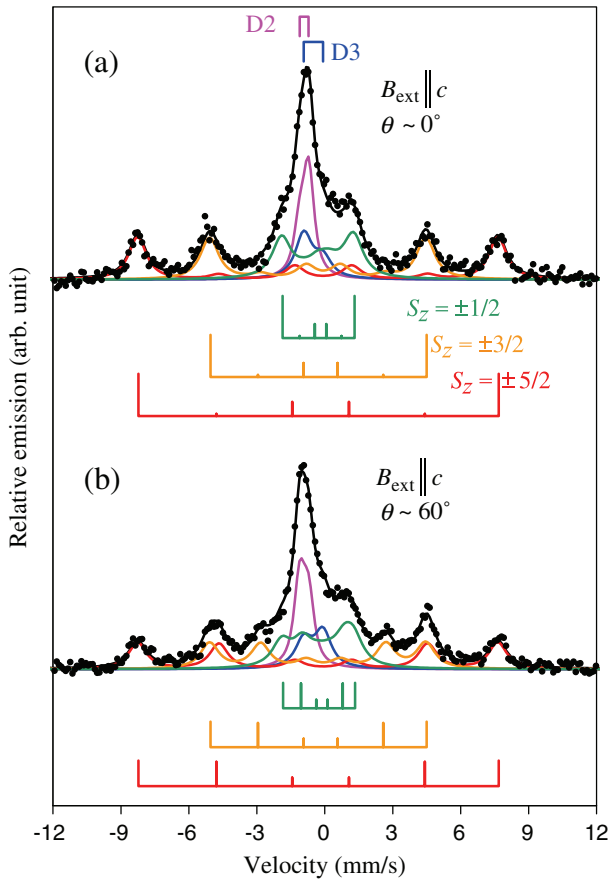

Fig. 3 Room temperature Mössbauer spectra obtained in $\mathbf{B}_{ext} = 0.6$ T applied parallel to the *c*-axis and at two different emission angles (θ) relative to the *c*-axis as indicated (adapted from [7])

other hand, if one assumes the experimental spectra to be of paramagnetic origin, then, as outlined above, one expects the spectrum to be the sum of the 3 Kramers doublets as indicated by bars which obviously fits the spectra very well. Table 1 shows the parameters drawn from these fits and assignments given to the components [7].

The sextet has small IS compatible with a high spin 3+ site which was determined from the magnetic behavior. The magnetic field $\mathbf{B}_{Hf} = 49.3$ T is in the range common for 3+ sites in oxides and can be estimated by using the free ion hyperfine constant 'a' slightly modified by the particular CF in which it is embedded, see above. D2 has large IS unique for a high spin 2+ state and can be attributed to Fe on a Zn lattice site in the 'natural' charge state. As expected the 2+ state with L = 2 shows fast relaxation of the $\mathbf{B}_{Hf}$ leaving only the QI which is mostly due to the lattice site having less than cubic symmetry. The magnetic fraction (3+) is also expected to substitute for Zn which is compatible with results from emission channeling which record more than 90% of the Fe ions after implantation on substitutional sites [8]. The different ΔE_Q for D2 and the sextet must be ascribed to the different electronic charge states surrounding the probe. D3 was assigned to interstitial Fe [6] showing large QI and likely is in a 2+ state (fast relaxation).

Table 1 Hyperfine parameters obtained from simultaneous analysis of the spectra in Fig. 3

Component	D2	D3	Param. sextet
Assignment	Fe_{Zn}^{2+}	Fe_I	Fe_{Zn}^{3+}
$\mathbf{B}_{Hf}$ (T)			49.3 (1)
δ (mm/s)	0.91 (1)	0.50 (3)	0.19 (1)
ΔE_Q (mm/s)	−0.39 (2)	+0.85 (4)	+0.12 (1)
Γ (mm/s)	0.17 (3)	0.5 (1)	0.63 (5)

The table lists the magnetic hyperfine field ($\mathbf{B}_{Hf}$) for the $S_Z = \pm 5/2$ sub-sextet, isomer-shift (δ) relative to α-Fe, quadrupole splitting/shift ($\Delta E_Q = 2\varepsilon$ for the sextet), FWHM line-width (Γ) with the detector line-width subtracted

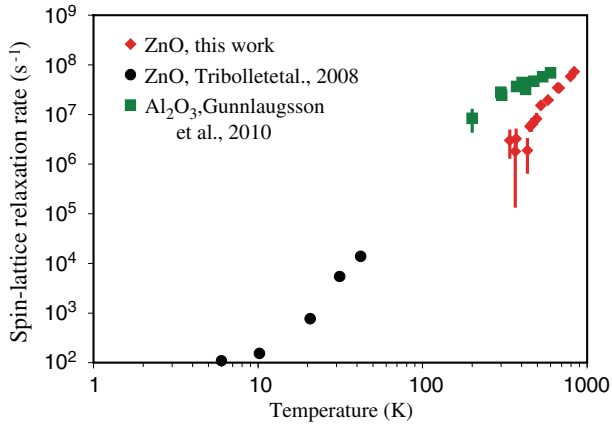

Fig. 4 Spin–lattice relaxation rates obtained here for ZnO using the semi-empirical method of Mølholt et al. [9], compared with the data for Tribollet et al. [11] using EPR technique. In addition data for Al_2O_3 are shown

Comparison of Figs. 1–3 shows more details of the implanted Fe: upon application of $\mathbf{B}_{ext}$ the lines of the magnetic fraction have sharpened and no background (distribution) has to be fitted. Zero field spectra have line widths rather constant up to 579 K above which broadening (relaxation) sets in. Looking at these broad spectral features several mechanisms can contribute: (i) as described above more than 6 lines may be present in each of the Kramers doublets which is especially serious for the inner sextets $\pm 1/2$ and $\pm 3/2$, (ii) distributions of hyperfine fields originating from paramagnetic defects caused by the implantation (e.g. Zn vacancies), (iii) distributions of QI from these defects. In addition to these static interactions (iiii) dynamic interactions like electron spin–electron spin interaction (with paramagnetic defects) expressed by T_2 might contribute. The high dilution prevents spin–spin interaction with other Fe (Mn) ions. The electron spin–nuclear spin interaction with surrounding nuclear spins is too small to be directly observed in MS. Application of $\mathbf{B}_{ext}$ removes effects from (i) as described above and is also able to decouple perturbing fields due to (ii). Feature (iii) will mostly survive and (iiii) is influenced by the field but not removed (if present at all). The relaxation onset above 400 K is mostly due to spin–lattice relaxation which is known to be strongly temperature dependent. Mølholt et al. [9] have recently expressed the line broadening in diverse oxides in terms of T_1 using a relaxation model by Blume and Tijon [10]. Figure 4 shows the result (given as relaxation rate $1/T_1$). Also plotted for comparison are data from Tribollet et al. [11] using EPR obtained in a external field in the low

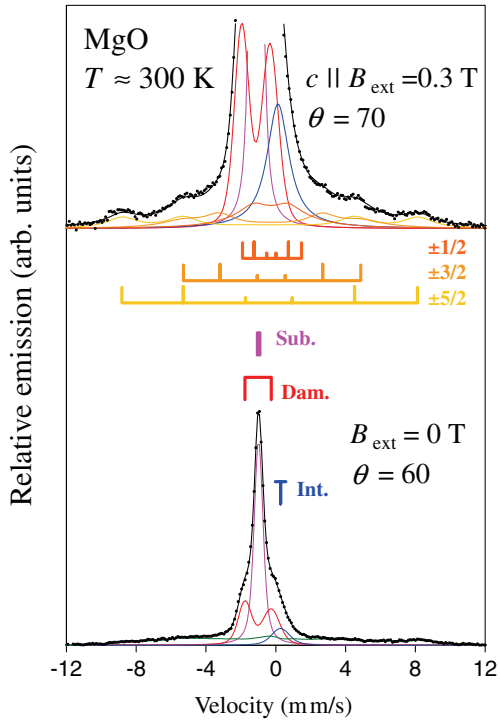

Fig. 5 Room-temperature Mössbauer spectra obtained after implantation into MgO single crystals. *Bottom figure* shows the spectrum obtained in zero field, and the *top spectrum* the wing part of the spectrum obtained in 0.3 T external magnetic field, analyzed in terms of three Kramer doublets

temperature region up to about 40 K. Relaxation data for Al_2O_3 also shown in this figure will be mentioned below.

Fe^{2+} is the 'natural' charge state in ZnO when substituting for Zn. When Fe appears as 3+ local charge compensation must occur, e.g., by nearby Zn vacancies [12]. In implantation experiments defects are provided abundantly and thus the large fraction of 3+ measured can possibly be related to the implantation. Also, implantation may locally decrease the Fermi level in the wide gap ZnO making 3+ more likely than 2+. The dependence on implantation conditions like fluence, preimplantation with non 3d ions (Na) and temperature will be given in a forthcoming paper.

4.2 MgO

A single crystal of MgO (cubic structure) was implanted with ^{57}Mn as described for ZnO [9]. Spectra at zero field and $\mathbf{B}_{ext} = 0.3$ T were taken. Contrary to ZnO four (instead of three) fractions are needed to describe a spectrum taken at RT, see Fig. 5. Magnetic spectral lines are seen at high velocities with $\mathbf{B}_{Hf}$ (about 50 T) similar to that in ZnO, clearly indicative of Fe^{3+}. The close similarity to ZnO shows that the value is mainly given by the hyperfine interaction constant modified by the CF. In addition a broad central part exists which needs for fitting, in addition to a substitutional component Fe_S (2+) and a component assigned to an interstitial line Fe_I, a broad doublet (Dam) indicative of a strongly damaged site or amorphous pocket. Such a component is not observed in ZnO. The reason might be more favorable annealing conditions (lower defect migration energies). The QS for Fe_S is surprising when Fe substitutes Mg in a cubic structure but was also seen in a former publication [13],

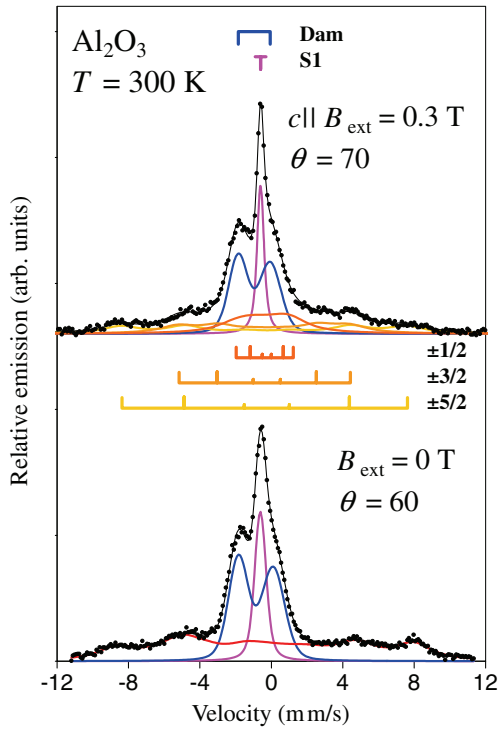

Fig. 6 Room-temperature Mössbauer spectra obtained after implantation into α-Al_2O_3 single crystals. *Bottom figure* shows the spectrum obtained in zero field, and the *top spectrum* the spectrum obtained in 0.3 T external magnetic field, analyzed in terms of three Kramer doublets

Table 2 Hyperfine parameters obtained for ^{57}Fe in α-Al_2O_3

Component	S1	Dam	Param. sextet
Assignment	Fe^{3+} in η-Al_2O_3?	Fe^{2+} in disordered environment	$Fe_{Al}{}^{3+}$
$\mathbf{B}_{Hf}$ (T)			50 (1)
δ (mm/s)	0.546 (4)	0.87 (1)	0.35 (1)
ΔE_Q (mm/s)	0	2.0 (1)	+0.11 (2)[c]
σ (mm/s)	0.007 (10)[a]	0.40(1)/0.48 (1)[b]	n/a

The table lists the magnetic hyperfine field ($\mathbf{B}_{Hf}$) for the $S_Z = \pm 5/2$ sub-sextet, isomer-shift (δ) relative to α-Fe, quadrupole splitting/shift ($\Delta E_Q = 2\varepsilon$ for the sextet), and the Gaussian broadening (σ) with the detector line width subtracted ($\sigma = 0.08$ mm/s) and the Lorentzian width (Γ) set to the natural line-width

[a] At T > 300 K

[b] σ given for left and right legs, respectively

[c] Determined from the $\mathbf{B}_{ext} = 0.3$ T measurement

however, at lower temperatures. The 'smearing' below the magnetic component again is strongly reduced by application of the magnetic field as in ZnO. Mølholt et al. have analyzed the magnetic part of the spectra with a sum of sextets to simulate the broad spectral lines and in particular the temperature dependent line broadening at elevated temperatures assuming T_1 to be responsible for the broadening [9]. It is seen in this analysis that the data overlap quite well with EPR data showing that the relaxation in zero field (MS) and with applied magnetic field (EPR) is comparable and hence, that T_1 can be used as fluctuation time τ_C for describing line broadening (relaxation) in MS.

4.3 Al_2O_3

In this material (single crystal α-Al_2O_3) the 'natural' charge state for Fe substituting Al is 3+. Upon Mn implantation again several components show up see Fig. 6 and Table 2 [14]. As described above for the case of MgO data were taken in zero field and with applied field of 0.3 T. The sextet has $\mathbf{B}_{\mathrm{Hf}}$ close to 50 T, again similar to the one observed in ZnO and MgO identifying this component as Fe^{3+}. The central part of the spectrum consists of an asymmetric doublet (Dam), indicative of an amorphous surrounding with IS compatible with 2+ which is still present at the highest temperature of 666 K, indicating large defect migration energies. A cubic component (S1) which possibly is a nano-precipitate of η-Al_2O_3 is assigned in addition [14]. An analysis of the relaxation rate of the magnetic component as described for ZnO is included in Fig. 4. Again the 'smearing' intensity below the magnetic component is reduced by application of the magnetic field.

5 Summary and conclusion

Implanted Mn/Fe ions in metal oxides lead to various charge states and lattice sites for the Fe ions. When in a 3+ charge state, the Fe ion has an extremely long relaxation time and displays paramagnetic spectra. This is most clearly seen in ZnO. Application of an external magnetic field decouples perturbing fields and yields spectra reflecting effective magnetic fields. Earlier expectations that the magnetic structure seen could correspond to an ordered magnetic state which might be promoted by magnetic defects produced in high concentration around the implanted Fe could not be confirmed.

Acknowledgements This work was supported by the European Union Sixth Framework through RII3-EURONS. K. Bharuth-Ram, W. Dlamini, H. Masenda, D. Naidoo and W. N. Sibanda acknowledge support from the South African National Research Foundation. T. E. Mølholt acknowledges support from the Icelandic Research Fund. Financial support of the German BMBF (contract no. 05KK4TS1/9) is also gratefully acknowledged, Y. Yoshida is acknowledged for help during data taking.

References

1. Das Sarma, S.: Am. Sci. **89**, 516 (2001)
2. Dietl, T., et al.: Science **287**, 1019 (2000)
3. Zunger, A., et al.: Physics **3**, 53 (2010)
4. Fedoseyev, V.N., et al.: Nucl. Instrum. Methods **B126**, 88 (1997)
5. Goldanskii, V.I., Herber, R.H. (eds.): Chemical Applications of Mössbauer Spectroscopy. Academic Press, New York (1968)
6. Weyer, G., et al.: J. Appl. Phys. **102**, 113915 (2007)
7. Gunnlaugsson, H.P., et al.: Appl. Phys. Lett. **97**, 142501 (2010)
8. Rita, E., et al.: Appl. Phys. Lett. **85**, 4899 (2004)
9. Mølholt, T.E., et al.: Hyperfine. Interact. (2010, accepted)
10. Blume, M., Tijon, J.A.: Phys. Rev. **165**, 446 (1968)
11. Tribollet, J., Behrends, J., Lips, K.: Europhys. Lett. **84**, 20009 (2008)
12. Azamat, D.V., Fanciulli, M.: Physica. B **401–402**, 382 (2007)
13. Leider, H.R., Pipkorn, D.N.: Phys. Rev. **165**, 494 (1968)
14. Gunnlaugsson, H.P., et al.: Hyperfine. Interact. (2010). doi:10.1007/s10751-010-0184-5

Paper VI

Spin-lattice relaxations of paramagnetic Fe^{3+} in ZnO

Mølholt, T. E., Gunnlaugsson, H. P., Johnston, K. Mantovan, R., Masenda, H., Naidoo, D., Ólafsson, S., Bharuth-Ram, K., Gislason, H. P., Langouche, G., Sielemann, R., Weyer, G., and the ISOLDE Collaboration:

*Physica Scripta, Volume **T148**,*
pp. 014006 (2012).

DOI: 10.1088/0031-8949/2012/T148/014006

IOP Publishing Physica Scripta
Phys. Scr. **T148** (2012) 014006 (4pp) doi:10.1088/0031-8949/2012/T148/014006

Spin–lattice relaxations of paramagnetic Fe^{3+} in ZnO

T E Mølholt[1], H P Gunnlaugsson[2], K Johnston[3], R Mantovan[4], H Masenda[5], D Naidoo[5], S Ólafsson[1], K Bharuth-Ram[6,7], H P Gislason[1], G Langouche[8], R Sielemann[9], G Weyer[2] and the ISOLDE Collaboration[3]

[1] Science Institute, University of Iceland, Dunhaga 3, 107 Reykjavík, Iceland
[2] Department of Physics and Astronomy, Aarhus University, DK-8000 Aarhus C, Denmark
[3] PH Department, ISOLDE/CERN, 1211 Geneva 23, Switzerland
[4] Laboratorio MDM, IMM-CNR, Via Olivetti 2, 20846 Agrate Brianza (MB), Italy
[5] School of Physics, University of the Witwatersrand, WITS 2050, South Africa
[6] School of Physics, University of KwaZulu-Natal, Durban 4001, South Africa
[7] iThemba LABS, PO Box 722, Somerset West 7129, South Africa
[8] Instituut voor Kern-en Stralingsfysika, University of Leuven, B-3001 Leuven, Belgium
[9] Helmholtz-Zentrum Berlin für Materialien und Energie, D-14109 Berlin, Germany

E-mail: tem4@hi.is (T Mølholt)

Received 23 September 2011
Accepted for publication 31 October 2011
Published 15 March 2012
Online at stacks.iop.org/PhysScr/T148/014006

Abstract
The spin–lattice relaxation rate of paramagnetic Fe^{3+} in single-crystalline ZnO has been determined following low-fluence ($\Phi < 10^{12}\,cm^{-2}$) 60 keV implantation of $^{57}Mn^{+}$ ($T_{1/2} = 1.5$ min) and emission Mössbauer spectroscopy on the ^{57}Fe daughter nucleus in the temperature range from 300 to 664 K. The spin–lattice relaxation of Fe^{3+} is found to follow a T^9 temperature dependence, in contrast to the T^2 dependence expected for a two-phonon Raman process determined in both single-crystal MgO and α-Al_2O_3 using the same analysis method of the Mössbauer spectra measured without an applied external magnetic field. This is an unexpected result since ZnO has a lower Debye temperature than both MgO and α-Al_2O_3.

PACS numbers: 76.30.Fc, 71.20.Be, 71.70.Ej, 71.55.Gs, 82.80.Ej, 82.56.Na, 81.05.Dz, 41.75.Ak

(Some figures may appear in colour only in the online journal)

1. Introduction

The ^{57}Fe Mössbauer spectra obtained after implantation of $^{57}Mn^{+}$ ($T_{1/2} = 85.4$ s) into selected single-crystal oxide samples at fluences $\Phi < 10^{12}\,cm^{-2}$ are characterized by sextet-like features assigned to Fe^{3+} exhibiting slow paramagnetic relaxation ($\tau^{-1} < 10^{7}\,s^{-1}$). Such features, which can be easily distinguished in the Mössbauer spectra as they have intensity in the wings of the spectrum for $|v| > 4\,mm\,s^{-1}$, have been reported in MgO [1], α-Al_2O_3 [2] and ZnO [3, 4].

In the absence of an applied external magnetic field, which is the case here, these paramagnetic Fe^{3+} features display complicated/smeared patterns, since the emission lines originate from mixed nuclear and electronic states. The $S_Z = \pm 5/2$ state is least affected by this effect and is often observed as a 'normal' sextet, while the $S_Z = \pm 1/2$, $\pm 3/2$ states give rise to more complicated spectral shapes [5]. The Kramers rule states that Kramers doublets cannot be separated by zero-field splitting. However, applying a sufficiently large external magnetic field (> 0.3 T), the electronic states decouple from the nuclear states, and the Mössbauer spectrum can be analysed in terms of three sextets originating from the three paramagnetic Kramers doublets ($S_Z = \pm 1/2, \pm 3/2$ and $\pm 5/2$) [3, 4].

The temperature dependence of Mössbauer spectra obtained without the application of an external magnetic field can be analysed in terms of an empirical model, making use of a number of sextets described by the Blume and Tjon [6] line shape, which takes into account the temperature-dependent

relaxation rate based on the sextet line shape in the Mössbauer spectra of the relaxing Fe [1]. This model can be used to extract the temperature-dependent broadening of the Fe^{3+} spectrum and thereby estimate the relaxation rate in the range of $\tau^{-1} \sim 4 \times 10^6 - 1 \times 10^8\,s^{-1}$. This sensitive range is directly related to the mean lifetime ($\tau_M = 140\,ns$) of the excited ^{57}Fe nuclear state [1, 5]. In the case of MgO, the relaxation rates extracted by this method [1] were found to be in agreement with the spin–lattice relaxation rates obtained by electron paramagnetic resonance (EPR) spectroscopy [7], proving that the proposed procedure based on Mössbauer spectroscopy is suitable for obtaining the temperature-dependent relaxation rates. Within the sensitivity range, this method is mostly sensitive to the lifetime broadening of the Blume–Tjon sextets, which is the same as that for the more general relaxation model based on the Clauser model [8]. The Clauser model was successfully applied to the analysis of spin–lattice relaxation of paramagnetic Fe^{3+} in $NH_4Al(SO_4)_2{\cdot}12H_2O$ by Bhargava *et al* [9], where the Mössbauer spectra were obtained in an applied magnetic field.

In this paper, we present the determination of spin–lattice relaxation rates of Fe^{3+} in ZnO by using the same empirical model, by analysing the line broadening of the Mössbauer spectra of Mn/Fe-implanted ZnO in the temperature range of 300–664 K. The results are compared with the results obtained in MgO and α-Al_2O_3.

2. Experimental details

A radioactive beam of $^{57}Mn^+$ ($T_{1/2} = 85.4\,s$) was produced at the ISOLDE facility at CERN by 1.4 GeV proton-induced fission in a heated UC_2 target and specific element-selective laser multi-photon ionization [10]. After acceleration to 60 keV and magnetic mass separation, a beam of $\sim 1.9 \times 10^8\ ^{57}Mn^+\,s^{-1}$ was obtained. The $^{57}Mn^+$ has been implanted into ZnO single crystals [0001] (commercially available from Crys-Tec GmbH), and Mössbauer spectroscopy has been performed on daughter ^{57}Fe impurities ($T_{1/2} = 98\,ns$). This method allows us to study Fe impurities at concentrations $< 10^{-4}$ at.%. The samples were mounted on an implantation chamber and held at temperatures ranging from 300 to 664 K.

The implantation was performed at an incident angle of 30° relative to the sample surface normal. Mössbauer emission spectra were measured online with an acetone gas-filled parallel-plate avalanche resonance detector, equipped with ^{57}Fe-enriched stainless steel. The detector was mounted outside the implantation chamber on a conventional constant-acceleration drive system at 90° to the beam direction (60° relative to the crystal surface normal). Velocities and isomer shifts are given relative to the centre of the α-Fe spectrum at room temperature.

3. Results and analysis

Figure 1 show a ^{57}Fe Mössbauer spectrum obtained after implantation of ^{57}Mn into a ZnO single crystal held at 644 K. The magnetic sextet structure has broadened compared to the Mössbauer spectrum at room temperature (see figure 2) and is close to collapsing at this high temperature but is still

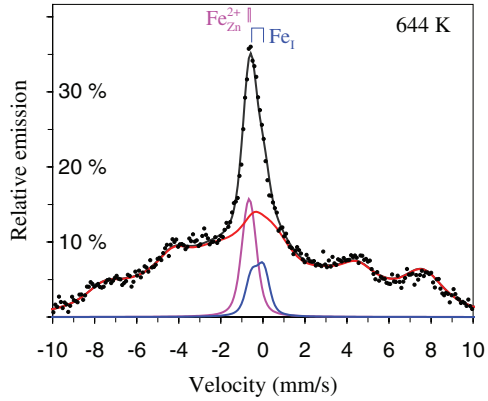

Figure 1. Dots represent the ^{57}Fe Mössbauer spectrum obtained after implantation of $^{57}Mn^+$ into single-crystal ZnO at 644 K. The solid lines show the fitting components and their sum. The two central components are indicated by bars.

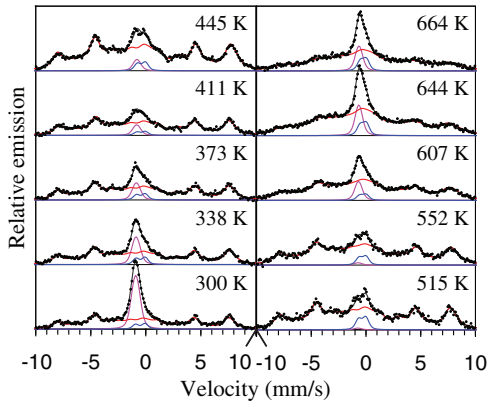

Figure 2. Representative ^{57}Fe Mössbauer spectra (dots) of the series at the temperatures indicated. The fitted components and their sum are shown by solid lines.

discernible. The central part has been analysed in terms of two quadrupole doublets assigned to substitutional Fe^{2+} on Zn sites (Fe^{2+}_{Zn}) and interstitial Fe (Fe_I) [3, 11]. The interstitial line is characterized by having a stable area fraction of about 5–10% throughout the temperature series, created by the recoil ($\langle E \rangle_R = 40\,eV$) imparted on the ^{57}Fe daughter atoms in the decay of ^{57}Mn. The room temperature values of the hyperfine parameters are taken from [3].

Figure 2 shows representative Mössbauer spectra of the temperature series from 300 to 664 K. The plot includes the spectral components used to analyse the spectra by performing a simultaneous fit of the whole temperature series data. Figure 3 summarizes the relative area fractions of the three spectral components Fe^{2+}_{Zn}, Fe_I and the magnetic sextet structure (labelled Mag).

The temperature dependence of the quadrupole splitting of Fe^{2+}_{Zn} was analysed in terms of the model of Ingalls [12] for high-spin Fe^{2+} in a near-tetrahedral environment. Here, the

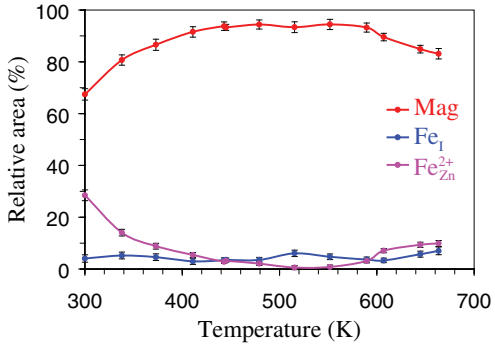

Figure 3. Relative area fractions in the analysed ZnO temperature series of the three components as indicated (Mag is the magnetic split component). Error bars correspond to a variance of 1σ.

temperature dependence is given by the equation

$$\Delta E_{\mathrm{Q}}(T) = \Delta E_{\mathrm{Q,L}} + \Delta E_{\mathrm{Q,V}} \cdot \tanh\left(\frac{E_{\mathrm{o}}}{2kT}\right), \qquad (1)$$

where $\Delta E_{\mathrm{Q,L}}$ is a contribution from the non-cubic arrangement of lattice atoms, which can be assigned the value $\Delta E_{\mathrm{Q,L}} = +0.12\,\mathrm{mm\,s^{-1}}$, based on the quadrupole shift of high-spin Fe^{3+}_{Zn} in ZnO [3]. E_{o} is the splitting of the $d_{x^2-y^2}$ and d_{z^2} orbitals and $\Delta E_{\mathrm{Q,V}}$ is the quadrupole splitting of Fe in the d_{z^2} orbital. Using the value $\Delta E_{\mathrm{Q,V}} = -2.5\,\mathrm{mm\,s^{-1}}$ [13], we obtain the fitting value $E_{\mathrm{o}} = 10(2)$ meV.

It is more difficult to estimate the appropriate temperature dependence of the quadrupole splitting of Fe_I from the experimental data, since this component only dominates the spectra in a relatively narrow temperature interval. An empirical model with a single exponent proved sufficient:

$$\Delta E_Q = Q_0 \exp(-(T - T_0)/\Delta_E), \qquad (2)$$

where the parameters have the following set of values: $T_0 = 300\,\mathrm{K}$ and $Q_0 = 0.85\,\mathrm{mm\,s^{-1}}$, and $\Delta_E = 841(120)\,\mathrm{K}$ is determined from the simultaneous fit of the data.

The magnetic component (labelled Mag in figure 3) and the line broadening of the structure are the focus of this work. The asymmetric magnetic structure, due to paramagnetic Fe^{3+}, was analysed using five relaxing sextets as described in [1]. This allows us to evaluate the spin–lattice relaxation rate which is related to the line broadening. For the spectrum at 300 K the relaxation rate was set to $\tau^{-1} = 0$ and the outermost relaxation sextet with a hyperfine field of $\sim 48\,\mathrm{T}$ was added and the other four smaller inner sextets were adjusted empirically before the simultaneous fitting of the complete temperature series.

Above 450 K, an increased broadening of the magnetic structure becomes visible, and at the highest measured temperature the sextet structure can still be discerned. Above about 730 K, the magnetic structure has completely collapsed and disappeared in the wings of the spectrum, leaving only the central structure [11]. The maximum temperature presented here is therefore 664 K, which is close to the limit for extracting the relaxation rate using the described method. The

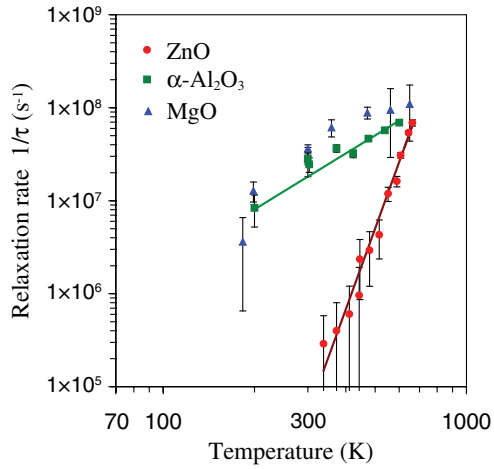

Figure 4. Relaxation rates ($1/\tau$) obtained in this work (red circles) in comparison with those previously measured for MgO (blue triangles) and α-Al_2O_3 (green squares) single-crystal oxides. Both MgO and α-Al_2O_3 follow a T^2 temperature dependence above about 300 K. The solid green line indicates a T^2 dependence of α-Al_2O_3 [2] and MgO data [1]. Clearly, ZnO follows a different slope and it fits with a T^9 dependence as shown by the solid red line. Error bars indicate a variance of 1σ.

relaxation rate obtained in this study of ZnO is shown in figure 4, and is compared together with the data obtained from α-Al_2O_3 [2] and MgO [1] using the same method.

All variables modelling the temperature series were analysed in a simultaneous fitting procedure and the isomer shifts of all components were set to follow the expected second-order Doppler shift.

The central components were fitted using Voigt profiles with temperature-independent Gaussian broadening. The Lorenztian broadening was set to the detector line width and the quadrupole splittings of the Fe^{2+}_{Zn} and Fe_I were restricted to following equations (1) and (2), respectively.

No evidence of any amorphous component, caused by the Mn ion implantation, was observed in our data at the explored temperatures. This is very likely due to ZnO being a radiation hard material [14, 15].

4. Discussion

The electronic spin relaxation in a crystal originates from spin–spin interaction between paramagnetic ions and spin–lattice interaction transferring energy between the electronic spin and the lattice phonons. In our experiments, the ion-implanted concentration of Mn/Fe is low ($< 10^{-4}$ at.%), which gives a spacing > 100 atomic lattice constants between the Mn/Fe atoms. Thus the probability of having interacting Mn/Fe pairs is low, which results in negligible spin–spin relaxation. Furthermore, the spin–spin relaxation process is usually independent of temperature. Therefore, we conclude that the observed temperature dependence of Fe^{3+} spin–lattice relaxation rates in ZnO (as in MgO and α-Al_2O_3) is due to

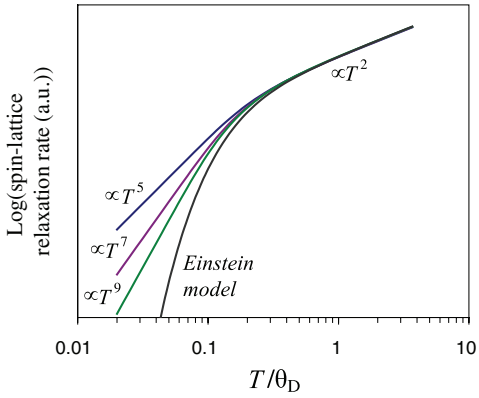

Figure 5. Graphical representation of equations (3) and (4) showing the different temperature dependences related to the Raman process involved. A feature of all the processes is that at $T > \theta_D/3$, they all follow a $\tau^{-1} \propto T^2$ dependence.

the weak spin–lattice interaction between the lattice and the spherical ^{6}S ground state of Fe^{3+}.

The extracted relaxation rate mainly reflects the broadening of the $S_Z = \pm 5/2$ state, as is well observable in the Mössbauer spectra having the largest splitting and sharpest sextet features [1].

A theoretical description of the temperature-dependent spin–lattice relaxation involves different processes that take place in different temperature intervals relative to the Debye temperature [5, 16, 17]. At low temperatures a direct process dominates the spin–lattice relaxation, to which only low-energy phonons contribute. In this case the relaxation rate is linear, i.e. $\tau^{-1} \propto T$. At higher temperatures the two-phonon Raman process dominates. Using the simple Debye approximation, the relaxation rate can be written as

$$\tau^{-1} \propto \left(\frac{T}{\theta_D}\right)^n \int_0^{\theta_D/T} \frac{x^{n-1}e^x}{(e^x-1)^2} dx, \qquad (3)$$

where θ_D is the Debye temperature and n is an integer depending on the process. The first-order and second-order Raman processes result in $n = 7$ and $n = 9$, respectively. For multiple ground states as well as non-Kramers doublets, usually $n = 5$. But for all Raman processes, one expects $\tau^{-1} \propto T^2$ for temperatures $T > \theta_D/3$. A graphical representation of this is shown in figure 5.

If optical phonons are responsible for the Raman process, the Einstein model for the phonon spectrum is usually more appropriate. In this case one finds that

$$\tau^{-1} \propto \frac{e^{-\theta_E/T}}{\left(1-e^{-\theta_E/T}\right)^2}, \qquad (4)$$

where θ_E is the Einstein temperature.

The obtained analysis yields relaxations rates extracted from the ZnO Mössbauer temperature series that follow a T^9 dependence. This is in contrast to the relaxation rates obtained using the same method of implantation and analysis in MgO and α-Al_2O_3, which follow the theoretically predicted T^2 dependence, for $T \gg \theta_D$. This is an unexpected result since the Debye temperature for ZnO has been reported to range from 305 K to above 800 K [18, 19], which is lower than the reported values for both MgO and α-Al_2O_3 of 946 and 1045 K, respectively [20].

5. Conclusion

We have extracted the temperature dependence of the paramagnetic spin–lattice relaxation rate of Fe^{3+} in ZnO, from Mössbauer spectroscopy measurements in the absence of an applied magnetic field. At elevated temperatures ($T > \theta_D/3$) the expected T^2 temperature dependence of the relaxation rate was not observed, as is the case for MgO and α-Al_2O_3. Instead a T^9 temperature dependence was found to fit the extracted data. Despite the fact that a wide range of different values for the Debye temperature has been reported for ZnO, none of them fulfils the criterion for the observed T^9 dependence illustrated in figure 5.

Acknowledgments

This work was supported by the European Union Sixth Framework through RII3-EURONS. KB-R, HM and DN acknowledge support from the South African National Research Foundations. TEM acknowledges support from the Icelandic Research Fund.

References

[1] Mølholt T E *et al* 2010 *Hyperfine Interact.* **197** 89
[2] Gunnlaugsson H P *et al* (The ISOLDE Collaboration) 2010 *Hyperfine Interact.* **198** 5
[3] Gunnlaugsson H P *et al* 2010 *Appl. Phys. Lett.* **97** 142501
[4] Gunnlaugsson H P *et al* (The ISOLDE Collaboration) 2010 *Hyperfine Interact.* **197** 43
[5] Mørup S 2010 *Mössbauer Spectroscopy and Transition Metal Chemistry: Fundamentals and Application* ed P Gütlich, E Bill and A X Trautwein (Berlin: Springer) chapter 6, pp 201–34
[6] Blume M and Tjon J A 1968 *Phys. Rev.* **165** 446
[7] de Biasi R S and Portella P D J 1980 *J. Magn. Magn. Mater.* **15** 737
[8] Clauser M J 1971 *Phys. Rev.* B **3** 3748
[9] Bhargava S C, Knudsen J E and Morup S 1979 *J. Phys. C: Solid State Phys.* **12** 2879
[10] Fedoseyev V N *et al* (The ISOLDE Collaboration) 1997 *Nucl. Instrum. Methods* B **126** 88
[11] Weyer G, Gunnlaugsson H P, Mantovan R, Naidoo D, Bharuth-Ram K, Fanciulli M and Agne T 2007 *J. Appl. Phys.* **102** 113915
[12] Ingalls R 1964 *Phys. Rev.* **133** A787
[13] Gunnlaugsson H P *et al* 2012 *Appl. Phys. Lett.* submitted
[14] Look D C, Reynolds D C, Hemsky J W, Jones R L and Sizelove J R 1999 *Appl. Phys. Lett.* **75** 811
[15] Auret F D, Goodman S A, Hayes M, Legodi M J, van Laarhoven H A and Look D C 2001 *Appl. Phys. Lett.* **79** 3074
[16] Abragam A and Bleaney B 1970 *Electron Paramagnetic Resonance of Transition Ions* (Oxford: Clarendon) chapter 10
[17] Srivastava K K P and Mishra S N 1980 *Phys. Status Solidi* b **100** 65
[18] Reeber R R 1970 *J. Appl. Phys.* **41** 5063
[19] Wang L and Giles N C 2003 *J. Appl. Phys.* **94** 973
[20] Sangster M J L, Peckham G and Saunderson D H 1970 *J. Phys. C: Solid State Phys.* **3** 1026

Paper VII

Lattice locations and properties of Fe in Co/Fe co-implanted ZnO

Gunnlaugsson, H. P., Johnston, K., **Mølholt, T. E.**, Weyer, G., Mantovan, R., Masenda, H., Naidoo, D., Ólafsson, S., Bharuth-Ram, K., Gíslason, H. P., Langouche, G., Madsen, M. B., and the ISOLDE Collaboration:

*Applied Physics Letters, Volume **100**,*
Issue 4, id. 042109 (4 pages) (2012).

DOI: 10.1063/1.3679692

Lattice locations and properties of Fe in Co/Fe co-implanted ZnO

H. P. Gunnlaugsson,[1,a)] K. Johnston,[2] T. E. Mølholt,[3] G. Weyer,[1] R. Mantovan,[4] H. Masenda,[5] D. Naidoo,[5] S. Ólafsson,[3] K. Bharuth-Ram,[6,7] H. P. Gíslason,[3] G. Langouche,[8] M. B. Madsen,[9] and the ISOLDE Collaboration[2]
[1]*Department of Physics and Astronomy, Aarhus University, DK-8000 Aarhus C, Denmark*
[2]*Physics Department, ISOLDE/CERN, 1211 Geneva 23, Switzerland*
[3]*Science Institute, University of Iceland, Dunhaga 3, IS-107 Reykjavík, Iceland*
[4]*Laboratorio MDM, IMM-CNR, Via Olivetti 2, 20864 Agrate Brianza (MB), Italy*
[5]*School of Physics, University of the Witwatersrand, WITS 2050, South Africa*
[6]*School of Physics, University of KwaZulu-Natal, Durban 4001, South Africa*
[7]*iThemba LABS, P.O. Box 722, Somerset West 7129, South Africa*
[8]*Instituut voor Kern-en Stralings fysika, University of Leuven, B-3001 Leuven, Belgium*
[9]*Niels Bohr Institute, University of Copenhagen, DK-2100 Copenhagen, Denmark*

(Received 8 November 2011; accepted 8 January 2012; published online 27 January 2012)

The lattice locations and electronic configurations of Fe in ^{57}Co/^{57}Fe implanted ZnO (to $(5\text{-}6)\times10^{14}$ Fe/cm^{-2}) have been studied by ^{57}Fe Mössbauer emission spectroscopy. The spectra acquired upon room temperature implantation show ~20% of the probe atoms as Fe^{2+} on perturbed Zn sites and the remaining fraction as Fe^{2+} in damage sites of interstitial character. After annealing at 773 K, ~20% remain on crystalline sites, while the damage fraction has partly disappeared and instead a ~30% fraction occurs as high-spin Fe^{3+}, presumably in precipitates. This suggests that precipitation of Co/Fe in ZnO likely takes place at relatively low temperatures, thus explaining some of the discrepancies in the literature regarding magnetic properties of 3d metal-doped ZnO. © *2012 American Institute of Physics*. [doi:10.1063/1.3679692]

An avalanche of experiments were initiated by theoretical predictions[1] that for ZnO, a partial replacement of Zn by magnetic transition-metal (TM) ions could give rise to dilute (ferro)magnetic semiconductors with potential applications in spintronics. Although positive results have been reported,[2] the origin of magnetism in TM-doped ZnO is poorly understood, and there are grossly inconsistent reports in the literature.[3,4]

^{57}Fe Mössbauer spectroscopy is a powerful technique to investigate Fe-doped ZnO as it can probe magnetic interactions on an atomic scale. However, in addition, using this method, contradicting results have been reported; Mössbauer emission spectra (MES) of ^{57}Fe impurities in ZnO single-crystals have been investigated for low fluence ($<10^{12}$ cm^{-2}) implantation of radioactive ^{57}Mn ($T_{1/2}=1.5$ min).[5,6] The spectra are characterized by three components assigned to substitutional Fe^{2+} (Fe^{2+}_{Zn}), substitutional Fe^{3+} (Fe^{3+}_{Zn}) exhibiting slow paramagnetic relaxation, and a minor interstitial Fe (Fe_I) component, created by the recoil ($\langle E_R\rangle=40$ eV) imparted on the ^{57*}Fe daughter atoms in the β^- decay of ^{57}Mn. Conversion electron Mössbauer spectroscopy (CEMS) on ZnO single-crystal samples implanted with $>10^{14}$ ^{57}Fe/cm^2 reveals a very different pattern which has been analyzed in terms of two doublets and a single line assigned to Fe in different charge states.[7–10] The obtained hyperfine parameters are completely different from those obtained by ^{57}Mn ion-implantations,[5,6] indicative of very different lattice locations and/or electronic configurations of Fe after high fluence ($>10^{14}$ cm^{-2}) Fe implantations and low fluence ($<10^{12}$ cm^{-2}) Mn implantations into ZnO.

To fully understand and effectively resolve this discrepancy and also determine whether the chemical nature of the implanted species plays a role, we have obtained ^{57}Fe MES on ZnO single crystals implanted with ^{57*}Co ($T_{1/2}=272$d) decaying to the Mössbauer state of ^{57}Fe.

Radioactive beams of $^{57}Co^+$ ion produced by proton-induced fission in a yttrium oxide target at ISOLDE/CERN were implanted with 60 keV energy at room temperature (RT) into hydrothermally grown ZnO (obtained from CrysTec, GMBH) to fluence $(5\text{-}6)\times10^{12}$ ^{57}Co/cm^2. The beam also contained a significant contribution of stable ^{57}Fe impurities that has been estimated to $(5\text{-}6)\times10^{14}$ ^{57}Fe/cm^2. The crystals were mounted on a rotatable holder to allow for measurements under different γ-ray emission angles (θ) with respect to the ZnO $\langle0001\rangle$ direction. MES were recorded using a resonance detector equipped with stainless steel electrodes enriched in ^{57}Fe. Measurements below RT were obtained by mounting the sample in a closed-cycle He cryostat. Annealing was performed in vacuum ($<10^{-5}$ mbar).

Isomer shifts (δ) and velocities are given relative to the center of the spectrum of α-Fe at RT. The velocity scale is inverted compared to conventional Mössbauer spectroscopy as is the convention in MES.

The RT MES of the as-implanted sample (cf. Fig. 1) under different emission angles clearly show an angular dependence indicating that some of the Co/Fe probes are situated in a local environment, in which their hyperfine interaction depends on the emission angle relative to the lattice orientation. The spectrum obtained at $\theta=0°$ (Fig. 1, top) is practically identical with the CEMS spectra of ^{57}Fe implanted ZnO (Refs. 7–10) when taking into account the reverse velocity scale and broader line-shape of the stainless steel resonance detector. In fact, this spectrum can be

a)Author to whom correspondence should be addressed. Electronic mail: hpg@phys.au.dk.

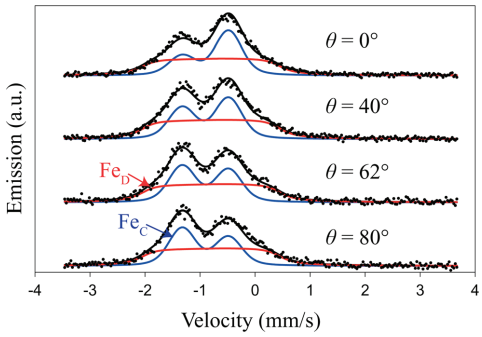

FIG. 1. (Color online) MES obtained on ^{57}Co as-implanted ZnO single crystal sample recorded at different emission angles relative to the sample normal. Fe_D (red) marks a damage component caused by the implantation process and Fe_C (blue) marks a component representing Fe substituting Zn (in crystalline sites).

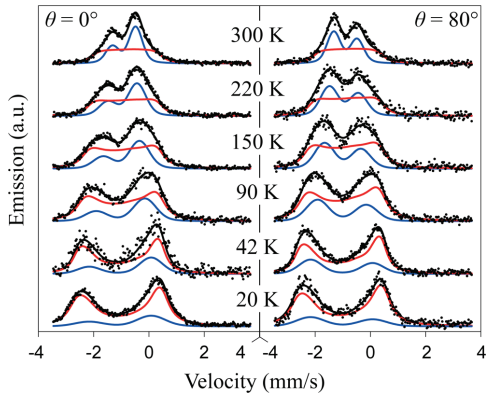

FIG. 2. (Color online) MES of the as-implanted ^{57}Co ZnO sample obtained at the temperatures and emission angles indicated. Red marks the damage component and blue marks the substitutional (crystalline) component. Note that the line-widths in the low temperature measurements are higher due to vibrations of the cryostat.

analyzed in terms of the parameters given in Ref. 7, but this fitting approach is incommensurable with the observed angular dependence of the spectra. The conclusion that there are no real differences in the spectra obtained by MES on ^{57}Co implanted samples and CEMS on ^{57}Fe implanted samples assures that possible after-effects due to the electron capture decay of ^{57}Co do not play a significant role for the interpretation of the data.

The angular dependence of the spectra lends itself to analysis in terms of two contributions: (1) a crystalline fraction (Fe_C) assigned to Fe^{2+} on substitutional Zn sites, showing angular dependence and (2) a damage fraction (Fe_D) showing no angular dependence. Both of these fractions display a pronounced quadrupole splitting. The Fe_D fraction likely originates from Co/Fe in a heavily damaged/amorphous environment due to the implantation process, where the local environment does no longer contain any information on the lattice orientation. The fitting strategy described above was applied for the angular dependent measurements at different temperatures (cf. Fig. 2).

The Fe_C component was analyzed using a Voigt lineshape taking into account the detector line-shape. The Fe_D component was analyzed using a distribution of quadrupole splittings based on linear segments in the distribution function.[11] It was assumed that the relative area fraction of the Fe_C component is independent of the emission angle but possibly temperature dependent. The positions of the Fe_C and Fe_D components were found to vary with the second order Doppler shift as expected, and in the final simultaneous analysis of all spectra, these were restricted to follow such dependence.

The isomer shift of the Fe_C component, $\delta = 0.905(6)$ mm/s, is practically identical with the value of $\delta = 0.91(1)$ mm/s determined for substitutional Fe^{2+}_{Zn} from ^{57}Mn implantation into pure ZnO.[5] The sign of the quadrupole splitting is determined from the angular dependence of the two legs of the doublet. This ratio follows an angular dependence described by $(3 + 3\cos^2\theta)/(5 - 2\cos^2\theta)$, in which θ is the angle between the γ-emission and the principal axis of the electrical field gradient tensor (along the c-axis). For $\Delta E_Q < 0$, the right hand leg will be more intense in MES under $\theta = 0°$. The quadrupole splitting, $\Delta E_Q = -0.82(1)$ mm/s, for Fe_C at RT is significantly higher than that determined from lower fluence ^{57}Mn implantations[5] ($\Delta E_Q = -0.39(2)$ mm/s). In the final simultaneous analysis, ~70% of full polarization of the angular dependence described the data. The temperature dependencies of the quadrupole splittings are illustrated in Fig. 3.

A rough expression for the quadrupole splitting of Fe^{2+} in near-tetrahedral environment can be written,[12]

$$\Delta E_Q(T) = \Delta E_{Q,L} + \Delta E_{Q,V} \cdot \tanh\left(\frac{E_c}{2kT}\right), \qquad (1)$$

where $\Delta E_{Q,L}$ is the lattice contribution to the quadrupole splitting, E_c the level splitting between the z^2 and the x^2-y^2 orbitals, and $\Delta E_{Q,V}$ is the valence electron contribution to the quadrupole splitting from the ion in the lowest lying orbital. Using the value $\Delta E_{Q,L} = +0.12$ mm/s (Ref. 5) gives $\Delta E_{Q,V} = -2.3(1)$ mm/s and $E_c = 20(1)$ meV for Fe_C (line in Fig. 3). The latter value is significantly higher than the value

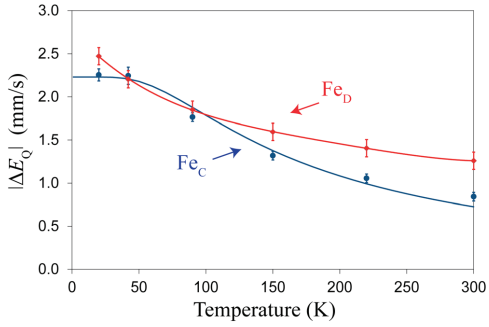

FIG. 3. (Color online) Quadrupole splittings of Fe_C and Fe_D as a function of temperature as determined from simultaneous analysis of the spectra in Fig. 2.

of 10(1) meV determined from low fluence ^{57}Mn implantations into pure ZnO,[13] which suggests that the lattice distortions due to the implantation damage result in an increase of this value or, probably more likely, lead to a distribution of E_c values, which effectively results in a higher average value of E_c as the splitting depends only on the absolute value of E_c. This would also explain that a full polarization of the angular dependence is not observed in the experiments presented here.

For the Fe_D spectral component, the value of the isomer shift, $\delta = 0.77(1)$ mm/s, and the temperature dependence of the quadrupole splitting unambiguously determines it to be due to Fe^{2+}.

The relative spectral area of Fe_C is found to be highly temperature dependent, ~50% at RT decreasing to ~20% at 20 K. This can be explained by a considerably lower Debye temperature (θ_D) of the Fe_D component compared to Fe_C. Using the value $\theta_D = 340$ K for Fe_C expected for Fe^{2+} replacing Zn^{2+} in ZnO[6] gives a value of $\theta_D = 150(20)$ K for the Fe_D component. This low value indicates an interstitial character of the Fe_D component, in accordance with the lower isomer shift value for this site due to less shielding from 3d-electrons in an environment with less rigid bindings to the lattice. However, the absolute spectral area could not be used to determine the Debye temperatures due to noise in the detector system.

The sample was annealed in two stages. After annealing at 673 K (20 min.), only minor changes are observed in the spectra, the main effect being a slightly lower quadrupole splitting of Fe_C of $\Delta E_Q = -0.73(2)$ mm/s, suggesting a less distorted lattice. After annealing at 773 K (30 min.), major changes were observed (cf. Fig. 4).

The fitting model adapted for analyzing the as-implanted ZnO (Figs. 1 and 2) is not adequate for interpreting the MES following the annealing at 773 K due to the occurrence of a new spectral component with $\delta \sim 0.4$ mm/s. The spectra obtained after annealing were, therefore, analyzed with Fe_C following both angular and temperature dependences, Fe_D without angular dependence restricted to follow exactly the same temperature dependence as found from the analysis of the as-implanted spectra and a new component, labeled Fe(III), was introduced to describe the missing area fraction. This new component was simulated as a symmetric quadrupole doublet without any angular dependence. The main findings are that Fe_C displays a smaller quadrupole splitting at RT ($\Delta E_Q = -0.65(2)$ mm/s), and Fe(III) has an isomer shift of $\delta = 0.41(1)$ mm/s and a temperature independent quadrupole splitting of $\Delta E_Q = 0.75(10)$ mm/s, which unambiguously identifies this component as due to high-spin Fe^{3+} showing fast ($>10^{10}$ Hz) paramagnetic relaxations. Using the Debye temperatures for Fe_C and Fe_D determined earlier, the Debye temperature of Fe(III) is determined to be $\theta_D = 360(50)$ K based on the relative areas. Applying the determined Debye temperatures and the spectral areas, it is found that ~20% of the Fe is still located on substitutional Fe^{2+} sites (Fe_C), ~40% is still interstitial Fe^{2+} (Fe_D), and the remainder (~30%) as the new fast-relaxing high-spin Fe^{3+}. The Debye temperature for Fe(III) suggests a substitutional location on Zn sites; however, a strongly disturbed site is indicated by the δ and ΔE_Q values compared to the known values for isolated, dilute Fe^{3+} obtained from ^{57}Mn implantations,[5] which was also found to show a slow paramagnetic relaxation ($<5 \times 10^7$ Hz), i.e., a fully split magnetic spectrum. It is difficult to identify the fast relaxation mechanism, however, for higher implanted fluences (4×10^{16} cm^{-2}) and similar implantation/annealing temperatures, the formation of α-Fe precipitates has been found.[7] Considering the interstitial nature of Fe_D, which is partially converted to Fe(III), it is tempting to suggest that this could reflect the embryonic formation of larger precipitates, i.e., dimers or slightly larger clusters. In this case, the relaxation mechanism would be expected to occur as spin-spin interaction. This is in accordance with a maximum concentration of Fe which is of the order ~0.04 at. %, in the implantation profile, which is much lower than the 0.1 at. %, when spin-spin relaxations start to dominate.[14,15] If the Fe^{3+} were dilutely distributed within the matrix at a concentration of ~0.04 at. %, one would expect it to show a smeared sextet-type of spectrum due to slow paramagnetic relaxation.[5] Therefore, it is concluded that the high relaxation rate is due to spin-spin interactions, presumably in precipitates. Based on the annealing data and concentration of Fe atoms, the necessary diffusion coefficient of interstitial Fe to form dimers is estimated to $D \sim 10^{-16}$ cm^2/s at 773 K.

In summary, ^{57}Fe MES following the ZnO implantation with ^{57*}Co/^{57}Fe up to (5–6) × 10^{14} cm^{-2} show that ~20% of the probe atoms is located on distorted substitutional Zn sites and the remainder as Fe^{2+} in damage sites with interstitial character, and we show that these data are compatible with CEMS measurements on $>2 \times 10^{16}$ ^{57}Fe implanted samples at 623 K.[7–10] Upon annealing at 773 K for 30 min, the Fe^{2+} on crystalline sites shows less distortion, and the interstitial fraction is partly transformed into high-spin Fe^{3+} (~30%), presumably located in precipitates. It is suggested that the precipitation pathway shown here is the origin also for larger α-Fe precipitates observed previously by CEMS for higher implanted fluences,[7] whereas the analysis and interpretation of the other components in those spectra are at least questionable as angular dependence was not taken into account. The results obtained here differ from results obtained with low fluence ($<10^{12}$ cm^{-2}) implantations of ^{57}Mn, where the crystalline fraction dominates with no damage fraction observed at RT, suggesting that the formation of interstitial damage fraction is related to the implantation fluence. The

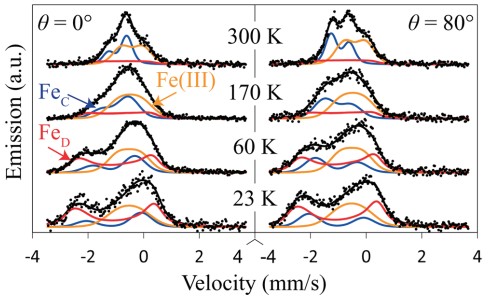

FIG. 4. (Color online) MES obtained on the ^{57}Co implanted ZnO single-crystal sample after annealing at 773 K for 30 min.

presented analysis and interpretation give a plausible explanation (precipitates formation) to some of the discrepancies found in the literature concerning dilute magnetism in 3d-metal-doped ZnO.

This work was supported by the European Union 7th Framework through ENSAR. K. Bharuth-Ram, H. Masenda, and D. Naidoo acknowledge support from the South African National Research Foundation. T. E. Mølholt acknowledges support from the Icelandic Research Fund. Financial support of the German BMBF Contract No. 05KK4TS1/9 is also gratefully acknowledged.

[1]T. Dietl, H. Ohno, F. Matsukura, J. Cibert, and D. Ferrand, Science **287**, 1019 (2000).
[2]R. Janisch, P. Gopal, and N. A. Spaldin, J. Phys.: Condens. Matter **17**, R657 (2005).
[3]K. Ando, Science **312**, 1883 (2006).
[4]Ü. Özgür, Y. I. Alivov, C. Liu, A. Teke, M. A. Reshchikov, S. Doğan, V. Avrutin, S.-J. Cho, and H. Morkoç, J. Appl. Phys. **98**, 041301 (2005).
[5]H. P. Gunnlaugsson, T. E. Mølholt, R. Mantovan, H. Masenda, D. Naidoo, W. B. Dlamini, R. Sielemann, K. Bharuth-Ram, G. Weyer, K. Johnston, G. Langouche, S. Ólafsson, H. P. Gíslason, Y. Kobayashi, Y. Yoshida, M. Fanciulli, and ISOLDE Coll., Appl. Phys. Lett. **97**, 142501 (2010).
[6]G. Weyer, H. P. Gunnlaugsson, R. Mantovan, M. Fanciulli, D. Naidoo, K. Bharuth-Ram, and T. Agne, J. Appl. Phys. **102**, 113915 (2007).
[7]K. Potzger, S. Zhou, H. Reuther, A. Mücklich, F. Eichhorn, N. Schell, W. Skorupa, M. Helm, J. Fassbender, T. Herrmannsdörfer, and T. P. Papageorgiou, Appl. Phys. Lett. **88**, 052508 (2006).
[8]K. Potzger, W. Anwand, H. Reuther, S. Zhou, G. Talut, G. Brauer, W. Skorupa, and J. Fassbender, J. Appl. Phys. **101**, 033906 (2007).
[9]S. Zhou, K. Potzger, H. Reuther, G. Talut, F. Eichhorn, J. von Borany, W. Skorupa, M. Helm, and J. Fassbender, J. Phys. D: Appl. Phys. **40**, 964 (2007).
[10]S. Zhou, K. Potzger, G. Talut, H. Reuther, J. von Borany, R. Grötzschel, W. Skorupa, M. Helm, J. Fassbender, N. Volbers, M. Lorenz, and T. Herrmannsdörfer, J. Appl. Phys. **103**, 023902 (2008).
[11]H. P. Gunnlaugsson, Hyperfine Interact. **167**, 851 (2006).
[12]R. Ingalls, Phys. Rev. **133**, A787 (1964).
[13]T. E. Mølholt, H. P. Gunnlaugsson, K. Johnston, R. Mantovan, H. Masenda, D. Naidoo, S. Ólafsson, K. Bharuth-Ram, H. P. Gislason, G. Langouche, R. Sielemann, G. Weyer, and ISOLDE Coll., Phys. Scr. "Spin-lattice relaxations of Fe3+ in ZnO", (in press).
[14]L. E. Campbell and S. DeBenedetti, Phys. Rev. **167**, 556 (1968).
[15]S. Mørup, in *Mössbauer Spectroscopy and Transition Metal Chemistry Fundamentals and Application*, edited by P. Gütlich, E. Bill, and A. X. Trautwein (Springer, Berlin Heidelberg, Berlin, 2011).

Paper VIII

Lattice Location and Diffusion of Interstitial Fe in MgO

Mølholt, T. E., Mantovan, R., Gunnlaugsson, H. P., Svane, A., Bharuth-Ram, K., Fanciulli, M., Gíslason, H. P., Johnston, K., Kobayashi, Y., Langouche, G., Masenda, H., Naidoo, D., Ólafsson, S., Sielemann, R., and Weyer, G.:

Manuscript in preparation (Nov. 2012)

Lattice Location and Diffusion of Interstitial Fe in MgO

T. E. Mølholt[1,†], R. Mantovan[2], H. P. Gunnlaugsson[3], A. Svane[3], K. Bharuth-Ram[4], M. Fanciulli[2,5], H. P. Gislason[1], K. Johnston[6], Y. Kobayashi[7], G. Langouche[8], H. Masenda[9], D. Naidoo[9], S. Ólafsson[1], R. Sielemann[10], G. Weyer[3]

[1]Science Institute, University of Iceland, Dunhaga 3, IS-107 Reykjavík, Iceland;
[2]Laboratorio MDM, IMM-CNR, Via Olivetti 2, 20041 Agrate Brianza (MB), Italy;
[3]Department of Physics and Astronomy, Aarhus University, DK-8000 Aarhus C, Denmark;
[4]School of Physics, University of KwaZulu-Natal, Durban 4000, South Africa;
[5]Dipartimento di Scienza dei Materiali, Università di Milano Bicocca, Milano, Italy;
[6]PH Dept, ISOLDE/CERN, 1211 Geneva 23, Switzerland;
[7]The Institute of Physical and Chemical Research (RIKEN), Wako, Saitama 351-0198, Japan;
[8]Instituut voor Kern-en Stralingsfysika, University of Leuven, B-3001 Leuven, Belgium;
[9]School of Physics, University of the Witwatersrand, WITS 2050, South Africa;
[10]Helmholtz-Zentrum Berlin für Materialien und Energie, D-14109 Berlin, Germany.

Abstract

^{57}Fe atoms excited in the 14.4 keV Mössbauer state have been created in MgO at 90–650 K as a result of ion-implanted ^{57}Mn. During its nuclear β^--decay the recoil imparted by the parent ^{57}Mn at substitutional sites re-implants a fraction of the ^{57}Fe directly into interstitial sites. The interstitial Fe in MgO has been identified from comparison of the hyperfine parameters of the spectral components observed in emission Mössbauer spectra and *ab initio* calculations of the isomer shifts for different lattice locations. Contrary to expectations, the stable interstitial Fe site is found on the face centre of the cubic rock-salt structure of MgO. The calculations predict a low energy barrier for diffusional jumps between different interstitial Fe sites, predicting a fast diffusion mechanism which is consistent with the experimental results. Fast diffusion of interstitial iron in MgO could be a source of precipitation of Fe into clusters, a factor that has to be taken into account when interpreting data on dilute magnetism in oxides.

PACS: 76.80.+y, 60.30.J-, 61.72.jj

Introduction

The detailed knowledge of metal impurities behaviour in MgO is of importance for the controlled fabrication of nano-precipitates for optical and spintronic applications [1–3]. For magnetic tunnel junctions such as Fe/MgO systems in spintronic devices it could be of interest for a full understanding of

thermal stability (see e.g. [4,5]). Recently, there have been reports of metal-defect-mediated magnetism in MgO single-crystals [1,6], and magnetism entirely due to intrinsic defects in the case of MgO nanograins [7] and thin films [8]. The mobility of metal impurities in binary oxides (at processing temperatures) often results in unintentional precipitation, a factor which should be considered when interpreting observed dilute magnetism in binary oxides such as MgO or ZnO. In MgO, anomalous diffusion of metal impurities has been reported by several authors [1,9–11]. Weeks *et al*. [9] found evidence for fast diffusion of Fe as Fe atoms was observed to aggregate at temperatures as low as 350ºC. This was reviewed by Sangster *et al*. [12] but they found vacancy assisted diffusion of Fe to be too slow to explain the results reported by Week *et al.*, and suggested grain boundary diffusion mechanisms. Other evidence of fast diffusion of metal impurities in MgO includes radiation enhanced diffusion of titanium in MgO upon implantation and annealing as reported by Lu *et al*. [10]. Zimmerman *et al*. [3] found Cu to form precipitates in MgO upon implantation at room temperature and the data of Fuchs *et al*. [11] suggest diffusion of Ag atoms below room temperature.

It is evident that, if a fast diffusion mechanism of Fe in MgO exists, this could lead to the (unexpected) formation of Fe precipitates. This mechanism has to be taken into account when interpreting data suggesting dilute magnetism in MgO. The detailed knowledge of this could be used to control beneficial precipitation of nanometre sized metal colloids for spintronic and/or optical applications [1–6,11,13].

Experimental

^{57}Fe emission Mössbauer spectra were measured upon implantation of radioactive $^{57}Mn^{+}$ ($T_{½}$ = 85.4 s) produced at ISOLDE/CERN by 1.4 GeV proton-induced fission in UC_2 target and elemental selective laser multi-photon ionization [14]. After acceleration to 50–60 keV and magnetic mass separation, a pure beam of ~2×10^{8} $^{57}Mn^{+}$/s was obtained. $^{57}Mn^{+}$ was implanted into MgO single-crystals (maximum fluence ~1×10^{12} cm^{-2}) mounted in an implantation chamber and held at temperatures ranging from 90–650 K. The implantation was performed at an incident angle of 30° relative to the sample surface normal. Mössbauer emission spectra were measured on-line, on the Mössbauer state of the daughter ^{57*}Fe ($T_{½}$ = 98 ns) with an acetone gas-filled resonance detector equipped with ^{57}Fe enriched stainless steel electrodes. The detector was mounted outside the implantation chamber on a conventional constant-acceleration drive system at 90° to the beam direction (60° relative to the crystal surface normal).

Velocities and isomer shifts are given relative to α-Fe at room temperature. In the decay of the implanted ^{57}Mn the daughter ^{57*}Fe nucleus receives an average recoil of 40 eV. This causes a sizeable fraction (~10%) of the Fe-atoms to be expelled into interstitial sites. The Mössbauer probe is sensitive only to its local environment (a few lattice constants) and gives information on its valence state, local symmetry and hyperfine magnetic field [15]. The method allows us to study truly dilute samples with concentrations of Fe below 10^{16} cm^{-3} [16].

Results

Fig. 1(a) shows the Mössbauer spectrum obtained at 90 K in detail and Fig. 1(b) shows the central part of representative spectra in the 90–650 K temperature range.

Above 295 K, the Mössbauer spectra are dominated by a single line Fe_S. The isomer shift of this line, $\delta \sim 1$ mm/s is characteristic for high spin Fe^{2+} and the vanishing quadrupole splitting with increasing temperature is consistent with substitutional Fe^{2+} on a cubic Mg site.

Below 295 K, a broadening of Fe_S is observed, and the spectra are dominated by an asymmetric quadrupole doublet, Fe_D, assigned to Fe^{2+} in implantation-related heavily damaged/amorphous regions showing considerable annealing at increased temperatures. In the analysis, this component was described with two Voigt profiles of the same spectral area but with different Gaussian broadening, similar to damaged/amorphous sites observed in Si [17,18] and α-Al_2O_3 [19].
At each temperature, the wings of the spectra show a magnetic sextet structure, which are attributed to Fe^{3+} species showing slow paramagnetic relaxations, similar to those observed in ZnO [20,21]. The temperature-dependent broadening of the magnetic features was found to be consistent with spin-lattice relaxation rates of paramagnetic Fe^{3+} in MgO [22].

The analysis of the central part of the spectra with the components described above was not sufficient, especially at temperatures below 200 K. In addition, a single line with isomer shift $\delta \sim$ -0.3 mm/s was required in order to obtain acceptable fits. This line is not observed in Mössbauer spectra of MgO implanted with ^{57}Fe [25] or ^{57}Co doped MgO [34]. A reasonable assumption is to assign this line to interstitial Fe (Fe_I) due to the $\langle E_R \rangle$ = 40 eV recoil imparted on ^{57*}Fe in the β^--decay of ^{57}Mn.

In the analysis presented in Fig. 1 the isomer shifts of all components, except Fe_D, were set to follow the second order Doppler shift (SOD) with temperature, and the magnetic part of the spectrum was analysed using the model described in

Ref. [22]. For both Fe_S and Fe_D the quadrupole splitting was set as a free variable in the temperature series.

All spectral lines were analysed using the Voigt profile, a convolution of a Gaussian profile with a standard deviation σ and a Lorentzian profile with a FWHM line-width Γ. This takes into account the intrinsic line-width of the detector as well as broadening effects due to the experimental setup (the experimental line-width based on the calibration spectrum has $\sigma_{Det.} = 0.1$ mm/s and $\Gamma_{Det} = 0.34$ mm/s). The extracted hyperfine parameters for Fe_S, Fe_D and Fe_I are collected in Table 1 and the spectral areas are shown in Fig. 2.

The isomer shift for Fe_S is in good agreement with values from the literature for substitutional Fe^{2+} on substituting Mg sites [23–25]. The isomer shift and quadrupole splitting of the Fe_D component are in agreement with average values of Fe^{2+} in implantation damaged regions from Mössbauer spectroscopy of samples implanted with stable ^{57}Fe [25].

The line-width of Fe_S is found to increase at low temperature (Fig. 1b). A broadening/splitting of the substitutional line at low temperatures ($T < 20$ K) has been observed and explained in terms of slow paramagnetic relaxation of the substitutional Fe^{2+} [24]. This is, however, at temperatures much lower than in our measurements, leading us to conclude that the broadening of the substitutional line in our experiments is related to lattice distortions, due to defects in the vicinity of the Fe atoms annealing at elevated temperatures.

Fe_D is found to have a decreasing quadrupole splitting with increasing temperature and shows strong annealing (i.e. less relative intensity at increasing temperatures, cf. Fig. 2). At temperatures below 295 K, the fitted isomer shift follows the SOD, but above, it tends to shift to a higher value.

To substantiate the assignment of Fe_I, quantum mechanical calculations based on the local density approximation to density functional theory [26] were performed for a 64-atom MgO supercell with an interstitial Fe atom. The total energy was evaluated as a function of the Fe position. All other atomic coordinates were relaxed in response to the forces exerted.

Somewhat surprisingly, the highly symmetric interstitial site, located at the centre of the cube equidistant to four Mg^{2+} and O^{2-} ions, is not energetically favourable (cf. Fig. 3, site *A*). The energy at this position is 1.2 eV higher than the lowest energy position which is found at, or close to, the face of the cube (Fig 3 site *B*).

The energy in the neighbourhood of site *B* was estimated (path from site *C* to *B*), and the diffusional barrier for long range diffusion of interstitial Fe from this site was found to be is only ~0.2 eV, as opposed to the barrier of 1.2 eV for diffusional jumps through site *A*. The energy landscape is quite shallow around

the facial position, and, within numerical accuracy, it is not possible to establish whether the minimum occurs exactly on the face (site *B*) or at a nearby position of lower symmetry.

The isomer shift of the interstitial Fe atom at the lowest energy site (*B* in Fig. 3) was evaluated using the calibration of Eriksson *et al*. [27]. For the equilibrium position, an isomer shift of δ = -0.33 mm/s was calculated, which is in a better agreement with the experimental value δ = -0.28(2) mm/s (cf. Table 1) than the value of δ = +0.66 mm/s for site *A*.

A lattice site at or close to the face of the rock-salt structure would be expected to give rise to a sizeable quadrupole splitting of the Fe_I line due to a non-zero electrical field gradient (*EFG*) at this location. However this is not observed in our experimental results. The explanation for this may be found in a careful study of the energy landscape around the face-site. For an energetically favourable position close (~0.2 Å) to the face, a cage motion of the interstitial Fe would be expected, i.e. jumps through the face to another favourable position without long range diffusion. Fast cage motion compared to the lifetime of the Mössbauer state would result in a vanishing quadrupole splitting [28], and reduced intensity of the interstitial line [29]. A transition from a slow to a fast cage motion has been reported in Al [30] and α-Zr [31], taking place at much lower temperatures than we can measure at in the current setup. Such a cage barrier would be expected to be of the order of tenths of meV, which is below the resolution of the numerical calculations.

The calculations predicts a low barrier for long range diffusion of the interstitial Fe atom in MgO (~0.2 eV, jump from site *B* through site *C* see Fig. 3). This should give rise to a broadening of the Mössbauer line [32]. In order to test this prediction, a re-analysis of the Mössbauer data was performed, where an additional Lorentzian broadening was included for the Fe_I line. Indeed, such an analysis was found to give lower χ^2 values of the simulation, which also made the isomer shift of Fe_D follow the SOD throughout the temperature range. The Lorentzian broadening of the interstitial line for the re-analysed temperature series is shown in Fig. 4. Above 360 K the interstitial line is too broad for the simulation to fit the broadening, but the analysis is consistent with increasing broadening throughout the whole measured temperature series. The hyperfine parameters obtained in this revised analysis changed less than the errors presented in Table 1, and the major change in the area fractions is a slightly increased area fraction (1–5% with the highest increase around 295 K) of the Fe_I component.

The low spectral intensity of the Fe_I line and its overlap with the right leg of the Fe_D doublet component (Fig. 1), make an accurate determination of the Fe_I

diffusional broadening difficult, but the main conclusion is that the Mössbauer data are consistent with a broadened Fe_I line as would be expected from the *ab initio* calculations.

At room temperature, the broadening is $\Delta\Gamma \sim 0.5$ mm/s. Using the relationship between the broadening and the diffusion coefficient, D, for jumps to adjunct sides of the rock salt structure [32] gives $D \sim 7(2)\times10^{-10}$ cm^2/s at room temperature which is orders of magnitude higher than that suggested for vacancy-assisted Fe diffusion in MgO [12], or observed in tracer studies [33]. Extrapolation of the values given by Wuensch *et al*. [33] to room temperature gives a diffusion coefficient $D = 5\times10^{-35}$ cm^2/s.

In view of the fast diffusion of interstitial Fe in MgO, we propose this mechanism as responsible for the unexpected precipitation of metal impurities in MgO, as observed by several authors [1,9,11]. This leads to the suggestion that the interpretation of the dilute magnetism sometimes observed in MgO has to consider the possible clustering of ferromagnetic impurities at relatively low temperatures, even lower than 295 K. Fe diffusion towards the CoFeB/MgO interface has been previously reported [5]. If one assumes that a fraction of Fe reaching the interface can diffuse into the MgO lattice at relatively low temperatures (present results), this could have an impact on the full understanding of the temperature behaviour of tunnel magnetoresistance in MgO-based magnetic tunnel junctions.

In summary, we have measured the ^{57}Fe Mössbauer spectra obtained after implantation of ^{57}Mn into MgO single crystals. A spectral feature assigned to interstitial Fe (Fe_I) has been identified. With *ab initio* calculations it has been possible to show that this component arises from an Fe atom sitting on the face of the cube of the rock-salt fcc structure. Our results suggest a possible broadening of the Fe_I spectral line consistent with a few jumps (0.5–2 jumps) of the probe atoms during the lifetime of the Mössbauer state. We have derived the diffusion coefficient $D \sim 7(2)\times10^{-10}$ cm^2/s at $T = 300$ K. Such a high diffusion could lead to unintentionally precipitation of Fe impurities, when e.g. samples containing Fe, are quenched from high temperatures.

Acknowledgments

This work was supported by the European Union Sixth Framework through RII3-EURONS. K. Bharuth-Ram, H. Masenda and D. Naidoo acknowledge support from the South African National Research Foundation. R. Mantovan acknowledges support from the Cariplo Foundation ($SPAM^3$ project, code n. 2008.2363). Financial support of the German BMBF (contract no. 05KK4TS1/9) is also gratefully acknowledged. T. E. Mølholt acknowledges support from the Icelandic Research Fund.

References

†Corresponding author: tem4@hi.is

[1] S. Ramachandran *et al*., Appl. Phys. Lett. **90**, 132511 (2007).
[2] J. Narayan *et al.*, J. Magn. Magn. Mater. **61**, 76 (2009).
[3] R. L. Zimmerman *et al*., Nucl. Instrum. Methods. **B141**, 308 (1998).
[4] S. Yuasa *et al.*, Nature Materials 3, 868 - 871 (2004), doi:10.1038/nmat1257.
[5] A. T. Hindmarch *et al.*. Appl. Phys. Lett **96**, 092501 (2010), 10.1063/1.3332576.
[6] L. Li *et al*., J. Phys. D, **42**, 155003 (2009).
[7] J. Hu *et al*., Appl. Phys. Lett. **93**, 192503 (2008).
[8] C. M. Araujo *et al*., Appl. Phys. Lett. **96**, 232505 (2010).
[9] R. A. Weeks *et al*., Phys Status Solidi A, **61**, 265 (1980).
[10] M. Lu *et al*., Appl. Phys. Lett., **81**, 5033 (2002).
[11] G. Fuchs *et al*., Nucl. Instrum. Methods, **B32**, 100 (1988).
[12] M. J. L. Sangster and A. M. Stoneham J. Phys. C, **17**, 6093 (1984).
[13] J. Narayan *et al*., Appl. Phys. Lett., **93**, 082507 (2008).
[14] V. N. Fedoseyev *et al*., Nucl. Instrum. Methods B, **126**, 88 (1997).
[15] V. I. Goldanskii, and R. H. Herber, in/by *Chemical Applications of Mössbauer Spectroscopy* (Academic, New York, 1968).
[16] G. Weyer *et al*., J. Appl. Phys., **102**, 113915 (2007).
[17] G. Weyer *et al*., Nucl. Instrum. Methods B, **206**, 90 (2003).
[18] H. P. Gunnlaugsson *et al*., Nucl. Instrum. Methods B, **186**, 55 (2002).
[19] H. P. Gunnlaugsson *et al.*, Hyp. Int. **198**, 5 (2010).
[20] H. P. Gunnlaugsson *et al*., Appl. Phys. Lett., **97**, 142501 (2010), doi:10.1063/1.3490708
[21] H. P. Gunnlaugsson *et al*., Hyp. Inter. **197**, 43(2010).
[22] T. E. Mølholt *et al.* Hyp. Inter. **197**, 89 (2010), doi:10.1007/s10751010-0214-3.

[23] D. J. Simkin *et al*., Phys. Lett., **19**, 536 (1965).
[24] H. R. Leider and D. N. Pipkorn, Phys. Rev. **165**, 494 (1968).
[25] A. Perez *et al*., Phys. Rev. B, **28**, 1227 (1983).
[26] M. Methfessel *et al*., Lecture Notes in Physics, edited by H. Dreysse (Springer-Verlag, Berlin, 2000) Vol. 535, p. 114.
[27] O. Eriksson and A. Svane, J. Phys. Cond. Matter, **1**, 1589 (1989).
[28] J. A. Tjon and M. Blume, Phys. Rev. **165**, 456 (1968).
[29] W. Petry and G. Vogl, Z. Phys. B - Condensed Matter **45**, 207 (1982).
[30] W. Petry, G. Vogl and W. Mansel, Phys. Rev. Lett **45**, 1862 (1980).
[31] Y. Yoshida *et al*., Phys. Rev. Lett. **61**, 195 (1988).
[32] K. S. Singwi and S. Sjölander, Phys. Rev., **120**, 1093 (1960).
[33] B. J. Wuensch and T. Vasilos, J. Chem. Phys. **36**, 2917 (1962).
[34] J. Chappert, R. B. Frankel and A. Misetich, Phys. Rev. 179, 578 (1969).

Tables and Figures

Table 1:
Table 1: Room temperature hyperfine parameters of paramagnetic components obtained from simultaneous analysis of the spectra in Fig. 1. The table lists the isomer shift (δ), quadrupole splitting (ΔE_Q), and the additional Gaussian broadening ($\Delta\sigma$) after having subtracted the intrinsic line-width of the experimental setup. Values with omitted errors were not included as fitting variables.

	Fe^{2+}_S	Fe^{2+}_D	Fe_I
δ (mm/s)	0.98(2)	1.01(2)	-0.28(2)
ΔE_Q (mm/s) [a]	0.16(2)	1.59(5)	0
$\Delta\sigma$ (mm/s)	0.05(2) [a]	0.35(2) 0.21(2)	0.08(2)

[a] At $T = 295$ K.

Figure 1

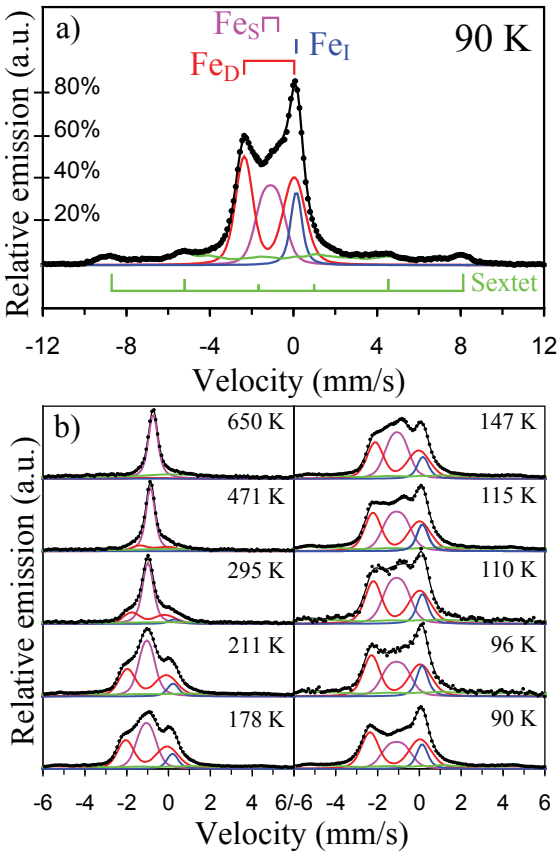

FIG. 1. a) The ^{57}Fe Mössbauer spectrum at full velocity scale obtained at 90 K with a bar diagram indicating fitting components. b) Central part of the spectra obtained at the temperatures indicated.

Figure 2

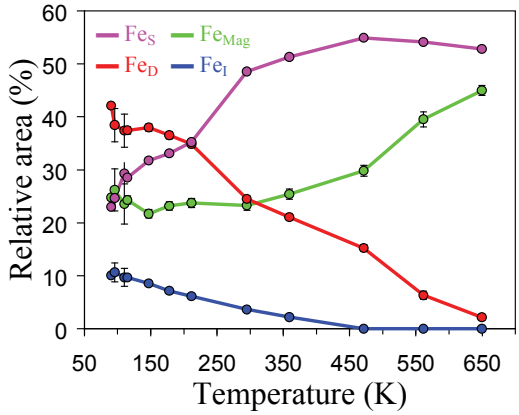

FIG. 2. The relative areas of the spectral components as a function of temperature.

Figure 3

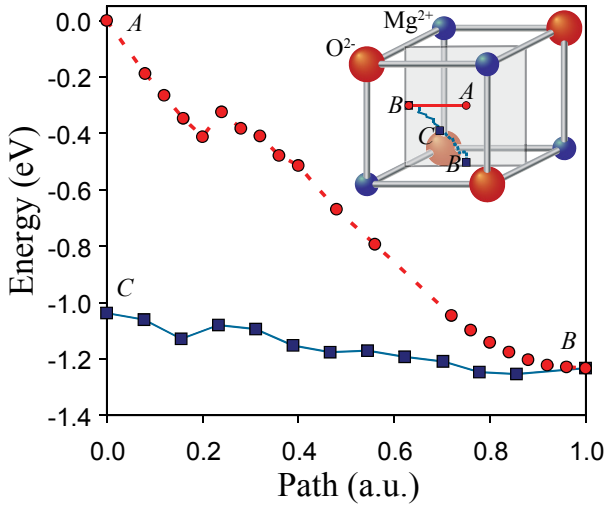

FIG. 3: Energy of the interstitial Fe atom calculated along the paths indicated in the insert figure showing the (004) plane within the unit cell. *A* indicates the interstitial site at the cube centre, *B* the interstitial site at the centre of the cube face and *C* on the path from one face side to the next.

Figure 4

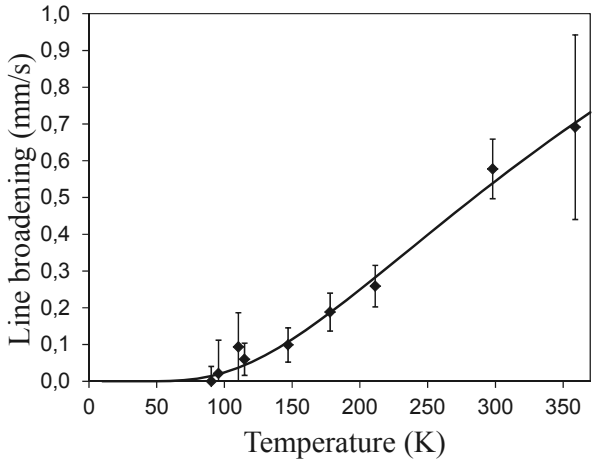

FIG. 4: Lorentzian broadening of single line assigned to interstitial Fe as a function of temperature. The solid line is to guide the eye.

9 References

Abragam A. and Bleaney B: Electron Paramagnetic Resonance of Transition Ions, Clarendon, Oxford, U.K., ISBN 978-0198512509, Ch. 10. (1970).

Ammar E.A.E. and Thorp J. S.: *J. Mat. Sci.* **12**, 2087. DOI: 10.1007/BF00561983. (1977).

Ando K.: *Science* **312**, 1883. DOI: 10.1126/science.1125461. (2006).

Auret F.D., Goodman S.A., Hayes M., Legodi M.J., van Laarhoven H.A. Look D.C., *Appl. Phys. Lett.* **79**, 3074. DOI:10.1063/1.1415050. (2001).

Bhargava S. C., Knudsen J. E., Mørup S.: *J. Phys. C: Solid State Phys.* **12**, 2879. DOI:10.1088/0022-3719/12/14/023. (1979).

de Biasi, R.S. and Portella, P.D.J.: *J. Magn. Magn. Mater.* **15**, 737. DOI:10.1016/0304-8853(80)90741-6. (1980).

Bloembergen N., Shapiro S., Pershan P.S., Artman J.O.: *Phys. Rev.* **114** 445. DOI:10.1103/PhysRev.114.445. (1959).

Blume M. and Tjon J.A.: *Phys. Rev.* **165**, 446. DOI: 10.1103/PhysRev.165.446. (1968).

CERN: European Organization for Nuclear Research http://public.web.cern.ch/ [Online; accessed] (2012).

Chambers S.: *Nature Materials* **9**, 956. DOI:10.1038/nmat2905. (2010).

Clauser M.J.: *Phys. Rev. B* **3**, 3748. DOI:10.1103/PhysRevB.3.3748. (1971).

Coey J. M. D., Venkatesan M., Fitzgerald C. B. : *Nature Materials* **4**, 173. DOI:10.1038/nmat1310 (2005).

Crangle J.: Solid state magnetism, Edward Arnold, Great Britten, ISBN 978-0-340-54552-2, (1991).

Deicher, M. and the ISOLDE collaboration: *Eur. Phys. J.* **A15**, 275. DOI:10.1140/epja/i2001-10267-y. (2002).

Dietl T.: *Semicond. Sci. Technol*. **17**, 377. DOI:10.1088/0268-1242/17/4/310. (2002).

Dietl T., Ohno H., Matsukura F., Cibert J., and Ferrand D.: *Science* **287**, 1019. DOI:10.1126/science.287.5455.1019 (2000).

Drouin D., Couture A. R., Joly D., Tastet X., Aimez V., Gauvin R.: *Scanning* **29**, 92. DOI:10.1002/sca.20000. (2007).

Dyar, M.D., Agresti, D.G., Schaefer, M.W., Grant, C.A., Sklute, E.C.: *Annu. Rev. Earth Planet. Sci.* **34**, 83 DOI: 10.1146/annurev.earth.34.031405.125049. (2006).

Fanciulli M., Bharuth-Ram K., Debernardi A., Gislason H.P., Gunnlaugsson H.P., Helgason Ö., Johnston K., Mantovan R., Olafsson S., Naidoo D., Sielemann R., Scare G., Weyer G.: CERN-INTC-2006-005 / INTC-P-203 (ISOLDE experiment nr. IS443) (2006).

Fedoseyev V.N., Bätzner K., Catherall R., Evens A.H.M., Forkel-Wirth D., Jonsson O.C., Kugler E., Lettry J., Mishin V.I., Ravn H.L., Weyer G., and ISOLDE Collaboration: *Nucl. Instrum. Methods Phys. Res. B* **126**, 88. DOI:10.1016/S0168-583X(96)01077-4. (1997).

Furdyna J.K.: *J. Appl. Phys*. **64**, R29. DOI:10.1063/1.341700. (1988).

Goldanskii V.I. and Herber R.H. (*Editors*): Chemical Applications of Mössbauer Spectroscopy, Academic, New York, ISBN 978-0-122-87350-8. (1968).

Gonser, U., Topics in Applied Physics Volume 5: Mössbauer Spectroscopy, Springer-Verlag, Berlin (1975).

Gražulis, S., Daškevič, A., Merkys, A., Chateigner, D., Lutterotti, L., Quirós, M., Serebryanaya, N. R., Moeck, P., Downs, R. T., LeBail, A.: *Nucleic Acids Research* **40**, D420. DOI:10.1093/nar/gkr900. (2012).

Gunnlaugsson H.P.: Vinda version B Setup10. Excel macros for analysis of Mössbauer spectra: http://users-phys.au.dk/hpg/vinda.htm [Online; accessed] (2012b).

Gunnlaugsson H.P., Langouche G., Johnston K., Masenda H., Mantovan R., Mølholt T.E., Bharuth-Ram K., Gislason H. P., Madsen M.B., Naidoo D., Ólafsson S., Weyer G., the ISOLDE Collaboration: Possible cage motion of interstitial Fe in α-Al_2O_3, *Hyp. Int.,* in press (2012a).

Gunnlaugsson H.P., Mølholt T.E., Mantovan R., Masenda H., Naidoo D., Dlamini W.B., Sielemann R., Bharuth-Ram K., Fanciulli M., Gíslason H.P., Johnston K., Kobayashi Y., Langouche G., Ólafsson S., Yoshida Y., Weyer G., Decoster S., Correia J.G., Araújo J.P., Barbosa M.B., Lopes A.L.: CERN-INTC-2010-003 / INTC-P-275 (ISOLDE experiment nr. IS501) (2010)

Gunnlaugsson H.P., Weyer G., Mantovan R., Naidoo D., Sielemann R., Bharuth-Ram K., Fanciulli M., Johnston K., Olafsson S., Langouche G.: *Hyp. Int.* **188**, 85. DOI:10.1007/s10751-008-9893-4. (2009).

Gunnlaugsson H.P., Fanciulli M., Dietrich M., Bharuth-Ram K., Sielemann R., Weyer G., the ISOLDE collaboration: *Nucl. Inst. Meth. B*, **186**, 55. DOI:10.1016/S0168-583X(01)00858-8. (2002).

Gütlich P., Bill E., Trautwein A.X. (*Editors*): Mössbauer Spectroscopy and Transition Metal Chemistry Fundamentals and Applications, Springer-Verlag Berlin Heidelberg, ISBN 978-3-540-88427-9. (2011).

Hong N.H., Sakai J., Brizé V.: *J. Phys. Condens. Matter* **19**, 036219. DOI:10.1088/0953-8984/19/3/036219. (2007).

Hong N.H., Brizé V., Sakai J.: *App. Phys. Lett.* **86**, 082505. DOI:10.1063/1.1875752. (2005).

Ingalls R., *Phys. Rev.* **133**, A787. DOI:10.1103/PhysRev.133.A787. (1964).

Janotti A. and Walle C.G. Van de: *Phys. Rev. B* **76**, 165202. DOI:10.1103/PhysRevB.76.165202. (2007).

Jung S.W., An S.-J., Yi Gyu-Chul, Jung C. U., Lee Sung-Ik, and Cho S.: *Appl. Phys. Lett.* **80**, 4561. DOI:10.1063/1.1487927. (2002).

Kalvius M., Kienle P. (*Editors*): The Rudolf Mössbauer Story His Scientific Work and Its Impact on Science and History, Springer-Verlag Berlin Heidelberg, ISBN 978-3-642-17951-8. (2012).

Kapilashrami M., Xu J., Ström V., Rao K.V., Belova L.: *Appl. Phys. Lett.* **95**, 033104. DOI:10.1063/1.3180708. (2009).

Kittel C.: Introduction to Solid State Physics, John Wiley & Sons Inc., U.S., ISBN 978-0471415268, (1996).

Lang G.: *Phys. Lett.* **26A**, 223. DOI: 10.1016/0375-9601(68)90613-0. (1968)

Look D.C., Reynolds D.C., Hemsky J.W., Jones R.L., Sizelove J.R.: *Appl. Phys. Lett.* **75**, 811. DOI:10.1063/1.124521. (1999).

Mantovan R., Gunnlaugsson H.P., Naidoo D., Ólafsson S., Johnston K., Masenda H., Mølholt T.E., Bharuth-Ram K., Fanciulli M., Gislason H.P., Langouche G., Sielemann R., Weyer G., and the ISOLDE Collaboration: Fe charge state adjustment in ZnO upon ion implantation, *Journal of Physics: Condensed Matter.*, accepted for publication (2012).

Mark S., Dürrenfeld P., Pappert K., Ebel L., Brunner K., Gould C., Molenkamp L. W.: *Phys. Rev. Lett.* **106**, 057204. DOI: 10.1103/PhysRevLett.106.057204. (2011).

Mayer J.W., Eriksson L., Picraux S.T., Davies J.A.: *Can. J. Phys*. **46**, 663. DOI :10.1139/p68-082. (1968).

Mørup S.: in Mössbauer Spectroscopy and Transition Metal Chemistry Fundamentals and Application, Gütlich P., Bill E., and Trautwein A.X. (*Editors*), Springer-Verlag Berlin Heidelberg, ISBN 978-3-540-88427-9 (2011) Ch. 6.

Narayan J., Sudhakar N., Pandya D.K., Avasthi D.K., Smirnov A.I.: *Appl. Phys. Lett.* **93**, 082507. DOI:10.1063/1.2977614. (2008).

NNDC: National Nuclear Decay Center, *Brookhaven National Laboratory*: http://www.nndc.bnl.gov/ [Online; accessed] (2012).

Ohno H.: *Science* **281**, 951. DOI:10.1126/science.281.5379.951. (1998).

Pearton S.J., Abernathy C.R., Norton D.P., Hebard A.F., Park Y.D., Boatner L.A., Budai J.D.: *Mater. Sci. Eng. R* 40, 137. DOI:10.1016/S0927-796X(02)00136-5. (2003).

Petry W. and Vogl G.: *Z. Phys. B - Condensed Matter* **45**, 207. DOI:10.1007/BF01307707. (1982).

Poole C.P.Jr.: Electron spin resonance: a comprehensive treatise on experimental techniques, John Wiley & Sons Inc. U.S., ISBN 978-0-471-04678-3 (1983).

Potzger K. and Zhou S.: *Phys. Status Solidi B* **246**, 1147. DOI: 10.1002/pssb.200844272. (2009).

Potzger K., Anwand W., Reuther H., Zhou S., Talut G., Brauer G., Skorupa W., Fassbender J.: *J. Appl. Phys.* **101**, 033906. DOI:10.1063/1.2427103. (2007).

Potzger K., Zhou S., Reuther H., Mücklich A., Eichhorn F., Schell N., Skorupa W., Helm M., Fassbender J., Herrmannsdörfer T., Papageorgiou T. P.: *Appl. Phys. Lett.* **88**, 052508. DOI:10.1063/1.2169912. (2006).

Rita E., Wahl U., Correia J.G., Alves E., Soares J.C., ISOLDE Collaboration: *Appl. Phys. Lett.* **85**, 4899. DOI: 10.1063/1.1825611. (2004).

Sangster M.J.L., Peckham G., Saunderson D.H.: *J. Phys. C: Solid State Phys.* **3**, 1026. DOI: 10.1088/0022-3719/3/5/017. (1970).

Schäfer, C. Potzel W., Adlassnig W., Pöttig P., Ikonen E., Kalvius G. M.: *Phys. Rev. B* **37**, 7247. DOI:10.1103/PhysRevB.37.7247. (1988).

Schünemann V. and Winkler H.: *Rep. Prog. Phys*. **63**, 263. DOI:10.1088/0034-4885/63/3/202. (2000).

Singwi K.S. and Sjölander S.: *Phys. Rev.*, **120**, 1093 (1960).

Srivastava K.K.P and Mishra S.N.: *Phys. Status Solidi B* **100**, 65. DOI:10.1002/pssb.2221000105. (1980).

Stöhr J., Siegmann H.C.: Magnetism From Fundamentals to Nanoscale Dynamics, Springer Berlin Heidelberg New York, ISBN 978-3-540-30282-7 (2006).

Sze S.: Physics of Semiconductor Devices, John Wileys & Sons, Inc. New York, ISBN: 978-0-471-84290-3 (1969).

Tjon J. A. and Blume M.: *Phys. Rev.* **165**, 456. DOI: 10.1103/PhysRev.165.456. (1968).

Wachtman Jr.J.B., Tefft, W.E., Lam D.G.: *Phys. Rev.* **122**, 1754. DOI:10.1103/PhysRev.122.1754. (1961).

Wang L. and Giles N.C.: *J. Appl. Phys.* **94**, 973. DOI:10.1063/1.1586977. (2003).

Wang Q., Sun Q., Jena P., Kawazoe Y.: *Phys. Rev. B* **79**, 115407. DOI:10.1103/PhysRevB.79.115407. (2009).

Wang Q., Sun S., Chen G., Kawazoe Y., Jenu P.: *Phys. Rev. B* **77**, 205411. DOI:10.1103/PhysRevB.77.205411. (2008).

Weeks R.A., Gastineau J., Sonder E.: *Phys Status Solidi A* **61**, 265. DOI:10.1002/pssa.2210610131. (1980).

Wertheim G.K. and Remeika J.P.: *Phys. Lett.* **10**, 14. DOI:10.1016/0031-9163(64)90547-5. (1964).

Weyer G., Gunnlaugsson H.P., Mantovan R., Fanciulli M., Naidoo D., Bharuth-Ram K., Agne T.: *J. Appl. Phys.* **102**, 113915. DOI: 10.1063/1.2821290. (2007).

Weyer G., Gunnlaugsson, H.P., Dietrich, M., Fynbo, H., Bharuth-Ram, K., the ISOLDE Collaboration: *Eur. Phys. J. Appl. Phys*. **27**, 317. DOI:10.1051/epjap:2004060. (2004).

Weyer G., Gunnlaugsson H.P., Dietrich M., Fanciulli M., Bharuth-Ram K., Sielemann R., the ISOLDE collaboration: *Nucl. Instr. Meth. B* **206**, 90. DOI:10.1016/S0168-583X(03)00688-8. (2003).

Weyer G., Burchard A., Fanciulli M., Fedoseyev V. N., Gunnlaugsson H. P., Mishin V. I., Sielemann R., The ISOLDE Collaboration: *Physica B* **273**, 363. DOI:10.1016/S0921-4526(99)00478-0. (1999).

Weyer G.: In Mössbauer Effect Methodology, Gruverman, I.J., Seidel, C.W. (*editors*), vol. 10, p. 301. Plenum, New York (1976).

Wickman H.H., Klein M.P., Shirley D.A.: *Phys. Rev.* **152**, 345. DOI: DOI: 10.1103/PhysRev.152.345. (1966b).

Wickman H.H. and Wertheim G.K.: *Phys. Rev.* **148**, 211. DOI:10.1103/PhysRev.148.211. (1966a).

Wickman H.H, Klein M.P, Shirley D.A.: *J. Chem. Phys.* **42**, 2113. DOI:10.1063/1.1696253. (1965).

Zhou S., Potzger K., Xu Q., Talut G., Lorenz M., Skorupa W., Helm M., Fassbender J., Grundmann M., Schmidt H.: *Vacuum* **83**, S13. DOI:10.1016/j.vacuum.2009.01.030. (2009).

Zhou S., Potzger K., Talut G., Reuther H., Borany J. von, Grötzschel R., Skorupa W., Helm M., Fassbender J., Volbers N., Lorenz M., Herrmannsdörfer T.: *J. Appl. Phys.* **103**, 023902. DOI:10.1063/1.2828060. (2008).

Zhou S., Potzger K., Reuther H., Talut G., Eichhorn F., Borany J. von, Skorupa W., Helm M., Fassbender J.: *J. Phys. D: Appl. Phys.* **40**, 964. DOI:10.1088/0022-3727/40/4/007. (2007).

Ziegler J.F.: SRIM/TRIM simulation software (SRIM-2012), http://www.srim.org [Online; accessed] (2012).

Zuckerman J. J.: *J. Chem. Educ.* **42**, 315. DOI:10.1021/ed042p315. (1965).

Zunger A., Lany S., Raebiger H.: *Physics* **3**, 53. DOI: 10.1103/Physics.3.53. (2010).

Xie Q.Y., Gu M.Q., Huang L., Zhang F.M., Wu X.S.: *AIP Advances* **2**, 012185. DOI:10.1063/1.3698320. (2012).

Özgür Ü., Alivov Ya. I., Liu C., Teke A., Reshchikov M.A., Doğan S., Avrutin V., Cho S.-J., Morkoç H.: *J. Appl. Phys.* **98**, 041301. DOI:10.1063/1.1992666. (2005).